

Julio Flecha Lescún

Computational planning tools in ophthalmology: Intrastromal corneal ring surgery

Director/es

Ariza Gracia, Miguel Ángel
Calvo Calzada, Begoña

<http://zaguan.unizar.es/collection/Tesis>



Universidad
Zaragoza

Tesis Doctoral

COMPUTATIONAL PLANNING TOOLS IN
OPHTHALMOLOGY: INTRASTROMAL CORNEAL
RING SURGERY

Autor

Julio Flecha Lescún

Director/es

Ariza Gracia, Miguel Ángel
Calvo Calzada, Begoña

UNIVERSIDAD DE ZARAGOZA
Escuela de Doctorado

2021

PhD candidate

Julio Flecha-Lescún

Thesis Advisors

PhD. Begoña Calvo Calzada

PhD. Miguel Ángel Ariza-Gracia

**COMPUTATIONAL PLANNING TOOLS
IN OPHTHALMOLOGY:
INTRASTROMAL CORNEAL RING SURGERY**

PhD Program in Biomedical Engineering. University of Zaragoza (December 2020)



Instituto Universitario de Investigación
de Ingeniería de Aragón
Universidad Zaragoza



Universidad
Zaragoza



Escuela de
Ingeniería y Arquitectura
Universidad Zaragoza

PhD candidate

Julio Flecha-Lescún

Thesis Advisors

PhD. Begoña Calvo Calzada

PhD. Miguel Ángel Ariza-Gracia

COMPUTATIONAL PLANNING TOOLS IN OPHTHALMOLOGY: INTRASTROMAL CORNEAL RING SURGERY

PhD Program in Biomedical Engineering. University of Zaragoza (December 2020)



Instituto Universitario de Investigación
de Ingeniería de Aragón
Universidad Zaragoza



Universidad
Zaragoza



Escuela de
Ingeniería y Arquitectura
Universidad Zaragoza

*If we knew what it was we were doing,
it would not be called research, would it?*
Albert Einstein

Copyright © 2020 Julio Flecha–Lescún

Published by PhD Program in Biomedical Engineering. University of Zaragoza (December 2020)

First printing, December 2020

PhD Candidate

Julio Flecha–Lescún

Aragón Institute of Engineering Research (i3A, University of Zaragoza)

Thesis Advisors

PhD. Begoña Calvo Calzada

Aragón Institute of Engineering Research (i3A) and CIBER–BBN. University of Zaragoza (Zaragoza, Spain)

PhD. Miguel Ángel Ariza–Gracia

Center for Biomedical Engineering Research (ARTORG). University of Bern (Bern, Switzerland)

Collaborators

PhD. Jesús Zurita *Department of Mechanical Engineering, Energetics and Materials, Public University of Navarra (Pamplona, Spain)*

PhD. Laura Remón *Department of Applied Physics, University of Zaragoza (Zaragoza, Spain)*

PhD. Philippe Büchler *(Reviewer) Center for Biomedical Engineering Research (ARTORG). University of Bern (Bern, Switzerland)*

PhD. Md. Joaquín Fernández *Department of Ophthalmology (Qvision). Vithas Virgen del Mar Hospital (Almería, Spain)*

PhD. Can Gököl *Center for Biomedical Engineering Research (ARTORG). University of Bern (Bern, Switzerland)*

Doctoral Committee

PhD. David P. Piñero Llorens *(President) Ophthalmology Department (OFTALMAR), Medimar International Hospital (Alicante, Spain)*

PhD. Sabinne Kling *(Member and Reviewer) Department of Information Technology and Electrical Engineering, ETH Zurich (Zurich, Switzerland)*

PhD. Jorge Grasa Orús *(Secretary) Aragón Institute of Engineering Research (i3A), University of Zaragoza (Zaragoza, Spain)*

PhD. José Félix Rodríguez Matas *(Substitute) LabS, Chemistry, Materials and Chemical Engineering Department "Giulio Natta". Politecnico di Milano (Milan, Italy)*

PhD. Mauro Malvè *(Substitute) Department of Mechanical Engineering, Energetics and Materials, Public University of Navarra (Pamplona, Spain)*

Contents

Summary	27
Chapter 1: Introduction	33
1. Vision problems worldwide	34
2. Project Framework	37
<i>CICYT DPI2014 - 54981R</i>	
<i>Personal Funding</i>	
3. Motivation	38
4. Objectives	40
5. Organisation of the thesis	43
Chapter 2: Eye, Keratoconus and Treatments for corneal ectasia	49
1. Introduction	50
2. Eye Anatomy	50
<i>Anatomical terms of reference</i>	
<i>General shape, size and position of the eye</i>	
<i>Cornea</i>	
<i>Sclera</i>	
<i>Limbus</i>	
3. Keratoconus disease	60
<i>Factors that promote the development of keratoconus</i>	
<i>Classifications of keratoconus</i>	
<i>Treatments against the keratoconus</i>	
4. Intrastromal corneal ring implants	72
<i>Surgical procedure</i>	
<i>Commercial intrastromal corneal rings</i>	
5. Retrospective clinical and numerical studies	80
<i>Keraring to stabilise keratoconus</i>	
<i>Ferrara to stabilise the keratoconus</i>	

Intacs to stabilise the keratoconus
MyoRing to correct myopia and to stabilise KC
In-silico studies about ICRS surgery

Chapter 3: Pressure-based ICRS implantation	99
1. Introduction	100
2. Material and methods	102
<i>3D FE template of the human eyeball</i>	
<i>3D FE model of the ICRS</i>	
<i>Computational simulation of the insertion of ICRS</i>	
<i>Determination of corneal optics</i>	
<i>Benchmark studies</i>	
3. Results	110
<i>Results of the parametric study</i>	
<i>Effect of ICRS in KC corneas</i>	
4. Discussion	117
Chapter 4: Displacement-based ICRS implantation	121
1. Introduction	122
2. Material and methods	124
<i>Corneal geometry</i>	
<i>Corneal mechanics</i>	
<i>Implants: geometry and material model</i>	
<i>Expansion tool: geometry and material model</i>	
<i>Simulation steps for ring implantation</i>	
<i>Optical and mechanical analysis</i>	
<i>Case studies</i>	
3. Results	131
<i>Optical impact of different modelling strategies</i>	
<i>Mechanical impact of different modelling strategies</i>	
4. Discussion	137
Chapter 5: Corneal biomechanics after intrastromal surgery	139
1. Introduction	140
2. Methods	142
<i>In-silico model of intrastromal corneal rings surgery</i>	
<i>Optical and mechanical analysis</i>	
<i>Model calibration and validation</i>	
<i>In-silico scenarios</i>	

3. Results	148
<i>In-silico model validation</i>	
<i>Ring design and position</i>	
<i>Effect of corneal biomechanics</i>	
4. Discussion	153
5. Conclusions	158
Chapter 6: Mechanical nomograms: Application on MyoRing	161
1. Introduction	162
2. Methods	163
<i>MyoRing surgery</i>	
<i>Mechanical and material model</i>	
<i>Virtual cohort of patients</i>	
3. Results	167
<i>Validation of in-silico models</i>	
<i>Contribution of mechanics and anatomy to the nomogram</i>	
<i>Corneal strengthening factor of MyoRing</i>	
<i>Predictions of refractive outcomes</i>	
4. Discussion	174
Chapter 7: Mechanical characterisation of ICRS	177
1. Introduction	178
2. Material and methods	180
<i>Experimental protocol</i>	
<i>Numerical protocol</i>	
3. Results	185
<i>Experimental results</i>	
<i>Uncertainty analysis results and iFEM optimisation</i>	
4. Discussion	187
Chapter 8: Outcomes and Future Lines	193
1. Main conclusions and original contributions	194
<i>Clinical contributions</i>	
<i>Biomechanical and computational contributions</i>	
2. Scientific publications (Journal Citation Report)	197
3. Conferences	198
4. External fundings	199
5. Other relevant publications	200
6. Future lines	200

Appendix I: Resumen y Conclusiones en Español	205
1. Resumen	206
2. Conclusiones principales y contribuciones originales	208
<i>Contribuciones clínicas</i>	
<i>Contribuciones biomecánicas y computacionales</i>	
3. Líneas futuras	211
Appendix II: Publications	213
1. Biomech. Model. Mechanobiol. 2018	214
2. Transl. Vis. Sci. Technol. 2020	215
Appendix III: Automatic model mesh to generate <i>in-silico</i> models	217
1. Introduction	218
2. Heading of Abaqus Scripting file	219
3. Geometry of the models	219
<i>Geometry of the cornea</i>	
<i>Geometry of the rings</i>	
4. Material and section assignment	247
<i>Material and section assignment for the cornea models</i>	
<i>Material and section assignment for the ring models</i>	
5. Mesh of the models	249
<i>Mesh of the cornea</i>	
<i>Mesh of the ring</i>	
6. Assembly of the axisymmetric models	269
7. Step modulus	270
8. Boundary conditions	270
9. Job and submission	270
10. Final considerations	271
Appendix IV: Additional Tables and Results	273
1. Additional tables	274
2. Additional results	275
Appendix V: Abbreviations	277
Bibliography	283

List of Figures

Chapter 1: Introduction

1.1	Keratoconus and surgical techniques to try to stabilise it	39
1.2	Scheme of the PhD thesis	47

Chapter 2: Eye, Keratoconus and Treatments for corneal ectasia

2.1	Diagram illustrating anatomical planes of reference	50
2.2	Schematic diagram of the human eye anatomy	52
2.3	Structure of the cornea	53
2.4	Form of keratoconus	61
2.5	Severity grade of keratoconus according Amsler–Krumeich classification	65
2.6	Phenotypes developed when KC is originated in a cornea without astigmatism	65
2.7	Phenotypes developed when KC is originated in a cornea with pro–rule astigmatism	66
2.8	Phenotypes developed when KC is originated against the rule astigmatism	66
2.9	Phenotypes developed when KC is originated with oblique astigmatism (meridian at 135°)	67
2.10	Phenotypes developed when KC is originated with oblique astigmatism (meridian at 45°)	67
2.11	Lens located in a cornea with keratoconus	68
2.12	Typologies of lenses to improve the vision in corneas with keratoconus	69
2.13	CXL treatment to stabilise the KC progression	71
2.14	Surgical procedure	73
2.15	Keraring implant	75
2.16	Corneal asymmetry classification of Keraring	76
2.17	Ferrara implant	77
2.18	Corneal asymmetry classification of Ferrara	78
2.19	Intacs implant	78
2.20	MyoRing implant	79
2.21	Chart of Snellen	91

Chapter 3: Pressure–based ICRS implantation

3.1	Definition of the finite element templates	104
3.2	Finite element model of the ICRS	105
3.3	Clinical and computational surgical procedure	107
3.4	Zernike representation of the geometries of reference	108
3.5	Parametric analysis (1): Pareto chart and main effect of the variables under analysis in the spherical and cylindrical powers	111
3.6	Parametric analysis (2): Interaction of the variables under analysis in the spherical and cylindrical powers	113
3.7	Kinematics of the KC cornea	114
3.8	Mechanics of the KC cornea	116
3.9	Zernike coefficients of the KC corneas	117

Chapter 4: Displacement–based ICRS implantation

4.1	Geometries and meshes of the models	125
4.2	Behaviour of corneal material in uniaxial test	127
4.3	Computational surgical procedure with tunnel surgery	130
4.4	Validation of the <i>in-silico</i> results with clinical results	132
4.5	Effect of the <i>in-silico</i> simulations: axisymmetric versus 3D model and material model	134
4.6	Effect of the cross–section of the rings in axisymmetric models	135
4.7	Effect of the friction between corneal tissue and ring	136

Chapter 5: Corneal biomechanics after intrastromal surgery

5.1	Schematic representation of the <i>in-silico</i> models used in this study	144
5.2	Validation of <i>in-silico</i> model	148
5.3	Main individual effect of positioning on the change in spherical equivalent	149
5.4	Effect of the interaction between size and diameter of the implant on the change in spherical equivalent	150
5.5	Post–surgical rotation of gIRS depending on the manufacturing angle of the cross–section	151
5.6	Spatial distribution of corneal strengthening factor (SFC _{3D})	152
5.7	Impact of the stromal biomechanical properties on refractive outcomes after continuous ring implantation	153
5.8	Conceptual diagram of corneal kinematics and biomechanics after ring implantation	155

Chapter 6: Mechanical nomograms: Application on MyoRing

6.1	Cornea and MyoRing cross–section	165
6.2	Calibration and verification of opto–mechanical simulation of MyoRing	168

6.3	Prediction of change in mean keratometry for three different MyoRing diameters	169
6.4	Spearman correlation between input parameters and refractive post-surgical outcomes	170
6.5	Corneal strengthening factor of MyoRing	171
6.6	Influence of Myoring's diameter and size on refractive outcomes	172
6.7	Influence of depth on Kmean and SE	173

Chapter 7: Mechanical characterisation of ICRS

7.1	Overview of the mechanical characterisation pipeline	182
7.2	ICRS geometry and finite element model	183
7.3	Results for ICRS with triangular cross-section	188
7.4	Results for ICRS with hexagonal cross-section	189
7.5	Uncertainty analysis: impact of variables	190
7.6	Young's Modulus statistical distribution for different populations and methods	191

Chapter 8: Outcomes and Future Lines

8.1	Support to hold the eyeball and to be able to make measurements with the topographer	201
-----	--	-----

Appendix II: Publications

II.1	Biomech. Model. Mechanobiol. 2018	214
II.2	Transl. Vis. Sci. Technol. 2020	215

Appendix III: Automatic model mesh to generate *in-silico* models

III.1	Input parameters to define the cross section of the cornea	220
III.2	Calculation of CA_{PF}	220
III.3	Calculation of CP_{PF}	221
III.4	Points used in code to perform the cornea cross section	221
III.5	Interior Point and origin of the system	222
III.6	Input parameters to define the cross-section of the surgery as a tunnel	223
III.7	Calculation of S_{p1} in tunnel surgery	223
III.8	Calculation of S_{p2} and distance d in tunnel surgery	224
III.9	Calculation of S_{p3} in tunnel surgery	224
III.10	Calculation of S_{Centre} in tunnel surgery	224
III.11	Calculation of S_M and S_m in tunnel surgery	225
III.12	Calculation of P_{int} , P_{Apex} , and P_{Limbus}	225
III.13	First cover ellipse	227
III.14	Second cover ellipse	227
III.15	Internal arcs within stroma corneal	228

III.16	Lines which cut the stroma around the surgery	228
III.17	Keratoconic section in tunnel configuration	229
III.18	Lines to cut the surgery	229
III.19	Points required to draw the largest cover ellipse and the regions where it must be traced	230
III.20	Sketch of the cornea with the cuttings made to obtain an accuracy mesh	230
III.21	Input parameters to define the cross-section of the surgery as a Pocket	231
III.22	Calculation of S_{p1} in pocket surgery	231
III.23	Calculation of S_{p2} and distance d in pocket surgery	232
III.24	Calculation of S_{p3} in pocket surgery	232
III.25	Calculation of S_{p4} and S_{Centre} in pocket surgery	232
III.26	Calculation of S_M , S_{m1} , and S_{m2} in pocket surgery	233
III.27	Representation of the ellipse by spline	233
III.28	Arcs of the circumference which close the pocket	234
III.29	Calculation of P_{int} , Q_{CA} , Q_{CP} , S_1 , and S_2	235
III.30	Internal arc to join the end of the pocket with the limbus	236
III.31	Lines which cut the stroma around the end of the pocket	236
III.32	Lines around the optical zone	237
III.33	Keratoconic section in pocket configuration	238
III.34	Lines to cut the pocket	238
III.35	Points required to draw the cover ellipse at the elliptical zone of the pocket	239
III.36	Sketch of the cornea with pocket including the cuttings made to obtain an accurate mesh	240
III.37	Cross-section of the generic ring	240
III.38	Inclination of the generic ring when the surgery is a pocket	241
III.39	Cuttings on the cross-section of the generic ring	242
III.40	Cross-section of the MyoRing	242
III.41	Procedure to obtain the MyoRing cross-section	243
III.42	References to obtain the points to trace the splines	244
III.43	Points to define the interior cuttings and the corner rounds	244
III.44	Corner rounding of the MyoRing	245
III.45	Points to draw the splines corresponding on internal cuttings and round corners	246
III.46	Sketch of the MyoRing including the cuttings to obtain an accurate mesh	247
III.47	Points in order to select the regions of cornea cross-section with tunnel	253
III.48	Meshing techniques and seeds in the cornea with tunnel as surgery	257
III.49	Mesh of the cornea cross-section with tunnel as surgery	258
III.50	Points to select the regions of cornea cross-section with pocket	259
III.51	Meshing techniques and seeds in the cornea with pocket as surgery	264
III.52	Mesh of the cornea cross-section with pocket as surgery	265
III.53	Points to select the regions of generic cross-section	266
III.54	Meshing techniques, seeds and mesh of generic ring	267

III.55	Internal and edge points of the MyoRing	268
III.56	Mesh techniques, seeds and mesh of MyoRing	269

Appendix IV: Additional Tables and Results

IV.1	Spatial distribution of corneal strengthening factor (SFC_{3D})	275
------	---	-----

List of Tables

Chapter 2: Eye, Keratoconus and Treatments for corneal ectasia

2.1	Contact lens modality chosen depends on severity of ectasia	70
2.2	Main characteristics of the intracorneal ring segments	72
2.3	Ferrara nomogram	77
2.4	Intacs nomogram	79
2.5	MyoRing nomogram	80
2.6	Pre- and Post-operatively clinical data of Keraring studies	94
2.7	Pre- and Post-operatively clinical data of Ferrara studies	95
2.8	Pre- and Post-operatively clinical data of Intacs studies	96
2.9	Pre- and Post-operatively clinical data of MyoRing studies	97

Chapter 3: Pressure-based ICRS implantation

3.1	Optical Powers (Cylinder and Sphere) and Low Order Aberrations (LOA)	115
3.2	High Order Aberrations (HOA)	117

Chapter 4: Displacement-based ICRS implantation

4.1	Geometry and mesh features of the different ring typologies	128
-----	---	-----

Chapter 5: Corneal biomechanics after intrastromal surgery

5.1	Pre-surgical morphological description of the <i>in-silico</i> models	142
5.2	Summary of the parameters used for the simulation of each scenario	147
5.3	Material parameters for the normal and pathological tissue	148

Chapter 7: Mechanical characterisation of ICRS

7.1	Geometrical and mesh features	183
7.2	Results of Young's Modulus corresponding with the boxplots of the Figure 7.6	186

7.3	Fixed damage value for each population	186
-----	--	-----

Appendix III: Automatic model mesh to generate *in-silico* models

III.1	Sets and surfaces definition to tunnel surgery	226
III.2	Sets and surfaces definition to pocket surgery	235
III.3	Sets and surfaces definition to generic ring	241
III.4	Sets and surfaces definition to MyoRing	247
III.5	Seeds of edges showed in Figure III.48	257
III.6	Seeds of edges showed in Figure III.51	264

Appendix IV: Additional Tables and Results

IV.1	Geometrical details for continuous ring in pocket	274
IV.2	Geometrical details for continuous ring in tunnel	274
IV.3	Geometrical details for ring segments in tunnel	274
IV.4	Corneal strengthening analysis.	275

Acknowledgements

After more than two years in the private company dedicated to the world of photovoltaic energy, in 2016 I decided to take the step and embarked on this PhD adventure. I never thought that it would be so tough and that without the support of my closest people, I would not have finished. Therefore, I want to thank my advisors *Begoña Calvo* and *Miguel Ángel Ariza-Gracia* who have helped me to solve each of the doubts that have arisen throughout more than 4 years. Thank you Miguel for preventing me from quitting the PhD thesis in the most difficult moments.

After that difficult moment, I started my doctoral stay at the University of Bern, at the Center for Biomedical Engineering Research (ARTORG) (before Institute for Surgical Technology and Biomechanics, ISTB). It was a turning point, where the pieces of the puzzle began to fit in. I would like to thank *Philippe Büchler*, responsible of my research stay, who promoted the success of the methodology developed to insert the rings into corneal stroma. I also want to thank *Can Gökçöl* who always had time to answer my doubts about Abaqus Explicit Solver and commented with me the solution. He was very patient with all my questions.

I cannot forget all the people who are part of *Qvision*, at Vitas Hospital in Almería. Thanks to *Joaquín Fernández* for opening the doors of his clinic, to *Javier Martínez* to help me to perform the operations. Part of this research could not be completed due to several problems but I am sure that in the future we will be able to carry them out. Thanks also to *David Piñero*, because he always had words of encouragement and mentoring every time we met. It is very comforting to hear them, giving the strength to go on.

Neither can I forget all the people who have made this research possible: Administrative staff, laboratory staff, especially *Carlos Marzo*, with whom I always had time for an entertaining talk, and the rest of the AMB group's colleagues, University of Zaragoza: *Estefanía Peña*, *Miguel Ángel Martínez*, *Elías Cueto*, *David González*, *Jorge Grasa*, and *Mauro Malvé* for their time, their words of encouragement and collaboration. I would also like to thank *Laura Remón* in making the characterisation of the rings possible. And, of course, I would like to thank my doctoral colleagues who have been there during the hardest moments of the research, especially *Beatriz Moya* who has always had positive advices, and encouraging and motivating words in the final moments of the thesis, demonstrating to me what a

great person she is. I know that you have an extraordinary future waiting for you. Neither do I want to forget *Jacobo Ayensa, Alberto Badías, Javier Ortún, Javier Escuer, Iulen Cabeza, Itziar Ríos*, and all those people who have spent some of their time to make my time at this stage of the university the best possible. Not only are you my colleagues, but also you are good friends. Thank you.

Thanks to all my friends who have helped me to disconnect from my daily work. *Miguel Ángel, Bea, Carlos, Raquel, Fernando, Violeta, Eduardo, Miguel, Alfonso, Ricardo, and Luis*. They always had words of encouragement. I cannot forget *Dani*, Miguel Ángel's brother; both of them always opened the doors of their house in Switzerland to me and made me feel I was not alone there. What amazing moments we had and hopefully in the future we will be able to live again. Thanks also to all their family, because they always welcomed me as one of them. Finally, thanks to all my basketball team's friends, especially *Raúl, Adrián, Nacho, and Pablo*, who have made of every weekend a great moment to recharge the batteries and to start a brand new week.

There is one person who has been very special throughout the thesis. Thank you, *Alicia*, for being there at all moments, withstanding my concerns and comments about the work. From these lines, I apologize for so many hours that I have not been able to dedicate to you. We have a future path which is now opening up and I am eager for us to live it together. I cannot forget her little podenco, *Lía*, because of the countless good times we have had with her. Many thanks also to your parents, *Araceli* and *Horacio*, because they have always welcomed me with a smile and I have learned a lot from them.

I would also like to thank my cousin *Carmen*, she has been as the sister I have not had. Although we do not live in the same city I have always had you very close.

Dedicated to my parents and family. Gracias *Mamá*, Gracias *Papá*. An important part of this work is yours. I am very proud of being your son. And although I do not tell you much, I love you. You have always had the patience and words to endure my mood when I had a bad day, as well as you have rejoiced at my success. We have a future that is waiting for us to be lived together. Of course, thanks to all my family, because everything I am today I owe it all to you.

This PhD thesis has a little bit of all of you. Thank you.

Summary

This thesis addresses the problem of the simulation of intrastromal corneal ring segment surgery for the reduction of myopia and astigmatism, as well as the stabilisation of keratoconus (KC). This disease causes high myopia, irregular astigmatism and reduction of the patient's visual acuity to the point of blindness. Therefore there are several techniques to try to stabilise it and, thus, prevent its progression. For mild keratoconus, it is enough to use special spectacles or lenses to try to correct it, but in more advanced cases it would be necessary to use refractive surgery to try to stop the progression of the disease. The most common ones to avoid the cornea transplant (PK) are the cross-linking and the additive surgery of intrastromal rings.

The current planning tools are empirical, based on the nomograms of the ring manufactures, and rely on the experience of the surgeon. Unfortunately, deterministic tools able to estimate the postsurgical visual results of this treatment do not exist. Therefore, the aim of the current thesis is to establish a realistic numerical framework to simulate intrastromal ring surgeries and estimate the mechanical and optical postsurgical outcomes.

There are different types of rings depending on their angle and cross-section. There are two large groups of rings: segments which have an angle of less than 360° and those that cover the entire circumference. In the first group we find rings of triangular section such as the Keraring (Mediaphacos, BeloHorizonte, Brazil) and the Ferrara (AJL Ophthalmic Ltd, Spain) and rings of hexagonal section like the Intacs (Additional Technology Inc.). In the second group we can find the MyoRing (Dioptex, GmbH.) whose cross-section is the combination of a parabola and a circumference and the Intacs SK whose section is oval.

Due to the complexity of the simulation, since multiple variables are involved, such as the type of rings, the model of the corneal material, the contact conditions between them, etc., two methodologies arised which simulated the insertion of the rings. Both are based on generating a hole in the corneal stroma, introducing the ring and closing the hole with the ring inside, establishing contact until the simulation is completed. In the first of the methodologies the hole was generated by introducing a pressure, while the second was used to an auxiliary tool, such as balloon angioplasty to introduce endovascular stents, which is displaced generating enough hole to insert the rings. As with all numerical simulations, they were not exempt of limitations, although with the first of the methodologies only circular cross-section rings were simulated and in some configurations, there was pressure inside the hole, so it

was decided to focus on the second. Nevertheless, interesting conclusions were obtained: the greatest correction was obtained by placing the rings with the largest section near the apex, and whether the ring is located near the epithelium, the stresses generated in the stroma can cause the ring to extrude.

With the second methodology based on a displacement control, it was possible to simulate most of the cross-sections and very interesting studies were carried out that gave conclusive results. The most important were: *i)* the most influential parameter is the depth of insertion; *ii)* considering the physiological depth of the surgery, the greater optical change is provided by the diameter of the ring, and the fine adjusted is reached with the size of the implant cross-section, i.e the diameter of the implant and the size of the cross-section are the key on regulating the refractive correction; *iii)* the friction between ring and stroma is important to consider it because a prediction of 2 or 3 diopters could be lost; *iv)* whether the KC progression is stress-driven, only MyoRing can stop its progression; *v)* when the covered arc of the segments is more than 320° , axisymmetric model could be used instead of tridimensional model, saving computational time; *vi)* the anisotropy of the model does not play an important role because the rings are much stiffer than corneal tissue; *vii)* the implants cannot consider such as second limbus since they act as a dynamic pivot that moves along the circadian cycles of intraocular pressure (IOP); *viii)* preliminary nomograms is built which allow the estimation of the optical outputs according to the size and typology of the ring and optical zone of implantation.

Additionally, a characterization of ring material was carried out by means two complementary methods: uncertainty analysis and iFEM optimisation, concluding that the manufacturing process of the rings could be the cause of the alteration of the material between the raw PMMA and the ring already prepared for its insertion.

Keywords: Intrastromal corneal ring segments, Intrastromal complete ring, finite element, corneal biophysics, surgery planning ICRS, optimisation, uncertainty analysis, optics, automatic mesh.

A mis padres, a mi familia, a mis amigos,
a Alicia

*Salid de casa y sonreíd.
Sonreíd a los imprevistos, a los problemas, al mal tiempo, a las personas ...
Al finalizar el día, quizás descubráis que no hubo ningún cambio, pero vosotros habréis sonreído.*



Chapter 1

Introduction

The current PhD thesis was born under the coverage of biomedical engineering within the field of ophthalmology. In this introductory chapter, the reader will get an idea of the current situation of visual health worldwide, and the pathology of keratoconus in particular, and how *in-silico* models can help surgeons to estimate the optical outputs after intrastromal ring insertion surgery. Not only that, *in-silico* models also provide the clinicians with an estimation of the post-surgical stress state of the cornea and the possibility of testing different intrastromal rings without performing the actual surgery. The next step is to present the project framework in which the thesis is embedded, as well as the necessary funding to carry it out. Finally, the organisation in chapters of the thesis is explained to be able to approach the objectives and to understand the motivation of this work.

Chapter Contents

1. Vision problems worldwide	34
2. Project Framework	37
<i>CICYT DPI2014 - 54981R</i>	37
<i>Personal Funding</i>	38
3. Motivation	38
4. Objectives	40
5. Organisation of the thesis	43

1. Vision problems worldwide

Vision, the most dominant of our senses, plays a critical role in every facet and stage of our lives. We take vision for granted, but without vision, we struggle to learn to walk, to read, to participate in school, and to work. Almost 90% of incoming information reaches the brain through the eyes. Vision impairment occurs when an eye condition affects the visual system and one or more of its vision functions. Vision impairment has serious consequences for the individual across the life course. Lots of these consequences can, however, be mitigated by timely access to quality eye care and rehabilitation. Eye conditions that can cause vision impairment and blindness, such as cataract, trachoma and refractive error, are, for good reasons, the main focus of prevention and other eye care strategies; nevertheless, the importance of eye conditions that do not typically cause vision impairment, such as dry eye and conjunctivitis, must not be overlooked. These conditions are frequently among the leading reasons for presentation to eye care services in all countries.

Due to the increased use of smartphones, digital tablets and computers that have a large screen, eye diseases and vision problems such as myopia, hyperopia, astigmatism and presbyopia are on the rise. Prolonged exposure to digital screens is the root cause of eye conditions, including Computer Vision Syndrome (CVS) or Digital Eye Strain (DES). Symptoms of these conditions include dry, irritated eyes, blurred vision, fatigue, neck and back pain, and headaches. What is most disturbing is that 65% of Americans experience these symptoms. Research suggests that continued long-term exposure to screens that radiate blue wavelength light can cause slow degeneration of the retina and could lead to long-term vision problems, such as age-related macular degeneration and cataracts.¹ Another ocular problem that can be associated not only with the use of digital screens but also with the eye rubbing, is the keratoconus (KC), a disease by which the corneal tissue weakens causing a local protrusion in the cornea causing an increase in myopia and astigmatism reducing the visual acuity.

According to World Health Organisation (WHO), at least 2.2 billion people have a vision impairment. In at least 1 billion, or almost half of these cases, vision impairment could have been prevented or has yet to be addressed.² Accurate estimates of the total number of people globally with vision impairment cannot be calculated based on current available data. This is because population-based surveys do not typically report vision

¹ Sheppard and Wolffsohn 2018

² Fricke et al. 2018, Bourne et al. 2017, Flaxman et al. 2017

impairment in those who wear spectacles or contact lenses to compensate for the vision impairment from a refractive error. Nonetheless, it can be assumed with cogency that at least 2.2 billion people globally have a vision impairment or blindness. This research takes into consideration those with near vision impairment due to presbyopia (1.8 billion, including both addressed and unaddressed presbyopia), and moderate to severe distance vision impairment or blindness due to unaddressed refractive error (123.7 million, e.g. myopia or hypermetropia), cataract (65.2 million), age-related macular degeneration (10.4 million), glaucoma (6.9 million), corneal opacities (4.2 million), diabetic retinopathy (3 million), trachoma (2 million), and other causes (37.1 million), including those causes that were not classified in surveys or do not fit into any of the aforementioned categories. In addition, this research also takes into consideration 188.5 million people with mild vision impairment in which the causes are unknown.

Apart from the most common diseases commented, the keratoconus, another ectatic disorder, which shows the major incidence in the general population (1 to 430/2000),³ but official statistics do not include those who have been, misdiagnosed, or lately diagnosed. Due to the disorder which generates in the cornea, keratoconus provokes the decrease of visual acuity, and has a lasting negative impact on all aspects of the patient's life. Keratoconus affects three million people worldwide, with a higher prevalence amongst females.⁴ Besides, South Asian ethnicity with an incidence probability of 4.4 times higher than Caucasians, are also more prone to be affected earlier.⁵ Another negative aspect, due to the progression of the disease, keratoconus can produce corneal blindness, which is responsible for 40,000 people needing a corneal transplant in Europe every year.⁶

The epidemiological burden of a disease informs the provision of health-care services. A review of early studies of the prevalence of keratoconus between 1936 and 1966 found a range of 50–2330 cases per 100,000 (0.05–0.23%).⁷ A review of later studies (1959–2011)⁸ found prevalence estimates ranging from 0.3 per 100,000 (0.0003%) in Russia to 2340 per 100,000 (2.3%) in Maharashtra, India.⁹

Many early studies were limited by their reliance on older imaging modalities. Kennedy *et al.* (1986)¹⁰ used the keratometry and keratoscopy to estimate the prevalence in Minnesota, USA as 54.5/100,000 (0.0545%). More recent studies using videokeratography (topography) provide more sensitive estimates.¹¹ For example, a prevalence of 3.18% was recorded in a population based study of Israeli Arabs,¹² consistent with other studies

³ *The Global Keratoconus Foundation (The Global Keratoconus Foundation link to digital version)*

⁴ *Fink et al. 2005*

⁵ *Pearson et al. 2000*

⁶ *CORDIS Europe link to digital version*

⁷ *Krachmer et al. 1984*

⁸ *Gordon-Shaag et al. 2012*

⁹ *Jonas et al. 2009*

¹⁰ *Kennedy et al. 1986*

¹¹ *Gordon-Shaag et al. 2015*

¹² *Shneor et al. 2014*

¹³ Millodot *et al.* 2011, Waked *et al.* 2012, Hashemi *et al.* 2013a, 2014

¹⁴ Gordon-Shaag *et al.* 2015

¹⁵ Millodot *et al.* 2011

¹⁶ Ambrosio *et al.* 2003

¹⁷ McMonnies 2014

¹⁸ Bamashmus *et al.* 2010

¹⁹ McMonnies 2014

²⁰ McMonnies 2014

²¹ Gomes *et al.* 2015

²² Jonas *et al.* 2009

²³ Millodot *et al.* 2011

²⁴ Hashemi *et al.* 2013a

²⁵ Hashemi *et al.* 2013a

²⁶ Gordon-Shaag *et al.* 2012

²⁷ Assiri *et al.* 2005

²⁸ Assiri *et al.* 2005

²⁹ Nielsen *et al.* 2007

from Israel, Iran, and Lebanon.¹³

Gordon–Shaag *et. al* (2015)¹⁴ provided an excellent summary of published prevalence studies and emphasised the important methodological differences between hospital or clinic based reports and population based studies. Hospital based studies tend to underestimate true prevalence because they fail to include asymptomatic patients, those with early disease and those being managed in a non hospital setting. Population based studies are considered the gold standard for measuring prevalence, but they can be also hampered by certain selection biases.¹⁵ They highlight important geographic variation in prevalence, as well as the increased estimates that have resulted from newer imaging modalities.

Whilst the heterogeneous methodology of prevalence studies limits the accuracy of direct comparisons between studies, it is clear that estimates of prevalence have increased over the last few decades. In fact, Ambrosio *et. al* (2003)¹⁶ employed Atlas anterior corneal topography, biomicroscopy and ultrasound pachymetry that found a keratoconus prevalence of 0.9% in refractive surgery candidates, i.e. four times the upper range of estimate of prevalence prior to 1966.¹⁷ A 2010 study in Yemen¹⁸ using TMS–2 topography, biomicroscopy and pachymetry found a combined keratoconus/forme–fruste keratoconus prevalence in LASIK/PRK candidates of 5.8%, i.e. 25 times greater than the mean prior to 1966.¹⁹ However, in these studies, sampled patients were candidates for keratorefractive surgery and as KC is strongly associated with myopia the data exposed to self–selection bias.²⁰

Middle Eastern and central Asian ethnicity is considered a risk factor for keratoconus.²¹ Studies have reported prevalence of 2.3% in India,²² 2.34% among Arab students in Israel²³ and 2.5% in Iran.²⁴ Although these studies had some methodological flaws, the concordance of results supports a true prevalence in some Asiatic countries of similar magnitude.²⁵ A lower prevalence of keratoconus in Japanese compared with Caucasian populations has been reported.²⁶

Estimates of annual incidence of keratoconus range from 1.4 to 600 cases per 100,000 population.²⁷ However, there is paucity of recent studies of incidence that have benefited from modern imaging technology and diagnostic sensitivity. Assiri *et. al* (2005)²⁸ reported an incidence of 20 per 100,000 per year in one Saudi Arabian province, although this was likely to have been an underestimate given that the figure was based on referrals to a tertiary clinic. Elsewhere, incidence has been estimated at 1.3/100,000/year in Denmark.²⁹ Ethnic differences are influential, with an

incidence of 25/100,000/year for Asians compared with 3.3/100,000/year for Caucasians ($p < 0.001$) having been demonstrated in a single catchment area.³⁰ In a similar UK study, Pearson *et. al* (2000)³¹ demonstrated annual incidence of keratoconus of 19.6/100,000 and 4.5/100,000 in Asian and Caucasian communities, respectively.

There are different techniques in order to try to halt the keratoconus progression. For mild states of keratoconus, it is possible that spectacles, rigid or soft contact lenses are enough to prevent its progression. However, for severe states of keratoconus, there are other techniques to avoid the corneal transplant (PK), such Cross-Linking (CXL) or additive surgery by means of intrastromal corneal ring segments (ICRS) insertion.

All surgical operations involve their own risks that the patient is aware of before undergoing any intervention. It seems logical to think that the only surgeon's experience is not enough to predict the optical changes that the operations may produce. Therefore, "ophthalmic engineering" is born, a new branch of knowledge based on *in-silico* models that simulate the different surgeries that will take place in the eyes of the patients. Thanks to them, surgeons are able to predict the optical outcomes after the intervention. Not only that, surgeons can use these computer techniques to propose improvements in the surgical interventions, or propose different solutions to find the optimal one. Therefore, the main target of the current thesis is to develop a methodology, which would be able to simulate the surgery of intrastromal corneal ring segment.

2. Project Framework

The current thesis has been developed within the framework of a research project of the Ministry of Economy and Competitiveness of the Spanish Government.

Corneal tissue response to cross-linking treatment. Application to keratoconus treatment (DPI2014 - 54981R)

This project is focused on the *in vivo* characterisation of corneal tissue. The main aim is to establish new biomarkers to diagnose pathologies associated to its weakening: keratoconus or keratitis produced by Acanthamoeba. The global objective of the project is to design a new methodology that will allow to evaluate the mechanical behaviour of the corneal tissue *in vivo*, so as to assess in the early diagnosis of pathologies linked to the tissue

³⁰ Georgiou *et al.* 2004

³¹ Pearson *et al.* 2000



weakening, as well as the evaluation of the Cross-Linking treatment.

Among all the tasks, those directly related with the present thesis are,

- To develop a methodology to simulate intrastromal ring insertion surgery as a treatment to stabilise keratoconus.
- To apply the methodology in cohort of virtual patient models to estimate the optical correction, and to generate more general nomograms.
- Mechanical characterisation of the intrastromal rings using uniaxial traction experiments combined with inverse analysis techniques.

Personal Funding

Contrato Predoctoral para la formación de doctores

J. Flecha-Lescún received funding (4 years) from the Ministry of Economy and Competitiveness of the Government of Spain in order to make the PhD thesis in the University of Zaragoza, whose reference was BES-2015-073630.

Within the project, part of the budget was set aside to fund the 4-month research stay at the Center of Biomedical Engineering (ARTORG), before Institute for Surgical Technology and Biomechanics (ISTB), University of Bern (Bern, Switzerland).

Ibercaja-CAI mobility program

J. Flecha-Lescún received funding (3 months) from the Ibercaja-CAI mobility program to continue the research stay at Institute for Surgical Technology and Biomechanics (ISTB), currently Center for Biomedical Engineering Research (ARTORG), of University of Bern (Bern, Switzerland) and to develop the research project entitled “*Simulación Numérica de la Cirugía de inserción de Anillos Intrastromales para la Estabilización del Queratocono (Numerical Simulation of the Intrastromal Ring Insertion Surgery to the Stabilization of the Keratoconus)*”. Reference IT 11/18.

3. Motivation

Keratoconus disease (see Figure 1.1.a) can appear due to genetic factors, after surgical procedures, the massive use of digital screens or eye rubbing. Keratoconus is a disease characterized by a weakening of an area of the cornea and formation of a conical protrusion located in the



u^b

^b
UNIVERSITÄT
BERN



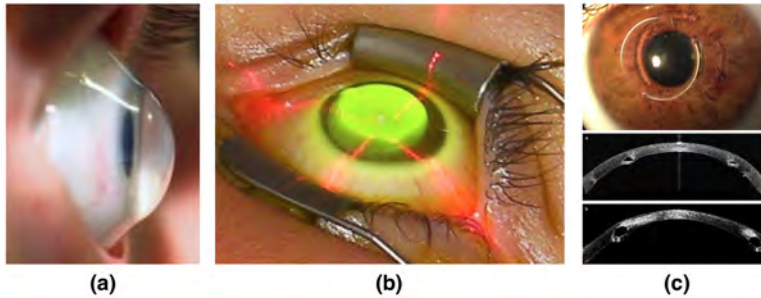


Figure 1.1: Keratoconus and techniques to try to stabilise it. (a) Keratoconus in cornea; (b) Cross-linking technique in order to halt the keratoconus progression; (c) Additive surgery to try to stabilise the keratoconus, the figure on top represents two rings located within cornea, and figure at bottom shows an optical coherence tomography (OCT) of intrastromal corneal ring with different section located within corneal stroma.

lower-temporal plane and central zone. As a consequence, keratoconus results in a reduction of visual acuity due to an irregular astigmatism and elevated myopia resulting from asymmetric topographic changes in the anterior surface of the cornea.³²

There are different ways to try to stabilise the disease and avoid corneal grafts through penetrating keratoplasty (PK). Two of most common techniques are the cross-linking (CXL) (see Figure 1.1.b)³³ and additive surgery by intrastromal corneal ring segment insertion (ICRS) (see Figure 1.1.c).³⁴

In short, predicting postsurgical outcomes after intrastromal ring insertion is a challenging. Current planning tools are empirical (nomograms) and rely on the experience of the surgeon.³⁵ Unfortunately, there are no deterministic tools able to estimate postsurgical visual outcomes for this treatment. This thesis approaches the prediction of postsurgical outcomes by using advanced computational models (finite element models), medical imaging and geometrical optics.

The combination of these disciplines will enable a deeper understanding of the visual impact of the treatment and, moreover, an estimation of the stress state of the cornea after ring insertions, which is impossible to measure with any clinical device available.

In-silico models have been used extensively in the field of ophthalmology to try to predict the behaviour of the cornea, both biomechanically and optically:

- Thanks to finite element model, it was possible to obtain the initial configuration of the eyeball and to introduce the internal stress due to the intraocular pressure.³⁶

³² Fangjun et al. 2016

³³ Maier et al. 2019, Kubrak-Kisza et al. 2016, Perez-Straziota et al. 2018, Kobashi and Rong 2017

³⁴ Jadidi et al. 2016, Janani et al. 2019, Daxer 2017, Daxer et al. 2016, Nobari et al. 2014, Mohebbi et al. 2016

³⁵ Alió et al. 2006, Fernández-Vega et al. 2016

³⁶ Ariza-Gracia et al. 2016, Elsheikh et al. 2013

- The behaviour of the corneal tissue can be reproduced by hyperelastic anisotropic models, such as the model from Gasser–Holzapfel–Ogden (G–H–O) for arteries and to be introduced in cornea.³⁷
- Patient–specific models have been successfully used to reproduce the physiological behaviour of the cornea.³⁸ In addition, it has been possible to establish numerical values of the constants that define the models of cornea material using *deep-learning* techniques.³⁹
- The *in-silico* models are also used to check if the results of optical devices, such as non–contact tonometers, are accurate enough.⁴⁰
- In addition, the *in-silico* models are used to study the accommodation of the human lens.⁴¹
- It is also possible to simulate optical devices such as lenses,⁴² and to use numerical models to predict which lens best fits a given cornea.

³⁷ Pandolfi and Holzapfel 2008

³⁸ Ariza-Gracia et al. 2016

³⁹ Ariza-Gracia et al. 2017b

⁴⁰ Ariza-Gracia et al. 2018

⁴¹ Breitenfeld et al. 2005

⁴² Remón et al. 2018

⁴³ Kling and Marcos 2013, Lago et al. 2015, Kahn and Shiakolas 2016, Ebrahimian et al. 2019

⁴⁴ Ariza-Gracia et al. 2017a

To date, very few numerical studies have been carried out able to simulate the surgery of insertion of intrastromal rings and no agreement has been reached as to which is the best technique since, although they are very interesting studies, they were not exempt of limitations.⁴³ The corneal material was always hyperelastic isotropic, some of them did not consider the pre–stress of the corneal tissue or the boundary conditions were applied on the surface of the cornea to facilitate convergence. Therefore, the motivation of the current thesis arises from the need to simulate the intrastromal rings surgery and to understand the mechanical behaviour of the cornea after the intervention. Thanks to an own ray–tracing algorithm,⁴⁴ the optical response is obtained, achieving an opto–mechanical coupling. The methodology is intended to be useful to clinicians, allowing them to estimate the result of the operation before it is performed, to test different surgical techniques, and to evaluate the effect of surgical variables on mechanical and optical outputs. Finally, it will be possible to build nomograms which allow the estimation of the optical outputs according to the size and typology of the ring and optical zone of implantation.

4. Objectives

The main objective of the present thesis is to establish a realistic numerical framework to simulate intrastromal ring surgeries and estimate the mechanical and optical postsurgical outcomes.

This *in-silico* framework will:

- Enable the use of different intrastromal ring geometries (cross-section shapes, sizes and diameters) for the same cornea.
- Yield an estimation of the optical effect of intrastromal rings.
- Yield an estimation of the stress state of the cornea after ring insertion.
- Help to answer current open questions such as: Why is there corneal extrusion? Is it true that continuous rings stiffen the cornea up to 2–3 times whilst intrastromal segments do not stiffen more than 1.5?⁴⁵
- Help to design deterministic nomograms that explicitly account for corneal mechanics and geometry, intraocular pressure and surgical features.

⁴⁵ Daxer 2015

To achieve such a challenging goal, different subgoals have been established:

To determine the best modelling strategy for simulating intrastromal ring surgeries

There are two main challenges concerning the simulation of the intrastromal ring surgery: first, how to create a continuous hole within the corneal stroma that simulates the tunnel created with a femtosecond laser (which will subsequently lodge the implant within the cornea) and how to introduce the implant within such tunnel; second, the complexity of the contact between the implant and the surfaces of the tunnel.

In particular, the following tasks were addressed:

- How to create a gap by removing elements. The proposed surgeries are based on generating gaps to house the intrastromal implants in its interior. Numerically, it consists of eliminating the group of finite elements that belong to the surgery and waiting for a new state of equilibrium to be reached with the generated gap. Thanks to the Abaqus tool **Model Change* it is possible to perform this action. The only drawback is it necessary to perform it in Abaqus standard solver. Therefore, if it was necessary to perform calculations in explicit solver, the *import* option to couple the implicit–explicit calculations should be used.
- Pressure–based or displacement–based insertion of the implant within the corneal stroma: how to “expand” the gap so that the implant can fit

in the tunnel. Two approaches were used: one based on expanding the corneal tissue using pressure and another one on expanding the corneal tissue using an auxiliary tool that displaces the tissue (i.e., similar to angioplasty procedures). The first of the techniques, based on pressure control, uses the **Fluid cavity* Abaqus tool to generate a volume inside the gap and introduce the ring. It has the advantage that it is not necessary to incorporate an auxiliary model but has the disadvantage that for commercial rings, it does not work properly since the contacts are not established well. The second of the techniques developed has the inconvenient that it is necessary to introduce an additional model to generate the hole, but has the great advantage that it is able to generate the geometry required for each case, saving computational resources. In this case, the contacts between tool–tissue and ring–tissue are much smoother favouring the convergence of the simulation.

- To compare 2D axisymmetric and 3D simulations: to decide whether we need 3D full simulations or not. This aspect is fundamental to be able to implement simulations in a computer cluster that help to predict what happens in reality (3D models), and to obtain valid conclusions to generate nomograms which help the clinicians to improve the planning of the surgery.
- To use rings with different cross–sections: generic cross–sections (circular or ellipsoidal cross–sections which are easier for the contact), and commercial cross–sections such as Ferrara or Keraring (triangular), Intacs (hexagonal) or MyoRing. Thanks to the study of the insertion of different types of rings, it will be possible to check which rings are able to stabilise the keratoconus, which rings should be used according to the different degrees of keratoconus severity, or which of the types introduces greater correction without increasing too much the internal stress of the corneal tissue.
- To discern whether anisotropy is needed or not. To date, no *in–silico* study has performed ring insertion considering the anisotropy of the corneal tissue. Therefore, it is important to evaluate whether there are both mechanical and optical differences to consider this factor in the average models and their subsequent adaptation to specific patient models.

To understand corneal biomechanics after intrastromal ring implantation from an optomechanical standpoint

First, it will be necessary to validate the trends of the model with reference to clinical trends. Second, the following step, once the models are validated, is to understand the biomechanics of the cornea, i.e., stress distribution after implant insertion. Finally, we will be able to give a mechanical point of view in order to answer the open questions in the Ophthalmological community.

To apply *in-silico* models on a first approximation to mechanical nomograms

We apply the previous knowledge to run a cohort of virtual patients for MyoRing in order to draft a mechanical nomogram. Thanks to these nomograms, we will be able to determine the correction that is achieved according to the variables that define the surgery, i.e., depth, optical zone of implantation, size of the ring, etc. After all the calculations have been made for a cohort of virtual patients, it is possible to extract conclusions about the variables that most affect the outcomes both from the mechanical and optical point of view. The combination of these two results can help not only to better plan the surgery but also to select the ring that provides better mechanical and optical results.

To characterise the mechanics of the implants

Finally, a mechanical characterisation of the rings was proposed based on the combinations of the uniaxial experimental test and the *in-silico* models. Combining uniaxial tensor tests with *in-silico* models can be determined for the mechanical characterisation of the two ring typologies analyzed (Ferrara Ophthalmic S.L and Intacs, Addition Technology Inc.). In addition, we will be able to answer if the milling procedure is affecting the mechanical properties or not.

5. Organisation of the thesis

This Doctoral thesis follows a traditional structure organised by chapter (see the thesis scheme in Figure 1.2): Chapter 1 serves as an introduction. Chapter 2 acts as a point of connection between the introduction and the main body of the thesis, explaining the anatomy of the eye including its most representative parts, then the disease of keratoconus is commented, and

the different ways in which clinicians try to stabilise it, with special interest in the treatment of additive surgery by means of intrastromal corneal ring segments. Both Chapter 3 and 4 explains the different methodologies used to simulate the insertion of the rings within corneal stroma. Chapter 5 focuses on answering several open questions of the ophthalmological community. Chapter 6 aims to generate a preliminary nomogram able to estimate the optical correction according to the MyoRing inserted. Chapter 7, mechanical study of the rings to characterize its material. Finally, Chapter 8 serves as final conclusions and to explain the futures lines opened from the current thesis.

Chapter 1: Introduction.

Scope, motivation and objectives of the current PhD thesis.

Chapter 2: Eye, Keratoconus and treatments for corneal ectasia.

This chapter focuses on describing the anatomy of the eye and its main parts such as the cornea, limbus and sclera, explaining keratoconus disease and the techniques ophthalmologists use to treat the progression of this disease. In addition, the different commercial intrastromal rings are exposed, from the mechanical and geometric point of view, which is key to be able to perform computational models.

Chapter 3: Pressure-based ICRS implantation.

This chapter copes with the first methodology developed to mimic the intrastromal corneal ring segment surgery. This work is based on generating a hole large enough to house the implants by means of a pressure control. The Abaqus tool used was **Fluid cavity*. All the related information of this chapter is published in *“Template-based methodology for the simulation of intracorneal segment ring implantation in human corneas”*. *Biomechanics and Modeling in Mechanobiology*, 2019, Impact Factor (IF): 2.527. Q2: 42/87 *Biomedical Engineering Web of Knowledge (inCite JCR)*.⁴⁶

⁴⁶ Flecha-Lescún et al. 2018

Chapter 4: Displacement-based ICRS implantation.

This chapter copes with the second methodology proposed to simulate the ICRS insertion surgery. The methodology is based on the approach used in balloon angioplasty to introduce endovascular stents.⁴⁷ With this novel methodology, we were able to simulate the insertion commercial rings of different cross-section and size within corneal stroma and evaluate the opto-mechanical outcomes. Besides, it is the first study

⁴⁷ Gökçöl et al. 2017

which introduces the anisotropy of the cornea in the simulation of ICRS insertion. Finally, the friction between ring and tissue was evaluated. All the related information of this chapter is under revision in “*Modelling strategies for the simulation of corneal intrastromal ring surgeries (Annals of Biomedical Engineering, 2020)* (Under preparation).⁴⁸

⁴⁸ Flecha-Lescún et al. a

Chapter 5: Corneal biomechanics after intrastromal surgery.

This chapter attempts to answer open questions in the ophthalmological world about what happens to the cornea, biomechanically speaking, when a ring is inserted into the corneal stroma using *in-silico* models that reproduce generic elliptical section ring insertion surgery. The hypothesis that the volume introduced is more important than the shape of the cross-section is strengthened. In addition, it is studied if this implant can act as a second limbus. All the related information of this chapter is published in “*Corneal biomechanics after intrastromal ring surgery: optomechanical in-silico assessment*”. *Translational Vision Science and Technology, 2020, IF: 2.112 (2019). Q2: 28/60 Ophthalmology. Web of Knowledge (inCite JCR)*.⁴⁹

⁴⁹ Flecha-Lescún[#] et al. 2020

Chapter 6: Mechanical nomograms: application to MyoRing.

The main aim of this chapter is the application of the displacement based methodology to the insertion of commercial continuous rings, MyoRing. From the automatic meshing, a cohort of virtual patients was generated in order to generate nomograms which help surgeons to plan better the surgery. Thanks this results, it was possible to evaluate the different variables involved in the surgery and to observe which of them have the greatest influence on the optics after the simulation of the surgery.

Chapter 7: Mechanical Characterisation of ICRS.

This chapter copes with the mechanical characterisation of the intrastromal corneal ring segments. Uniaxial traction tests are performed, as well as models *in-silico* that reproduce the test to perform the characterisation. All the related information of this chapter is under revision in “*Mechanical characterization of intrastromal corneal ring implants*” (*Journal of the Mechanical behavior of Biomedical Materials, 2020*). (Under preparation)⁵⁰

⁵⁰ Flecha-Lescún et al. b

Chapter 8: Outcomes and Future Lines.

This chapter contains the main conclusions of the current work, and

research lines which are currently opened and constitute the main future lines of a post-doctoral research.

Appendix I: Resumen y Conclusiones en Español.

This appendix contains the information of the Summary and Conclusions to Spanish (required by the University of Zaragoza).

Appendix II: Publications.

In this appendix appears the title page of those articles already published.

Appendix III: Automatic model mesh to generate in-silico models.

This appendix aims to develop all the information concerning the automatic mesh proposed in the current thesis. With this automatic tool, virtual patient meshes can be prepared to evaluate not only different geometries but also to study the effects of surgical variables such as depth, diameter of the implantation area, ring size, etc.

Appendix IV: Additional Results.

This appendix incorporates additional results which has been obtained in the clinical works (Chapters 5 and 6).

Appendix V: Abbreviations.

This appendix shows the description of overall abbreviations used in the current thesis.

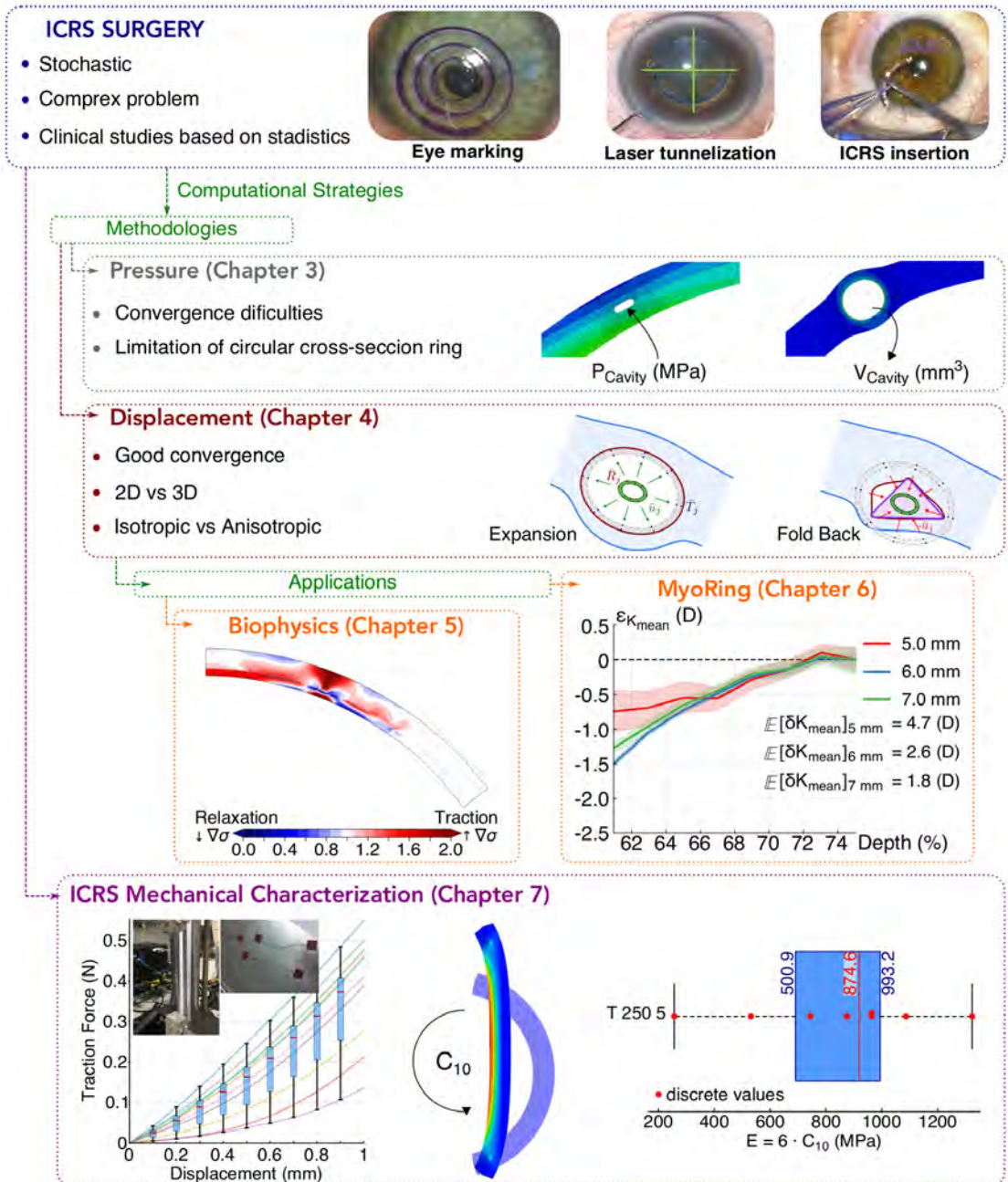


Figure 1.2: Scheme of the PhD thesis. Structure of the thesis organisation which was born from necessity of understand the ICRS surgery. Two methodology of ICRS insertion has been proposed (Chapter 3 and 4), but only the second one had a good convergence. From the methodology based on displacement, arise the applications: Biophysics of the problem (Chapter 5) and Influence of the surgery variables in MyoRing insertion (Chapter 6). In parallel, other study appeared: Mechanical characterisation of the rings through uniaxial traction test (Chapter 7).



Chapter 2

Eye, Keratoconus and Treatments for corneal ectasia

Main features about eye, its diseases and treatments are introduced.

Chapter Contents

1. Introduction	50
2. Eye Anatomy	50
<i>Anatomical terms of reference</i>	50
<i>General shape, size and position of the eye</i>	51
<i>Cornea</i>	51
<i>Sclera</i>	58
<i>Limbus</i>	59
3. Keratoconus disease	60
<i>Factors that promote the development of keratoconus</i>	60
<i>Classifications of keratoconus</i>	64
<i>Treatments against the keratoconus</i>	67
4. Intrastromal corneal ring implants	72
<i>Surgical procedure</i>	72
<i>Commercial intrastromal corneal rings</i>	75
5. Retrospective clinical and numerical studies	80
<i>Keraring to stabilise keratoconus</i>	80
<i>Ferrara to stabilise the keratoconus</i>	83
<i>Intacs to stabilise the keratoconus</i>	86
<i>MyoRing to correct myopia and to stabilise KC</i>	88
<i>In-silico studies about ICRS surgery</i>	91

1. Introduction

The eye is a specialised organ of photoreception, the process by which light energy from the environment produces changes in specialised nerve cells in the retina, the rods and cones. These changes result in nerve action potentials, which are subsequently relayed to the optic nerve and then to the brain, where the information is processed and, as a consequence, appreciated as vision. All the other structures in the eye are secondary to this basic physiological process, although they may be part of the system necessary for focusing and transmitting the light to the retina, for instance: cornea, lens, iris and ciliary body, or they may be necessary for nourishing and supporting the tissues of the eye, for example the choroid, aqueous outflow system and lacrima apparatus.

2. Eye Anatomy

2.1. Anatomical terms of reference

The internationally accepted terminology for description of the relations and position of structures in the body requires reference to a series of imaginary planes (see Figure 2.1). Thus, relative positions of anatomical structures are referred to in terms of:

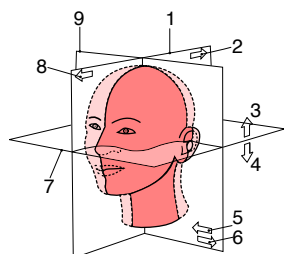


Figure 2.1: Diagram illustrating anatomical planes of reference. 1. Median or mid-sagittal plane; 2. Posterior; 3. Superior; 4. Inferior; 5. Medial; 6. Lateral; 7. Horizontal plane; 8. Anterior; 9. Coronal plane.

Medial Plane: nearer the median or mid-sagittal plane.

Lateral Plane: away from this plane.

Anterior Plane: refers to the front surface of the body.

Posterior Plane: makes reference to the back surface of the body.

Superior Plane: (cranial or rostral) or inferior (caudal) refer to vertical position.

Superficial and deep: specify distance from the surface of the body.

A combination of these terms can be used to describe the relative position of structures that do not fit exactly any of the other terms, for instance, ventrolateral, posteromedial, etc.

2.2. General shape, size and position of the eye

The eye (see Figure 2.2) is approximately a sphere of 2.5 cm in diameter with a volume of 6.5 ml. However, in reality it is part of two spheres, a smaller one anteriorly, the cornea, that has a greater curvature than the sclera, which constitutes the large sphere. The cornea forms one-sixth of the circumference of the globe and has a radius of 7.8 mm; the remaining five-sixths is formed by the sclera, which has a radius of 11.5 mm. There is variation in size between individuals but the average axial length of the globe is 24 mm (range 21-26 mm). The diameter is 23 mm and the horizontal length approximately 23.5 mm. Small eyes (<20 mm) are hyperopic or hypermetropic, while large eyes (26-29 mm) are myopic. The eye is situated in the anterior portion of the orbit, closer to the lateral than the medial wall and nearer the roof than the floor. The eye is made up of three basic layers or coats, often known as tunics. These are the fibrous (corneoscleral) coat, the uvea or uvea tract (composed of choroid, ciliary body and iris), and the neural layer (retina). The coats surround the contents, namely the lens and the transparent media (aqueous humour and vitreous body).

Together, the cornea and sclera form a tough fibrous coat which also provides important structural support for intraocular contents and for extraocular muscle attachment. The cornea meets the sclera at a region known as the limbus or corneoscleral junction.

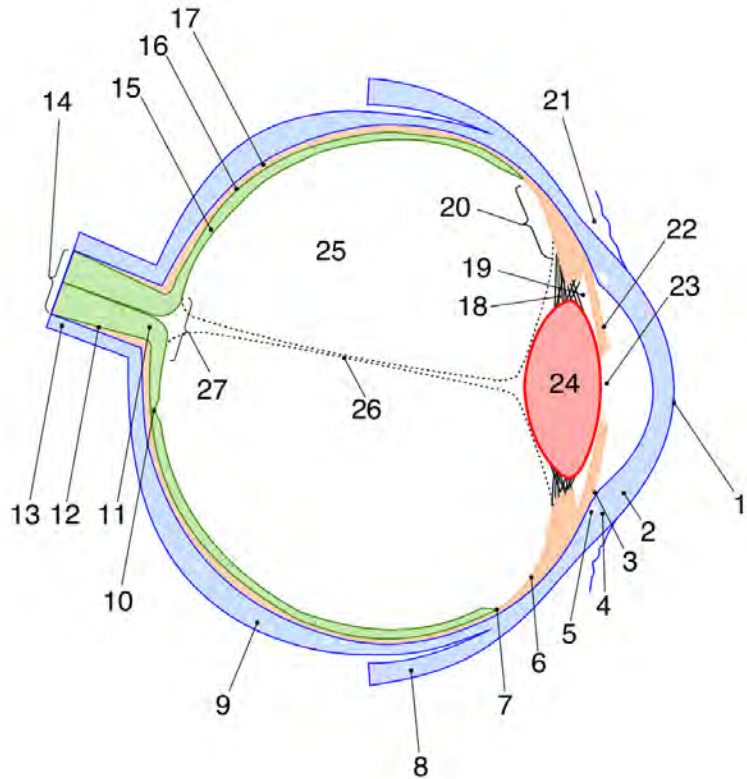
2.3. Cornea

The surface of the cornea (air-tissue interface) and associated tear film are responsible for most of the refraction of the eye. The transparency of the cornea is the most important property, although because of its highly exposed position it must also present a tough physical barrier to trauma and infection. Corneal transparency is the result of a number of related factors: its avascularity; the regularity and smoothness of the covering epithelium; and the regular arrangement of the extracellular and cellular components in the stroma, which is dependent on the state of hydration, metabolism and nutrition of the stromal elements.

2.3.1. Shape

The cornea is smaller in the vertical than in the horizontal diameter. However, viewed from behind, the circumference appears circular. The central radius is 7.8 mm with the peripheral corneal curvature being less

Figure 2.2: Schematic diagram of the human eye in horizontal section revealing the major components and the arrangement of the three layers. Corneoscleral envelope (blue), the uveal tract (orange), and the inner neural layer (green). *Parts of the Eye:* 1. Corneal epithelium; 2. Cornea; 3. Iridocorneal angle; 4. Limbus; 5. Canal of Schlemm; 6. Pars plana; 7. Ora serrata; 8. Rectus muscle tendon and belly; 9. Sclera; 10. Fovea; 11. Lamina cribrosa; 12. Sub-arachnoid space; 13. Dura mater; 14. Optic nerve; 15. Retina (neural layer); 16. Retinal pigment epithelium; 17. Choroid; 18. Lens zonules; 19. Posterior chamber; 20. Ciliary body; 21. Conjunctiva; 22. Iris; 23. Pupil; 24. Lens; 25. Vitreous; 26. Hyaloid (Cloquet's) canal; 27. Optic disk.



marked. The cornea is also thicker at the periphery (0.67 mm) than in the centre (0.52 mm).¹

¹ All values are the average of population.

2.3.2. Structure

The cornea is composed of five layers (see Figure 2.3):

Corneal epithelium: the corneal epithelium is a *stratified* (possessing five or six layers) *squamous non-keratinized* epithelium (the superficial cells are flattened, nucleated and non-keratinized). It is 50–60 μm in thickness and adjacent cells are held together by numerous *desmosomes* and to the underlying basal lamina by *hemidesmosomes* and anchoring filaments. The anterior surface of the corneal epithelium is characterised by numerous microvilli and microplicae (ridges) whose glycocalyx coat interacts with, and helps stabilise, the precorneal tear film. New cells

are derived from mitotic activity in the limbal basal cell layer and these displace existing cells both superficially and centripetally. The corneal epithelium responds rapidly to repair disruptions in its integrity by amoeboid sliding movements of cells on the wound margin followed by cell replication. The basal epithelial cells rest on a thin, but prominent, *basal lamina* (lamina lucida, 25 nm; lamina densa, 50 nm). Corneal epithelial adhesion maintained by a basement membrane complex, which anchors the epithelium to *Bowman's layer* via complex mesh of anchoring fibrils (type VII collagen) and anchoring plaques (type VI collagen), which interact with the lamina densa and the collagen fibrils of Bowman's layer. The corneal epithelium is devoid of melanocytes. Myeloid-derived major histocompatibility complex (MHC) class II antigen-positive dendritic cell (Langerhans cells) are present in the limbus and peripheral cornea, but decline sharply in density in a centripetal gradient, and are rare in the central cornea. However, MHC classII-negative dendritic cells have been identified in the mouse central cornea and recent *in-vivo* confocal microscopy (IVCM) suggests that the normal human central corneal epithelium contains dendritic cells although their immunophenotype cannot be ascertained from ICVM. The comparative paucity of potential antigenpresenting cells, such as dendritic cells, and the avascular nature of the cornea are considered crucial factors to the success of corneal grafting.

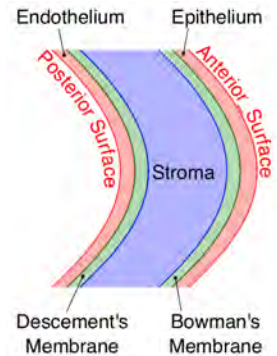


Figure 2.3: Structure of cornea. Conceptual diagram of the different corneal layers: from the most external layer (Epithelium) to the most internal layer (Endothelium). Stroma represents almost the 90% of the corneal thickness.

Anterior limiting lamina (Bowman's layer): Bowman's layer (a modified acellular region of the stroma; 8-12 μm thick) consists of fine, randomly arranged, collagen fibrils (20–30 nm diameter, types I, III, V and VI). The anterior surface is well delineated and is separated from the epithelium by the thin basal lamina, while the posterior boundary merges with the stroma. Bowman's layer terminates abruptly at the limbus.

Substantia propria or corneal stroma: the corneal stroma is a dense connective tissue of remarkable regularity. It makes up the vast majority of the cornea and consists predominantly of 2 μm thick, flattened, *collagenous lamellae* (200–250 layers) oriented parallelly to the corneal surface and continuous with the sclera at the limbus. Between the lamellae lie extremely flattened, modified fibroblasts known as *keratocytes*. These cells are stellate in shape with thin cytoplasmic extensions containing conspicuously few distinctive organelles when viewed in conventional cross-sections. However, frontal sections reveal an abundance

of organelles and a novel network of fenestrations on their surface which may facilitate the diffusion of metabolites or the mechanical “anchoring” or attachment of collagen bundles. The density of keratocytes in the anterior stroma is 20,000–24,000 cells/mm² and that density decreases posteriorly before increasing again near Descemet’s membrane. Keratocytes are connected by gap junctions to their neighbouring cells and arranged on a corkscrew pattern spiralling from the epithelium to the endothelium. The collagenous lamellae form a highly organised orthogonal ply, adjacent lamellae being oriented at right angles, with the exception of the anterior third in which the lamellae display a more oblique orientation. The collagen fibres are predominantly of type I (30 nm diameter, 64–70 nm banding) with some type III, V and VI also present. The transparency of the cornea is highly dependent on the regular diameter (influenced by the presence of type V collagen in particular) and spacing of the collagen fibres (interfibrillary distance), which in turn is regulated by glycosaminoglycans (GAG) and proteoglycans forming bridges between the collagen fibrils. The GAGs in the human cornea are predominantly keratan sulphate and chondroitin (dermatan) sulphates. The corneal stroma normally contains no blood or lymphatic vessels, but sensory nerve fibres are present in the anterior layers en route to the epithelium.

Posterior limiting lamina (Descemet’s membrane): This is a thin, homogeneous, discrete, periodic acid–Schiff–positive layer between the posterior stroma and the endothelium, from which it can become detached. It is 8–12 μm in thickness and represents the modified basement membrane of the corneal endothelium. It consists of two parts, an anterior third that is banded and a homogeneous or non-banded posterior two-thirds. It is rich in basement membrane glycoproteins, laminin and type IV collagen. The anterior banded region is reported to contain type VIII collagen. Types V and VI collagen may be involved in maintaining adherence at the interface of Descemet’s membrane with the most posterior lamellae of the stroma. Descemet’s membrane is continuous peripherally with the cortical zone of the trabeculae in the trabecular meshwork. Microscopic wart-like protuberances (Hassall–Henle bodies) containing “long banded” (100 nm) deposits of unknown nature appear in the periphery of Descemet’s membrane with age. It is frequently thickened at its peripheral termination (Schwalbe’s line, the anterior limit

of the trabecular meshwork). If disrupted, Descemet's membrane tends to curl inwards towards the anterior chamber.

Corneal endothelium: This layer, a *simple squamous epithelium* on the posterior surface of the cornea, has a critical role in maintaining corneal hydration and thus transparency. Fluid is constantly being lost via evaporation at the ocular surface, a fact illustrated by increased cornea thickness after a night of lid closure and when an impermeable lens is placed over the epithelium. The endothelial cells rest on Descemet's membrane and form an uninterrupted polygonal or hexagonal array, or mosaic, which can be clearly seen *in vivo* with the aid of *specular microscopy* and *in vivo confocal microscopy*. The cells are 5–6 μm in height and 18–20 μm in diameter. Their lateral surfaces are highly interdigitated and possess apical junctional complexes that, together with abundant cytoplasmic organelles including mitochondria, are indicative of their crucial role in active fluid transport.

2.3.3. Nerve supply of the cornea

The cornea is richly supplied by sensory fibres derived from the ophthalmic division of the *trigeminal nerve*, mainly via *long ciliary nerves*. Occasionally the inferior cornea receives some branches from the maxillary division of the trigeminal. Nerve bundles enter the peripheral cornea in a radial manner and as they travel centrally below the anterior one-third of the stroma and approximately 1 mm from the limbus they lose their perineurium and myelin sheaths. This alteration in myelination is thought to be related to the importance for transparency. They divide into smaller branches and begin to change direction towards the epithelium where they must pierce Bowman's layer, whereupon they further divide into smaller bundles to form the *subepithelial* or *subbasal plexus* in the interface between Bowman's layer and the basal aspect of the cornea epithelium. There are apparently no specialised end organs associated with these terminal axons, which are predominantly within the size range 0.1–0.5 μm consistent with A-delta and C fibres that function to transmit the sensory modalities of pain and temperature. Individual beaded fibres penetrate the epithelial layers and terminate in the superficial layers in the form of an intraepithelial plexus. There are approximately 7,000 nociceptors per mm^2 in the human corneal epithelium.

2.3.4. Material models

It can be deduced from anatomy of the eye that cornea is a highly porous tissue formed by a laminar structure. To sum up and although it has a high water content ($\approx 80\%$), the cornea is formed by three main layers: the epithelium, the endothelium, and the central stroma (see in Figure 2.3). Apart from the main layers, there are two additional layers which connect the epithelium and the endothelium with the stroma: Bowman and Descemet's membranes.² In spite of the constitution of each layer is different, the most important is the stroma, which represents the 90% of the corneal thickness. Its structure presents several overlapping collagen lamellae composed of bundles of collagen fibrils surrounded by a gelatinous matrix mostly composed of glycoproteins. The microstructure of the stroma is highly heterogeneous, depending on the specific region and corneal layer being evaluated.³ The anterior stromal lamellae are more closely packed and less hydrated than the posterior stroma, with stronger junctions between collagen lamellas. Thus, the anterior stroma is suggested to hold a main role in maintaining the corneal strength and curvature. This anisotropy in the stromal architecture is also suggested to result in an anisotropic mechanical behaviour of the corneal tissue, being supported by experimental and clinical studies⁴ However, due to the material of the implants is stiffer than the cornea, hyperelastic model has been used to model it in the numerical studies.⁵

Three different models has been used in the current thesis:

Neo–Hookean Model

In Chapter 3, where the opening of the gap to house the implant is made by means of pressure control, the cornea was modelled as a Neo–Hookean hyperelastic material (see in Equation 2.1). In addition, due to the difference in rigidity between the corneal material and the ring, it is not such an important variable.

$$\psi_N = \frac{1}{D} \cdot \left(\frac{J_{el}^2 - 1}{2} - \ln(J_{el}) \right) + C_{10}^N \cdot (\bar{I}_1 - 3) \quad (2.1)$$

where C_{10}^N is the parameter of the Neo–Hookean model \bar{I}_1 is the first invariant of the modified right Cauchy–Green tensor $\bar{C} = J_{el}^{-2/3} C$, J_{el} is the elastic volumen ratio, and $\frac{1}{D}$ is the bulk modulus.

² Seiler et al. 1992, Sancho 2010

³ Winkler et al. 2013, Benoit et al. 2016

⁴ Pandolfi and Holzapfel 2008, Ariza-Gracia et al. 2016, 2017b

⁵ Ebrahimiyan et al. 2019, Kling and Marcos 2013, Lago et al. 2015

Finally, we did not try to reproduce exactly the topography but the difference between pre- and post-surgical, and observe the aberrations that are introduced when implying a ring in an average healthy eye or an eye with central keratoconus.

Yeoh Model

In Chapter 4, the material was changed to a Yeoh hyperelastic model (see in Equation 2.2) in which the behaviour of the material is softer at the beginning and then stiffer at the end. The material constants are calculated according to the tangent module of the material considered in Ariza-Gracia *et al.* (2016)⁶ where the fibres are considered.

⁶ Ariza-Gracia *et al.* 2016

$$\psi_Y = \sum_{i=1}^3 C_{i0} \cdot (\bar{I}_1 - 3)^i + \sum_{k=1}^3 \frac{1}{D_k} \cdot (J - 1)^{2k} \quad (2.2)$$

where C_{i0} are the material parameters, \bar{I}_1 is the first invariant of the modified right Cauchy-Green tensor, $1/D_k$ is the bulk modulus and J is the determinant of the modified right Cauchy-Green tensor.

Combination of the Demiray and Gasser-Holzapfel-Ogden model

Finally, to continue with the complete validation, and due to the fact that it is impossible to add the reinforced material caused by the fibres in axisymmetric model, the anisotropy of the eye is introduced using the same model to Ariza-Gracia *et al.* (2016)⁷ in tridimensional model (see in Equation 2.3).

⁷ Ariza-Gracia *et al.* 2016

$$\begin{aligned} \psi = & D_1 \cdot \{\exp[D_2 \cdot (\bar{I}_1)] - 1\} + \frac{k_1}{2 \cdot k_2} \cdot \sum_{\alpha=1}^N \{\exp[k_2 \langle \bar{E}_\alpha \rangle^2] - 1\} \\ & + K_0 \cdot \left(\frac{J_{el}^2 - 1}{2} - \ln(J_{el}) \right) \end{aligned}$$

with $\bar{E}_\alpha = \kappa \cdot (\bar{I}_1 - 3) + (1 - 3\kappa) \cdot (\bar{I}_{4(\alpha\alpha)} - 1)$

(2.3)

where the first term of the equation refers to the matrix where the fibres are embedded, the second term refers to the behaviour of the families of fibres considered for the cornea and the last term is the volumetric term. The families of fibres considered are 2 orthogonal to each other.

2.4. Sclera

The sclera forms the main part of the outer fibrous coat of the eye and functions both to protect the intraocular contents and to maintain the shape of the globe when distended by intrinsic intraocular pressure. The globe is maintained even during contraction of the extraocular muscles, whose tendons insert in its surface. The sclera is relatively avascular and in adults appears white externally. The viscoelastic nature of the sclera (great tensile strength, extensibility and flexibility) allows only limited distension and contraction to accommodate minor variations in intraocular pressure.

The sclera is thicker posteriorly (1 mm) and thinner (0.3–0.4 mm) behind the insertions of the aponeurotic tendons of the extraocular muscles. It is covered by the *fascia bulbi* posteriorly and the conjunctiva anteriorly. The sclera consists of dense irregular connective tissue comprising extracellular matrix and matrix-secreting fibroblasts. The matrix consists mainly of collagen type I, although types III, IV, V, VI, VIII, XII and XIII have been identified.⁸ Unlike the cornea, the scleral collagenous lamellae are irregularly arranged and are interspersed with elastic fibres, each consisting of an elastin core surrounded by longitudinally arranged microfibrils composed of a number of glycoproteins including fibrillin. The opaque nature of the sclera, in contrast to the transparency of the cornea, can be partly ascribed to this irregular arrangement of the collagen fibres, but also to the variable fibre diameter (25–250 nm), variable and irregular fibrillar spacing, higher water content, and the reduced coating of the GAGs on collagen fibres. Indeed, the sclera contains one-quarter of the proteoglycan and GAG content of the cornea. Dermatan sulphate and chondroitin sulphate proteoglycans are the most abundant in the sclera.

Collagen fibrils take up tensile force and are aligned with the direction of the greatest tensile strength. The arrangements of scleral collagen can be studied using the “split-line” technique, which has revealed that the collagen fibrils in the outer sclera are arranged in bundles that course in whorls, loops and arches, particularly around the muscle insertions and optic nerve. The collagen fibrils on the internal aspect of the sclera are arranged in a rhombic pattern.

The sclera extends anteriorly from the *limbus* to the *lamina cribrosa* posteriorly. The scleral collagen fibrils are arranged in circles or figure-of-eight patterns at the lamina cribrosa. Histologically, the sclera has three layers: the lamina fusca, stroma and episclera.

⁸ Rada et al. 2006

2.4.1. Material model

The sclera is only considered in the methodology developed in Chapter 3. It follows a Yeoh hyperelastic model (see Equation 2.2) with the constants taken from the model of Ariza–Gracia *et al.* (2016):⁹ $C_{10} = 0.81$ MPa, $C_{20} = 56.050$ MPa, $C_{30} = 2,332.26$ MPa, $D_i = 0$ MPa⁻¹.

⁹ Ariza-Gracia *et al.* 2016

2.5. Limbus

It is becoming increasingly appreciated that the *limbus* is more than the border zone between the cornea and sclera; it has multiple functions including nourishment of the peripheral cornea, corneal wound healing, immunosurveillance of the ocular surface and hypersensitivity response; it contains the pathways of aqueous humour outflow and is thus involved in the control of intraocular pressure.

The limbus is 1.5–2.0 mm in width and the change in the radius of curvature between the sclera and cornea produces a shallow *external scleral sulcus* and an *internal scleral sulcus*; the latter is deepened by the scleral spur and houses the canal of Schlemm and trabecular meshwork. The longitudinally ciliary muscle fibres attach to the posterior aspect of the *scleral spur*, and its anterior surface gives rise to the corneoscleral trabeculae.

Several important transitions take place at the limbus:

- The regularly arranged corneal lamellae give way to the more random array of lamellae in the sclera. The corneal termination is V-shaped.
- The stratified squamous non-keratinized corneal epithelium with its parallel internal and external surfaces gives way to conjunctival epithelium, characterised by a folded basal surface and interdigitating subepithelial connective tissue (sometimes forming distinct papillae).
- The conjunctival epithelium contains goblet cells and a rich network of MHC class II⁺ CD11c⁺ dendritic (Langerhans) cells.
- Loops or arcades of conjunctival capillaries (derived from the anterior ciliary arteries) and lymphatic capillaries terminate at the limbus. The smaller vessels are not under neuronal control and are particularly susceptible to the effects of vasoactive amines (e.g. histamine, leukotrienes, prostaglandins) released by local immune cells (see below).
- Desçemet's membrane and Bowman's layer terminate in this region.

- The loose conjunctival subepithelial vascularised connective tissue (substantia propria), containing immunocompetent cell types such as mast cells, plasma cells and lymphocytes, tapers off at the limbus and is absent in the cornea.

2.5.1. Material model

Finally, although the limbus also presents a circumferential direction of fibres,¹⁰ it was modelled as a Neo–Hookean model (see Equation 2.1) being $C_{10} = 0.05$ MPa.

¹⁰ Ariza-Gracia et al. 2016, Pandolfi and Vasta 2012

3. Keratoconus disease

Keratoconus is an idiopathic, non-inflammatory and degenerative corneal disease that typically develops in the inferior-temporal and central zones, mainly.¹¹ Despite its ethiology being still partially unknown,¹² corneas with keratoconus or ectasia present a loss of organisation in the corneal collagen fibrils that results in a localised thinning and a conical protrusion (see Figure 2.4.a–b).¹³ In KC, the corneal surface presents a progressive asymmetric deformation with irregular astigmatism and high myopia that worsens visual acuity.¹⁴ KC is ethnic-dependent¹⁵ and targets on young to mid-age patients, appearing during the adolescence and progressing until maturity.¹⁶ Although its incidence is low, 0.05–2.5%, the absence of a cure and its long-term blinding effects put KC on the spot (see Figure 2.4).

¹¹ Auffarth et al. 2000, Fangjun et al. 2016, Sakellaris et al. 2019

¹² Ramez et al. 2017, Sherwin et al. 2017, Dan Z. et al. 2017, O'Brat 2017

¹³ Auffarth et al. 2000

¹⁴ Fangjun et al. 2016

¹⁵ Ramez et al. 2017

¹⁶ O'Brat 2017

3.1. Factors that promote the development of keratoconus

3.1.1. Environmental and Genetic Factors

Keratoconus is thought to be caused by a complex interplay of environmental and genetic factors, as well as biomechanical and biochemical disorders.¹⁷ Whilst their exact nature remains unclear, the relevance of environment and genetic factors explains the wide variation in prevalence across geographic areas. Varying prevalence among groups of different ethnicity living in the same geographic location suggests a genetic basis for disease. For instance, higher prevalence than the British average has been found in Indian, Pakistani and Bangladeshi communities living in the United Kingdom.¹⁸ Further evidence of a genetic basis to the disease includes a significant association with consanguinity;¹⁹ for example, in one study, 10% of patients with keratoconus had a family history of the disease, compared with just 0.05% of the age-matched control group.²⁰ While both dominant

¹⁷ Gomes et al. 2015, Sugar and Macsai 2012, Edwards et al. 2001, Malecaze et al. 2012

¹⁸ Georgiou et al. 2004, Pearson et al. 2000

¹⁹ Gordon-Shaag et al. 2013

²⁰ Rabinowitz 2003

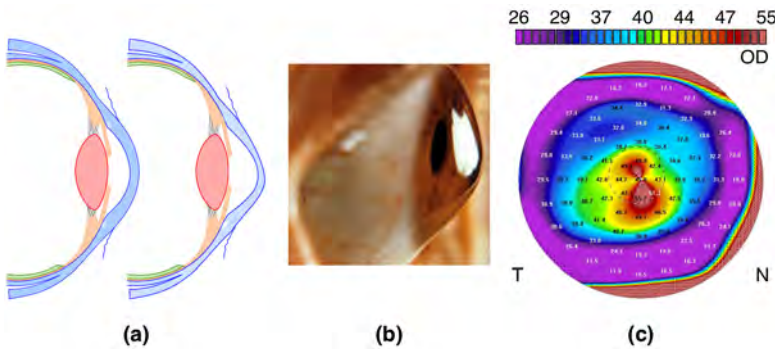


Figure 2.4: Form of keratoconus. (a) Schematic form of keratoconus, the image on the left shows a normal cornea and the image on the right represents a cornea with keratoconus; (b) keratoconus in cornea where appears the typical conical protrusion caused by a loss of organisation in the corneal collagen fibrils; (c) Topographic tangential map of a keratoconus in showman form.

and recessive patterns of autosomal inheritance have been proposed,²¹ most cases of keratoconus to date have been deemed sporadic.²²

Current thinking is that geographic variations in prevalence can be explained by specific environmental factors promoting the expression of genetic factors related to ethnicity.²³ This may occur through epigenetic modifications including DNA methylation, which alters gene expression and subsequent phenotype.²⁴ Epigenetic modifications may result from environmental stressors including toxins and microbial exposure,²⁵ but the most widely discussed are ultraviolet light exposure and eye rubbing.²⁶

3.1.2. Ultraviolet Light Exposure

Higher prevalence of keratoconus has been identified in Saudi Arabia,²⁷ Iran,²⁸ New Zealand,²⁹ Israel³⁰ and some Pacific Islands populations.³¹ One explanation for this distribution is that these are areas with high ultraviolet (UVA) light exposure (an environmental factor widely implicated in keratoconus).³² Excess UV exposure may be geographical in origin (latitudinal and altitudinal), or related to outdoor pursuits including work and leisure activities. It is proposed that UV light increase the production of reactive oxygen species within the cornea³³ and that keratoconic corneas lack the ability to process excess reactive oxygen species³⁴ which leads to oxidative stress, cytotoxicity and corneal thinning.³⁵

3.1.3. Eye Rubbing and Allergy

The association between eye rubbing and keratoconus was first described in 1956.³⁶ While some studies have found similar rates of eye rubbing among patients with keratoconus and normal controls,³⁷ the asso-

²¹ Shneor et al. 2014, Burdon et al. 2008

²² Nowak and Gajecka 2011

²³ McMonnies 2014

²⁴ Barros and Offenbacher 2009

²⁵ Barros and Offenbacher 2009

²⁶ McMonnies 2014

²⁷ Assiri et al. 2005

²⁸ Hashemi et al. 2013b

²⁹ Owens and Gamble 2003

³⁰ Shneor et al. 2014

³¹ Gordon-Shaag et al. 2012

³² McMonnies 2014

³³ Marchitti et al. 2011

³⁴ Kenney et al. 2000

³⁵ Kenney and Brown 2003

³⁶ Ridley 1956

³⁷ Millodot et al. 2011, Weed et al. 2007

³⁸ Gordon-Shaag et al. 2015

ciation with eye rubbing is now widely accepted.³⁸

³⁹ Gomes et al. 2015

Recurrent epithelial trauma may cause epigenetic modifications that facilitate the gene expression required for development of keratoconus.³⁹

⁴⁰ McMonnies 2009

Raised intraocular pressure caused by eye rubbing has also been cited as a contributory factor.⁴⁰ In hot and dry climates, high levels of dust may induce frequent eye rubbing, providing another potential explanations for the higher prevalence in these areas.⁴¹

⁴¹ Gordon-Shaag et al. 2015

⁴² Romagnani 2004

The prevalence of atopic/allergic disease in developed countries has risen in recent years,⁴² and similar increases in keratoconus could be related to this.⁴³ Similar to keratoconus, the aetiology of atopy is thought to be a combination of genetic and environmental factors, linked via epigenetic modifications.⁴⁴ Whilst allergic eye disease causes itch that leads to the urge for patients to rub their eyes, atopy is common in the general population as well as the population of keratoconics. Some studies have recorded low correlations between atopy and keratoconus in large series⁴⁵ but other have reported strong associations.⁴⁶

⁴³ McMonnies 2004

⁴⁴ McMonnies 2014

⁴⁵ Spencer and Fischer 1959, Galin and Berger 1958, Roth and Kierland 1964

⁴⁶ Davies et al. 1976, Rahi et al. 1977, Gasset et al. 1978

⁴⁷ Bawazeer et al. 2000

⁴⁸ Bawazeer et al. 2000

More recently, using univariate analysis, Bawazeer *et. al* (2000)⁴⁷ found that keratoconus was associated with eye rubbing, atopy and family history. However, multivariate analysis of the same data by the same group revealed eye rubbing as the only significant predictor of disease.⁴⁸ Therefore, while atopy may contribute to keratoconus, it is thought to be caused more frequently through the promotion of eye rubbing than the atopic process itself.⁴⁹

⁴⁹ Bawazeer et al. 2000

3.1.4. Gender

⁵⁰ Jonas et al. 2009, Laqua 1971, Amsler 1961, Hammerstein 1972

⁵¹ Ertan and Muftuoglu 2008, Street et al. 1991, Fatima et al. 2010, Poulliquen et al. 1981, Owens and Gamble 2003

⁵² Kennedy et al. 1986

There is not a correspondence on the keratoconus evolution between males and females. While some studies demonstrated the preponderance of 53%, 57%, 65%, and 66%⁵⁰ female dominance, others affirmed the male preponderance of 62%, 53%, 57%, and 59%.⁵¹ However, Kennedy *et. al* (1986)⁵² assured no significant gender difference and overall keratoconus is not considered to favour one gender over the other.

3.1.5. Age

⁵³ Galvis et al. 2015

⁵⁴ Krachmer et al. 1984, Sakellaris et al. 2019

Keratoconus is a disease of adolescence and young adulthood typically presenting between the ages of 20 and 30 years,⁵³ and diagnosis uncommon after the age of 35 years.⁵⁴ An exception to this is the diagnosis of older patients when presenting for other reasons, e.g. as candidates for cataract or keratorefractive surgery, where ectasia went undetected in

earlier life due to either mild symptoms or less sophisticated imaging.

It should be noted that age of diagnosis is quite different from age of onset, and the latency between the two remains unclear. Younger age of onset predicts greater severity,⁵⁵ faster progression and/or shorter time to penetrating keratoplasty.⁵⁶ Early diagnosis of keratoconus is crucial, as treatment including corneal collagen cross-linking can now be offered to arrest disease progression, and this has been facilitated by recent advances in imaging. In a Finnish cohort, Ihalainen (1986)⁵⁷ reported that 73% of patients were aged 24 years or below at the first onset of symptoms, with a mean age of 18 years. Olivares-Jimenez *et. al* (2008)⁵⁸ reported a mean age of symptom onset of 15.39 years in a Spanish cohort. Again, ethnic differences are apparent, with Asians having a significantly lower age (4–5 years less) of first presentation compared with Caucasians.⁵⁹

Low number of patients reported as diagnosed with keratoconus aged over 50 years are somewhat surprising given the chronic nature of the disease.⁶⁰

3.1.6. Associations with other Diseases

Keratoconus has been associated with several other syndromic conditions. This has helped understand both the epidemiology and pathophysiology of the disease.

Down Syndrome: Patients with Down syndrome tend to have a higher than average prevalence of keratoconus⁶¹ varying between 0 and 30% across several studies. However, some works did not find keratoconus among 157 children with Down syndrome aged 1 month – 18 years,⁶² and a similar finding was reported in separated studies of Malaysian and Chinese children.⁶³ Therefore, it is unclear whether the higher prevalence of keratoconus in some populations of Down syndrome is related to eye rubbing and atopy, or some other phenotypic consequences of the chromosomal abnormality.

Leber's Congenital Amaurosis: Keratoconus is more commonly found with Leber's congenital amaurosis (LCA) than other hereditary blinding disease.⁶⁴ While some hypothesise that eye rubbing due to poor vision is the associating factor, it is now considered more likely to be genetic factors that link keratoconus with LCA.⁶⁵

Connective Tissue Disorders: Connective tissue disorders encompass a wide range of conditions characterised by defective collagen or elastin.

⁵⁵ Caroline *et al.* 2008

⁵⁶ Caroline *et al.* 2008

⁵⁷ Ihalainen 1986

⁵⁸ Caroline *et al.* 2008

⁵⁹ Georgiou *et al.* 2004, Pearson *et al.* 2000, Cozma *et al.* 2004

⁶⁰ Gordon-Shaag *et al.* 2015

⁶¹ van Splunder *et al.* 2004

⁶² Fimiani *et al.* 2007

⁶³ Fimiani *et al.* 2007, García-García and Belmonte-Martínez 2008, Koppen *et al.* 2010

⁶⁴ Elder 1994

⁶⁵ Elder 1994

⁶⁶ Akcay et al. 2014⁶⁷ Castori 2012⁶⁸ Greenfield et al. 1973, Beckh et al. 1995⁶⁹ Maumenee 1981

Several of these syndromes have been associated with keratoconus: Mitral Valve Prolapse,⁶⁶ Ehlers–Danlos Syndrome,⁶⁷ Osteogenesis Imperfecta,⁶⁸ Marfan syndrome.⁶⁹

3.2. Classifications of keratoconus

3.2.1. Amsler–Krummeich criterium to classify the Keratoconus

The classification of Amsler–Krummeich⁷⁰ establishes four grades of keratoconus, combining values of refraction, keratometry, pachymetry and clinical findings and Figure 2.5:

Grade I: Central mean keratometry ≤ 48 D, RMS for corneal coma between 1.5 and 2 μm (for 6 mm diameter area), and absence of scars.

Grade II: Central pachymetry (CCT) > 400 μm , with central mean keratometric reading between 48 and 53 D, absence of corneal scars and RMS for corneal coma between 2.5 and 3.5 μm (for 6 mm diameter zone).

Grade III: Central pachymetry (CCT) between 300 and 400 μm , mean central keratometric reading between 53 and 55 D, no scarring, and RMS for corneal coma between 3.5 and 4.5 μm (for 6 mm diameter zone).

Grade IV: Central pachymetry (CCT) ≤ 200 μm , mean keratometric readings > 55 D, with central corneal scars and RMS values for the corneal coma > 4.5 μm (for 6 mm diameter zone).

3.2.2. Keratoconus classification based on clinical phenotypes

It is necessary to remember two basic concepts to understand the different phenotypes that constitute this new proposal for the classification of keratoconus. The first is that in keratoconus, the thinnest point of the cornea is located in the lower temporal quadrant. The second concept is that keratoconus can develop in a cornea with or without previous astigmatism. Therefore, the morphology (phenotype) of keratoconus in one or the other scenario will be completely different. For the description of each phenotype, a right eye (RE) is always taken as an example.

⁷⁰ Alió and Shabayek 2006

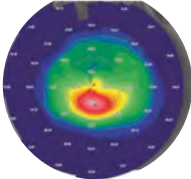
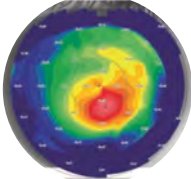
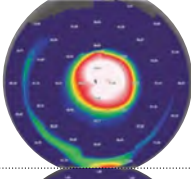
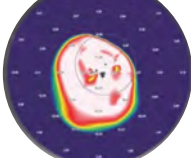
Grades	Topography	K_{mean} (D)	RMS at 6 mm area (μm)	CDVA (logMAR)
I		$K_{\text{mean}} \leq 48$	$1.5 \leq \text{RMS} < 2$	$\text{CDVA} > 0.9$
II		$48 < K_{\text{mean}} \leq 53$	$2.5 \leq \text{RMS} < 3.5$	$0.6 \leq \text{CDVA} < 0.9$
III		$53 < K_{\text{mean}} \leq 55$	$3.5 \leq \text{RMS} < 4.5$	$0.4 \leq \text{CDVA} < 0.6$
IV		$K_{\text{mean}} > 55$	$\text{RMS} > 4.5$	$0.2 \leq \text{CDVA} < 0.4$

Figure 2.5: Severity grade of keratoconus according Amsler–Krumeich classification. Figure which shows the classification of the keratoconus grade according to Amsler–Krumeich criterion.

CORNEA WITHOUT ASTIGMATISM

Regarding a flat cornea (OD), without astigmatism, the development of a keratoconus in it gives rise to two different phenotypes, depending on where the thinnest point is located (see Figure 2.6). If the thinnest point appears in the centre of the cornea, we have the phenotype called central hyperprolate (CHP) or “nipple”. In these cases, there is a high corneal asphericity and also an increase in spherical aberration. On the other hand, when the thinnest point appears in any other area of the lower temporal quadrant, the phenotype called paracentral with coinciding topographic and comatose axes (PCC) “croissant” is produced.

CORNEAL WITH PRO–RULE ASTIGMATISM

Considering a cornea (OD) with pro–rule astigmatism, i.e. meridian

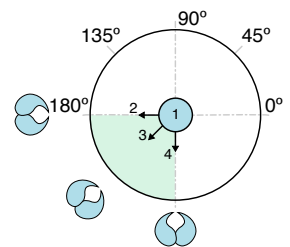


Figure 2.6: Phenotypes developed when KC is originated in a cornea without astigmatism. 1. Central hyperprolate (CHP) or “nipple”; 2-3-4. Paracentral with coinciding topographic and comatose axes (PCC) or “croissant”.

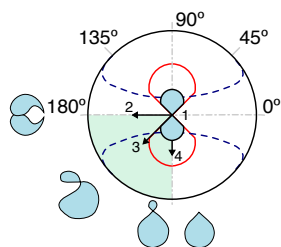


Figure 2.7: Phenotypes developed when KC is originated with pro-rule astigmatism. 1. Central phenotype with symmetrical astigmatism (CAS) or “bow tie”; 2. Paracentral with coinciding topographic and comatose axes (PCC) or “croissant”; 3. Paracentral phenotype with non-matching topographic and comma axes (PCnC) or “duck”; 4. Paracentral phenotype with perpendicular topographic and comatose axes (PCP) or “snowman”.

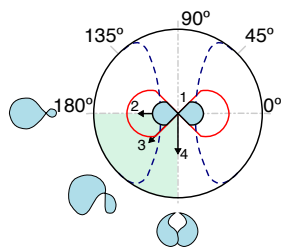


Figure 2.8: Phenotypes developed when KC is originated against the rule astigmatism. 1. Central phenotype with symmetrical astigmatism (CAS) or “bow tie”; 2. Paracentral phenotype with perpendicular topographic and comatose axes (PCP) or “snowman”; 3. Paracentral phenotype with non-matching topographic and comma axes (PCnC) or “duck”; 4. Paracentral phenotype with coinciding topographic and comatose axes (PCC) or “croissant”.

more curved at 90° , curvature map with typical image “in eight” vertical, meridian no more flat at 0° , anterior elevation map with image in horizontal band, the keratoconus can manifest itself according to four different phenotypes (see Figure 2.7). If the thinnest point appears in the centre of the cornea, the central phenotype with symmetrical astigmatism (CAS) or “bow tie” is originated; because of its central location, corneal asphericity and spherical aberration may increase. Whether the ectasia appears in the vertical line that delimits the quadrant, then the paracentral phenotype with perpendicular topographic and comatose axes (PCP) or “snowman” is produced. When the ectasia appears on the bisector line of the quadrant, the paracentral phenotype with non-matching topographic and comma axes (PCnC) or “duck” is produced. The image is a “duck” looking to the right. If the ectasia appears in the horizontal line that delimits the quadrant, the phenotype is produced again in “croissant”, which also appeared in the corneas without astigmatism.

CORNEAL WITH ASTIGMATISM AGAINST THE RULE

Considering a cornea (OD) with astigmatism against the rule, i.e. meridian more curved at 0° , curvature map with typical image “in eight” horizontal, meridian more flat at 90° , anterior elevation map with image in vertical band, the keratoconus can also be manifested, according to four different phenotypes (see Figure 2.8). If the thinnest point appears in the centre of the cornea, the phenotype originates in “bow tie”. When the ectasia appears in the vertical line that delimits the quadrant, the phenotype in “croissant” is produced. If the ectasia appears on the bisector line of the quadrant, the phenotype is produced in “duck”, but with the particularity of presenting an inverted image. Finally, when the ectasia appears on the horizontal line that delimits the quadrant, the phenotype in “snowman” is presented.

CORNEA WITH OBLIQUE ASTIGMATISM

Focussing on a cornea (OD) with oblique astigmatism and the most curved meridian at 135° , i.e. curvature map with typical “in eight” image at 135° , meridian plus plan at 45° , anterior elevation map with oblique band image at 45° , the keratoconus can be also manifested itself according to four different phenotypes (see Figure 2.9). When the thinnest point appears in the centre of the cornea, the phenotype already described in “bow tie” originates. Whether the ectasia appears in the vertical line that delimits the square, the phenotype is produced in “duck” looking towards the horizon.

If the ectasia appears on the bisector line of the quadrant, the phenotype is produced in “croissant”. When the ectasia appears on the horizontal line that delimits the quadrant, a “duck” phenotype is produced, but with the particularity of having an inverted morphology caused by the special relationship between the astigmatism axis and the direction of the ectasia.

Regarding a cornea (OD) with oblique astigmatism, but in the other direction, more curved meridian at 45° , i.e curvature map with typical image “in eight” at 45° , flatter meridian at 135° , anterior elevation map with image in oblique band at 135° , the keratoconus can be also manifested itself according to four distinct phenotypes (see Figure 2.10). When the thinnest point appears in the centre of the cornea, the phenotype originates in “bow tie”. The phenotype in “duck” is produced looking upwards when the ectasia appears in the vertical line that delimits the quadrant. Whether the ectasia appears on the bisector line of the quadrant, the “snowman” phenotype is produced. Finally, if the ectasia appears on the horizontal line that delimits the quadrant, a “duck” phenotype is produced looking to the right.

3.3. Treatments against the keratoconus

There are different forms or techniques to try to stabilise the keratoconus and to avoid the penetrating keratoplasty or cornea grafts:⁷¹ Contact lenses, corneal collagen cross-linking (CXL) or intrastromal corneal ring segments (ICRS) implantation.

3.3.1. Contact lenses for keratoconus

There are a lot of different contact lens modalities that can be used to improve the visual acuity in patients with keratoconus. Patients with mild keratoconus are often able to achieve clear vision with spectacles simply by correcting for spherical and regular astigmatism components of refractive error. However, in order to optimize visual acuity in patients with moderate to severe keratoconus, contact lenses are used to mask the irregular astigmatism and reduce the higher order aberrations. An example of lens in a cornea with keratoconus is shown in the Figure 2.11.

Corneal rigid gas permeable (RGP) contact lenses: Corneal RGPs remain the most popular contact lens modality for improving vision in patients with keratoconus (see Figure 2.12.a). As the name implies, these lenses are “rigid” and hold their shape when placed on a irregular cornea. The irregular surface between the back of the contact lens and

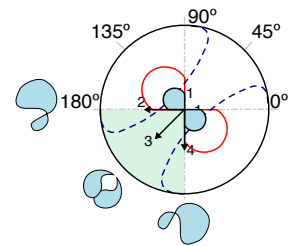


Figure 2.9: Phenotypes developed when KC is originated with oblique astigmatism (the most curved meridian at 135°).
 1. Central phenotype with symmetrical astigmatism (CAS) or “bow tie”; 2. Paracentral phenotype with non-matching topographic and comma axes (PCnC) or “duck”; 3. Paracentral with coinciding topographic and comatose axes (PCC) or “croissant”; 4. PCnC Phenotype.

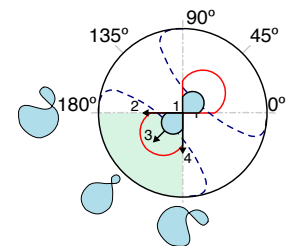


Figure 2.10: Phenotypes developed when KC is originated with oblique astigmatism (the most curved meridian at 45°).
 1. Central phenotype with symmetrical astigmatism (CAS) or “bow tie”; 2. Paracentral phenotype with non-matching topographic and comma axes (PCnC) or “duck”; 3. Paracentral phenotype with perpendicular topographic and comatose axes (PCP) or “snowman”; 4. Paracentral phenotype with non-matching topographic and comma axes (PCnC) or “duck”.

⁷¹ Gomes et al. 2015

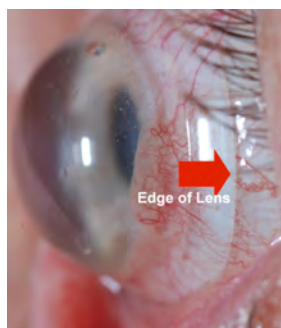


Figure 2.11: Lens located in a cornea with keratoconus. The keratoconus is located under the lens. This regularises the corneal surface and protects the keratoconus under the lens.

the front of the cornea is filled in with tears and creates what is called a “lacrima lens”. This interaction creates an optically improved surface by masking the regular and irregular astigmatism and reducing the high order aberrations (HOA).

Piggyback Lens: Some patient’s corneal epithelium may not tolerate the RGP lens touch at the apex of the cone and dense superficial punctate keratitis may occur. To improve patient comfort and increase lens wear time, some practitioners may place a soft contact lens beneath the RGP, called piggybacking. They are normally made of hydrogel or silicone hydrogel. The Flexlens Piggyback is designed with a central cutout depression, which keeps the RGP centered on the cornea to optimize acuity and comfort.

Scleral Lenses: The scleral lenses are large diameter RGP lenses that rest completely on the insensitive sclera and vault over the cornea without touching it (see Figure 2.12.b). The lenses are designed with a central optic zone, an area of limbal clearance, and the edge of the lens, called haptic. The haptic is fitted to the sclera and supports the weight of the lens. The main advantages of scleral lenses are: they can be used in severe cases of ectasia, they are excellent for patients with nodules at the apex, they also work well in patients with concurrent ocular surface disease, and their centration is usually excellent, due to their large diameter. However, they also have disadvantages since they can be complicated to fit properly and require a provider with experience in fitting this type of lens, and they are contraindicated in patients with glaucoma drainage device since the haptic can press on the device causing IOP to increase.

Hybrid Lenses: Hybrid lenses have an RGP centre and a soft silicone hydrogel or hydrogel surrounding skirt. Lenses are 14.5 mm in overall diameter with 8.5 mm central RGP (see Figure 2.12.c). The main advantage of this type of lens is that due to the soft skirt, the lenses tend to centre well, are well retained, and often have superior comfort. Compared to corneal RGP’s, patients may also experience an improvement in visual acuity due to the excellent centration of this lens. But also, they have some drawback as the limited parameters can not fit patients with severe ectasia, the insertion is more challenging than with a corneal RGP since the lens has to be filled with saline prior to insertion, they are

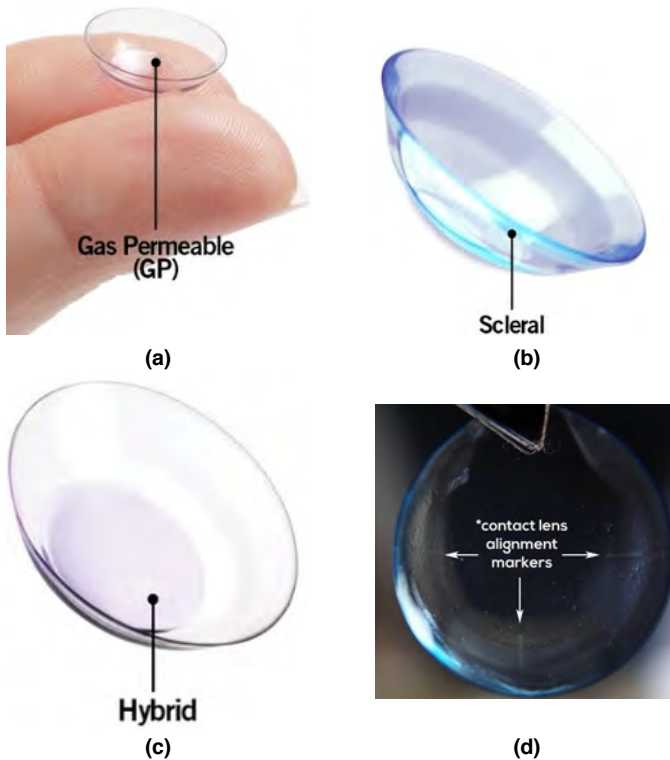


Figure 2.12: Typologies of lenses to improve the vision in corneas with keratoconus. (a) Corneal rigid gas permeable (RGP) contact lens; (b) Scleral Lens designed with a central optic zone, an area of limbal clearance, and the haptics whose aim is to fit to the sclera and to avoid the centre of the lens touches the apex; (c) Hybrid Lens has an RGP centre and the haptic is made of a soft silicone hydrogel or hydrogel; (d) Soft Toric Lens has alignment markers to avoid the rotation of the lens.

difficult to remove, they are expensive, and they can tear at the junction of the soft skirt and RGP centre necessitating replacement.

Soft Toric: Kerasoft, Novakone, Flexlens: This type of lenses are higher modulus soft toric lenses that can correct myopia, high regular astigmatism, and some irregular astigmatism (see Figure 2.12.d). The modulus refers to the stiffness or rigidity of the lens where a high modulus lens will have slight rigidity and ability to hold its shape over an irregular corneal surface. The advantage of these lenses is that patients report excellent comfort and they work well in dusty environments. These lenses work well for mild keratoconus or in instance when all other modalities have failed due to comfort. The drawbacks are that the patients may find vision unacceptable, and the thickness of lens reduces oxygen to the cornea.

To sum up, the Table 2.1 refers the use of different contact lens depending on the grade of keratoconus according to Amsler–Krumeich criterium.

Table 2.1: Contact lens modality chosen depends on severity of ectasia. Different grades of keratoconus refer to Amsler–Krumeich criterium to define the severity of the keratoconus; therefore, Early, Mild, Moderate, and severe KC correspond to Grade I, II, III, and IV, respectively.

Lens modality	Early KC	Mild KC	Moderate KC	Severe KC
Corneal RGP	✓	✓	✓	✓
Piggyback		✓	✓	
Scleral			✓	✓
Hybrid	✓	✓	✓	
KC soft toric	✓	✓		

3.3.2. Corneal collagen cross-linking (CXL)

The concept of treating ectatic corneal disorders, as keratoconus, with Riboflavin (vitamin B₂/ultraviolet A (UVA) (370 nm), CXL was first postulated at the University of Dresden by Spoerl and Selier (see Figure 2.13).⁷² They hypothesized that photochemical CXL of collagen within the corneal stroma could be achieved by utilizing the interaction between Riboflavin and UVA to create free radicals (oxygen singlets) which then activate the normal physiological Lysyl Oxidase pathway.⁷³ Riboflavin is thought to prevent injury to internal ocular structures, i.e. the endothelium, lens and retina, by absorbing the potentially mutagenic and cytotoxic UVA within the superficial corneal tissue.⁷⁴

The exact location of the cross-links at molecular level is unknown as these bonds cannot be seen microscopically. Cross-links cannot be formed between the collagen fibrils themselves, as the distance between them is too great for any intramolecular bond to be possible. Hayes *et al.* (2013)⁷⁵ postulated that it was possible that the cross-links were occurring on the outside of the collagen fibrils, rather than within them, and in the protein network surrounding the collagen.

Whilst the cross-links between the proteins within the stroma cannot be visualized and their existence directly corroborated, *ex vivo* laboratory studies have reported several changes in the mechanical and chemical properties of the stroma consistent with their existence. Stress-strain measurements of stromal tissue are increased appreciably,⁷⁶ both immediately as well as several months following CXL.⁷⁷

Whilst the investigations described earlier confirm the expected improvements in biomechanical and biochemical properties of corneas following CXL, it must be remembered that UVA is cytotoxic. It has been shown to

⁷² Spörl *et al.* 1997, 1998, 2000, Wollensak *et al.* 2003b, Sakellaris *et al.* 2019

⁷³ Wollensak *et al.* 2003b

⁷⁴ Wollensak *et al.* 2003b

⁷⁵ Hayes *et al.* 2013

⁷⁶ Spörl *et al.* 2000, Wollensak *et al.* 2003b,c

⁷⁷ Wollensak and Iomdina 2009

cause keratocyte apoptosis and corneal endothelial cell damage/depth as well as possible lens and even retinal injury.⁷⁸ In the clinical setting this occurs in human corneas to a depth of 300 μm .⁷⁹

Therefore, despite the technique of cross-linking being minimally invasive, the cornea must satisfy a series of requirements to be able to undergo this intervention.

3.3.3. Additive Surgery

It is called additive surgery since an external implant is introduced within the stroma. There are two different type of rings: the intrastromal corneal ring segments (ICRS) or the intrastromal continuous rings (ICR), which both are small devices made of plastic which are introduced within corneal stroma to regularise the corneal surface and correct high refractive errors. Nowadays, there are several types of ICRS that are commercially available, but the ones that are commonly used in the clinical practice are the Keraring (Mediphacos, Belo Horizonte, Brazil), the Intacs (Addition Technology Inc.) and the Ferrara segments (AJL Ophthalmic). Table 2.2 summarises the main characteristics of these ICRS. Triangular designs generate a prismatic effect of the light coming through the implant, being reflected, thus reducing incidence of glare and halos. In addition, there are the continuous rings which due to their smaller diameter and different design have more flattening capabilities and are reserved for those keratoconic eyes that present high myopic refractive errors: the Intacs SK (Addition Technology Inc.), and the MyoRing (Dioptex GmbH). The features of these two types of ICR are shown in the two last columns of Table 2.2. Intacs SK (SK means severe keratoconus) are designed with rounded edges to potentially reduce the incidence of visual symptoms since SK segments are placed closer to the patient's visual axis than the standard Intacs segments. They are indicated for the treatment of moderate to severe keratoconus (SK) with steep keratometric values greater than 55 D. Intacs SK segments seem to offer a compromise between the standard Intacs with 7 mm in diameter and the Ferrara or Kerarings with 5 mm, because the diameter is inversely proportional to the effectivity. Finally, the only full ring (360°) is the MyoRing. It is the only design with published clinical data, and it is implanted within a corneal stromal pocket. It has a greater capacity to flatten and reduce the spherical equivalent (SE) than the segments, but do not usually significantly reduce astigmatism and therefore their use is limited to cases in which patients have a high spherical error and low astigmatism.

⁷⁸ Wollensak et al. 2004, 2003a,d, Spörl et al. 2007

⁷⁹ Wollensak et al. 2004

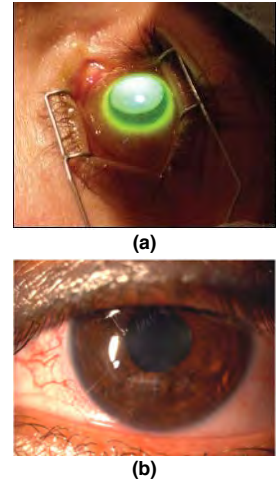


Figure 2.13: CXL treatment to stabilise the KC progression
(a) Cornea during the application of the cross-linking treatment;
(b) Cornea after the Cross-linking treatment.

Table 2.2: Main characteristics of the intracorneal ring segments.

The Keraring, Ferrara and Intacs are the most commonly used in the clinical practice. Intacs SK and MyoRing have higher flattening capabilities, reserved of those eyes with high myopic refractive errors.

⁸⁰ Daxer 2015

Design	Keraring	Ferrara	Intacs	Intacs SK	MyoRing
Arc length(°)	90 – 355°	90 – 210°	150°	150°	360°
Thickness (mm)	0.15 – 0.35	0.15 – 0.30	0.21 – 0.45	0.40 – 0.45	0.15–0.45
Inner diameter (mm)	6.00	4.8	6.77	6.00	5.00–8.00
Outer diameter (mm)	7.00	5.4	8.10	700	5.00–8.00

Daxer *et al.*⁸⁰ support that, while the incomplete segments (ICRS) are biomechanically neutral, MyoRing strengthens and stabilizes the cornea considerably and subsequently it is no longer necessary to combine it with CXL in progressive keratoconus. This statement still requires long-term studies before its confirmation.

Due to the fact that the thesis focuses on intrastromal rings for myopia reduction or keratoconus stabilization, the following section explains more extensively the surgical procedure and the commercial rings.

4. Intrastromal corneal ring implants

4.1 Surgical procedure

In order to implant the rings into the deep cornea, previously, it is necessary to perform tunnels or a pocket within the stroma where the segments (Keraring, Ferrara or Intacs) or continuous ring (MyoRing), respectively, will be inserted. For this purpose, there are two different surgical options both for tunnels and pockets: mechanical and femtosecond laser-assisted technique.⁸¹

⁸¹ Sakellaris *et al.* 2019

4.1.1. Surgery to intrastromal corneal ring segments

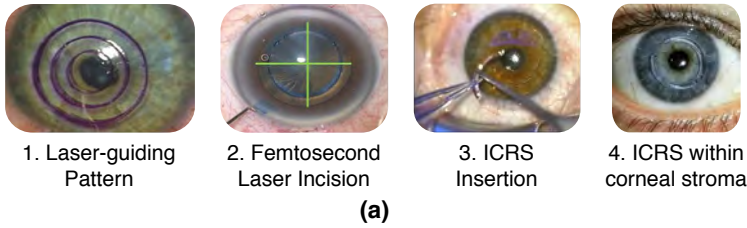
When the implant chosen to treat myopia or try to stabilise keratoconus is a segment, the surgery must be performed in a tunnel. Whether a single ring is inserted, it will be located in the lower plane and the tunnel will only cover 180°. However, if two segments are inserted, then the tunnel will cover the complete circumference.

⁸² Coskunseven *et al.* 2008

The surgical intervention consists of five steps (see Figure 2.14.a):⁸²

1. The surgeon must mark the centre of the pupil in order to use it as a reference point during the procedure.
2. A dissection plane, which is usually arch-shaped, is generated by a calibrated diamond knife or by a femtosecond laser in the peripheral region of the cornea at 70% or 80% of stromal depth.

Surgery to Intrastramal ring segments



Surgery to Intrastramal continuous rings

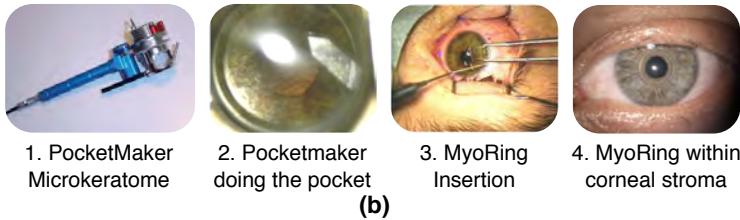


Figure 2.14: Surgical procedure.

(a) Procedure to insert the segments within corneal stroma. 1. centre of the cornea is located in order to mark the tunnel; 2. Tunnel is made with a mechanical tool or with femtosecond laser; 3. Implant is introduced by the surgeon in the correct position; 4. Segment located in corneal stroma; (b) Procedure to insert the continuous ring (MyoRing) within corneal stroma. 1. PocketMaker Microkeratome; 2. View through the transparent applanator of the PocketMaker microkeratome during formation of the pocket; 3. Insertion of the MyoRing into the corneal pocket through the small incision tunnel. Note the change in the shape of the ring during implantation; 4. Appearance of the MyoRing implanted. The first and second steps would be substituted by one step if the surgery was with femtosecond laser.

3. The dissection plane is visually cleared.
4. ICRS are manually implanted under full aseptic condition with a special guidance tools.
5. The final position of the segments is fine-tuned with a Sinsky hook using the dialling holes at both ends of the ICRS.

4.1.2. Surgery to intrastramal continuous rings

On the other hand, whether the surgeon decides to implant a complete ring or MyoRing, a pocket should be created that cuts the complete cornea at 300 μm depth. This pocket can be made manually with the technique created by Daxer⁸³ or using a femtosecond laser.⁸⁴ The surgical technique consists of the following four steps (see Figure 2.14.b):

⁸³ Daxer 2008
⁸⁴ Alió et al. 2011

1. A pocket of 8 or 9 mm in diameter and 300 μm depth is created within the cornea with a tool called PocketMaker microkeratome or with a femtosecond laser. The pocketmaker microkeratome consists of a suction ring, an applicator with a guiding mean for the handpiece, a handpiece containing a motor-driven blade that vibrates in the cutting plane, a control unit, and a disposable transparent applanator.

⁸⁵ Daxer 2015

2. An incision in the cornea with enough width is made (less than 5.5 mm)⁸⁵ to introduce the MyoRing.
3. The continuous and deformable ring implant is introduced into the corneal pocket via the small incision tunnel. The particular shape and dimensions of the MyoRing permit folding, which makes implantation in the pocket via the small incision tunnel possible. The implantation procedure is performed with an implantation forceps.
4. Centering the implant in the pocket can be performed by a hook or a forceps. Finally, the incision tunnel is self-sealing and does not require suturing.

4.1.3. Differences between mechanical and femtosecond laser techniques

Femtosecond laser produces a more precise and controlled stromal dissection than the manual technique. However, if we are talking about visual and refractive outcomes, most studies that have been conducted concur that both techniques produce similar results in cases of ICRS implantation for keratoconus. On the other hand, femtosecond laser makes the process faster, easier and more comfortable for the patient.⁸⁶ Apart from the safety and efficacy differences between both techniques, Alió *et al.* found that intrastromal segment implantation using femtosecond laser is a method that produces a greater reduction in corneal high order aberrations in eyes with coma aberration greater than 3.0 μm .⁸⁷

⁸⁶ Shabayek and Alio 2007, Alió *et al.* 2011, Rabinowitz 2006, Ertan *et al.* 2007

⁸⁷ Shabayek and Alio 2007, Alió *et al.* 2011

Regardless of the technique used to make the tunnels in the corneal stroma, the number, thickness, position and arc length of the segments are determined based on the manufacturer's nomograms. Likewise, rings are chosen from the nomogram taking into account the refractive error and the topographic map of the disease. It should also be noted that the incision guiding implantation of the segments in the tunnel is located on the axis of the steepest meridian of the corneal topography.

It is important to consider that although several authors have reported good results implanting ICRS in keratoconic eyes, the main limitations that nomograms have is that most of them are based on anecdotic clinical data, or variables that are very subjective in patients with keratoconus, such as spherocylindrical refraction and topographic pattern of the cone. For example, it was found that based on the topographic pattern of the

keratoconus the best choice was to implant one segment in those cases of inferior steepening and two segments in central cones.⁸⁸

Other works published in the literature support that the best location to implant the segments is by placing the corneal incision in the temporal site of the cornea⁸⁹ or in the steepest meridian of the cornea⁹⁰ There are other works that have reported good results when implanting the ICRS guided by the comatic axis.⁹¹ Recently, Alió *et al.* published a scientific work in which we concluded that the best outcomes for implanting ICRS were observed in those cases where the refractive and topographic cylinder did not differ in more than 15°.⁹²

Finally, surgeons could take advantage of computational simulations in planning the surgery, or in providing qualitative post-surgical information in different surgical scenarios such as the residual astigmatism that will arise from the intervention, or if the ICRS stabilize the progression of the keratoconus.

4.2 Commercial intrastromal corneal rings

4.2.1. Keraring implant

Triangular section ring from the commercial company Mediaphacos, BeloHorizonte (Brazil), made of PMMA as it is shown in Figure 2.15. It has different sizes depending on the thickness of the ring (H_{Keraring}), different diameters (OZ) and angles covered (α). The thickness varies from 150 to 350, with increments of 50 μm , the optical zone is 5 or 6 mm, there are 5 angles covered: 90°, 120°, 160°, 210°, and 355°; and the width (b) of cross-section ring is 600 μm or 700 μm .

There are three types of nomograms (A, B and C) that are used based on the type of corneal asymmetry (Figure 2.16), on keratometric values and on corrected distance visual acuity (BCVA). The corneal asymmetry type is determined by studying the distribution of corneal irregularity (red) relative to the reference meridian. Accordingly, each case is classified according to Figure 2.16:

Type 1: 100% of the steep area is located on one side of the reference meridian.

Type 2: The distribution of the steep area is approximately 20/80%.

Type 3: The distribution of the steep area is approximately 40/60%.

Type 4: The distribution of the steep area is approximately 50/50%.

⁸⁸ Alió *et al.* 2005

⁸⁹ Colin *et al.* 2001, Hellstedt *et al.* 2005, Kanellopoulos *et al.* 2006, Kwitko and Severo 2004

⁹⁰ Alió *et al.* 2006, Shetty *et al.* 2008

⁹¹ Alfonso *et al.* 2012

⁹² Peña-García *et al.* 2014

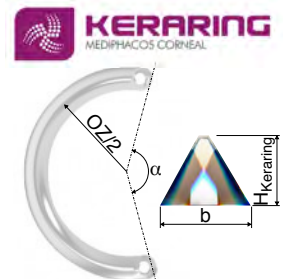


Figure 2.15: Keraring implant. Keraring, Mediaphacos, BeloHorizonte (Brazil) is an intrastromal corneal ring segment whose cross-section is triangular. OZ: optical zone in mm; α : covered arc in degrees; b: width of ring in μm ; H_{Keraring} : thickness of ring in μm .

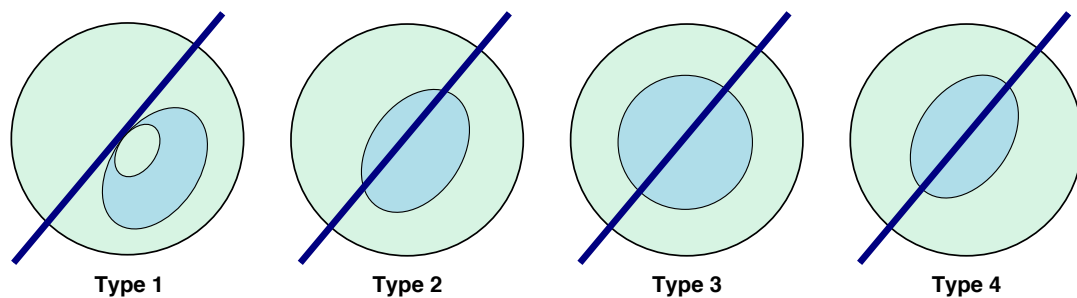


Figure 2.16: Corneal asymmetry classification of Keraring.

Classification according to the area where the corneal irregularity (light green) is found relative to the reference meridian (Blue line)

For each type of corneal asymmetry according to the area where the corneal irregularity is found, nomogram A, B or C should be used. The nomograms should be considered as a general guideline only and they should be customised by the surgeon depending on each patient particularities and the results obtained.

The steps and measures to be taken for ICRS implantation are shown below:

1. Obtain manifest subjective refraction.
2. Perform corneal topography (axial map).
3. Take pachymetric map. Determine the minimum corneal thickness at 5.5 and 6.5 mm optical zones.
4. Determine the steepest corneal meridian (SIM-K). If the refractive axis and the steepest topographic axis do not match, select the topographic meridian.
5. Compare the thickness of the proposed segment according to the selected nomogram with the minimal corneal thickness obtained in the 6 mm optical zone. The thickness of the segment should not exceed 60% of the minimal corneal thickness. If it does, a segment with less thickness should be selected.

Then, the reference meridian should be selected: If the BCVA is greater than 0.5, the steepest meridian must be selected. On the other hand, if the BCVA is less than 0.5, the total coma aberration axis or the steepest

meridian by topography (SIM–K) should be chosen. Then, a line along the reference meridian selected should be drawn.

In order to determine the treatment strategy: If the BCVA is greater than 0.4, the treatment based on refractive sphere and cylinder obtained by manifest refraction should be programmed. If the BCVA is less than 0.3 or the manifest refraction is not very reliable, the treatment based on kerometric values should be performed.

When it comes to implantation, when the nomogram suggests using two segments, the nomogram data appearing on the top line of the box should be used for the segment implanted in the area where the ectasia is smaller (flatter meridian), and the data on the lower line shall be for the segment implanted on the steepest meridian. When the nomogram suggests only one segment, this should be implanted on the steepest meridian, where the ectatic area is greater.

4.2.2. Ferrara implant

Implant of triangular cross–section too, but from the commercial company AJL Ophthalmic Ltd (see Figure 2.17). As Keraring implant, it is made of PMMA and has different size or thickness (H_{Ferrara}), diameter (OZ) and covered arc (α). You can find thickness which varies from 150 μm to 350 μm , in increments of 50 μm , two optical zones can be chosen, 5 or 6 mm, and there are 8 possible covered arc: 90°, 120°, 140°, 150°, 160°, 180°, 210°, and 320°. Finally, the width (b) of the cross–section ring varies depending on the optical zone: if the optical zone is 5 mm, the width is 600 μm ; and on the other hand, if the optical zone is 6 mm, the width is 800 μm . In addition, two rings can be implanted at the same time within the corneal stroma.

Similar tasks must be performed before implanting these segments.

1. Define the type of keratoconus: sag, bowtie or nipple.
2. Distribution of the ectatic area in the cornea: 0/100, 25/75, 33/66 and 50/50 (Figure 2.18).
3. Corneal asphericity (Q).
4. Topographic astigmatism.
5. Pachymetry at incision site and ring track.

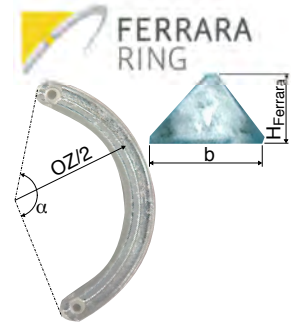


Figure 2.17: Ferrara implant. Ferrara, AJL Ophthalmic Ltd (Spain) is an intrastromal corneal ring segment whose cross–section is triangular. OZ: optical zone in mm; α : covered arc in degrees; b: width of ring in μm ; H_{Ferrara} : thickness of ring in μm .

Topographic astigmatism (D)	ICRS thickness (μm)
<i>Symmetric bowtie keratoconus</i>	
< 2.00	150/150
2.25 – 4.00	200/200
4.25 – 6.00	250/250
> 6.25	300/300
<i>KC 0/100% and 25/75% asymmetry index</i>	
< 2.00	None/150
2.25 – 4.00	None/200
4.25 – 6.00	None/250
6.25 – 8.00	None/300
8.25 – 10.00	150/250
> 10.00	200/300
<i>KC 33/66% asymmetry index</i>	
< 2.00	None/150
4.25 – 6.00	200/250
<i>Nipple keratoconus (210 arc ring)</i>	
< 2.00	150
2.25 – 4.00	200
4.25 – 6.00	250
> 6.25	300

Table 2.3: Ferrara nomogram. Ferrara ICRS thickness choice according to zone where is located the disease.

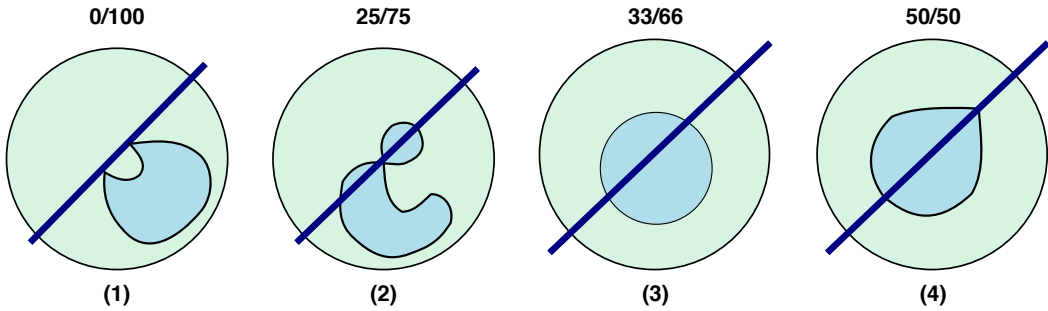


Figure 2.18: Corneal asymmetry classification of Ferrara. Classification according to the percentage of disease (light green) relative to the reference meridian (Blue line). (1) **0/100** All the ectatic area is located at one side of the cornea; (2) **25/75** 75% of the ectatic area is located at one side of the cornea; (3) **33/66** 66% of the ectatic area is located at one side of the cornea; (4) **50/50** The ectatic area is symmetrically distributed on the cornea.

The nomogram of topographic astigmatism, based on the thickness of the ring is defined in Table 2.3. However, in the case of nipple keratoconus, this measurement is not used and the spherical equivalent is used to define the thickness of the ring, which it should be a 210° arc ring (exclusive for this type of keratoconus) (Table 2.3.Bottom).

4.2.3. Intacs implant

These rings are of hexagonal cross-section, bigger than the two previous ones. They belong to the commercial company Addition Technology Inc. and depending on the severity of the corneal ectasia they want to correct, they are chosen in different sizes (H_{Intacs}), diameters (OZ) and covered angles (α) (see Figure 2.19). Therefore, it is possible to find thickness which varies between 210 μm and 450 μm , optical zones is 6 mm and the covered arc is 150°.

The recommendation is to select between symmetric or asymmetric segments depending on the ectatic area and spherical and cylindrical refractive power.

- Use *symmetric* segments when the ectatic area is within the 3–5 mm central optical zone and when, in the manifest refraction with the positive cylinder, the spherical power is greater than the cylindrical power (Table 2.4).
- Use *asymmetric* segments when the ectatic area is outside the 3 mm geometric centre and when, in the manifest refraction with the positive cylinder, the cylindrical power is greater than the spherical power (Table 2.4).

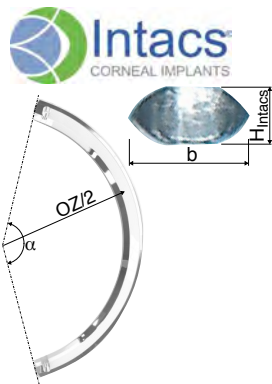


Figure 2.19: Intacs implant. Intacs, Addition Technology Inc. is an intrastromal corneal ring segment whose cross-section is hexagonal. OZ: optical zone in mm; α : covered arc in degrees; b: width of ring in μm ; H_{Intacs} : thickness of ring in μm .

<i>Symmetric</i>		
Spherical Power (D)	Inferior Intacs (μm)	Superior Intacs (μm)
0.00 to -1.00 D	210	210
-1.00 to -1.75 D	250	250
-2.00 to -2.75 D	300	300
-3.00 to -3.75 D	350	350
-4.00 to -4.75 D	400	400
> -5.00 D	450	450
<i>Asymmetric</i>		
Cylindrical Power (D)	Inferior Intacs (μm)	Superior Intacs (μm)
2.00 to 3.00 D	350	210
3.00 to 4.00 D	400	210
> 4.00 D	450	450

Table 2.4: Intacs nomogram. Intacs nomogram for symmetric (upper) and asymmetric segments (bottom).

4.2.4. MyoRing implant

The form of the MyoRing Dioptex GmbH (see Figure 2.20) cross-section is not usual, compared with the previous intrastromal corneal ring segments. The cross-section shows a convexity in the front part (parabolic shape) and a minimal concavity on the backside. The backside is designed as to rest on a sphere with 8 mm radius and, therefore the inclination of the back surface from periphery to central can be calculated whether one knows the inner and the outer diameter. The thickness of the MyoRing was measured from the top of the parabolic front surface to the back surface by drawing a vertical line (orthogonal to the ring plane). The MyoRing is currently available in a diameter range of 5 to 8 mm and a thickness range of 200 to 400 μm in 20 μm increments.

Some inclusion criteria must be met before its nomogram (Table 2.5) can be applied:

- Uncorrected distance visual acuity (UCVA) < 0.3.
- Minimal corneal thickness > 360 μm .
- Average central keratometry (ACK) $(K_1 + K_2)/2 > 44$ D.
- No central corneal scarring.
- No history of previous corneal surgery.
- Age <50 years.

In spite of all these nomograms, complete predictability in postoperative results is still not possible due to changes in corneal biomechanics in

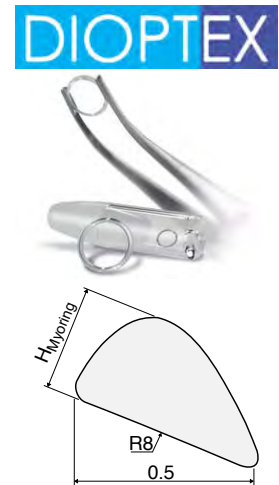


Figure 2.20: MyoRing implant. MyoRing, Dioptex GmbH is an intrastromal continuous ring whose cross-section shows a convexity in the front part (parabolic shape) and a minimal concavity on the backside.

Table 2.5: MyoRing implantation nomogram.

Average central keratometry (D)	Implant diameter (mm)	Implant thickness (μm)
ACK < 44	7	280
44 < ACK < 48	6	240
48 < ACK < 52	6	280
52 < ACK < 55	5	280
ACK > 55	5	320

⁹³ Piñero et al. 2010⁹⁴ Piñero et al. 2010

keratoconic eyes.⁹³ It has been found a significant correlation between the corneal resistance factor (CRF), measured using an ocular response analyzer (ORA; Reichert) and the magnitude of the corneal spherical-like aberrations.⁹⁴ Also it has been shown that the visual outcomes post-ICRS implantation correlated inversely with the magnitude of some corneal higher order aberrations. It should therefore be considered that larger amounts of corneal higher order aberrations are an important factor especially in advanced keratoconic corneas where biomechanical alteration would be more pronounced. Therefore, the predictability models could be improved if high order corneal aberrations were included. In other words, the introduction of the aberrometric factor could be an indirect way of considering part of the bio-mechanical corneal factor. In any case, this indirect contribution of aberrometry to corneal biomechanics is limited, and it does not account for the total biomechanical effect. The analysis of the corneal biomechanical properties of the cornea in vivo is not an easy task in clinical practice and the exact contributions of the elastic and viscous components to the magnitude of these parameters are not yet fully understood.

5. Retrospective clinical and numerical studies

This section aims to make a summary of the works and studies about different rings, segments or complete rings, in order to avoid the progression of keratoconus or correct the myopia. Some of them are used along the thesis to compare or validate our results. Both clinical and numerical studies will be included. To sum up each section, a table summary with the most relevant data are included.

5.1. Keraring to stabilise keratoconus

⁹⁵ Abdellah and Ammar 2019

Abdellah et al. (2019)⁹⁵ evaluated the outcomes of femtosecond laser-assisted implantation of a Keraring of 355° in patients with keratoconus in the three-year follow-up. 38 eyes of 26 patients with keratoconus had implantation after tunnel creation with a femtosecond laser. They

evaluated the uncorrected (UCVA) and best-corrected (BCVA) visual acuities, sphere, cylinder and manifest refraction spherical equivalent (SE), mean keratometry (K_{mean}), K_{max} and K_{min} preoperatively and 3, 6, 12, 24 and 36 month postoperatively. They obtained as results that the mean UCVA improved from 0.93 ± 0.21 to 0.63 ± 0.21 logMAR ($P \leq 0.001$) and the mean BCVA improved from 0.67 ± 0.22 to 0.43 ± 0.26 logMAR ($P \leq 0.001$). The mean sphere, cylinder, and SE have been changed dramatically from preoperative to 3 month postoperative, which is statistically significant ($P \leq 0.001$), and the changes between one, two, and three years were also statistically significant. The safety and efficacy indices were changes through the three-year follow-up. They had complications such as corneal neovascularization (36.84%), corneal melting (26.3%), and ring extrusion (31.5%) at the end of the study. They concluded that the implantation of Keraring improved the visual, refractive, and topographic parameters in keratoconus patients, with a high rate of ICR extrusion and instability.

Abd Elaziz et al. (2018) ⁹⁶ studied the behaviour of the anterior surface cornea after the implantation of a Keraring with a 355° covered arc and $300 \mu\text{m}$ thickness in 30 eyes with central advanced keratoconus (grade 3) The tunnel was created by femtosecond laser. BCVA improved significantly. There were also significant changes in the measured parameters with marked reconstruction of the cornea and anterior chamber. However, the actual depth of the ring segment was shallower than the intended depth.

⁹⁶ Abd-Elaziz et al. 2018

Gatzioufas et al. (2018) ⁹⁷ aimed to evaluate the long-term clinical outcomes after Keraring implantation for keratoconus in 11 eyes of 11 patients older than 40 years. The surgery was performed by femtosecond laser-assisted. The results showed that UCVA, BCVA and keratometric readings improved at 6 months postoperatively. They concluded that the data showed significant keratometric amelioration and visual improvement after Keraring implantation at 6 months postoperatively.

⁹⁷ Gatzioufas et al. 2018

Al-Tuwairqi et al. (2017) ⁹⁸ aimed to compare the outcome measures following implantation of two types of ICRS. 44 keratoconic eyes were randomly assigned to femtosecond laser-assisted Keraring ICRS (Group A) or MyoRing (Group B) implantation. Both Group A, composed by 26 eyes, and Group B, composed by 18 eyes, UCVA was increased

⁹⁸ Al-Tuwairqi et al. 2016

($P < 0.05$). However, the BCVA increased only in Group A ($P < 0.05$) after 6 months postoperatively. The K_{mean} was reduced by 4.55 D ($P < 0.0001$) in Group A and 6.51 D ($P < 0.001$) in Group B. The mean refraction spherical equivalent (MRSE) decreased by 2.90 and 3.60 D in Groups A and B, respectively ($P < 0.0001$) after 6 months postoperatively. Coma was more reduced ($P = 0.035$) in Group B than A. They concluded that Keraring and MyoRing corneal implants both performed well in improving vision and stabilising the cornea. Implantation of the MyoRing caused greater reduction in coma and better satisfaction, but BCVA improved only in the Keraring group.

⁹⁹ *Jadidi et al. 2015*

Jadidi et al. (2014) ⁹⁹ evaluated the efficacy and safety of Keraring 355° implantation aided by PocketMaker microkeratome for the correction of keratoconus. The clinical study was composed by 15 eyes. At the final postoperative examination, there was a statistically significant reduction in the spherical equivalent refractive error compared to preoperative measurements. All patients were satisfied with ICRS implantation. No intraoperative or postoperative complications were demonstrated.

¹⁰⁰ *Kubaloglu et al. 2010a*

Kubaloglu et al. (2010) ¹⁰⁰ compared the outcomes of implantation of 2 models of intrastromal corneal ring segment to manage the keratoconus. One group of 100 eyes were implanted the Keraring and the second group of 68 were inserted the Intacs. The corneal tunnels were created mechanically or with a femtosecond laser. The postoperative increase the UCVA and BCVA was statistically significant in both groups. The first group had greater improvement in BCVA than the second group at 6 months and 1 year. At 1 year, the decrease in the mean maximum K power was statistically significant in the first group (51.27 ± 4.46 D to 47.87 ± 3.39 D) and in the second group (51.12 ± 4.54 D to 47.58 ± 3.66 D). The mean reduction in maximum K was statistically significantly greater in the first group at 6 months and 1 year. There were no statistically significant differences in visual or refractive results between femtosecond laser and mechanical tunnel creation. They conclude that Keraring led to more improvement in BCVA and UCVA and a greater reduction in the maximum K value.

¹⁰¹ *Kubaloglu et al. 2010b*

Kubaloglu et al. (2010) ¹⁰¹ aims to compare the effects on the stabilization of the keratoconus when the surgery was made by femtosecond laser or mechanically. It is a clinical study where Keraring ICRS were

implanted. In all cases, ICRS had the same geometry: 5 mm diameter of optical zone and 160° of covered arc. Two groups of patients were built divided by mechanically and femtosecond laser tunnel surgery. The UCVA and BCVA, refraction and keratometry was read for each patient pre-operation and 1-year post-operation. After one-year follow-up, UCVA, BCVA, keratometry and spherical equivalent were significantly improved. The authors concluded that the visual and refractive outcomes were similar, although the mechanical group had some intraoperative complication.

Shabayek et al. (2007)¹⁰² reported the outcomes after the implantation of Keraring intrastromal corneal ring segments aided by femtosecond laser for the correction of keratoconus. The clinical study included 21 eyes with keratoconus: 45% of patients were keratoconus grade I, 20% grade II, 15% grade III and 20% were grade IV. Keraring implantation significantly increased UCVA from 0.06 to 0.3 ($P \leq 0.0001$), BCVA from 0.54 to 0.71 ($P \leq 0.0003$), and decreased the spherical equivalent by 2.28 D and the average keratometric values (K value) by 2.24 D ($P < 0.001$). There was no significant difference between the 3 and 6 months follow-up. Forty percent (8 eyes with a relatively low RMS of total HOA) showed a nonsignificant increase in the RMS of total HOA and 60% (12 eyes with a relatively higher RMS of total HOA $\geq 3.0 \mu\text{m}$) showed significant ($P \leq 0.01$) decrease in the RMS of total HOA due to a significant ($P \leq 0.003$) reduction in coma and coma-like aberrations. The amount of change in corneal curvature (biomechanical response) ranged from a decrease of 18% from its initial value to an increase of 2.75% and was not correlated to any preoperative parameter. Localized infectious keratitis occurred in only 1 eye (4.8%), and incision opacification occurred in 8 eyes (38%).

The clinical preoperatively and postoperatively data of these works and others can be observed in Table 2.6¹⁰³

5.2. Ferrara to stabilise the keratoconus

Rocha et al. (2018)¹⁰⁴ showed how the new long-arc length of 320° of intrastromal corneal ring segment was efficient and safe for keratoconus stabilization. A total of 34 keratoconic eyes of 31 patients were enrolled in the study. Patients were divided into two groups based on the strategy used for 320° ICRS thickness selection. In one group, this

¹⁰² Shabayek and Alio 2007

¹⁰³ Abdellah and Ammar 2019, Abd-Elaziz et al. 2018, Gatzio-ufas et al. 2018, Guber et al. 2018, Heikal et al. 2017, Yousif and Said 2018, Al-Tuwairqui et al. 2016, Bayoumy et al. 2014, Jaididi et al. 2015, Gharaibeh et al. 2012, Kubaloglu et al. 2010a,b, Shabayek and Alio 2007

¹⁰⁴ Rocha et al. 2018

selection was based on spherical equivalent (SE group) and in the other on the mean asphericity (Q group). For astigmatism improvement, they analyzed the corneal tomographic vectorial astigmatism change preoperatively and at 6 months postoperatively. The mean follow-up period was 6.63 ± 0.96 months. The mean UCVA and BCVA improved with a significant spherical improvement ($p < 0.05$), with no differences between the 320° intrastromal corneal ring segment groups. All corneal tomographic parameters improved significantly ($p < 0.05$) between the preoperative and postoperative intervals, with a significant better performance when they used spherical equivalent for the 320° ICRS segment thickness selection. The mean vectorial corneal tomographic astigmatism improved significantly after 6 months, again with no differences between groups. They suggested that implanting a 320° ICRS was a safe and effective procedure for treating patients with keratoconus. Besides, the best strategy for thickness selection was the spherical equivalent.

¹⁰⁵ Fernández-Vega et al. 2016

Fernández-Vega et al. (2016) ¹⁰⁵ assessed the efficacy outcomes of implanting ICRS to correct paracentral keratoconus. 409 patients were evaluated before and after the implantation of Ferrara ICRS. The mean UCVA and BCVA improved after the treatment. The spherical equivalent declined steeply after ICRS insertion. Cylinder power decreased by more than 50% in 71% of the eyes. Therefore, ICRS implantation is a safe and effective procedure for treating patients with keratoconus that meets the morphological characteristics of the sample under study.

¹⁰⁶ Torquetti et al. 2016

Torquetti et al. (2016) ¹⁰⁶ evaluated the corneal parameters measured with a dual Scheimpflug analyzer in 50 keratoconic eyes of 40 patients who were implanted Ferrara segments. The mean follow-up after the procedure was 12.7 months. The mean UCVA improved from 0.82 to 0.31 ($P < 0.001$); the mean BCVA improved from 0.42 to 0.05 ($P < 0.0001$), the mean spherical refraction changed from -3.06 ± 3.80 D to -0.80 ± 2.5 D ($P < 0.0001$) and the mean refraction astigmatism reduced from -4.51 ± 2.08 D to -2.26 ± 1.18 D ($P < 0.0001$). The changes from preoperative to postoperative, in terms of anterior and posterior cornea, were statistically significant except the posterior elevation at the apex of the cornea and posterior asphericity. They concluded that the implantation of Ferrara ICRS induced changes in both anterior and posterior surfaces of the cornea.

¹⁰⁷ Torquetti et al. 2013

Torquetti et al. (2013) ¹⁰⁷ evaluated the clinical outcomes after Ferrara

ICRS reoperation in patients with keratoconus. 37 keratoconic eyes in which were implanted with ICRS, had an ICRS exchange, addition, reposition or removal were implanted. The mean follow-up time after reoperation was 30.5 ± 9.7 months. The mean UCVA improved from 20/300 to 20/80 ($P=0.005$); the mean BCVA improved from 20/160 to 20/50 ($P=0.0002$); K_{mean} was reduced from 49.33 ± 4.19 D to 46.16 ± 3.90 ($P=0.0001$); the mean pachymetry at the thinnest point increased from $450 \pm 42.9 \mu\text{m}$ to $469 \pm 40.8 \mu\text{m}$ ($P=0.0001$). The asphericity increased from -0.84 ± 0.74 to -0.35 ± 0.81 ($P=0.15$) and the spherical equivalent reduced from -4.64 ± 4.87 D to -3.04 ± 3.45 D ($P=0.137$). The changes in the asphericity and spherical equivalent were not statistically significant. They concluded as Ferrara ICRS implantation was a reversible and readjustable surgical procedure for keratoconus treatment. Good outcomes can be obtained even after removal, addition, reposition or exchange of ICRS.

Kwitko et al. (2004)¹⁰⁸ assessed the outcomes of Ferrara intracorneal ring segment for keratoconus. In this retrospective noncomparative interventional case series, 51 keratoconic eyes of 47 patients had Ferrara intracorneal ring segment implantation were analyzed. At a mean follow-up of 13.0 ± 8.7 months, the UCVA improved in 86.4% of eyes, was unchanged in 7.8%, and worsened in 5.8%; the BSCVA improved in 86.4% of eyes, was unchanged in 1.9% and worsened in 11.7%. The mean spherical equivalent (SE) was reduced from 6.08 ± 5.01 D to 4.55 ± 5.71 D and the mean refractive astigmatism, from 3.82 ± 2.13 D to 2.16 ± 2.07 D. The K_{mean} was reduced from 48.76 ± 3.97 D to 43.17 ± 4.79 D. Eyes with central keratoconus had statistically significantly better results than eyes with inferior keratoconus in topographic astigmatism, SE, and refraction cylinder. There were some problems associated to ICRS decentration which occurred in 2 eyes (3.9%), segment extrusion in 10 eyes (19.6%), bacterial keratitis in 1 eye (1.9%) with segment extrusion, and a disciform keratitis in 1 eye (1.9%). However, penetrating keratoplasty (PK) was avoided in 38 eyes (74.5%) during the follow-up. They concluded that implantation of Ferrara ICRS in patients with keratoconus was a safe and reversible procedure that led to stable results and avoided or delayed PK in many cases.

More information about the preoperatively and postoperatively data of these works and others address in Table 2.7.¹⁰⁹

¹⁰⁸ Kwitko and Severo 2004

¹⁰⁹ Alfonso et al. 2019, da Candalaria et al. 2019, Fernández-Vega et al. 2019, Rocha et al. 2018, Sandes et al. 2018, Lyra et al. 2017, Fernández-Vega et al. 2016, Gauthier et al. 2016, Torquetti et al. 2016, Ameerh et al. 2012, Ancèle et al. 2011, Kwitko and Severo 2004

5.3. Intacs to stabilise the keratoconus

¹¹⁰ Kang et al. 2019

Kang et al. (2019) ¹¹⁰ analyzed the effectiveness of intrastromal corneal ring segment to try to halt the keratoconus after five years. 30 eyes diagnosed with keratoconus and treated with Intacs were evaluated. UCVA and spherical equivalent were improved for three years. However, they worsened at five years to preoperative values. On the other hand, BCVA was improved for five years. Topographic keratometry was flattened, and corneal irregularity indices were improved after 5 years. Finally, coma RMS was improved continuously for five years. ICRS has advantages in improving BCVA with topographic stabilization and decreasing coma in keratoconus for five years.

¹¹¹ Shahhoseini et al. 2018

Shahhoseini et al. (2018) ¹¹¹ compared the actual depth of the tunnel created with femtosecond laser for ICRS implantation with the target depth in keratoconus patients. The mean of the follow-up time after ring implantation was 25.8 ± 10 months. The implants were always Intacs of $450 \mu\text{m}$. They concluded that after implantation, ring segments were placed at shallower depth that originally intended.

¹¹² Piñero et al. 2009

Piñero et al. (2009) ¹¹² compared visual, refractive and corneal aberrometric outcomes in keratoconic eyes implanted with ICRS using either a mechanical or a femtosecond laser-assisted procedure. It is a clinical study where 146 eyes with keratoconus were included. Two groups were created according to the surgical technique used for corneal tunnelization. 63 eyes formed the mechanical group and 83 completed the femtosecond group. The Keraring models were used in 8 eyes and the Intacs models were implanted in 55 eyes in the mechanical group, besides 25 eyes were implanted with Intacs and 58 eyes were implanted with Keraring in the femtosecond group. UCVA improved in both groups at 6 months ($P \leq 0.02$) and BCVA improved in the Femtosecond group ($P < 0.01$). The refraction improved in both groups at 6 months ($P \leq 0.02$). The cornea on average was flatter in both groups at 6 months ($P < 0.01$). Root mean square astigmatism was reduced in the Femtosecond group ($P = 0.03$), but there was an increase in some higher-order aberrations ($P = 0.03$). Significant differences were found between the 2 groups for eyes implanted with Intacs for primary spherical aberration, coma, and other higher-order aberrations, favouring the Femtosecond group ($P \leq 0.01$). A significant negative correlation was found between the preoperative corneal aberrations and the postoperative BCVA in the

Mechanical group ($r > 0.63$, $P < 0.04$).

Colin et al. (2007)¹¹³ studied the long-term safety and efficacy of Intacs segments for the treatment of keratoconus in terms of intraoperative and postoperative complications, visual outcomes, restoration of contact lens tolerance, and inhibition of disease progression. The prospective study of 2-year follow-up comprised 100 keratoconic eyes with clear central corneas and contact lens intolerance. After 2 years, UCVA and BCVA improved in 80.5% and 68.3% of the eyes, respectively ($P < 0.001$). The proportion of eyes with a $BCVA \geq 0.5$ (20/40) increased from 22.0% at baseline to 51.2% and 53.7% at 1 year and 2 years, respectively ($P < 0.001$). The MRSE improved from a mean of 6.93 ± 3.91 D preoperatively to 4.01 ± 3.16 D at 1 year and 3.80 ± 2.73 D at 2 years ($P < 0.001$). The K_{mean} decreased from 50.1 ± 5.6 D preoperatively to 46.4 ± 5.3 D at 1 year and 46.8 ± 4.9 D at 2 years ($P < 0.001$). Contact lens tolerance was restored in over 80% of the cases. They concluded that Intacs implantation was a safety and efficacious treatment for keratoconus. Significant and sustained improvements in objective visual outcomes were achieved in most cases, with restoration of contact lens tolerance.

¹¹³ Colin and Malet 2007

Alió et al. (2006)¹¹⁴ evaluated the long-term results and stability of intracorneal ring segments implantation for keratoconus correction. The retrospective study comprised 13 eyes, which were implanted with Intacs segments. The eyes were divided in 2 groups. The cones of Group 1 were limited to half of the corneal surface and were implanted with 1 segment ($450 \mu\text{m}$), and the cones of group 2 exceeded the half of the corneal surface and 2 segments were inserted. They concluded the Intacs increased the BCVA and decreased I-S¹¹⁵ asymmetry with stability up to 36 months. In spite of the decrease of the K-values at 6 months, a further significant increase was detected 36 months after surgery.

¹¹⁴ Alió et al. 2006

¹¹⁵ Inferior-Superior

Alió et al. (2005)¹¹⁶ evaluated the effect of implanting 1 or 2 intracorneal rings as a device to correct, stabilise, and/or improve the BCVA in patients with clear cornea keratoconus. One Intacs was implanted if keratoconus did not cross the 180° meridian (Group 1), and on the other hand, two Intacs were introduced when keratoconus did cross the 180° meridian (Group 2). The Spherical equivalent error and refractive astigmatism were significantly reduced. The K_{mean} was reduced in both

¹¹⁶ Alió et al. 2005

groups. They concluded that the treatment of keratoconus with 1 or 2 segments proved to be effective in decreasing the corneal topography and astigmatism and improving the BCVA.

¹¹⁷ Colin et al. 2001

Colin et al. (2001) ¹¹⁷ studied the use of Intacs in 10 patients who were contact lens intolerant and had keratoconus with clear corneas. After reviewing corneal pachymetry and topography of each patient, Intacs of 450 μm thickness were placed in the inferior cornea to lift the cone and Intacs of 250 μm thickness were inserted superiorly to counterbalance and flatten the overall anterior corneal surface. Spherical equivalent error and refractive astigmatism were reduced with Intacs segment introduction. The topographic corneal shape was improved for all subjects after the insertion. Both uncorrected and corrected visual acuity improved significantly. They concluded that Intacs micro-thin prescription inserts seem to provide a viable method for treating clear corneal keratoconus, getting a corneal stepping and astigmatism reduction.

¹¹⁸ Kang et al. 2019, Hashemian et al. 2018, Amanzadeh et al. 2017, Al-Muammar 2015, Hashemian et al. 2014, Kubaloglu et al. 2010a, Piñero et al. 2009, Shetty et al. 2008, Colin and Malet 2007, Alió et al. 2006, Kanellopoulos et al. 2006, Alió et al. 2005, Colin et al. 2001

More information about the preoperatively and postoperatively data of these works and others are addressed in Table 2.8.¹¹⁸

5.4. MyoRing to correct Myopia and to stabilise KC

5.4.1. MyoRing to correct myopia

¹¹⁹ Rattan 2018

Rattan (2018) ¹¹⁹ is also a clinical study where only both eyes of one patient are analyzed. The results were collected during a 4-year follow-up period. One MyoRing of 5 mm OZ and 280 microns' thickness was implanted in each eye. The pocket created had 8 mm of diameter and 300 microns' corneal depth and it was created by laser femtosecond. The study showed a reduction of the myopia of 8 D and near of 5 D in mean keratometry for both eyes.

¹²⁰ Daxer 2017

Daxer (2016) ¹²⁰ is a clinical study where 19 myopic eyes of 12 patients were implanted MyoRing to reduce the Myopia and astigmatism since they were not suitable for laser surgeries. 84% of them showed UCVA greater than 0.5 and all of them kept the BCVA. Depending on MyoRing implanted, different results could be observed: when MyoRing 5/280 was implanted, the myopia reduction was 10.8 D; when model implanted was 6/280, the reduction was 6.17 D and, finally, when MyoRing was implanted in 7 mm OZ with a thickness of 280 microns, the reduction was 3.31 D.

Daxer (2015)¹²¹ is an analytic study where the corneal biomechanics, based on biomechanics models and mathematic theory, were evaluated in order to treat the myopia and keratoconus. In that work, Daxer used the Laplace equation to calculate the corneal strengthening factor (SFC), a mechanical marker based on the ratio between Cauchy stress (σ) in the corneal tissue before and after the ring implantation ($SFC = \sigma_{Before} / \sigma_{After}$). Using this simple approach, he estimated a SFC of 2–3 for continuous rings and a SFC of 1 for ring segments. In his opinion, this difference was explained by the fact that continuous rings restricted the corneal movement acting as an auxiliary limbus, which was not the case for ring segments.

¹²¹ Daxer 2015

Daxer (2008)¹²² presented the novel surgical technique to insert their own segments called MyoRing. He developed the steps to follow in order to introduce the ring: (i) a pocket of 9 mm diameter and 300 μm depths is created within the cornea with a tool called PocketMaker microkeratome; (ii) to make an incision in the cornea with enough width (calculated in Daxer *et al.* (2015)¹²³) to introduce the Myoring; (iii) to introduce the MyoRing located in its correct position within the stroma; (iv) finally, the opening is closed without suture.

¹²² Daxer 2008

¹²³ Daxer 2015

5.4.2. MyoRing to stabilise keratoconus

Yousif *et al.* (2018)¹²⁴ is a clinical study which aimed to compare the evolution of central keratoconus progression after the insertion of 3 different rings: 2 ICRS of 160° triangular cross-section symmetric, 1 ICRS of 320° and triangular cross-section and MyoRing introduced within a pocket created with femtosecond laser. The statistical analysis was composed by 73 eyes divided in 3 groups. The near total ring and the continuous ICRS were more effective than the 2 symmetric segments of 160° in improving UCVA and reducing the SE, especially in moderate to severe cases of central keratoconus. Finally, the study concluded that there was a strong correlation between the degree of post-operative topographic and corneal asphericity and improvement and the degree of postoperative BCVA improvement in cases with central keratoconus that were managed using all 3 intracorneal implants.

¹²⁴ Yousif and Said 2018

Khosravi *et al.* (2017)¹²⁵ is a clinical study which aimed to evaluate and compare the magnitude and the axis orientation of total and corneal

¹²⁵ Khosravi *et al.* 2017

astigmatism axis before and after MyoRing implantation in 34 eyes of 28 patients with keratoconus. MyoRings were implanted into a pocket which was performed with the PocketMaker microkeratome. The study treated the total astigmatism defining the axis as “with-the-rule” (60° – 120°), “against-the-rule” (0° – 30° or 150° – 180°) or oblique whether the axis orientation was neither WTR nor ATR. The study concluded the total astigmatism decreased 2.08 D after MyoRing implantation. Finally, the MyoRing surgical procedure was able to correct more optical changes of spherical and cylinder than intrastromal corneal ring segments.

¹²⁶ *Jadidi et al. 2016*

Jadidi et al. (2016) ¹²⁶ is a clinical study that involved 32 eyes of 32 patients and the aim was to evaluate the effect of mechanical implantation of MyoRing in patients with severe keratoconus and high myopia. From their own nomogram and the own features of the disease of the patients, MyoRing implanted had 5 OZ and $280\ \mu\text{m}$ thickness or 6 mm OZ and $320\ \mu\text{m}$ thickness. Apart from UCVA and BCVA, which presented an improvement after MyoRing implantation, the myopia reduced in near 8 diopters and the astigmatism reduced practically 3 diopters.

¹²⁷ *Daxer et al. 2016*

Daxer et al. (2016) ¹²⁷ is a clinical long follow-up study, where MyoRing is implanted in keratoconic corneas. Spherical and cylindrical power presented an improvement during the first 5 months but then kept constant during the next 5 years. Due to the UCVA and BCVA presented a continuous improvement during 5 years, MyoRing implantation got to detain the disease progression. Daxer assured that MyoRing acted a second limbus, absorbing a meaningful load of the cornea. Also, an important conclusion of this study was there was no relationship between type and location of keratoconus with the optical outcomes since the pocket had 9 mm of diameter and the ring covered 360° .

¹²⁸ *Janani et al. 2016*

Janani et al. (2016) ¹²⁸ is a clinical study of 40 eyes of 37 patients, where MyoRing was used to stop the keratoconus progression. MyoRing was implanted by mechanical procedure using the PocketMaker microkeratome. After a 3-year follow-up, the spherical and cylindrical power reduced nearly 3 diopters, and both UCVA and BCVA improved 8 and 4 lines in Snellen Chart¹²⁹ (see Figure 2.21), respectively.

¹²⁹ *Hetherington 1954*

¹³⁰ *Hosny et al. 2015*

Hosny et al. (2015) ¹³⁰ compared the complete versus incomplete ring implantation for keratoconus correction. They investigated 25 keratoconic eyes, of which 15 had had femtosecond-assisted MyoRing corneal

implantation (Group 1) and 10 had femtosecond–assisted Keraring segments (Group 2). The main outcomes were measured preoperatively and at 4 weeks postoperatively. Changes in mean of the main outcomes (UCVA, BCVA, K_{mean}) did not significantly differ between groups, except K_{mean} change, which was significantly greater in Group 1 than in Group 2. Both complete ring and ring segment implantation were effective for improving corneal and visual parameters in keratoconus. Complete ring implantation could have a greater flattening effect on the anterior corneal surface.

Alió et al. (2011)¹³¹ is a clinical study of MyoRing implantation using femtosecond laser to create the pocket. The pocket had a 9 mm of diameter and 300 μm corneal depth. The MyoRings implanted were 5 mm optical zone and 280 μm thickness. After some periods of follow–up, 1 week, 1 month, 3 months, and 6 months after surgery, the study concluded: Significant improvement of UCVA after 1 week but then kept constant. The spherical, cylindrical and spherical equivalent power presented a significant reduction but then, kept constant. BCVA did not present significant changes during the follow–up. After 1 week of surgery, the eyes presented a flattening in the apex zone. Then, between 1 week and 3 months, the flattening kept constant. However, 6 months after, a regression of this effect could be observed. The aberrations of first order increased 1 month after the surgery, but then reduced. Finally, the CCT increased at the end of the follow–up.

The clinical preoperatively and postoperatively data of these works and others can be observed in Table 2.9¹³²

5.5 In–silico studies about ICRS surgery

Ebrahimian et al. (2019)¹³³ developed a novel methodology for numerical simulation of MyoRing surgery by adopting a simple representation of the corneal geometry and material model. They considered both the patient specific geometry and *in vivo* material model to assess the effect of different types of MyoRing on surgery outcome. In the work, a straightforward approach was addressed to analyze the effect of MyoRing in keratoconus corneas using 3D finite element methods based on anterior segment optical coherence tomography (AS–OCT). The corneal keratometry of the keratoconus cornea under intraocular pressure (IOP) after MyoRing surgery was the result of diameter and thickness and

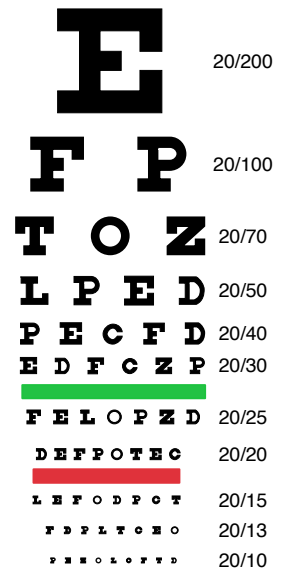


Figure 2.21: Chart of Snellen. Diagram used to measure the visual acuity of the eye. The standard chart distance is 6 meters (20 ft), and normal acuity is designated 6/6 or 20/20.

¹³¹ Alió et al. 2011

¹³² Rattan 2018, Daxer 2017, Jaididi et al. 2016, Khosravi et al. 2017, Yousif and Said 2018, Pirhadi et al. 2018, Bikbova et al. 2018, Daxer et al. 2016, Janani et al. 2016, Al-Tuwairqui et al. 2016, Mohebbi et al. 2016, Nobari et al. 2014, Saeed 2014, Alió et al. 2011

¹³³ Ebrahimian et al. 2019

their interactions. The target of the study was to investigate the relative contribution of these parameters to the keratometry data of keratoconus cornea predicted by a hyperelastic finite element model. The outcome of MyoRing implantation was predicted by variations in the MyoRing thickness and inserted optical zones showed enough influence of MyoRing parameters on the patient's post-operative result. Therefore, well-characterized individual MyoRing selection and position could be critical in cornea remodeling after MyoRing surgery.

¹³⁴ Kling and Marcos 2013

Kling and Marcos (2013) ¹³⁴ analyzed the effect of the insertion of ICRS in average healthy and ectatic corneas. A 2D axisymmetric model was used including the external structures of the eyeball, i.e., cornea, limbus and sclera, and triangular and hexagonal ICRS. The material behaviour was assumed as hyperelastic and isotropic for all the ocular tissues. For the insertion of the rings, a previous gap was included in the pre-surgical configuration of the cornea. However, the pre-stress of the ocular tissue due to the intraocular pressure was not accounted for. Different ICRS thickness (150–350 μm) and optical zone implantation (4.4–6.6) mm were simulated. In addition, a central keratoconus was introduced in the axisymmetric model, where corneal elasticity was decreased locally. ICRS geometry had a significant influence on corneal power. Changes from 4.08 to -17.7 D and 3.31 to -20.5 D for healthy and keratoconic tissue, respectively were observed. They predicted an increment of central corneal thickness of 38 μm for healthy and 97.8 μm for ectatic. Spherical aberration also changed upon ICRS implantation. The protusion of the posterior cornea behind the rings was well predicted. The model followed the trends of clinical reports on the effect of ring geometry. They concluded that a good combination between FE models with individual biomechanical properties and geometry of patients could assure a good predictability of ICRS surgery.

¹³⁵ Lago et al. 2015

Lago et al. (2015) ¹³⁵ built a patient-specific (PS) model of the cornea, without additional structures, such as limbus or sclera, to predict the post-surgical effects of ICRS. As boundary condition, the displacements of the corneal periphery were restrained. The material behaviour was also assumed as hyperelastic and isotropic and included the pre-stress of the ocular tissue. For the insertion of the rings, a previous gap was included in the pre-surgical configuration of the cornea and the ICRS were not simulated as solid inside the cornea, but the nodes of the gap

were morphed into the shape of the ring instead. 7 patients diagnosed with keratoconus and treated by implantation of ICRS were considered in the study. Finally, the predicted curvature was compared with the real curvature after the surgical intervention. The results showed a flattening of the cornea which was in consonance with the real improvement of the corneal curvature. The mean difference obtained was of 0.74 mm using properties of healthy corneas. It was the first study, capable of simulate the ICRS insertion in patient-specific models and to predict the optical outcomes with clinical data.

Kahn and Shiakolas (2016) ¹³⁶ utilized finite element analysis techniques to develop a high fidelity and computationally efficient two-dimensional axisymmetric cornea model to study the relative effects of MyoRing implant geometry and surgical conditions on the postsurgical shape of the cornea utilizing corneal apical displacement results. The FE analysis results indicated that MyoRing implantation reduces myopia. The amount of myopic rectification was dependent on the control parameters, which MyoRing geometry and surgical condition were included. The results showed that the greater MyoRing thickness, the greater increment of myopic rectification, and the greater MyoRing radius, the less myopic rectification. The depth of MyoRing implantation suggested that corneal depth of 40–75% provided steady myopic rectification. Corneal pocket diameter analysis revealed that smaller corneal pockets lead to an increase in myopic rectification. The results followed the trends of clinical studies. Finally, the combined impact of the control parameters on myopic rectification was studied by conducting a sensitivity analysis and an equation relating myopic rectification with control parameters was developed using a simple regression analysis.

¹³⁶ Kahn and Shiakolas 2016

Study	Ring (ZO/hICRS/Angle)		Pre-Surgical Values					Post-Surgical Values				
			K _{mean} (D)	CCT (μm)	SE (D)	Sph (D)	Cyl (D)	K _{mean} (D)	CCT (μm)	SE (D)	Sph (D)	Cyl (D)
Abdellah, 2019	<i>Keratoconus – Clinical Study, 38 eyes. 3 years follow-up</i> -/-355°		51.3 ± 3.5	-	-12.6 ± 3.6	-9.7 ± 3.1	-5.8 ± 1.6	47.5 ± 2.0	-	-9.6 ± 3.7	-7.5 ± 3.2	-4.3 ± 1.2
Abd Elaziz, 2018	<i>Advance keratoconus – Clinical Study, 30 eyes. 6 months follow-up</i> 5/300/355°		52.1 ± 4.5	-	-10.3 ± 3.1	-7.8 ± 4.8	-6.4 ± 2.2	42.9 ± 4.2	-	-2.7 ± 4.9	-1.6 ± 4.8	-2.3 ± 2.5
Gatzioufas, 2018	<i>Keratoconus – Clinical Study, 11 eyes (patients older than 40 year)</i> 5/150–300/-		51.4 ± 4.5	467 ± 39	-11.7 ± 4.5	-9.4 ± 2.6	-4.5 ± 3.7	48.4 ± 5.3	473 ± 37.5	-4.4 ± 4.0	-3.1 ± 2.8	-2.8 ± 2.2
Guber, 2018	<i>Keratoconus – Clinical Study, 10 eyes. 6 months follow-up</i> -/-/-		53.2 ± 4.5	412 ± 18.3	-12.8 ± 5.1	-9.2 ± 3.9	-7.3 ± 2.4	48.5 ± 5.8	416 ± 22.5	-6.5 ± 4.1	-4.8 ± 3.0	-3.3 ± 2.2
Heikal, 2017	<i>Keratoconus – Clinical Study, 30 eyes. 6 months follow-up</i> 5/150–350/90–120–160–210°		55.9 ± 5.4	-	-12.8 ± 5.1	-	-	44.1 ± 1.6	-	-2.4 ± 1.0	-	-
Yousif, 2017	<i>Central Keratoconus – Clinical Results, 73 eyes (comparing between 3 different types – 23 eyes with Keraring)</i> 5/200/320° 5/250/320° 5/300/320°		50.5 ± 4.5	-	-5.9 ± 1.4	3.8 ± 0.7	4.7 ± 1.1	44.9 ± 5.8	-	-1.5 ± 2.0	3.1 ± 0.8	2.0 ± 1.5
Al-Tuwairqui, 2016	<i>Keratoconus – Clinical Study, 34 eyes. MyoRing (18 eyes) and Keraring (26 eyes) implantation (Only Keraring data are shown)</i> 5/150–350/90, 120, 160°		48.1 ± 3.0	478 ± 26.6	-4.7 ± 3.0	-2.6 ± 2.9	-4.4 ± 1.8	43.6 ± 2.1	481 ± 33.4	-1.8 ± 2.5	-0.8 ± 2.0	-2.2 ± 1.6
Bayoumy, 2014	<i>Keratoconus – Clinical Study, 60 eyes. 6 months follow-up</i> 5/150–350/160°		51.5 ± 3.0	-	-7.4 ± 2.5	-9.7 ± 1.7	4.5 ± 1.6	47.4 ± 2.6	-	-3.1 ± 2.3	-4.4 ± 1.5	-2.6 ± 1.7
Jadidi, 2014	<i>Keratoconus – Clinical Study, 15 eyes. 6 months follow-up</i> 6/200–300/355°		48.1 ± 2.0	-	-5.5 ± 1.5	-2.4 ± 1.9	-4.3 ± 1.3	43.3 ± 2.3	-	-2.0 ± 1.6	-0.3 ± 2.3	-1.9 ± 1.0
Gharaibeh, 2012	<i>Keratoconus – Clinical Study, 55 eyes. 6 months follow-up</i> 6/150–350/90–120–160–210°		51.8 ± 4.1	-	-6.8 ± 2.9	-7.75	-5.35	47.3 ± 3.7	-	-3.2 ± 2.8	-4.57	-4.22
Kubaloglu, 2010a	<i>Keratoconus – Clinical Study 2 rings comparison (Only Keraring is shown), 100 eyes. 1 year follow-up</i> 5/-/-		48.8 ± 4.1	424 ± 51.4	-5.0 ± 3.4	-3.5 ± 3.0	-3.3 ± 1.9	46.3 ± 3.2	415 ± 58.2	-2.2 ± 1.6	-1.3 ± 0.9	-2.0 ± 1.3
Kubaloglu, 2010b	<i>Keratoconus – Clinical Study 2 ways of performing the tunnel (Mechanical and Femtosecond), 100 eyes. 1 year follow-up</i> Mechanical 5/150-350/90, 120, Femtosecond 160, 210°		49.9 ± 4.8	-	-5.8 ± 3.0	-4.0 ± 2.3	-3.5 ± 1.3	46.9 ± 3.4	-	-2.6 ± 1.8	-1.5 ± 1.1	-2.0 ± 1.2
Shabayek, 2007	<i>Keratoconus – Clinical Study, 16 eyes. 6 months follow-up</i> 5/150–350/160°		49.2 ± 5.2	-	-6.3 ± 3.7	-3.9 ± 3.4	-4.8 ± 2.1	46.54	-	-3.96	-2.88	-2.15

Table 2.6: Pre- and Post-operatively clinical data of Keraring studies

Study	Ring (ZO/hICRS/Angle)	Pre-Surgical Values					Post-Surgical Values				
		K _{mean} (D)	CCT (μm)	SE (D)	Sph (D)	Cyl (D)	K _{mean} (D)	CCT (μm)	SE (D)	Sph (D)	Cyl (D)
Alfonso, 2019	<i>Pediatric keratoconus – Clinical study, 118 eyes, 36 months follow-up</i> 5-6/150-300/ 90-120-150-210°	47.2 ± 2.9	-	-1.8 ± 2.4	0.1 ± 1.1	-3.6 ± 2.5	46.6 ± 2.6	-	-1.4 ± 1.9	-0.4 ± 0.1	-2.1 ± 1.2
Candelaria, 2019	<i>Keratoconus – Clinical study, 15 eyes, 12 months follow-up</i> 5-6/200/160° (2 rings)	50.8 ± 3.4	496 ± 37.2	-7.6 ± 3.6	-	-	48.1 ± 3.5	495 ± 44.9	-5.9 ± 3.1	-	-
Fernández-Vega, 2019	<i>Keratoconus with "bow-tie" shape – Clinical study, 20 eyes, 6 months follow-up</i> Low astig.: -/-/150° (1 ring) Med. astig.: -/-/120° (2 rings) High astig.: -/-/90° (2 rings)	44.8 ± 1.9	-	-2.5 ± 2.0	-1.0 ± 1.4	-3.0 ± 1.2	43.9 ± 1.6	-	-1.5 ± 1.7	-1.0 ± 1.5	-1.0 ± 0.4
Rocha, 2018	<i>Keratoconus – Clinical study, 34 eyes, 6 months follow-up</i> SE Group 6/150-300/ Q Group 320° (1 ring)	51.9 ± 3.9 50.8 ± 4.4	- -	-8.5 ± 4.1 -6.4 ± 4.1	- -	- -	46.95 47.47	- -	-3.9 ± 4.6 -3.2 ± 2.6	- -	- -
Sandes, 2018	<i>Keratoconus – Clinical study, 58 eyes, 16 months follow-up</i> 5-6/200/ Group 1 140-200° (2 rings) 5-6/150/ Group 2 140-150° (1 ring) 5-6/200/ Group 3 140-200° (1 ring) All Patients	54.4 ± 6.6 - - 49.9 ± 7.0	- - - -	-10.3 ± 2.9 -6.3 ± 2.9 -7.5 ± 3.9 -8.0 ± 3.5	- - - -	- - - -	49.3 ± 4.3 - - 47.3 ± 4.9	- - - -	-5.7 ± 1.8 -3.8 ± 2.2 -3.7 ± 2.2 -4.5 ± 2.5	- - - -	- - - -
Lyra, 2017	<i>Keratoconus – Clinical retrospective study, 241 eyes, 30 months follow-up</i> -/-/-	48.6 ± 4.4	-	-	-	-	46.4 ± 3.7	-	-	-	-
Fernández-Vega, 2016	<i>Paracentral keratoconus – Clinical study, 409 eyes, 6 months follow-up</i> 6/150-300/ 90-120-150-210°	46.2 ± 3.5	-	-4.2 ± 5.1	-2.1 ± 5.1	-4.2 ± 2.1	45.5 ± 3.2	-	-2.8 ± 4.7	-1.9 ± 4.6	-1.8 ± 1.4
Gauthier, 2016	<i>Keratoconus with irregular astigmatism – Clinical study, 32 eyes, 12 months follow-up</i> 5-6/150-300/ 90-120-150-210°	48.0 ± 3.6	453 ± 65.9	-2.6 ± 2.8	-0.2 ± 2.7	-4.8 ± 2.5	46.1 ± 3.3	465 ± 59.7	-1.3 ± 1.9	-0.4 ± 2.1	-2.4 ± 1.9
Torquetti, 2016	<i>Keratoconus – Clinical study, dual Scheimpflug analyzer, 50 eyes, 12 months follow-up</i> 5/-/140° (13 eyes) 5/-/160° (25 eyes) 5/-/210° (12 eyes)	48.5 ± 3.5 48.4 ± 1.9 50.9 ± 2.0	482 ± 49.6	-4.5 ± 3.9	-3.1 ± 3.8	-7.3 ± 2.7 -4.2 ± 1.8 -6.0 ± 1.5	44.9 ± 3.8 44.4 ± 2.6 45.5 ± 1.8	519 ± 53.8	-1.5 ± 2.4	-0.8 ± 2.6	-2.9 ± 1.5 -2.1 ± 1.3 -3.2 ± 1.5
Ameerh, 2012	<i>Keratoconus – Clinical study, 79 eyes, 6 months follow-up</i> 5-6/150-350/ 90-120-140-160-210°	50.5 ± 5.1	-	-5.4 ± 3.4	-3.3 ± 3.5	-4.2 ± 1.6	46.8 ± 4.7	-	-2.0 ± 1.9	-0.7 ± 1.5	-2.9 ± 1.7
Ançele, 2011	<i>Keratoconus – Clinical study, 25 eyes, 6 months follow-up</i> 5/-/160°	51.4 ± 6.1	-	-6.6 ± 5.1	-4.4 ± 5.2	-4.2 ± 2.1	48.7 ± 4.8	-	-3.1 ± 3.3	-1.8 ± 3.2	-2.6 ± 1.5
Kwitko, 2004	<i>Keratoconus – Clinical study, 51 eyes, 13 months follow-up</i> 5/250/120-160° (5 eyes) 5/300/120-160° (43 eyes) 5/350/120-160° (3 eyes)	48.8 ± 4.0	-	-6.1 ± 5.0	-	-	43.2 ± 4.8	-	-3.8 ± 4.0	-	-

Table 2.7: Pre- and Post-operatively clinical data of Ferrara studies

Study	Ring (ZO/hICRS/Angle)		Pre-Surgical Values					Post-Surgical Values				
			K _{mean} (D)	CCT (μm)	SE (D)	Sph (D)	Cyl (D)	K _{mean} (D)	CCT (μm)	SE (D)	Sph (D)	Cyl (D)
Kang, 2019	<i>Keratoconus – Clinical Study, 87 eyes, 12 months follow-up</i> 6/-/- (2 rings)		50.7 ± 2.6	-	-5.5 ± 4.8	-5.2 ± 0.3	-7.8 ± 4.9	48.5 ± 2.7	-	-5.0 ± 4.0	-3.5 ± 0.1	-5.9 ± 3.9
Hashemian, 2018	<i>Keratoconus – Clinical Study, 71 eyes, Intacs SK implantation, 6 months follow-up</i> 6/210-450/-		49.7 ± 4.0	-	-2.1 ± 2.8	-3.7 ± 1.5	-4.0 ± 3.0	47.2 ± 3.6	-	-0.6 ± 2.2	-2.6 ± 1.1	-1.9 ± 2.2
Shahhoseni, 2018	<i>Keratoconus – Clinical Study, 30 eyes, 12 months follow-up</i> 7/450/- (1 ring)		-	-	-	-	-1.6 ± 2.3	-	-	-	-	-1.5 ± 2.0
Amanzadeh, 2017	<i>Keratoconus – Clinical Study, 42 eyes, 4 months follow-up</i> 7/-/-		48.0 ± 2.8	-	-	-	-3.9 ± 1.7	45.9 ± 2.6	-	-	-	-2.0 ± 1.5
Al-Muammar, 2015	<i>Keratoconus – Clinical Study, 34 eyes, comparison between Intacs and Intacs SK</i>											
	Intacs (16 eyes)	7/210-450/150°	45.7 ± 1.7	-	-2.6 ± 2.4	-3.1 ± 1.1	-4.1 ± 2.4	43.5 ± 2.2	-	-0.5 ± 1.4	-2.9 ± 1.2	-1.4 ± 1.6
Intacs SK (18 eyes)	6/400-450/-	47.7 ± 2.8	-	-3.3 ± 2.3	-3.4 ± 1.3	-5.0 ± 2.5	44.6 ± 2.9	-	-0.6 ± 1.9	-2.8 ± 1.1	-1.7 ± 1.9	
Hashemian, 2014	<i>Keratoconus – Clinical Study, 33 eyes, comparison between Intacs and Intacs SK, 12 months follow-up</i>											
	Intacs (17 eyes)	7/210-450/150°	50.0 ± 2.9	-	-2.3 ± 0.0	-5.2 ± 4.5	-4.9 ± 2.3	48.0 ± 3.4	-	-1.6 ± 0.9	-4.0 ± 2.6	-3.6 ± 2.2
Intacs SK (16 eyes)	6/400-450/-	47.4 ± 2.8	-	-4.0 ± 0.7	-0.5 ± 2.3	-4.2 ± 1.8	46.3 ± 4.2	-	-2.0 ± 0.8	-3.2 ± 2.1	-3.6 ± 1.9	
Kubaloglu, 2010a	<i>Keratoconus – Clinical Study, 2 rings comparison (Only Intacs is shown), 68 eyes. 12 months follow-up</i>											
	7/-/150°	-	48.6 ± 3.5	410 ± 54.8	-3.3 ± 2.6	-3.1 ± 1.3	-4.1 ± 2.8	45.5 ± 2.7	419.60 ± 60	-1.3 ± 0.8	-1.9 ± 0.9	-2.2 ± 0.9
Piñero, 2009	<i>Keratoconus – Clinical Study, 2 surgical techniques (mechanical vs femtosecond), 2 rings comparison (Keraring vs Intacs), 80 eyes with Intacs are shown. 24 months follow-up</i>											
	Mechanical (55 eyes)	-/450/- (1 ring) or -/250/- (S)	50.1 ± 5.2	-	-3.4 ± 3.7	-4.3 ± 2.3	-5.6 ± 3.9	47.9 ± 4.7	-	-2.5 ± 5.1	-2.7 ± 1.6	-3.9 ± 5.2
Femtosecond (25 eyes)	and -/450/- (I)	49.0 ± 5.1	-	-3.6 ± 4.5	-3.7 ± 2.5	-5.4 ± 5.2	47.0 ± 5.0	-	-1.2 ± 2.1	-2.7 ± 1.4	-2.5 ± 2.1	
Shetty, 2008	<i>Advance Keratoconus – Clinical Study, 14 eyes, 6 months follow-up</i> 7/250/150° (S) and 7/450/150° (I)		53.0 ± 3.7	-	-6.7 ± 6.4	-4.9 ± 1.9	-9.1 ± 5.6	49.4 ± 3.8	-	-3.1 ± 3.1	-3.6 ± 1.3	-4.9 ± 3.2
Colin, 2007	<i>Keratoconus – Clinical Study, 100 eyes. 24 months follow-up</i> -/400-450/-		50.1 ± 5.6	478 ± 55.0	-4.7 ± 3.8	-4.6 ± 2.8	-6.9 ± 3.9	46.8 ± 4.9	421 ± 540	-2.2 ± 2.7	-3.3 ± 1.8	-3.8 ± 2.7
Alió, 2006	<i>Keratoconus – Clinical Study, 6 eyes. 48 months follow-up</i>											
	7/450/- (1 ring)	-	48.5 ± 3.3	-	-2.8 ± 3.8	-5.2 ± 3.2	-5.4 ± 4.1	45.9 ± 2.4	-	-2.4 ± 3.5	-3.1 ± 1.7	-3.9 ± 5.0
Kanellopoulos, 2006	<i>Moderate and advance keratoconus – Clinical Study, 20 eyes. 12 months follow-up</i>											
	Nomogram in study		49.5 ± 1.6	-	-3.4 ± 3.1	-3.8 ± 2.0	-5.3 ± 3.4	46.5 ± 1.2	-	-1.5 ± 2.2	-1.3 ± 0.9	-1.9 ± 1.8
Alió, 2005	<i>Keratoconus – Clinical Study, 1 and 2 rings implantation, 6 eyes. 48 months follow-up</i>											
	1 Segment	7/450/150°	46.3 ± 4.1	570 ± 76.3	-2.3 ± 3.6	-5.4 ± 2.8	-5.0 ± 3.8	42.6 ± 2.9	-	-0.3 ± 0.8	-2.9 ± 1.4	-1.7 ± 1.5
2 Segments	7/250-450/150°	50.8 ± 4.5	542 ± 50.2	-3.2 ± 3.9	-4.7 ± 2.3	-5.5 ± 4.3	46.7 ± 5.0	-	-2.1 ± 1.9	-2.3 ± 1.2	-3.3 ± 2.6	
Colin, 2001	<i>Keratoconus – Clinical Study, 10 eyes. 12 months follow-up</i> 7/250/150° (S) and 7/450/150° (I)		50.6 ± 3.6	479 ± 32.0	-	-	-	46.5 ± 2.6	-	-	-	-

Table 2.8: Pre- and Post-operatively clinical data of Intacs studies

Study	Ring (ZO/hICRS)		Pre-Surgical Values					Post-Surgical Values				
			K _{mean} (D)	CCT (μm)	SE (D)	Sph (D)	Cyl (D)	K _{mean} (D)	CCT (μm)	SE (D)	Sph (D)	Cyl (D)
Rattan, 2018	<i>Myopia Treatment</i>											
	RE	5/280	44.7	501	-10	-8.0	-4.0	39.8	-	-1.13	-0.5	-1.3
	LE	5/280	45.2	496	-9.75	-8.0	-3.5	40.4	-	-0.75	0.0	-1.5
Daxer, 2016	<i>Myopia Treatment – Statistical Analysis 19 eyes of 12 patients</i>											
		5/280	-	-	-11.72 ± 2.6	-11.0 ± 2.7	1.45 ± 1.2	-	-	-0.88 ± 1.2	-0.45 ± 0.4	-0.88 ± 0.9
		6/280	-	-	-6.83 ± 0.8	-7.58 ± 2.5	1.75 ± 1.3	-	-	-0.67 ± 0.8	-1.42 ± 2.0	-1.33 ± 0.6
		7/280	-	-	-2.81 ± 0.3	-7.58 ± 2.5	1.75 ± 1.3	-	-	0.5 ± 0	-1.00 ± 0.4	-1.00 ± 0.7
Jadidi, 2016	<i>Myopia Treatment – Statistical Analysis 32 eyes of 32 patients</i>											
		5/280 or 6/320	51.1 ± 3.3	-	-10.5 ± 2.8	-8.2 ± 2.6	-4.6 ± 1.9	47.5 ± 3.6	-	-1.3 ± 2.3	-0.3 ± 2.2	-2.0 ± 1.5
Khosravi, 2017	<i>Keratoconus – Clinical Results, 34 eyes–Astigmatic axis</i>											
			-	-	-6.8	-4.7 ± 3.8	-4.3	-	-	-2.52	-1.5 ± 3.7	-2.1
Yousif, 2017	<i>Central Keratoconus – Clinical Results, 73 eyes (comparing between 3 different types – 12 eyes with MyoRing)</i>											
		5/240 or 6/280	51.1 ± 2.4	-	-6 ± 4.5	-4.7 ± 2.4	-5.1 ± 1.1	45 ± 2.4	-	-1.3 ± 1.2	-2.1 ± 1.1	-2.4 ± 1.1
Pirhadi, 2017	<i>Keratoconus – Clinical Results, 39 eyes – Manual Mechanical Pocket (18 eyes) and Microkeratome PocketMaker (21 eyes)</i>											
	Manual	-	53.2 ± 5.1	421 ± 45.6	-10.7 ± 4.3	-7.9 ± 4.5	-5.6 ± 2.1	46.6 ± 3.5	448 ± 27.9	-2.8 ± 3.4	-1.5 ± 3.5	-2.7 ± 1.4
	PocketMaker	-	50.8 ± 4.9	452 ± 60.4	-9.7 ± 2.9	-7.5 ± 3.0	-4.4 ± 1.3	44.8 ± 2.9	468 ± 44.6	-1.1 ± 1.5	-0.4 ± 1.6	-1.5 ± 0.8
Bikvova, 2017	<i>Keratoconus – MyoRing and MyoRing + CXL, 41 eyes (only MyoRing Data)</i>											
		5/240	-	-	-	-	-	-	-	-	-	-
		5/280 5/320	51.2 ± 5.4	-	-9.0 ± 4.1	-9.0 ± 4.1	-4.9 ± 4.1	43.1 ± 2.7	-	-1.3 ± 3.2	-1.3 ± 3.2	-1.5 ± 2.3
Daxer, 2016	<i>Keratoconus – Clinical results, 53 eyes follow-up</i>											
			50.7 ± 1.1	440 ± 9	-7.6 ± 1.3	-5.2 ± 1.1	-4.8 ± 0.4	45.8 ± 0.7	442 ± 7	-1.5 ± 0.7	-0.9 ± 0.5	-1.2 ± 0.3
Janani, 2016	<i>Keratoconus – Clinical results, 40 eyes follow-up</i>											
			49.9 ± 3.5	-	-6.5 ± 4.5	-4.0 ± 3.6	-5.1 ± 1.7	47.5 ± 3.4	-	-2.0 ± 2.6	-1.0 ± 2.2	-2.1 ± 0.9
Al-Tuwairqui, 2016	<i>Keratoconus – Clinical Study, 34 eyes. MyoRing (18 eyes) and Keraring (26 eyes) implantation (Only MyoRing data are shown)</i>											
			49.8 ± 3.6	473 ± 3.6	-5.1 ± 5.6	-3.3 ± 5.3	-3.6 ± 1.3	42.6 ± 1.8	463 ± 46.4	-1.4 ± 2.3	-0.4 ± 2.2	-2.1 ± 1.4
Mohebbi, 2016	<i>Keratoconus – Clinical Study, 47 eyes. 18 month follow-up</i>											
	23 eyes	5/320	-	-	-	-	-	-	-	-	-	-
	15 eyes 9 eyes	5/280 6/280	51 ± 3.3	440 ± 34.3	-5.76	-3.37	-4.78	46.3 ± 2.9	446 ± 33.8	-0.39	-0.87	-2.52
Nobari, 2014	<i>Keratoconus – Clinical Study, 54 eyes. 18 month follow-up</i>											
			50.2 ± 3.1	-	-6.1 ± 3.5	-4.6 ± 3.7	-5.2 ± 1	45.8 ± 2.4	-	-0.1 ± 0.9	0.6 ± 0.1	1.5 ± 0.7
Saeed, 2014	<i>Keratoconus – Clinical Study, 23 eyes.</i>											
			51.3 ± 3.6	-	-	-	-	45.8 ± 3.0	-	-	-	-
Alió, 2011	<i>Keratoconus – Clinical Study, 12 eyes.</i>											
		5/280	-	457 ± 45.9	-8.2 ± 4.9	-4.8 ± 5.5	-6.8 ± 3.0	-	469 ± 53.4	-0.9 ± 2.3	0.3 ± 2.6	-2.5 ± 1.4

Table 2.9: Pre- and Post-operatively clinical data of MyoRing studies



Chapter 3

Pressure-based ICRS implantation¹

¹ J. Flecha-Lescún, B. Calvo, J. Zurita, and M. Á. Ariza-Gracia. **Template-based methodology for the simulation of intracorneal segment ring implantation in human corneas.** *Biomech. Model. Mechanobiol.*, 17 (4):923–938, Aug 2018. ISSN 1617–7940. DOI: <https://doi.org/10.1007/s10237-018-1013-z>

The chapter aims to implement the first methodology of the ICRS insertion within corneal stroma. Different surgical scenarios are built so as to evaluate the behaviour of both average cornea and central keratoconus cornea after ICRS insertion.

Chapter Contents

1. Introduction	100
2. Material and methods	102
<i>3D FE template of the human eyeball</i>	102
<i>3D FE model of the ICRS</i>	105
<i>Computational simulation of the insertion of ICRS</i>	105
<i>Determination of corneal optics</i>	107
<i>Benchmark studies</i>	109
3. Results	110
<i>Results of the parametric study</i>	110
<i>Effect of ICRS in KC corneas</i>	112
4. Discussion	117

1. Introduction

Cornea is the outermost, transparent layer of the eye that is responsible of two-thirds of the optical power, as you can see in the previous chapter. It is structured in different layers that are the epithelium, the Bowmann layer, the stroma, and the endothelium, from the outermost to the innermost. Between them, the stroma represents almost the 90% of the corneal thickness and it is composed of water ($\approx 90\%$) and collagen fibres embedded in a ground substance called extracellular matrix.² Collagen fibres, which are organised in a network, alongside with the extracellular matrix provide structural integrity and transparency to the cornea.³

Keratoconus (KC) (see Section 3 of Chapter 2 is summarized as an idiopathic, non-inflammatory and degenerative corneal disease that typically develops in the inferior-temporal and central zones.⁴ Despite its etiology is still partially unknown,⁵ corneas with keratoconus or ectasia present a loss of organisation in the corneal collagen fibrils that results in a localised thinning and a conical protrusion.⁶ In KC, the corneal surface presents a progressive asymmetric deformation with irregular astigmatism and high myopia that worsens visual acuity.⁷ KC is ethnic-dependent⁸ and targets on young to mid-age patients, appearing during the adolescence and progressing until maturity.⁹ Although its incidence is low, 0.05–2.5%, the absence of a cure and its long-term blinding effects put KC on the spot.

There are different techniques to treat the disease depending on the severity of the ectasia (see Section 3.3 of Chapter 2), although this study focus on the ICRS insertion.¹⁰ Their main clinical setback is related to the planning of the clinical procedure (see Section 4.1 of Chapter 2). The treatments usually rely on the experience of the ophthalmologist¹¹ and population-based nomograms that implicitly account for the mechanics, but explicit patient-specific information is missing. Hence, unexpected outcomes can arise such as corneal extrusion in which, from 24 hours to few weeks after surgery,¹² ICRS are expelled out the cornea, or imprecise post-surgical visual acuity that results in patient discomfort.¹³

Rings are surgically placed depending on the location and degree of severity of the ectasia. Different surgical parameters must be accounted for to achieve the desired effect such as the distance from the corneal centre where rings will be placed, the diameter and shape of the ring's cross-section, the angle embraced, or whether single or paired ICRS should be inserted.¹⁴ In actual practice, both triangular and hexagonal

² Garcia-Porta et al. 2014, Peris-Martínez and Cisneros Lanuza 2014

³ Benoit et al. 2016

⁴ Auffarth et al. 2000, Fangjun et al. 2016

⁵ Ramez et al. 2017, Sherwin et al. 2017, Dan Z. et al. 2017, O'Brat 2017

⁶ Auffarth et al. 2000

⁷ Fangjun et al. 2016

⁸ Ramez et al. 2017

⁹ O'Brat 2017

¹⁰ Akaishi et al. 2004, Zare et al. 2007

¹¹ Alió et al. 2006, Fernández-Vega et al. 2016

¹² Liu et al. 2015, Zare et al. 2007

¹³ Colin and Kiliç 2012, Torquetti et al. 2013

¹⁴ Vega-Estrada and Alio 2016, Kahn and Shiakolas 2016, Kling and Marcos 2013

cross-sectioned ICRS are used.¹⁵ The former are inserted close to the optical axis whereas the latter are inserted at a larger distances due to their bigger cross-section.

Despite the interest and novelty of previous *in-silico* methodologies, commented in Section 5.5 of Chapter 2,¹⁶ two main points could be improved: *i)* a mechanical weakness is introduced beforehand when considering the gap of the tunnel from the beginning, which could be inaccurate when representing the mechanical equilibrium prior to the surgery; *ii)* the solid rigid motion of the ICRS after its insertion is missing if the rings are not represented as a foreign body inserted in the incision and interacting with the surrounding tissue.

In the present work, we present the first semi-automatic tool that is template-based to simulate the 3D implantation of ICRS in human corneas. Our numerical framework allows for simulating the optical and mechanical effect of three different key parameters of the ICRS surgery that are the stromal depth at which the ring is inserted (sDI - stromal depth of insertion), the horizontal distance with respect to the corneal centre where the rings are placed (hDRI - horizontal distance of ring insertion), and the diameter of the cross-section (ϕ_{ICRS}). Besides, the pretension of the tissues is included,¹⁷ the gap associated to the laser incision is not present in the pre-surgical configuration of the cornea, and the rings are introduced as solid bodies that contact with the corneal stroma.

For the sake of simplicity, and since the target of this work is to show a numerical methodology, we assume three main simplifications: the use of an average human cornea,¹⁸ the description of the cornea as a hyperelastic isotropic material,¹⁹ and the use of ICRS with circular cross-section, which are seldom applied in clinic. Independently of these simplifications, the procedure remains valid whether more complex scenarios are introduced, e.g., patient-specific corneas, anisotropy of the tissues, or other ICRS cross-sections such as triangles or hexagons.

To determine whether our computational model is behaving physiologically, we perform a 3^k full-factorial parametric study²⁰ that analyses the impact of these three key parameters (i.e, sDI, hDRI, and ϕ_{ICRS}) in the optics, the mechanics and the kinematics of the cornea. Using an in-house ray-tracing algorithm,²¹ we also analyse the optical effect in the post-surgical cornea including the aberrations of the eye related to the Zernike coefficients, and the spherical and cylindrical powers, which are typically used to assess in the visual acuity of the patient. Based on this 3^k

¹⁵ Piñero et al. 2009, Shabayek and Alio 2007

¹⁶ Kahn and Shiakolas 2016, Kling and Marcos 2013, Lago et al. 2015, Guarnieri et al. 2015

¹⁷ Ariza-Gracia et al. 2016

¹⁸ Navarro et al. 2006

¹⁹ Ariza-Gracia et al. 2016

²⁰ Montgomery 2019

²¹ Ariza-Gracia et al. 2017a

parametric study, we also try to discern the most influential parameters that affect patient's optics.

Finally, the methodology is applied to an average cornea that presents a central keratoconus to determine whether the methodology can be further applied to assess in the management of the disease. The kinematics, the mechanics and the optics of the post-surgical cornea are analysed for two different ring diameters (ϕ_{ICRS}) and two different stromal depths of insertion (sDI).

2. Material and methods

In this section, the template-based computational methodology is presented. In particular, the methodology gathers the following aspects: *i*) the definition of the average finite element templates and their numerical features, i.e., mesh, boundary conditions and material behaviour; *ii*) the definition of the finite element model of the ICRS; *iii*) the computational procedure proposed to simulate the long-term insertion of the ICRS in the cornea; and *iv*) the optical criteria used for analysing the results.

Then, a 3^k full-factorial parametric analysis is used to study the influence of different ICRS's parameters in the corneal optics, and whether our models and procedure yield physiological outcomes. Finally, a theoretical study in keratoconus (KC) corneas is performed to discern whether the computational framework could help in its management by determining the mechanical and kinematic response of the cornea after the insertion of ICRS.

2.1. 3D finite element template of the human eyeball: mesh, constitutive behaviour, and boundary conditions

Two geometries of reference are considered to build the finite element (FE) templates: an average healthy cornea and an average cornea with central keratoconus. All structures in the model, i.e., cornea, sclera and limbus, present symmetry of revolution (see in Figure 3.1.a). The dimensions of the healthy cornea are based in an emmetropic eye:²² radio of curvature of 6.7 mm and 7.5 mm for the posterior and anterior surfaces respectively, and a variable and incremental thickness from the centre to the periphery with a fixed central corneal thickness of 600 μm . The thickness of the limbus is variable, from 1 mm in the interface with the sclera to 0.7 mm in the interface with the cornea. The keratoconus is derived from the healthy

²² Navarro et al. 2006

cornea simulating that the healthy patient develops the disease. It has a central thinning of 400 μm , and a mechanical weakening that is affecting 2 mm in diameter (see in Figure 3.1.b). The inner diameter of the sclera is set to 24 mm²³ with a constant thickness of 1 mm. The limbus is defined as the short strip of tissue that acts as transition between the cornea and the sclera.

²³ Navarro et al. 2006

Our methodology is semiautomatic as it relies on previously generated templates that gather a discrete set of surgical scenarios. Meaning that, if one specific set of surgical parameters is desired to be evaluated and was not previously associated to a particular template, the methodology would not be able to evaluate the surgical scenario unless a new template is generated ad hoc. In particular, nine templates were build by combining three variations of hDRI, i.e., 5, 6, and 7 mm, and three variations of sDI, i.e., 50%, 65%, and 80% (see in Figure 3.1.c).

All geometries are meshed with 8–node linear hybrid hexahedral elements (C3D8H). To determine the optimal size of the mesh, a convergence analysis has been carried out with three different meshes with a different level of refinement. The point of interest in our analysis, i.e., the corneal apex, showed a percentage variation of less than 2% between the finest and the coarsest mesh. As the problem is dominated by the biaxial stress state induced by the intraocular pressure (IOP) and the bending is negligible,²⁴ the mesh size at the centre of the cornea is not critical. However, areas close to the insertion of the ICRS undergo great deformation and, thus, precise of a fine mesh definition (see in Figure 3.1.b). Hence, the cornea is overmeshed in some regions to avoid a bad mesh transition between the fine mesh surrounding the ICRS and the ideal coarse mesh in the rest of the cornea. Depending on the combination under analysis, the number of elements of the mesh will vary from 184,572 to 311,052 elements, i.e., from 773,055 to 977,604 degrees of freedom (d.o.f).

²⁴ Ariza-Gracia et al. 2016

To simulate the material behaviour of the ocular tissues, we use hyper-elastic isotropic strain–energy functions. Despite the fact that the human cornea presents two orthogonal families of fibres,²⁵ the limbus presents one circumferential family of fibres,²⁶ and the sclera presents a random distribution of fibres far from the optical nerve insertion,²⁷ they are not modelled as fibre–reinforced materials. This assumption does not affect the proposed methodology to simulate the insertion of the ICRS, but allows for a less time-consuming analysis. While the cornea and the limbus are modelled using Neo–Hookean strain–energy functions, ψ_N ,²⁸ the sclera is

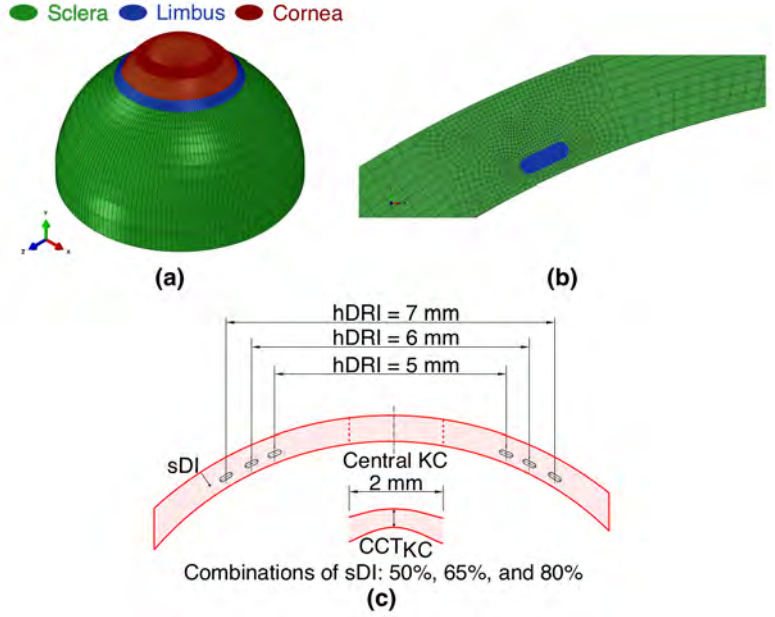
²⁵ Ariza-Gracia et al. 2016, Pandolfi and Vasta 2012

²⁶ Ariza-Gracia et al. 2016, Pandolfi and Vasta 2012

²⁷ Coudrillier et al. 2015

²⁸ Ariza-Gracia et al. 2015

Figure 3.1: Definition of the finite element templates: (a) 3D numerical model of the eyeball including cornea (red), limbus (blue), and sclera (green); (b) Detail of the mesh in the surroundings of the ICRS. Elements in blue will be removed during the simulation to allow the insertion of the ring; (c) Schematic transversal section of the cornea highlighting two of the variables controlled in the template: stromal depth of insertion (sDI), and horizontal distance of ring insertion (hDRI). Detail of KC geometry with a central thickness (CCT_{KC}) of 400 microns.



²⁹ Ariza-Gracia et al. 2016

modelled using a Yeoh strain–energy function, ψ_Y .²⁹

$$\psi_N = \frac{1}{D} \cdot \left(\frac{J_{el}^2 - 1}{2} - \ln(J_{el}) \right) + C_{10}^N \cdot (\bar{I}_1 - 3) \quad (3.1)$$

$$\psi_Y = \sum_{i=1}^3 D_i \cdot (J_{el} - 1)^{2 \cdot i} + \sum_{i=1}^3 C_{i0}^Y \cdot (\bar{I}_1 - 3)^i \quad (3.2)$$

where \bar{I}_1 is the first invariant of the modified right Cauchy–Green tensor $\bar{C} = J_{el}^{-2/3} C$, J_{el} is the elastic volumen ratio, and $\frac{1}{D_i}$ is the bulk modulus. The material constants for the healthy tissues are retrieved from our previous work:³⁰ $C_{10}^N = 0.05$ MPa, $C_{10}^Y = 0.81$ MPa, $C_{20}^Y = 56.050$ MPa, $C_{30}^Y = 2,332.26$ MPa, $D_i = 0$ MPa⁻¹. The material weakening associated to the KC is assumed to be a 50% of the stiffness of the healthy material: $C_{10}^{KC} = 0.025$ MPa.

As model–dependent boundary conditions, i.e., not related to the surgical procedure, there are two main restrictions: the intraocular pressure (IOP) that is set to a physiological pressure of 15 mmHg (2 kPa), and a condition of symmetry on the equatorial plane of the sclera.³¹ Moreover,

³¹ Ariza-Gracia et al. 2016

the initial pre-stress of the corneal tissue is introduced by using an iterative algorithm previously reported.³² The free-stress algorithm determines a reference geometry, generally smaller, such that when the eyeball is pressurised to the physiological IOP, the corneal shape returns to its original shape but including the stress and stretch fields.

2.2. 3D finite element model of the ICRS

For the sake of simplicity and numerical stability, ICRS with three different circular cross-section diameters ($\phi_{ICRS} = 200, 300$ and 500 microns) and a fixed opening angle, α , of 150° are used. The diameter of the circular rings corresponds to the maximum limiting dimension of clinical rings (i.e., triangular or hexagonal, see in Figure 3.2). In this vein, we ensure that the minimum size of the laser incision will house any ICRS typology, even when commercial triangular or hexagonal ICRS geometries are introduced.

ICRS are made of PMMA isotropic polymer and modelled as an elastic material with a Young's modulus of $3,300$ MPa and a Poisson's ratio of 0.4 (data from Addition Technology, Inc., Sunnyvale, CA, USA). They are meshed using 8-node linear hexahedra (C3D8) with a variable number of elements ranging from $3,343$ to $9,024$, i.e., from $12,783$ to $32,460$ DOF. Regarding their model-dependent boundary conditions, there are not special considerations as they will lay over the cornea until their insertion inside the laser incision. Once inside, a frictionless, hard-contact, surface-to-surface contact between the rings and the incision is activated.

2.3. Computational simulation of the insertion of ICRS

Three stages of the surgery must be simulated in Abaqus 6.13–5 (Dassault Systèmes Simulia Corporation) to mimic the surgical procedure: *i*) the creation of the laser incision in the stroma, *ii*) the widening of the incision to introduce the rings, and *iii*) the insertion of the ICRS. Since our interest is in the long-term impact of the ICRS in the mechanics and the optics of the cornea, and not in the damage mechanisms of the photodisruption, incisions are already “included” in the FE template but “filled” with corneal stroma (see Figures 3.1 and 3.3). In this way, the pre-stress of the pre-surgical geometry of the cornea can be done without introducing a fictitious weakening due to the gap.³³ After pre-stressing the cornea, the elements of the incision are removed using the Abaqus Standard tool, *Model Change, that allows erasing elements during a simulation step. As a mechanical instability is introduced, a new mechanical equilibrium needs

³² Ariza-Gracia et al. 2016

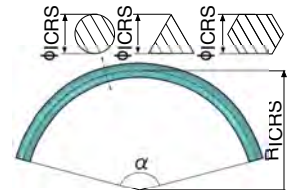


Figure 3.2: Finite element model of the ICRS. The main variables are the radius of the ring (R_{ICRS}), the opening angle (α), and the diameter of the transverse section of the ring (ϕ_{ICRS}). The diameter of the circular ring is set to the maximum limiting dimension of commercial rings (triangular and hexagonal).

³³ Kahn and Shiakolas 2016, Kling and Marcos 2013, Lago et al. 2015

to be achieved.

Once the incision is empty, it is enlarged using a pressurisation to give room for the ICRS. In particular, the **Fluid Cavity* boundary condition that allows for introducing a hydrostatic pressure is used. This hydrostatic pressure can be either controlled by fixing the pressure degree of freedom, or by introducing a volume of fluid in the cavity. Since, the amount of fluid to introduce is not known beforehand, the pressure is fixed and the volume flowing in the cavity is monitored (see in Figure 3.3). When the incisions are expanded, their centre lines are calculated and the rings are registered into the correct position. Finally, the pressure is slowly released allowing the incision to shrink and to establish the contact with the ICRS.

There are two critical computational restrictions that must be satisfied to obtain the convergence of the problem. First, the incision must be sensitively bigger than the diameter of the ICRS (ϕ_{ICRS}) or the surface normals will not cross, the contact will not be detected, and meshes will penetrate. Second, different levels of pressure are needed to obtain the same volume inside the cavity depending on the material stiffness of the area surrounding the incision, the hDRI, and the sDI. A preliminary analysis is carried out to define the level of pressure needed to open the incision and to insert the ICRS without violating any of the computational restrictions. To allow the insertion of the different ICRS at different sDIs and hDRIs, the following levels of pressure are needed: *i*) at 50% depth, 400 kPa with an average volume of $5.035 \pm 0.569 \text{ mm}^3$; *ii*) at 65% depth, 385 kPa with an average volume of $5.034 \pm 0.605 \text{ mm}^3$; *iii*) at 80% depth, 275 kPa with an average volume of $4.774 \pm 0.494 \text{ mm}^3$.

The complete procedure (see in Figure 3.3) consists of the following steps: *i*) determining the free-stress configuration of the cornea (1st simulation); *ii*) physiological pre-stressing of the cornea due to the intraocular pressure (2nd simulation); *iii*) removing the elements inside the laser incision (2nd simulation); *iv*) expanding the incisions (2nd simulation); *v*) calculating the centre lines of the incisions (2nd simulation); *vi*) registering the ICRS to the incisions (3rd simulation); *vii*) closing up the incisions to force contact with the ICRS (3rd simulation); *viii*) achieving the mechanical stability (equilibrium step)

During the simulation, the elevation of the anterior and posterior corneal surfaces are saved. For the pre- and post-surgical geometries, the Cartesian coordinates (x, y, z) of the points defining the anterior and posterior surfaces are saved to a text file using the *URDFIL* subroutine. With this

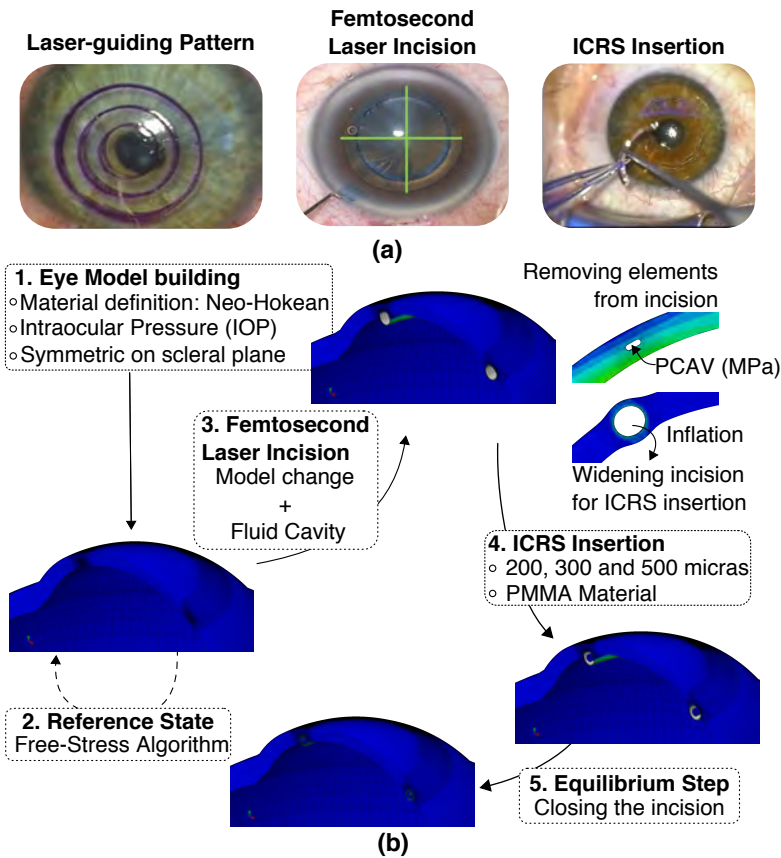


Figure 3.3: Clinical and computational surgical procedure: (a) Clinical procedure: a pattern is marked so as to the laser can perform the incision and the rings can be manually inserted; (b) Computational procedure: (1) the numerical template is built; (2) the reference configuration is achieved and the ocular tissues are pre-stressed using an iterative algorithm; (3) the incisions, which were already presented in the model, are removed using **Model Change* and inflated using **Fluid Cavity*; (4) the ICRS is inserted and the pressure slowly released; (5) the ICRS reaches the equilibrium inside the incision.

information, the optical assessment of the pre- and post-surgical influence of the ICRS is carried out.

2.4. Determination of corneal optics

To use metrics that are of clinical relevance, our in-house ray-tracing software³⁴ is used. Such software allows for the numerical simulation of clinical topographers³⁵ and aberrometers³⁶ using as input information the corneal elevation of both surfaces.

In particular, we use the concept of wavefront aberration in optical systems.³⁷ The wavefront aberration is the measure of the degree of imperfection of the optical system: while in a perfect system planar waves transform into perfect spherical waves, in real systems the same planar

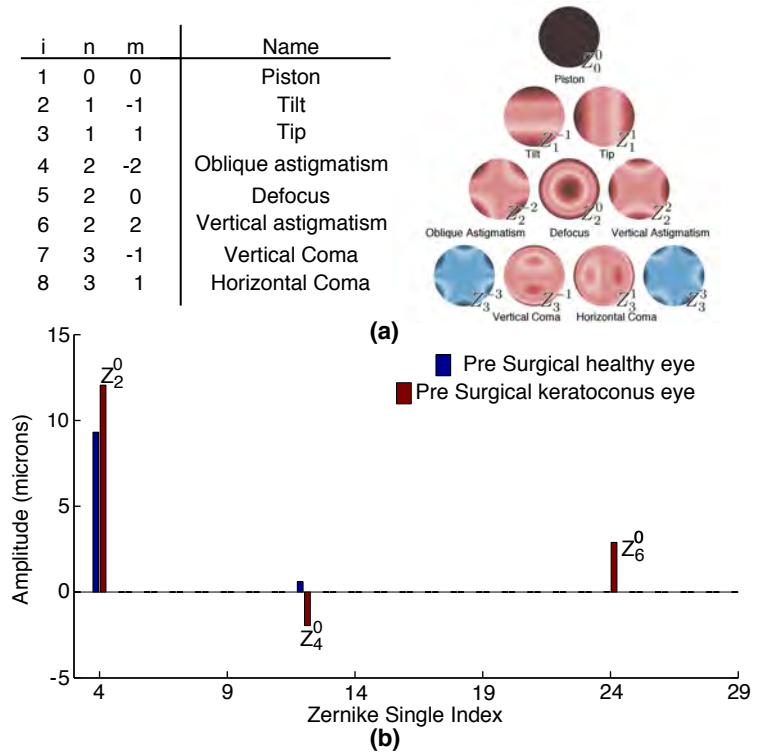
³⁴ Ariza-Gracia et al. 2017a

³⁵ Fangjun et al. 2016, Garzón and Galán 2013, Hong et al. 2013

³⁶ Piñero et al. 2009, Lakshminarayanan and Fleck 2011

³⁷ Dai 2008, Malacara and Malacara 2003

Figure 3.4: Zernike representation of the geometries of reference: (a) summary of the most representative Zernike coefficients (Z_m^n) and their graphical representation. The cylindrical power (astigmatism) and the spherical power (defocus) are related to the second-order Zernike coefficients (Z_2^{-2} -oblique astigmatism, Z_2^0 -defocus, and Z_2^2 -vertical astigmatism). Keratoconus is related to vertical and horizontal coma (Z_1^{-3} and Z_1^3); (b) Zernike coefficients of the average healthy (blue) and average KC (red) geometries. The healthy geometry only presents primary and secondary spherical aberrations (Z_2^0 and Z_4^0). The KC geometry, as it is derived from the healthy geometry, worsens the primary and secondary spherical aberrations and introduces high order spherical aberrations (Z_6^0). Moreover, astigmatism is not present as the KC is of central type.



waves would transform into distorted spheres. This distortion gives direct information of the imperfections of the system, either in geometry or in the transmission of the light, i.e., refraction indexes. Importantly, the wavefront aberration can be represented as a surface and, thus, it can be fitted to Zernike polynomials.³⁸

These polynomials have a direct relation to clinical practice since some of their coefficients (Z_m^n) are indicator of common pathologies such as astigmatism, which is related to Z_2^{-2} and Z_2^2 , or keratoconus, which is related to Z_1^{-3} and Z_1^3 (see brief summary in figure 3.4).

In ophthalmology, the spherical (Sph) and cylindrical (Cyl) powers (diopters, D) are used to assess on the visual acuity of the patient, for example in the prescription of lenses.³⁹ Patient's astigmatism can be determined with the second-order coefficients of Zernike, i.e., Z_2^{-2} , Z_2^0 , and Z_2^2 , by calculating the cylindrical power and the axis of orientation of the

³⁸ Lakshminarayanan and Fleck 2011

³⁹ Thibos et al. 2004

cylinder (ϕ) (Eq.3.3):⁴⁰

$$\begin{aligned}
 Sph(D) &= \frac{-Z_2^0 4\sqrt{3}}{R_p^2} - \frac{Cyl}{2} \\
 Cyl(D) &= -2 \cdot \sqrt{\left(\frac{-Z_2^2 2\sqrt{6}}{R_p^2}\right)^2 + \left(\frac{-Z_2^{-2} 2\sqrt{6}}{R_p^2}\right)^2} \\
 \phi(^{\circ}) &= \frac{1}{2} \operatorname{atan}\left(\frac{\frac{-Z_2^{-2} 2\sqrt{6}}{R_p^2}}{\frac{-Z_2^2 2\sqrt{6}}{R_p^2}}\right)
 \end{aligned} \quad (3.3)$$

⁴⁰ Thibos et al. 2004

where R_p is the radius of the pupil under analysis, i.e., typically 3 mm.⁴¹

⁴¹ Hernández-Gómez et al. 2014

The optical outcomes of the FE templates are gathered in Figure 3.4.b. The initial average cornea presents primary and secondary spherical aberrations (Z_2^0 , and Z_4^0), whereas the evolution of the central KC worsens the previous aberrations (Z_2^0 , and Z_4^0) and promotes new high order aberrations (Z_6^0). As the case of study is a theoretical perfect central KC, primary astigmatism (Z_2^{-2} , and Z_2^2) is not present in the relation of aberrations.

2.5. Benchmark studies

A 3^k full-factorial protocol is used to design a batch of experiments that is based on the FE templates of the healthy cornea and in the *in-silico* surgical methodology. This parametric study presents 3 levels (low, mid, high) of combinations of k variables to assess in the impact of one, or several, objective variables.⁴² In particular, our parametric study is build using a 3^3 full-factorial analysis with 27 simulations that combines three levels of: sDI (50%, 65% and 80%), hDRI (5, 6 and 7 mm), and ϕ_{ICRS} (200, 300, and 500 microns).

⁴² Montgomery 2019

With this parametric study, we analyse the impact of different clinical scenarios on two optical variables: the spherical power (Sph), and the cylindrical power (Cyl). Note that the astigmatic axis (ϕ) was not analysed since we are using average corneas and rings are always placed in the same corneal meridian. Thus, the astigmatic axis will always align with the ICRS axis and will not present variation between clinical scenarios. Thanks to the level-wise structure of the dataset, the main effect of the principal variables and their interaction on the optical response is analysed.⁴³

⁴³ Montgomery 2019

Finally, the kinematics, the mechanics, and the optics are studied for both the healthy and KC corneas. In particular, three cases are analysed:

i) Case 1: 200 micron ICRS placed at 80% depth; *ii)* Case 2: 500 micron ICRS placed at 80% depth; and *iii)* Case 3: 200 micron ICRS placed at 50% depth. The main outcomes of interest are: the movement of the corneal apex, the stress field in the corneal stroma next to the ring, the stress relaxation of the anterior and the posterior cone, and the corneal optics.

FE simulations were performed using Abaqus, whereas the optical analysis and data management were performed using Matlab (Matrix Laboratory, Mathworks).

3. Results

In this section, benchmark studies are discussed. First, the parametric study used to discern whether the model behaves physiologically and to study the impact of different ICRS features on corneal optics. Second, the kinematic, mechanical, and optical analysis of different clinical scenarios in KC corneas. For the sake of clarity, only the results for KC corneas are showed since both corneal configurations, healthy and KC, behaved similarly.

3.1. Results of the parametric study

The most influential parameter of the surgery is the stromal depth of insertion (sDI). The impact of the variation of the sDI represents slightly more than a 70% of the variation of spherical power and more than a 50% of the variation in cylindrical power (see in Figure 3.5.a–b). This is in line with several clinical studies where depth was reported to be critical in the definition of the ICRS surgery.⁴⁴ The deeper the location of the ICRS, the greater the impact in both powers but, interestingly, with opposite slopes (see in Figure 3.5.c-d). This is essential when performing a surgery since there is not an optimal trade-off when minimising aberrations: if the spherical aberration aims at being minimised, the astigmatism (cylindrical power) will increase and viceversa. Physically, this means that the curvature of the surface is greatly affected due to the kinematics and mechanics of the cornea after the insertion of the ring. As we consider the material fixed, we do not know exactly how much of this contribution is derived from the material or the shape, but we can infer that mechanics is playing a role that is driving the response. Furthermore, the cylindrical power presents a nonlinear behaviour with a transition zone at 65% depth from which there will be negligible changes (see sDI in Figure 3.5.d).

⁴⁴ Al-Tuwairqui et al. 2016, Fernández-Vega et al. 2016, Jadidi et al. 2015, Torquetti et al. 2016

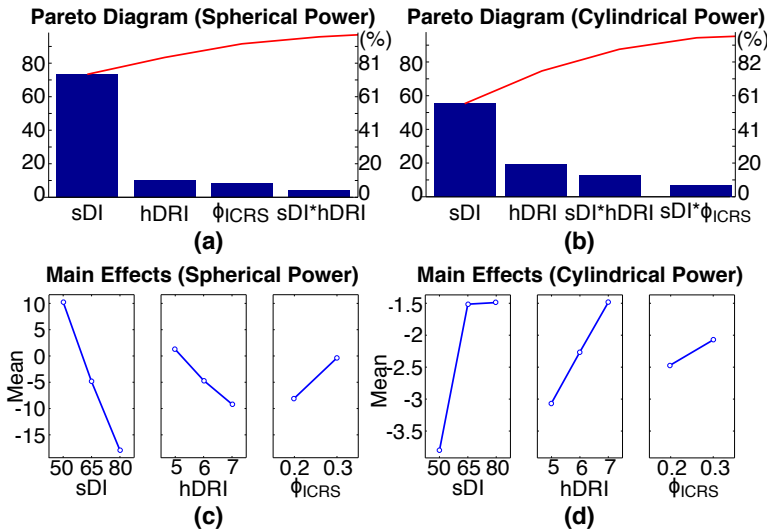


Figure 3.5: Parametric analysis (1): Pareto chart and main effect of the variables under analysis in the spherical and cylindrical powers. (a-b) Influence of the variation of the variables under analysis (sDI, hDRI and ϕ_{ICRS}) in the spherical (a) and the cylindrical (b) powers. **(c-d)** Main effect of the variation of the variables under analysis in the spherical (c) and the cylindrical (d) powers.

The influence of the hDRI ranges from 10 to 20% for the spherical and cylindrical powers, respectively (see in Figure 3.5). Also this feature affects the spherical and cylindrical powers with opposite linear trends, being impossible to obtain an optimal trade-off between both powers when performing a surgery. For example, if the astigmatism wanted to be minimised, the optimal hDRI would lie between 6 and 7 mm, but this would imply that a certain amount of spherical aberration would be induced.

The diameter of the ICRS (ϕ_{ICRS}) only affects the spherical power whereas the cylindrical power presents much less sensitivity to it (see in Figure 3.5.a–b). Besides, both power could be minimised in terms of ϕ_{ICRS} as they present linear positive trends (see in Figure 3.5.c–d). At this point, we must stress that the ICRS with a diameter of 500 μm was calculated but removed from the statistical analysis as they resulted in anomalous values and distorted the analysis. In fact, the inclusion of such rings is related to the 3^k full-factorial analysis where the levels of variation must be fixed and complete. Nevertheless, this is not affecting either the conclusions or the results, since such ICRS are scarcely used in clinics and always far away the centre (i.e., > 7 mm).⁴⁵

When observing the interaction between ICRS's features, we can conclude that the spherical power is mainly controlled by the sDI whereas it

⁴⁵ Al-Tuwairqui et al. 2016, Fernández-Vega et al. 2016, Jadidi et al. 2015, Torquetti et al. 2016

is almost independent from hDRI and ϕ_{ICRS} . In particular, rings located farther and deeper affect more to spherical aberration than other combinations (see in Figure 3.6.a). Regarding the cylindrical power, sDI is also controlling the overall astigmatic change (see in Figure 3.6.b). In particular, sDI presents a nonlinear variation with hDRI, with a great variation for rings placed at 50% depth and a null variation for rings placed at 80% depth. Despite different diameters of ICRS affect the cylindrical power, the difference between using 200 or 300 μm is negligible. Once more, the inversion of behaviour between 65% and 80% depth is observed in the interaction between sDI and hDRI, and sDI and ϕ_{ICRS} . This fact also suggests that a mechanical change in the cornea is occurring when overpassing 65% depth, which is modifying its overall behaviour.

3.2. Effect of ICRS in KC corneas: kinematics, mechanics, and optics

The average KC cornea (see Case 0 in Figure 3.7) presented an apical displacement after pressurisation of 0.17 mm, 3 times bigger than in the healthy average cornea, i.e., 0.05 mm. The apex moved back when inserting two ICRS of different diameter, 200 and 500 μm , at 80% depth. The backward movement of the smaller ICRS is larger than the one of the bigger ICRS, i.e., $\delta_1 = -0.12$ and $\delta_2 = -0.03$ mm respectively (see cases 1 and 2 in Figure 3.7.e). Results previously reported⁴⁶ support the behaviour of the numerical model after the insertion of ICRS. It is worth to note that, when inserting the 200 μm ICRS at 50% depth, the apex moves forward instead of backwards with $\delta_3 = 0.12$ mm (see Case 3 in Figure 3.7.d–e).

When the ring is placed at 80% depth, i.e., the recommended insertion depth in therapeutic treatments, the corneal stroma mostly works in a (heterogeneous) biaxial stress state that does not vastly differ from the physiological stress state of the cornea solely subjected to the eyeball's intraocular pressure⁴⁷ (see in Figure 3.8.a). However, when the ring is placed at 50% depth, the cornea is working in a mixed stress state where the anterior stroma is compressed and the posterior stroma is in tension (see in Figure 3.8.b). The stresses in the cone also outline the inversion of the stress field depending on the sDI. The anterior stroma bears more load whereas the posterior stroma unloads when the ring is placed to the clinical depth, and viceversa when it is placed at 50% depth (see C_1 and C_3 in Figures 3.8.c–d). This inversion in the mechanical behaviour of the cornea leads to a change in the corneal surface and kinematics that could

⁴⁶ Kahn and Shiakolas 2016, Kling and Marcos 2013, Lago et al. 2015

⁴⁷ Ariza-Gracia et al. 2016

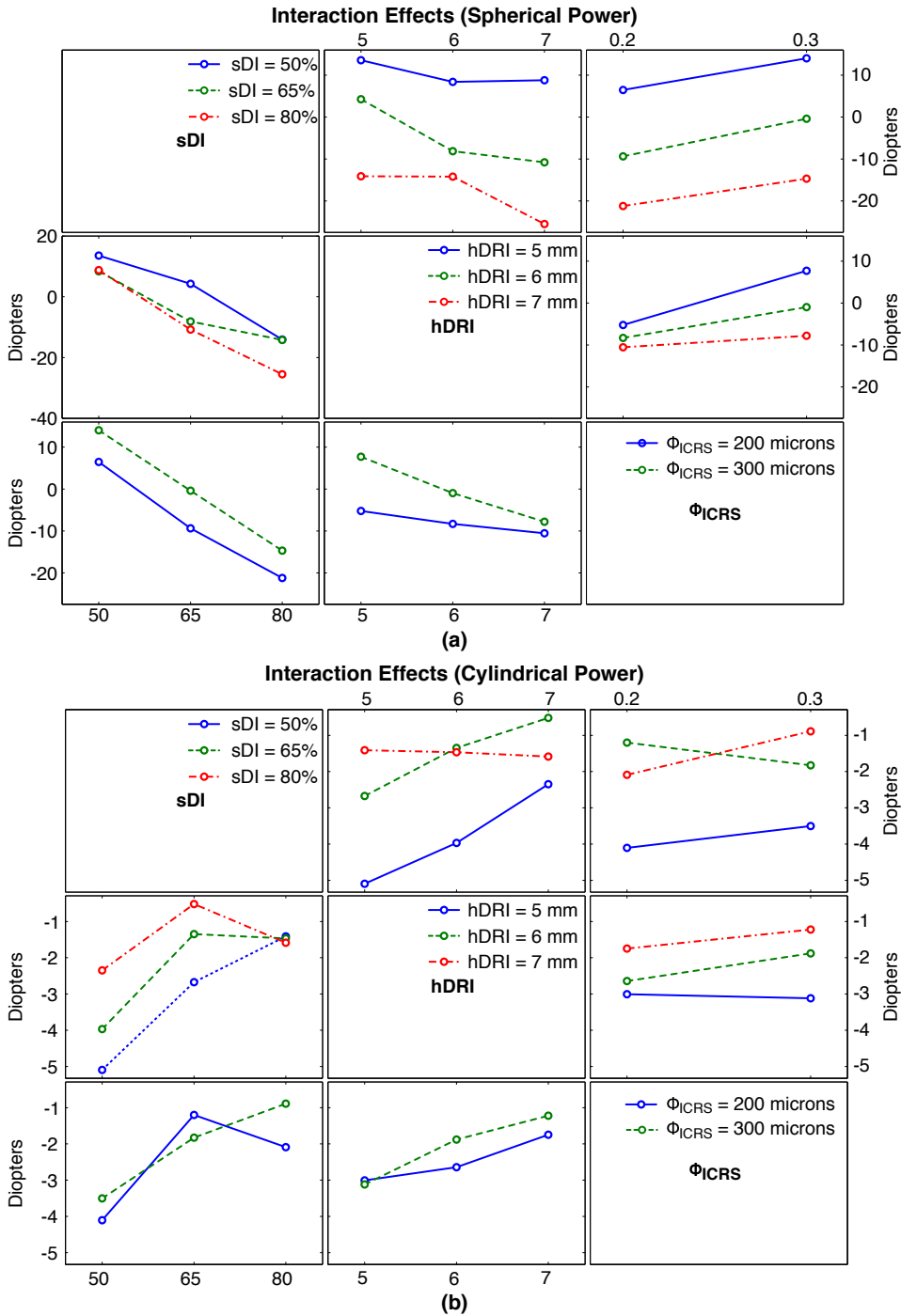


Figure 3.6: Parametric analysis (2): Interaction of the variables under analysis in the spherical (a) and cylindrical (b) powers. Row values are hold constant while column values present 3 levels of variation. *Note:* diameter of 500 microns is an outlier and was removed from the plots for the sake of clarity.

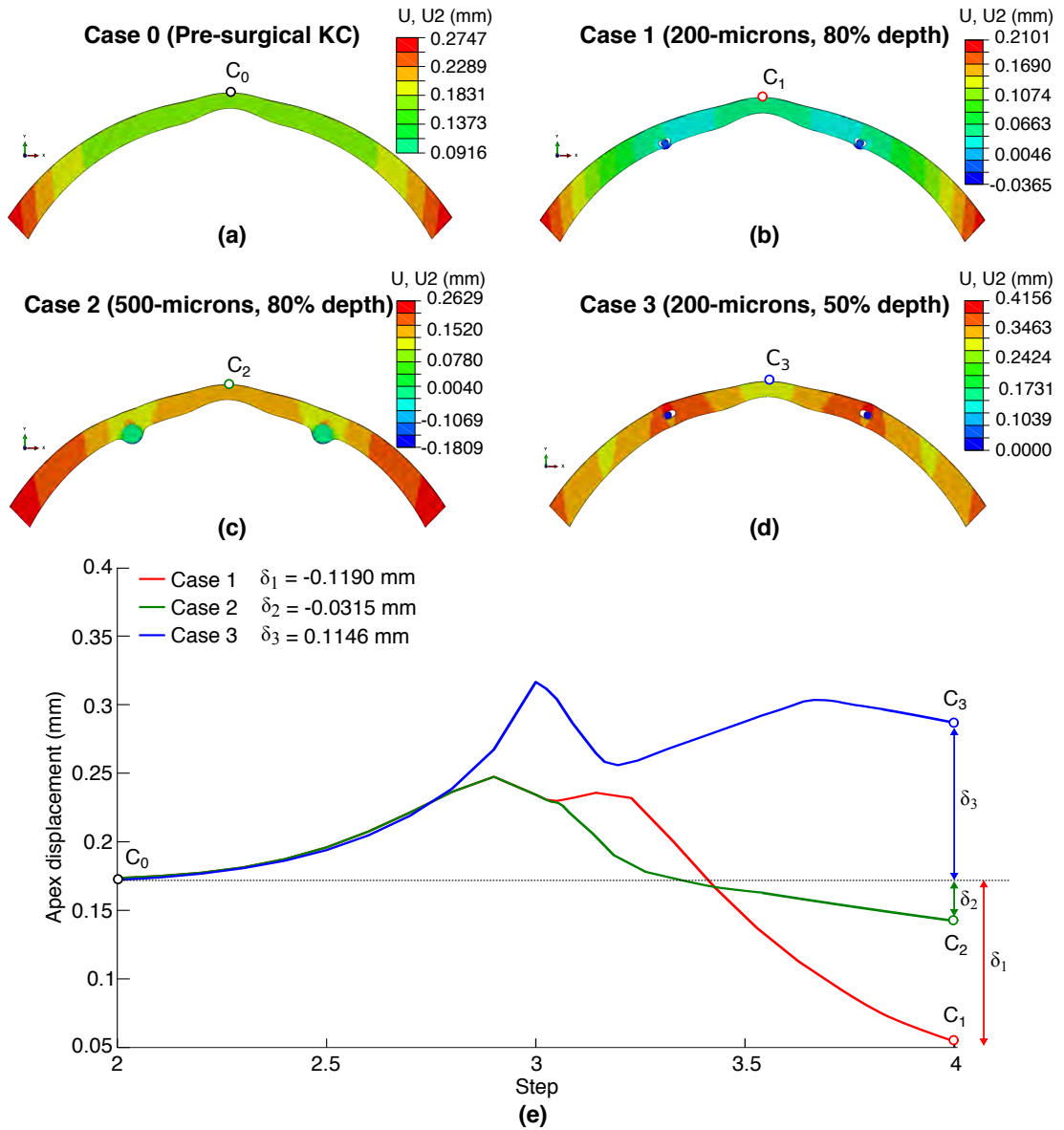


Figure 3.7: Kinematics of the KC cornea: (a–d) Transverse section of the vertical displacement field of the cornea in four different cases. Case 0 is the pre-surgical configuration, Case 1 is the equilibrium configuration after the insertion of 200 μm rings at 80% depth, Case 2 is the equilibrium configuration after the insertion of 500 μm rings at 80% depth, and Case 3 is the equilibrium configuration after the insertion of 200 μm rings at 50% depth; (e) Displacement of the apex during the simulation procedure. Due to the pre-stress of the cornea the apex raised to 0.17 mm. After the insertion of the rings, the apex moved backward (Case 1 and 2) or forward (Case 3) a δ_i , decreasing or increasing the axial length of the eye. The displacement of the corneal apex for Case 1 is also reported in the video provided as supplementary material (lower left panel).

explain the differences observed in the transition from 65% to 80% depth (see Figures 3.5–3.8).

However, this hypothesis cannot be supported entirely by experimental facts⁴⁸ as rings placed at 50% are usually rejected by the cornea. When an ICRS is inserted at 50% depth (see in Figure 3.8.a), the tissue surrounding it is abnormally tense resulting in a higher stretch of the corneal stroma. The positive tension in the posterior stroma and close to the endothelium is causing the tissue to push the ICRS up to the epithelium, whereas the positive tension in the anterior stroma is causing the tissue to excessively stretch in the surroundings of the surgery, i.e., the hole through where ICRS are inserted. On the contrary, tensions in the anterior stroma do not appear when the ICRS is placed at 80% depth (see in Figure 3.8.b). In this case, the ICRS is equilibrated and fastened by tensions in the posterior stroma and intraocular pressure, whereas the fibrous weak tissue of the scar in the epithelium does not support an excessive load bearing. We hypothesise that this mechanical behaviour close to the scar is promoting, among other factors, the extrusion of the ICRS.

The insertion of ICRS will also cause the corneal optics to worsen (see in Tables 3.1, 3.2, and Figure 3.9). Any ICRS generates different optical aberrations: primary, secondary, and tertiary spherical aberrations (Z_2^0 , Z_4^0 , Z_6^0) and first and second order astigmatism (Z_2^2 , Z_4^2), which are low order aberrations (LOA), and high order aberrations (HOA: Z_4^4 , Z_6^4 , Z_6^6). Optical powers and low order aberration values are shown in Table 3.1 and high order aberration values in Table 3.2. In particular, the 500 μm ICRS generates the larger aberrations and affects all Zernike coefficients (see Case 2 in figure 3.9). The 200 micron ICRS at 50% depth is generating larger high order aberrations, and affecting less to the spherical power (related to Z_2^0). On the contrary, placing it at 80% depth is barely affecting the spherical power while is inverting the sign and magnitude of the Zernike coefficient related to the cylindrical power (Z_2^2). This worsening of the

⁴⁸ Zare et al. 2007, Liu et al. 2015, Colin and Kiliç 2012

	Optical powers			LOA	
	Sph (D)	Cyl (D)	$\phi(^{\circ})$	Z_2^0 (Z_4)	Z_2^2 (Z_5)
Pre-H	-16.9	0.0	20.680	9.310	0.000
Pre-KC	-21.1	0.0	0.13	12.060	0.000
Case 1	-19.5	0.9	0.0	11.940	-0.392
Case 2	-18.5	-8.2	0.0	14.044	3.608
Case 3	-5.7	-3.0	0.0	93.476	1.034

Table 3.1: Optical Powers (Cylinder and Sphere) and Low Order Aberrations (LOA). Pre-surgical healthy (Pre-H) and KC (Pre-KC) configurations, and post-surgical KC configurations: Case 1 (200 μm , 80% Depth), Case 2 (500 μm , 80% Depth), and Case 3 (200 μm , 50% Depth).

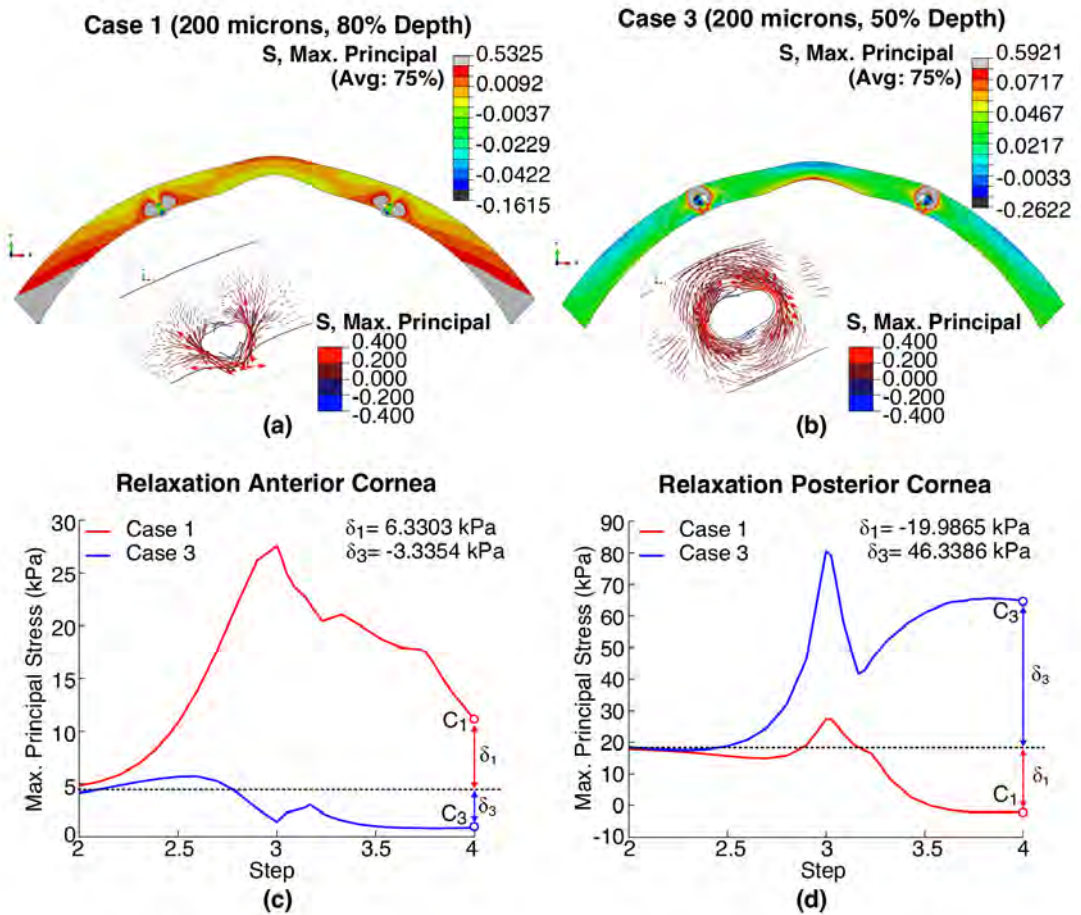


Figure 3.8: Mechanics of the KC cornea: (a) Stress field (MPa) in the stroma for Case 1 (200 μm and 80% depth) in which cornea presents an heterogeneous biaxial stress state. (a-zoom) Principal stresses (MPa) in the surroundings of the incision. Above the ICRS there is almost no stress while under the ring there is maximum traction. This state of stress will fasten the ring in the incision; (b) Stress field (MPa) in the stroma for Case 3 (200 μm and 50% depth) in which cornea presents a mixed stress state with compression in the anterior surface and tension in the posterior surface. (b-zoom) Principal stresses (MPa) in the surroundings of the incision. There is traction above and under the ring. This state of stress could tear up the fibrous tissue of the scar in the epithelium while pushing the ring out of the incision from the posterior stroma; (c) Relaxation of the cone in the anterior cornea. The cone is more tensioned in Case 1 while it is relaxed in Case 3; (d) Relaxation of the cone in the posterior cornea. The cone is more tensioned in Case 3 while it is relaxed in Case 1. The gradient of the maximum principal stress around the ICRS (upper right panel) and the temporal evolution of the maximum principal stress in the anterior and posterior cone (lower right panel) for Case 1 is also reported in the video provided as supplementary material.

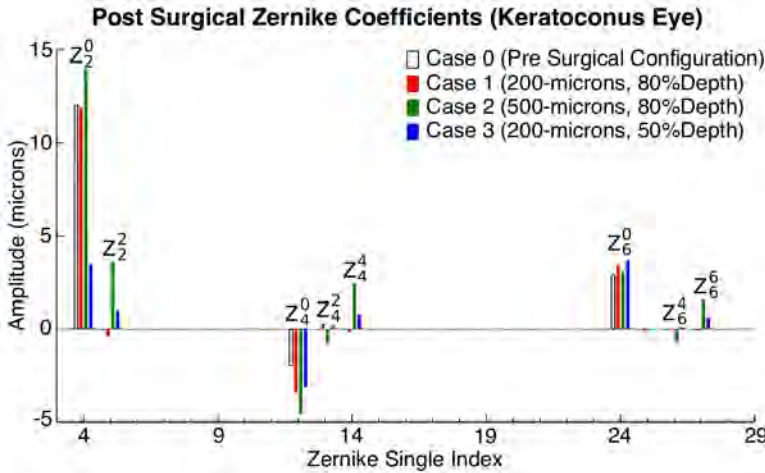


Figure 3.9: Zernike coefficients of the KC corneas. Pre-surgical configuration is depicted in black and white. The inclusion of the rings worsened the spherical aberrations (Z_2^0 , Z_4^0 , and Z_6^0) while introducing astigmatism (Z_2^2 , and Z_4^2) and high order aberrations (Z_4^4 , Z_6^4 , and Z_6^6).

visual acuity of the numerical models is also supported by different clinical studies⁴⁹ that showed an increment in astigmatism, related to the cylindrical power, although there is a slight improvement in defocus, related to the spherical power (see in Tables 3.1 and 3.2).

⁴⁹ Al-Tuwairqui et al. 2016, Fernández-Vega et al. 2016, Jadidi et al. 2015, Torquetti et al. 2016

	$Z_4^0 (Z_{12})$	$Z_4^2 (Z_{13})$	$Z_4^4 (Z_{14})$	$Z_6^0 (Z_{24})$	$Z_6^4 (Z_{26})$	$Z_6^6 (Z_{27})$	Table 3.2: High Order Aberrations (HOA). Pre-surgical healthy (Pre-H) and KC (Pre-KC) configurations, and post-surgical KC configurations: Case 1 (200 μm , 80% Depth), Case 2 (500 μm , 80% Depth), and Case 3 (200 μm , 50% Depth)
Pre-H	0.605	0.0	0.0	0.023	0.0	0.0	
Pre-KC	-1.950	0.0	0.0	2.897	0.0	0.0	
Case 1	-3.397	0.299	-0.175	3.404	0.076	-0.082	
Case 2	-4.584	-0.773	2.457	3.109	-0.708	1.584	
Case 3	-3.149	0.191	0.788	3.699	0.105	0.604	

4. Discussion

A novel template-based methodology for the simulation of the long-term effects of ICRS is presented. The main advantage of the methodology is that is suitable for a semi-automatic simulation of different clinical scenarios and allowing for setting up an optimisation procedure straightforwardly. Moreover, we go beyond the current state of the art⁵⁰ by solving key aspects such as avoiding the subtle weakening of accounting for a gap in the pre-surgical corneal configuration, and allowing for the free three-dimensional solid rigid motion of the ring after the insertion. Moreover,

⁵⁰ Kahn and Shiakolas 2016, Kling and Marcos 2013, Lago et al. 2015

⁵¹ Ariza-Gracia et al. 2017a

thanks to our opto-mechanical analysis,⁵¹ our methodology is capable of providing a comprehensive optical assessment of different post-surgical scenarios that improves the translation of *in-silico* models to clinic.

We assumed three main simplifications since our interest is in the computational methodology and we are not presenting a numerical framework for clinical application. Nevertheless, the methodology is designed to easily cope with further and more complex characteristics.

⁵² Ariza-Gracia et al. 2016

First, the inclusion of patient-specific geometries is the next natural step and can be done, based on our previous experience,⁵² by morphing the FE template into the patient-specific corneal topography provided by commercial topographers. In addition, we did not take into account epithelium redistribution as its mechanical contribution has been suggested to be minimum.⁵³

⁵³ Elsheikh et al. 2008

⁵⁴ Kahn and Shiakolas 2016, Kling and Marcos 2013, Lago et al. 2015

Second, as the previous works in the literature,⁵⁴ we use an isotropic hyperelastic material behaviour for the ocular tissues. Despite the sclera could be assumed as such far from the optical nerve insertion,⁵⁵ the cornea and the limbus are still anisotropic. In this line, an anisotropic hyperelastic material behaviour with two families of orthogonal collagen fibres in the cornea and one family of circumferential collagen fibres in the limbus will be included. This will modify the kinematics and the optics of the cornea, and the stress field in the stroma and, thus, it must be further investigated.

⁵⁵ Coudrillier et al. 2015

Third, we use circular-shaped ICRS with a diameter that is equivalent to the maximum dimensions of commercial triangular or hexagonal rings (see in Figure 3.2). In terms of methodology, we ensure that the incision is big enough to house any typology of ICRS. The next steps of our research will focus on including triangular and hexagonal rings and on solving the contact with the incisions.

A final remark regarding the limitations encompasses the semi-automatisation of the methodology. As it is a template-based approach, we are constrained by the number of FE templates available, which are discrete and do not allow for continuous inspection of the different parameters. In the future, we will fully automatise the procedure allowing to set a complete clinical scenario in a non-supervised process.

⁵⁶ Al-Tuwairqui et al. 2016, Fernández-Vega et al. 2016, Jadidi et al. 2015, Torquetti et al. 2016

The methodology generates outcomes that behave as expected based on clinical findings.⁵⁶ The 3^k full-factorial analysis outlined this physiological behaviour through different key findings (see in Figures 3.5 and 3.6). First, the sDI is the most influential parameter in the post-surgical visual acuity of the patient,⁵⁷ representing between a 50 and a 70% of the im-

⁵⁷ Kahn and Shiakolas 2016, Barbara et al. 2016

pact in the spherical (see in Figure 3.5.a) and cylindrical powers (see in Figure 3.5.b). Second, the farther the hDRI, the higher the impact on the spherical power but the lower in the cylindrical power.⁵⁸ Third, the ϕ_{ICRS} does not present a large variability when using 200 or 300 μm . Moreover, 500 μm rings should not be used in diameters lower than 7 mm as they are causing incredible aberrations.

The kinematic and optical behaviours are also in line with those reported in the literature⁵⁹ and support the physiological behaviour of the model and the methodology. In terms of kinematics, when the ICRS is inserted at 80% depth, i.e., the insertion depth used in clinic, there is a move backward of the corneal apex that changes the axial length of the eye and the curvature (see in Figure 3.7). Optically, the insertion of the ICRS seems to regularise the corneal surface as the spherical power decreases. However, it worsens the overall visual acuity of the patient and, in particular, astigmatism and high order aberrations.

Interestingly, there is a transition zone between 65 and 80% depth where the mechanical behaviour of the cornea completely changes. When the rings are inserted close to the anterior stroma, the cornea tends to slightly bend as the anterior surface is in compression and the posterior surface is in tension. However, when the rings are inserted close to the endothelium, the corneal stroma is still working in a (heterogeneous) biaxial stress state similar to the physiological stress state of the cornea.⁶⁰

As the evolution of KC is suggested to be stress-driven,⁶¹ we hypothesise that its progression could be differently affected depending on where it spatially develops. If the KC rises from the posterior surface and propagates towards the epithelium, it would be advisable to place the ICRS at 80% depth as it would relax the posterior cornea and stretch the anterior cornea. However, if the origin of the pathology is in close to the epithelium, it would be advisable to place a ring at 50%. However, rings placed at 50% depth presented corneal extrusion of the ICRS in clinic.⁶²

Thanks to our study of the mechanical influence of the stromal depth of insertion (sDI), we also hypothesise that corneal extrusion is related to the gradient of principal stresses in the surroundings of the incision (see in Figure 3.8). When the ICRS is placed at 50% depth, the positive stresses above the ring tend to tear up the tissue in the surroundings of the scar through where the ring was inserted. At the same time, the positive stresses under the ICRS tend to stretch the tissue and push the ring up. In combination, both behaviours could cause the fibrous tissue of the scar to

⁵⁸ Abdelmassih et al. 2017

⁵⁹ Kahn and Shiakolas 2016, Kling and Marcos 2013

⁶⁰ Ariza-Gracia et al. 2016

⁶¹ Zare et al. 2007, Colin et al. 2001, Rabinowitz 1998

⁶² Zare et al. 2007, Liu et al. 2015, Colin and Kiliç 2012

tear up and the corneal stroma to expel the ring. Although we are using an isotropic material and further research must be done, this is the first mechanics-based hypothesis that, to the best of our knowledge, explains the corneal extrusion and is supported by an *in-silico* study.

In conclusion, the methodology proposed is suitable for simulating the long-term mechanical and optical effects of ICRS insertion. Currently, we are investing further efforts in extending the methodology to cope with patient-specific geometries, to instruct material models with anisotropy, to use different commercial rings, and to achieve a fully automatic methodology with continuous inspection of the ICRS's parameters involved in the surgery.

Chapter 4

Displacement–based ICRS implantation¹

¹ J. Flecha-Lescún, P. Büchler, B. Calvo, and M. Á. Ariza-Gracia. **Modelling strategies for the simulation of corneal intrastromal ring surgeries.** *Ann. Biomed. Eng.*, (Under Preparation), a

The present chapter aims at explaining a novel methodology to simulate the implantation of commercial intrastromal rings. The simulation of stent's deployment in balloon–angioplasty inspired this novel methodology.

Chapter Contents

1. Introduction	122
2. Material and methods	124
<i>Corneal geometry</i>	124
<i>Corneal mechanics</i>	126
<i>Implants: geometry and material model</i>	127
<i>Expansion tool: geometry and material model</i>	128
<i>Simulation steps for ring implantation</i>	128
<i>Optical and mechanical analysis</i>	129
<i>Case studies</i>	131
3. Results	131
<i>Optical impact of different modelling strategies</i>	131
<i>Mechanical impact of different modelling strategies</i>	133
4. Discussion	137

1. Introduction

The surgical procedure for the implantation of intrastromal corneal ring segments (ICRS), or complete ring segments (ICR), is considered as an additive refractive surgery which primarily attempts to regularize pathological corneas with keratoconus (KC)² or post-LASIK ectasia.³ Not only that, but several clinical studies report the use of intrastromal rings to stabilise the progression of keratoconus.⁴ In addition, these implants can be used to correct corneal disorders such as high myopia when patients cannot be treated using a laser refractive interventions,⁵ astigmatism,⁶ or marginal pellucid degeneration.⁷

There are two groups of commercially available intrastromal rings. First, intrastromal complete rings (ICR) which are 360-degree continuous implants. Within this group, clinicians can find Intacs SK (Additional Technology, Inc. USA) and the MyoRing (Dioptex, GmbH.), with elliptical and proprietary (combination of a parabola and a circumference) cross-sections, respectively. Second, intrastromal corneal ring segments (ICRS) which account for different angles and that can be placed either alone or in pairs, depending on the arc-length of the implant and the type of pathology. Many different commercial options with two different cross-sections are available: triangular (Keraring, Mediaphacos, BeloHorizonte, Brazil; Ferrara, AJL Ophthalmic Ltd.) or hexagonal (Intacs, Additional Technology, Inc.). Regardless the group, there are several implant diameters (optical zones of implantation) and cross-section thicknesses available depending on the degree of corneal ectasia and the amount of refractive correction to achieve (see the Section 4.2 of Chapter 2).

Choosing the ring usually drives how the surgical procedure will be performed. When ICRS are chosen, segments are lodged in the stroma within a canal (or tunnel). When ICR are chosen, implants are lodged in a dissection stromal plane (pocket). In both situations, the dissection planes (or tunnels) can be either manually performed using a micrometer diamond knife or the PocketMaker microkeratome⁸ or created using a femtosecond laser (see the surgical techniques in Section 4.1 of Chapter 2).

A well calibrated *in-silico* model can really help to clinicians to better plan the surgery of the rings into the corneal stroma. Currently, the surgery plans are based on empirical models which depended on commercial manufactures, and rely on the surgeons experience.

Until now, different computational simulations have been used in an

² Rabinowitz 1998, Daxer et al. 2016

³ Yildirim et al. 2014

⁴ Kang et al. 2019, Hosny et al. 2015, Alió et al. 2005, Daxer 2008

⁵ Rattan 2018, Daxer 2017

⁶ Jadidi et al. 2015

⁷ Akaishi et al. 2004

⁸ Daxer 2008

attempt of predicting the post-surgical opto-mechanical outcomes of this refractive surgery. The summarised characteristics of those simulations⁹ are: corneas were mostly simulated as an axisymmetric solid, except for Lago *et al.*¹⁰ and Flecha-Lescun *et al.*,¹¹ soft tissues were considered to behave as isotropic hyperelastic materials, such as Neo-Hookean, Mooney-Rivlin or Yeoh models, always neglecting anisotropic material models; implant's cross-sections were not commercial; contact between the implant and the corneal tissue was considered as frictionless; and pre-stretch of the corneal tissue due to the eyeball's intraocular pressure was disregarded. None of the studies presented all the characteristics.

Eventually, there is not a clear, easy-to-follow methodology for the simulation of the intrastromal ring insertion surgery and all the studies presented different pitfalls. Kling and Marcos¹² presented a two-dimensional incrustation method in which the ring was press-fitted inside the dissection plane whose main pitfall was lacking of corneal pre-stretch. Lago *et al.*¹³ presented a three-dimensional methodology in which the nodes of the dissection plane were forced to move to create the shape of the implant cross-section. However, the main pitfall of this methodology was to not consider the implant as a foreign three-dimensional body inside the corneal stroma, neglecting the post-surgical mechanical accommodation of the implant within the stroma and, thus, the post-surgical mechanical equilibrium of the cornea. Finally, Flecha-Lescun *et al.*¹⁴ presented a three-dimensional pressure-based methodology (Chapter 3) to create a hole in the corneal stroma to lodge the rings. The main pitfalls of this methodology were related to the convergence of the method, the impossibility of completely removing the pressure boundary condition, and the use of non-commercial circular cross-sections. More information about the most relevant *in-silico* studies are summarised in Section 5.5 of Chapter 2.

The present work arises from the need to simulate the introduction of commercial rings in the corneal stroma and to improve the convergence problems that appeared in the simulations of Chapter 3. Therefore, the aim of this chapter is to establish a generic methodology for the simulation of any intrastromal ring implantation, which is inspired by the approach used to simulate endovascular stents in balloon angioplasty.¹⁵ Using the proposed methodology, we will first validate the models using the post-surgical refractive outcomes at a population level and, then, we will study what are the minimum requirements needed to simulate this refractive surgery. In particular, we will focus on determining when to use two-dimensional

⁹ Ebrahimian *et al.* 2019, Kling and Marcos 2013, Kahn and Shidakolas 2016, Lago *et al.* 2015, Flecha-Lescun *et al.* 2018

¹⁰ Lago *et al.* 2015

¹¹ Flecha-Lescun *et al.* 2018

¹² Kling and Marcos 2013

¹³ Lago *et al.* 2015

¹⁴ Flecha-Lescun *et al.* 2018

¹⁵ Gökgöl *et al.* 2017

axisymmetric or three-dimensional models, whether accounting for the anisotropy of the tissue is needed for a sufficient opto-mechanical simulation, and whether accounting for the friction between the implant and the stroma modifies post-surgical refractive outcomes.

2. Material and methods

2.1. Corneal geometry

For the sake of comparison, the same cornea was used to set up the methodology and to compare across models. The corneal topology corresponds to a virtual healthy patient with high myopia (>8D) and typical values for healthy corneas: a central corneal thickness (CCT) of 550 μm ,¹⁶ average corneal keratometry (K_{mean}) of 45 D, an axial length (AL) of 26.5 mm,¹⁷ a scotopic pupil size of 4 mm and a refraction error (spherical equivalent, SE) of -9.4 D.¹⁸

For the two-dimensional axisymmetric models, the cross-section of the cornea was modelled as a spherical dome with a symmetry of revolution around the optical axis (see in Figure 4.1.a–b). This geometric description was enough to capture the average curvature at the cornea centre (K_{mean}) and the overall defocus of the optical system (Zernike coefficient, Z_2^0 , and Spherical Equivalent, SE). For the three-dimensional models, the spherical cross-section of the cornea was revolved along the Y-axis to create a three-dimensional spherical cornea.

Surgical features were introduced in the two-dimensional corneal cross-section depending on the implants: for ICRS a femtosecond laser tunnel of 500 μm in length was created, while for ICR a full intrastromal 8-mm pocket cutting through the stroma was created (see in Figure 4.1.a–b). Dissection planes were located at a clinical recommendation depth¹⁹ corresponding to the 75% of the corneal stroma thickness where the implants are inserted. The thickness of the dissection planes was 5 μm , the size of the bubble created by the vaporization of the tissue using the femtosecond laser.²⁰

Corneal meshes for the different surgical scenarios were automatically generated using a python scripting (see Appendix III). Axisymmetric models were built based on the anterior and posterior radius of curvature and the central corneal thickness. The axisymmetric models were meshed with $\approx 9,000$ 4-node hybrid bilinear axisymmetric quadrilateral elements with reduced integration (CAX4RH) and had $\approx 18,000$ degrees of freedom (d.o.f.), depending on the automatic meshing (see Figure 4.1.a–b). The

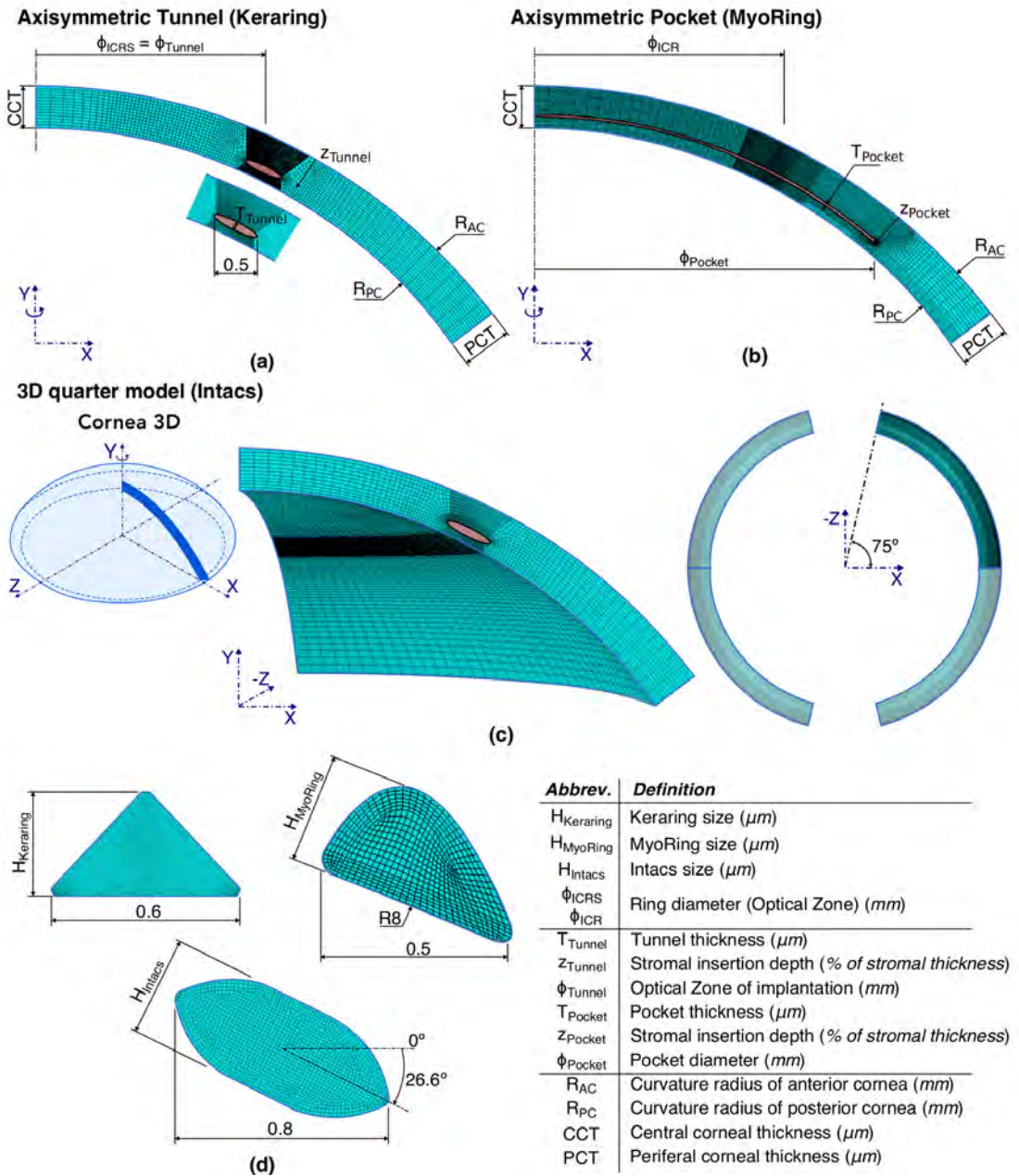
¹⁶ Sorkin et al. 2019

¹⁷ Sorkin et al. 2019

¹⁸ Rattan 2018

¹⁹ Hashemi et al. 2013c

²⁰ Lubatschowski et al. 2000



Abbrev.	Definition
$H_{Keraring}$	Keraring size (μm)
$H_{MyoRing}$	MyoRing size (μm)
H_{Intacs}	Intacs size (μm)
ϕ_{ICRS}	Ring diameter (Optical Zone) (mm)
ϕ_{ICR}	Ring diameter (Optical Zone) (mm)
T_{Tunnel}	Tunnel thickness (μm)
Z_{Tunnel}	Stromal insertion depth (% of stromal thickness)
ϕ_{Tunnel}	Optical Zone of implantation (mm)
T_{Pocket}	Pocket thickness (μm)
Z_{Pocket}	Stromal insertion depth (% of stromal thickness)
ϕ_{Pocket}	Pocket diameter (mm)
R_{AC}	Curvature radius of anterior cornea (mm)
R_{PC}	Curvature radius of posterior cornea (mm)
CCT	Central corneal thickness (μm)
PCT	Periferal corneal thickness (μm)

Figure 4.1: Geometries and meshes of the models. (a) Axisymmetric cornea with surgery as a tunnel. This geometry is used to simulate the Keraring–355° (almost complete ring) and Intacs in 2D; (b) Axisymmetric cornea with surgery as a pocket. This geometry is used to simulate the MyoRing; (c) 3D Cornea model, where 2 Intacs segments of 150° were implanted. Due to symmetry, only a quarter of cornea is necessary, saving computational and resources time; (d) Cross–section ring implanted; left–top Keraring; right–top, MyoRing and bottom, Intacs.

three-dimensional (3D) quarter models of the cornea (Figure 4.1.c) were meshed with $\approx 115,000$ 8-node linear hybrid hexahedral elements (C3D8H) and had $\approx 370,000$ d.o.f. However, the 3D-meshes were built with a semi-automatic process controlled by the user, revolving the axisymmetric models taking as reference to the optical axis (axis Y in Figure 4.1.c).

Two boundary conditions were considered. First, the physiological intraocular pressure (IOP) was set as a distributed pressure of 2 kPa (15 mmHg)²¹ in the posterior surface. Second, an encastred boundary condition (no displacement) at the interface between the cornea and the limbus was considered. The physiological pre-stretch of the cornea was accounted for following a previously reported iterative procedure.²² Finally, the corresponding symmetry conditions ($x = 0$ and $z = 0$ planes in Figure 4.1.c) were accounted for in the three-dimensional models.

2.2. Corneal mechanics

A hyperelastic isotropic strain-energy function (SEF) was used to simulate the non-linear mechanical response of the corneal tissue in the two-dimensional axisymmetric models. For this particular case, we used a previously validated Yeoh strain-energy function (ψ_Y) (see in Flecha-Lescun *et al*²³ and in Equation 2.2, Section 2.3.4, Chapter 2).

Although cornea is highly anisotropic, the orthogonal distribution of collagen fibres cannot be included in two-dimensional axisymmetric models.²⁴ Despite this limitation, Yeoh's strain energy function presented a non-linear stiffening behaviour for increasing deformation similar to other fibre-reinforced strain energy functions (see in Figure 4.2).

Moreover, the few small regions in the models that were in compression did not present a high compressive deformation and, thus, the strain energy function did not suddenly stiffen in compression and behaved mostly linearly. The constants of the Yeoh's strain energy were calibrated so as to the average keratometry (K_{mean}) was 45D: $C_{10} = 35.53$ kPa, $C_{20} = 3.22$ kPa, $C_{30} = 1.87$ kPa and $D_k = 10^{-5}$ kPa, corresponding on a tangent modulus at corneal pre-stretch of 210 kPa.²⁵

To study the impact of accounting for the anisotropy of the corneal tissue we introduced in a modified version of the model proposed by Gasser-Holzapfel-Ogden²⁶ developed by Ariza-Gracia *et. al*²⁷, where the Neo-Hookean term has been replaced by an exponential term (see the Equation 2.3, Section 2.3.4, Chapter 2).

The material parameters for the anisotropic model were estimated us-

²¹ Cunningham and Barry 1986

²² Ariza-Gracia *et al.* 2016

²³ Flecha-Lescun[#] *et al.* 2020

²⁴ Pandolfi and Holzapfel 2008, Pandolfi and Vasta 2012

²⁵ Flecha-Lescun[#] *et al.* 2020

²⁶ Gasser *et al.* 2006

²⁷ Ariza-Gracia *et al.* 2017b

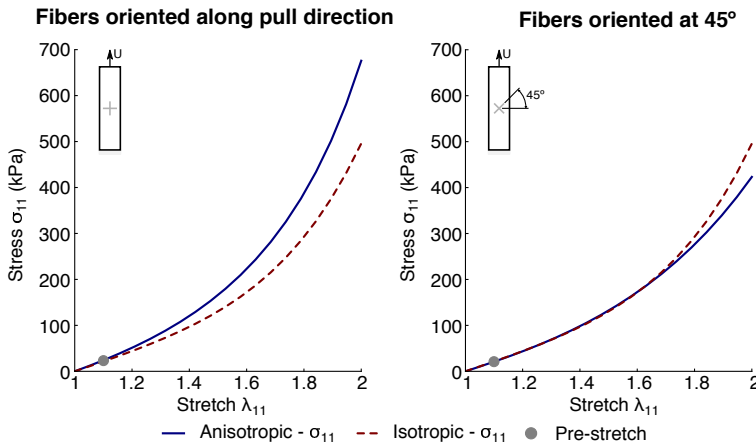


Figure 4.2: Behaviour of corneal material in uniaxial test. Left Panel, fibres oriented along pull direction; Right panel, fibres arrangements at 45° . Blue line represent the stress of anisotropic model and the dashed red line represent the stress of isotropic model.

ing an optimisation procedure. First, using the previously calibrated Yeoh model, the stress–stretch relationship for a uniaxial tensile test was calculated. Afterwards, an iterative procedure was set up for the anisotropic material model in order to approximate the isotropic stress–stretch relationship. Parameter’s estimation resulted in $D_1 = 194.59$ kPa, $D_2 = 0.17237$, $k_1 = 10.116$ kPa, $k_2 = 0.0834$ kPa and $\kappa = 0.05$.

2.3. Implants: geometry and material model

Three different geometries were used in this study: Keraring (Mediaphacos, BeloHorizonte, Brazil), MyoRing (Dioptex, GmbH.), and Intacs (Additional Technology, Inc.). In particular, their cross–sections are triangular, proprietary (a combination of circumference and parabola), and hexagonal (see Figure 4.1.d), respectively. Details on the ring models, i.e geometry and mesh, can be found in Table 4.1.

The mechanical behaviour of the implants was considered as linear elastic with a Young’s modulus of 3,300 MPa and Poisson’s ratio of 0.4 (data from Addition Technology, Inc., Sunnyvale, CA, USA).

No boundary conditions are directly specified on implants, being free to move inside the surgery. The contact between the corneal stroma and the different ring typologies was considered as a hard contact, with a friction of 0.1.²⁸ However, it was examined how the optical change (δ SE) would evolve when the friction coefficient (μ) varied between frictionless ($\mu = 0$) and $\mu = 1$ for the MyoRing of 6 mm in diameter and 200 μ m in thickness.

²⁸ Flecha-Lescúin et al. 2018

Typology	Cross-Section	Arc Length [°]	ϕ [mm]	H [μ m]	Elements	d.o.f	
Keraring	Triangular	355	5	280	CAX4R	1,884	3,972
			5	300	CAX4R	2,196	4,604
MyoRing	Proprietary	360	5	280	CAX4R	644	1,368
			5	300	CAX4R	695	1,470
			6	200	CAX4R	622	1,320
			6	210	C3D8	37,200	121,914
Intacs	Hexagonal	150	5	300	CAX4R	1,937	4,024
			6	210	CAX4R	1,511	3,172

Table 4.1: Geometry and mesh features of the different ring typologies. Depending on the ring typology, ϕ would be ϕ_{ICRS} or ϕ_{ICR} , and H would be $H_{Keraring}$, $H_{MyoRing}$, or H_{Intacs} . The proprietary cross-section of the MyoRing is a combination of a parabola and a circumference.

²⁹ Gökçöl et al. 2017

2.4. Expansion tool: geometry and material model

The proposed methodology includes an additional component solely used for simulation-purposes: a rigid expansion tool used to open a hole in the corneal stroma and allow for the insertion of the implant. This element for the simulation was inspired by the approach used by Gökçöl et al.²⁹ for the simulation of a stent implantation in balloon-angioplasty. In particular, an elliptical expansion tool was automatically built, with small enough dimensions so as to fit within the dissection plane (both tunnel and pocket), and considered as a solid rigid.

Two-dimensional axisymmetric models were meshed with 4-node bi-linear axisymmetric quadrilateral elements with reduced integration and consisted of 100 elements and 200 d.o.f. Three-dimensional models were built by revolving two-dimensional models around the optical axis and were meshed with 3,600 linear hexahedral elements (C3D8) and 22,200 d.o.f.

2.5. Simulation steps for ring implantation

The whole simulation procedure encompasses four main stages. All stages were simulated in Abaqus 6.13–5 (Dassault Systèmes Simulia Corporation).

First, the corneal tissue is pre-stretched to its physiological intraocular pressure using an iterative algorithm previously developed (see Figure 4.3–1).³⁰ In short, a smaller reference configuration is determined such that, when pressurised to the a physiological IOP (15 mmHg or 2 kPa), it recovers the original shape of the cornea and includes the tissue pre-stretch (see

³⁰ Ariza-Gracia et al. 2016

Figure 4.3–2).

Second, after the corneal pre–stretch, the creation of the dissection planes is simulated by using **Model Change* in order to remove the elements belonging to either the pocket (ICR) or the tunnel (ICRS). At the same time, the expansion tool is included within the gap created in the stroma and the contact (frictionless and hard contact) between both is activated. An intermediate mechanical equilibrium is reached due to the mechanical instability create by the gap (see Figure 4.3–3).

Third, in order to create a gap in the corneal stroma, the expansion tool is augmented by applying a displacement vector field (see Figure 4.3, detail). The displacement field (\bar{u}_j) is calculated for each individual commercial ring in such a way that, after deployment, the implant fits inside the stroma. In particular, \bar{u}_j is calculated as the difference between the coordinates of the micro–expansion tool introduced in step 2 (\bar{R}_j), and the final coordinates of the expansion tool which would house the desired commercial implant (\bar{T}_j).

Fourth, the implant is lodged inside the gap using **Model Change* and the contact between implant and tissue is activated. After that, the displacement filed is slowly removed ($-\bar{u}_j$) in order to establish a smooth contact between the stroma and the implant (hard contact with and without friction). Eventually, the post–surgical mechanical equilibrium is achieved.

2.6. Optical and mechanical analysis

To analyse corneal optics, the coordinates of the anterior and posterior corneal nodes were extracted using a Python³¹ script for both the physiological state and the post–surgical mechanical equilibrium. Two optical metrics were used: the average keratometry (K_{mean}) and the spherical equivalent (SE).

K_{mean} ³² was calculated by considering only the refraction of the central part of the anterior cornea (see Equation 4.1)

$$K_{mean}(D) = \frac{n - 1}{R} \quad (4.1)$$

where $n = 1.3375$ is the keratometric index of the cornea, R is the radius of curvature (in meters) of the sphere that best fits of the anterior corneal surface in a diameter of 3 mm around its centre.

The wavefront error of the optical system was calculated using an in–house ray tracing algorithm³³ and fitted using Zernike polynomials³⁴ to calculate the SE,³⁵

³¹ van Rossum and Drake 2009

³² Savini et al. 2017

³³ Ariza-Gracia et al. 2017a

³⁴ Lakshminarayanan and Fleck 2011

³⁵ Jaskulski et al. 2017

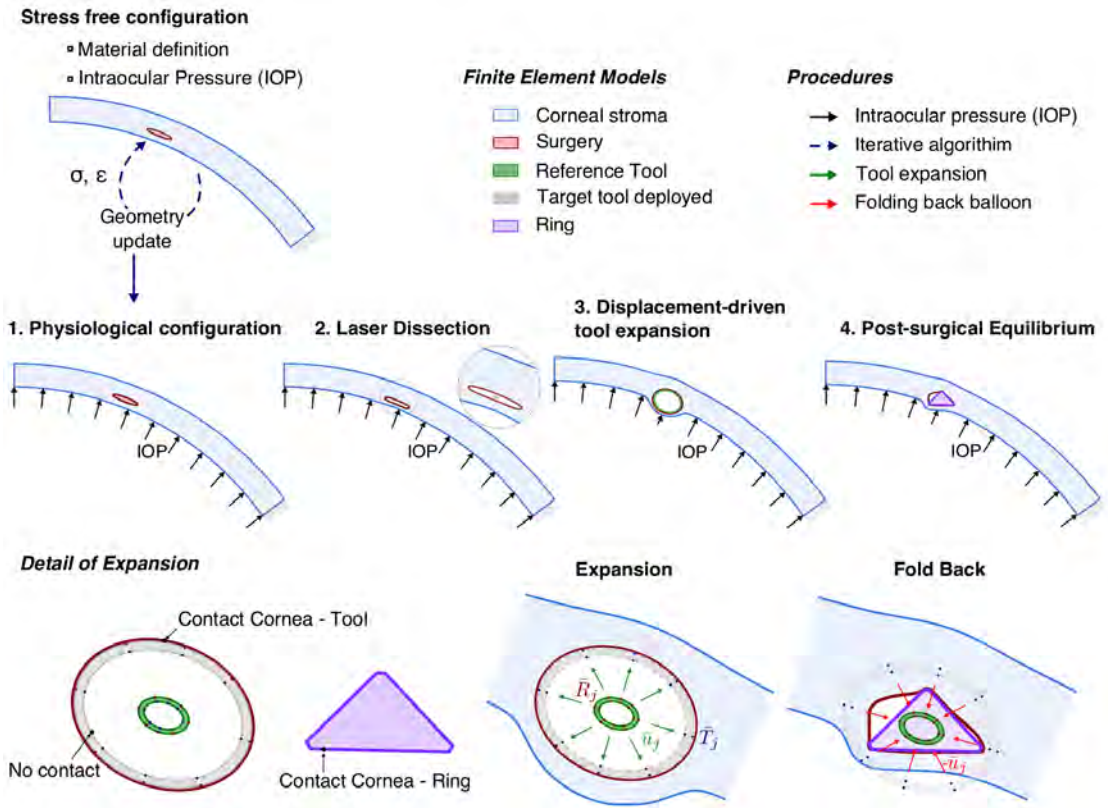


Figure 4.3: Computational surgical procedure with tunnel. The initial state of the cornea free of stress σ is reached by an iterative algorithm; **1.** the cornea is pressurized to physiological state; **2.** the surgery is created by means the Abaqus tool *Model Change* and the expansion tool is introduced in it; **3.** the expansion tool is increased by applying a displacement vector field in order to create the enough gap to introduce the implant; **4.** the implant is introduced within the gap and the contacts involved are activated. Finally the displacement field is slowly removed and the contact between the implant and corneal tissue is established and the post-surgical mechanical equilibrium is reached.

$$SE(D) = \frac{-4\sqrt{3} \cdot Z_2^0}{r_0^2} \quad (4.2)$$

where Z_2^0 (μm) is the Zernike coefficient corresponding to the defocus and r_0 (mm) is the radius of the exit pupil of the optical system.

To analyse mechanics, the Cauchy stress tensor and principal stresses were extracted at the centroid of each element using the same Python³⁶ script for both the physiological state and the post-surgical mechanical equilibrium. Stress analysis was mostly focused at the corneal centre in which main human refraction occurs.

³⁶ van Rossum and Drake 2009

2.7. Case studies

All the following *in-silico* cases studied have been validated with the results of the different clinical cases according to the type of ring.

The first study aims to compare both optical and mechanical results between three-dimensional (3D) anisotropic and isotropic behaviour of the cornea. In addition a comparison between 3D model and 2D-axisymmetric models is added to discern whether it is necessary to increase the complexity of the model. The hexagonal cross-section ring of 6 mm in diameter, 210 μm in thickness, and 150° was the ring chosen to make the study.

The goal of the second study is to see the effect of the different topologies of the ring within corneal stroma. The triangular, hexagonal and MyoRing with the same dimensions, i.e. 300 μm in thickness and 6 mm in diameter are compared. In this case, the differences between both surgical techniques arise.

Finally, the purpose of the third study aims to see what is the effect of the friction between the implant and the corneal tissue. The model chosen to evaluate the friction was the MyoRing of 200 μm in thickness and 6 mm in diameter.

3. Results

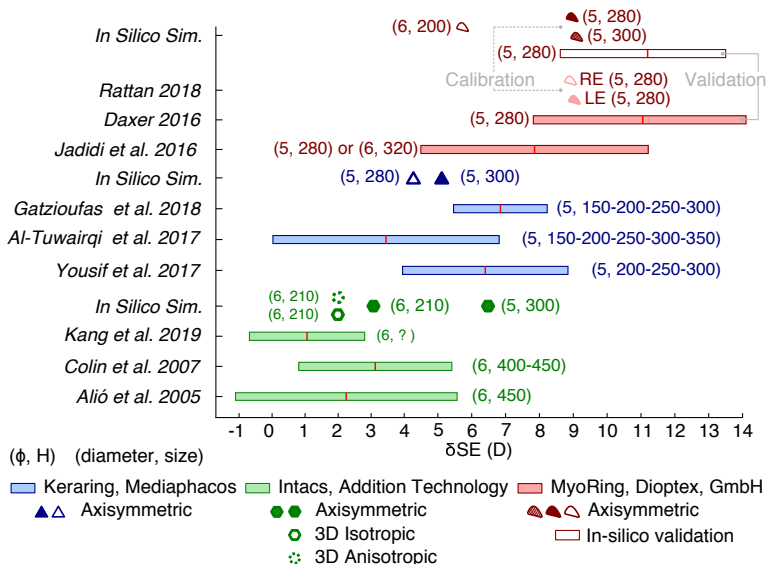
3.1. Optical impact of different modelling strategies

In-silico models were calibrated for MyoRing (ICR) using clinical data for two eyes (see Myoring 5 mm-280 μm in Figure 4.4, Chapters 5 and 6),³⁷ and validated using data for patients with high myopia at a population level (see empty *in-silico* boxplot and filled Daxer 2016 boxplot in Figure 4.4).³⁸

³⁷ Rattan 2018, Flecha-Lescúñ[#] et al. 2020

³⁸ Daxer 2017

Figure 4.4: Validation of the *in-silico* results with clinical results. In red, the validation with the results of the MyoRing is shown; in blue, the validation with the results corresponding to the Keraring are shown; and in green, the validation of the results of the Intacs rings is shown.



³⁹ Daxer 2017, Jadidi et al. 2016, Rattan 2018
⁴⁰ Gatzioufas et al. 2018, Al-Tuwairqi et al. 2016, Yousif and Said 2018
⁴¹ Kang et al. 2019, Colin and Malet 2007, Alió et al. 2005

All predictions for realistic *in-silico* models fell inside the clinical range for MyoRing,³⁹ Keraring,⁴⁰ and Intacs.⁴¹

From a simulation standpoint, two-dimensional axisymmetric models were valid for MyoRing and Keraring as they both predicted a change in spherical equivalent (SE) within the clinical range reported. Intacs presented a great over correction in SE when using axisymmetric models, falling out of the clinical range. In terms of material model, both isotropic and anisotropic hyperelastic models presented no optical difference (see Intacs in green in Figure 4.4).

From a clinical standpoint, MyoRing provided the maximum change in SE, followed by Keraring and Intacs, respectively. In fact, Keraring provides less correction than MyoRing for roughly the same amount of added volume, which suggests that the surgical technique (tunnel vs pocket) might be differential. For different cross-section shapes but the same conditions (300 μm cross-section size and continuous rings), a hexagonal cross-section introduces more material volume than a triangular cross-section and, thus, increases in 1.5 D the refractive correction.

3.2. Mechanical impact of different modelling strategies

From a mechanical point of view, the main difference between axisymmetric and three-dimensional models, or between isotropic and anisotropic models, was related to the behaviour of the shear stresses. On the one hand, using an isotropic axisymmetric model instead of a three-dimensional isotropic model resulted in 10% increment in the circumferential stresses at the posterior stroma and almost a 30% in the out-of-plane shear. On the other hand, using an isotropic material law resulted in virtually no difference in normal stresses whereas shear stress was mostly existent in the fibres plane (fibres at 90° , see τ_{xz} in Figure 4.5). Nevertheless, after corneal pre-stretch, all the models presented the same level of stretch (see in black in Figure 4.2).

From a clinical point of view, using a stromal pocket as a dissection plane for the corneal stroma introduces a discontinuity in shear stress which results in a more compliant cornea (see τ_{xy} in red, Figure 4.6). Not only that, but the pocketing procedure relaxes the stresses in the anterior stroma (see σ_{xx} and σ_{zz} in red, Figure 4.6) instead of increasing the level of stress through the entire stroma as implants in tunnels do. When comparing implants in tunnels, Intacs presented a higher increment in stress than Kerarings, mostly related to the 35% additional volume introduced by hexagonal sections for the same cross-section size.

An increment in friction of only 0.1 increased the stress distribution in the cornea (see top-left panel in Figure 4.7). This change in stress distribution and, therefore, mechanical equilibrium introduced an error of more than 1 D in the optical predictions of the surgical model (see top-right panel in Figure 4.7). When the friction increased up to $\mu = 0.3$ (friction between contact lens and cornea),⁴² the prediction error increased up to 2.5 D. Beyond a $\mu = 0.4$ the prediction error stabilised around 3 D (change below 5%).

A discontinuity in the stress distribution can be observed at the interface of the dissection plane (pocket) as the transmission of shear stresses between the anterior and posterior regions of the corneal stroma are limited. Accounting for the friction between the implant and the stroma does not affect the distribution of shear stress or radial forces (Y-axis). However, it modifies up to a 10% the in-plane stresses behaviour (see bottom panel in Figure 4.7).

⁴² Roba et al. 2011

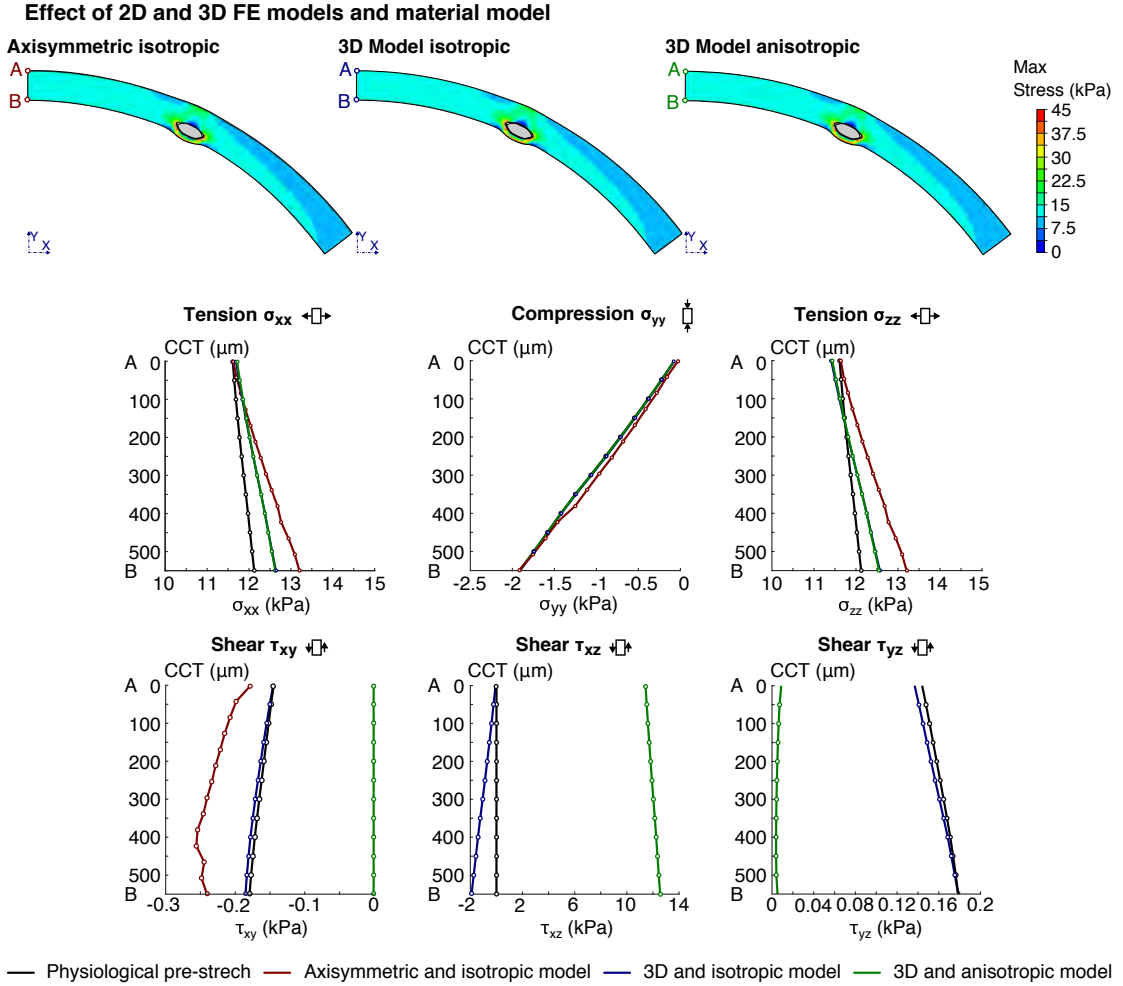


Figure 4.5: Effect of the *in-silico* simulations: axisymmetric versus 3D model and material model. (First row) Main principal stress of axisymmetric model with isotropic behaviour (in red), 3D model and isotropic model (in blue) and 3D model and anisotropic model (in green); **(Second row)** Stress diagram in the apex zone (Line AB) for stress compounds in the main direction, σ_{xx} , σ_{yy} , and σ_{zz} ; **(Third row)** Shear compound of stress in the apex zone (Line AB), τ_{xy} , τ_{xz} , and τ_{yz} .

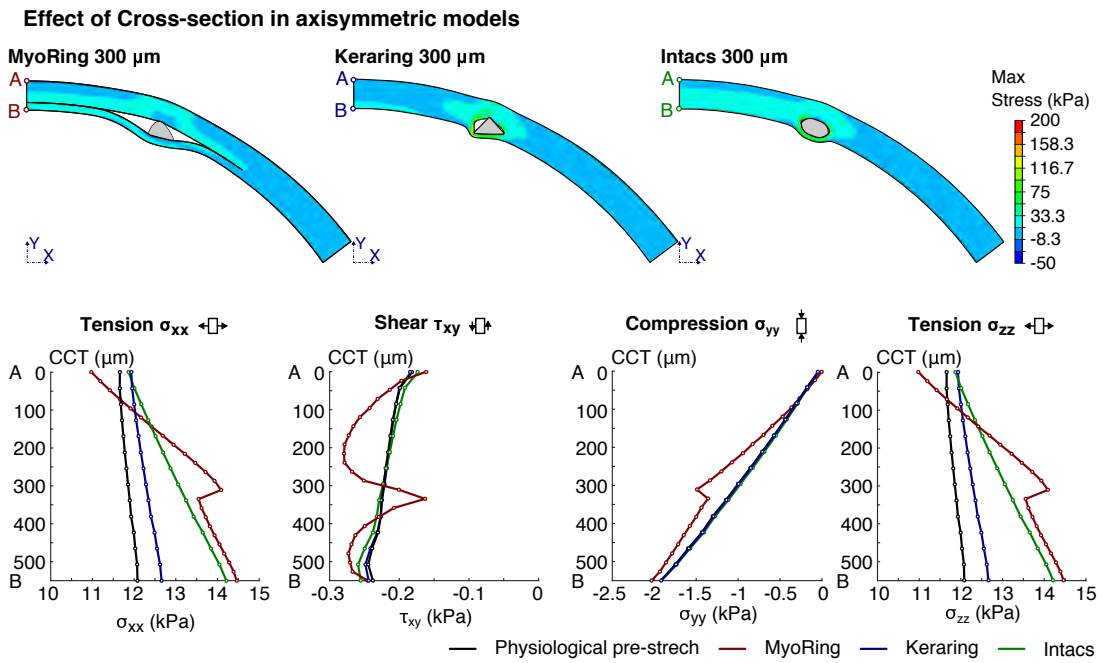


Figure 4.6: Effect of the cross-section of the rings in axisymmetric models. (First row) Main principal stress of the corneal cross-section of MyoRing (red), Keraring(blue) and Intacs (green), respectively; **(Second row)** Stress diagram in the apex zone for stress compounds, σ_{xx} , τ_{xy} , σ_{yy} , and σ_{zz} .

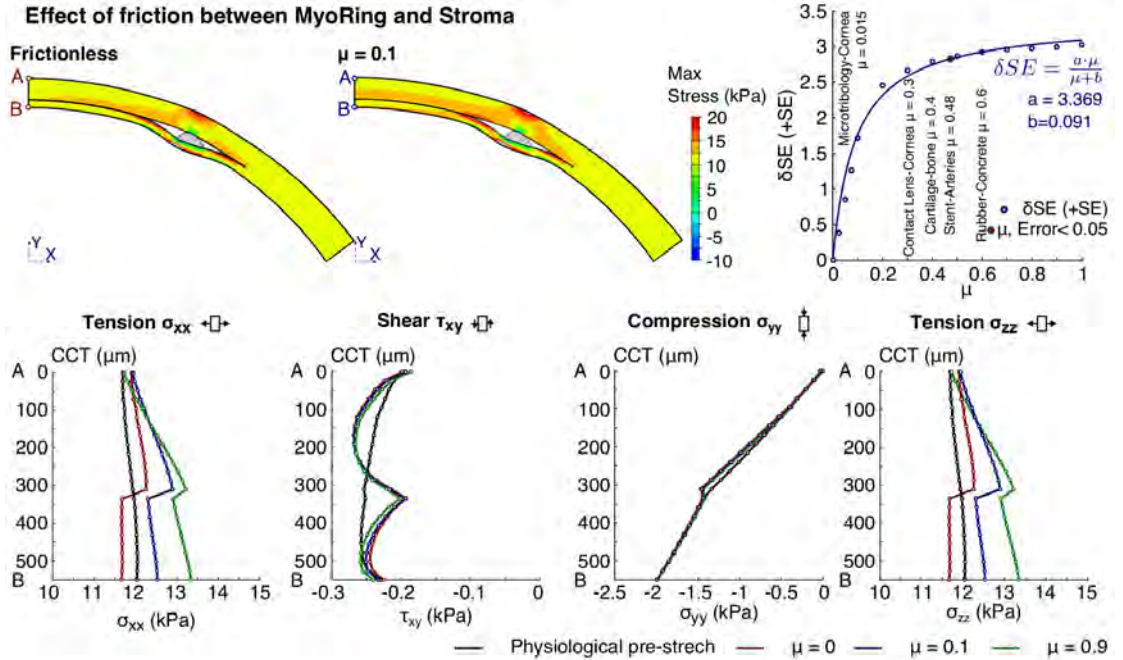


Figure 4.7: Effect of the friction between corneal tissue and ring. (First row) First and second scheme show the main principal stress of the corneal cross-section of $\mu = 0$ (red) and $\mu = 0.1$ (blue); the third scheme show the parabolic behaviour between friction and change in SE, taking the frictionless as baseline; (Second row) Stress diagram in the apex zone for stress compounds, σ_{xx} , τ_{xy} , σ_{yy} , and σ_{zz} .

4. Discussion

A novel methodology to simulate the surgical implantation of intrastromal corneal segments has been developed. This methodology has proven to be stable and allowed us to simulate different commercially–available intrastromal corneal ring segments or continuous implants in both two- and three–dimensions. Not only that, but our methodology allowed for the use of anisotropic material models for the corneal tissue. After a proper model calibration, our approach allowed to estimate the clinical change in corneal refraction after the intervention.

From a purely methodological perspective, two–dimensional axisymmetric models were accurate enough in estimating the overall change in refraction of the cornea for continuous and almost-continuous rings ($\geq 320^\circ$). However, three–dimensional models were needed to estimate an accurate change in refraction for intrastromal ring segments. Using two–dimensional axisymmetric models resulted in an excessive estimation of the refractive correction. On the other hand, from a mechanical standpoint of the simulation of 3D intrastromal rings, using either isotropic or anisotropic material models for the corneal tissue yielded an almost identical estimation of the post–surgical refractive correction even though corneal shear stresses were different.

Traditionally, the friction between the implant and the stroma has been long disregarded.⁴³ However, our parametric study suggested that taking into account the friction between the ring and the corneal stroma was a key feature that could result in an underestimation of up to 3D in refractive correction depending on the friction coefficient. Thus, further experiments and studies should address this issue.

From a clinical perspective, our simulations supported that the MyoRing implant (i.e., continuous implant) achieved the highest refractive correction,⁴⁴ followed by 320–degree Keraring implants (almost continuous).⁴⁵ Since our simulations considered both as continuous rings, this difference was mainly related to the presence of a dissection pocket through the corneal stroma, which modifies the mechanical equilibrium of the cornea by making it more compliant. In this regard, dissection tunnels should always provide less correction because the cornea is not “weakened” by a complete dissection plane. For the same implant conditions (i.e., cross–section size and diameter) and surgical technique, the shape of the cross–section leads the amount of volume introduced in the cornea and, in general, the greater

⁴³ Kling and Marcos 2013, Kahn and Shiakolas 2016, Ebrahimian et al. 2019

⁴⁴ Rattan 2018, Daxer 2017, Jaididi et al. 2016

⁴⁵ Gatziofias et al. 2018, Al-Tuwairqui et al. 2016, Yousif and Said 2018

⁴⁶ Flecha-Lescún# et al. 2020

the volume, the greater the refractive correction.⁴⁶ Interestingly, such a dissection pocket as the one used for MyoRing implantation introduces an in-plane stress relaxation in the anterior stroma. If the progression of the keratoconus disease would be stress-driven and would develop anteriorly, only the surgical techniques creating an intrastromal pocket could slow down its progression as it has been suggested in clinics.⁴⁷

⁴⁷ Daxer 2015

⁴⁸ Yousif and Said 2018, Al-Tuwairqui et al. 2016, Gatziooufas et al. 2018, Kang et al. 2019, Colin and Malet 2007, Alió et al. 2005, Daxer 2017, Jadidi et al. 2016, Rattan 2018

Finally, the results are consistent with the clinical results⁴⁸ and can help to answer clinical questions (see the Chapter 5).⁴⁹ In addition, both mechanical and optical changes followed the tendencies of the results of the Chapter 3.

⁴⁹ Flecha-Lescún# et al. 2020

Although the present study is not exempt of limitations, our methodology should cope with all of them successfully. First, all the corneal models used in the present study were average models of healthy corneas with high myopia. Although additional information about astigmatism and coma could be retrieved by using patient-specific geometries, the overall estimation of the spherical equivalent would remain mostly unchanged as it mostly depends on the spherical aberration (Z_0^2). Second, for the sake of simplicity, the mechanical description of the pathological weaker tissue in the region of the keratoconus has not been accounted for. Nevertheless, previous studies suggested that implants would correct healthy or pathological corneas in a similar fashion.⁵⁰ Third, viscoelasticity was not accounted for as the target of the study was to analyse the long-term effects of the surgery (i.e., ≥ 6 months) and not the transient effects.⁵¹

⁵⁰ Flecha-Lescún# et al. 2020

⁵¹ Kling et al. 2014, Fraldi et al. 2010, Simonini et al. 2016

In summary, we have developed a stable methodology that can help to estimate the post-surgical corneal refraction after the surgery. It can be applied to any commercial implant and can make use of corneal anisotropy. In the near future, this tool could be extended to cope with patient-specific geometries and to help to design the surgical intervention with the best optical outcomes for each patient.

Chapter 5

Corneal biomechanics after intrastromal surgery¹

¹ J. Flecha-Lescún[#], M. Á. Ariza-Gracia[#], P. Büchler, and B. Calvo. **Corneal biomechanics after intrastromal ring surgery: opto-mechanical *in-silico* assessment.** *Transl. Vis. Sci. Technol.*, 9(11):26: 1–16, Oct 2020. ISSN 2164–2591. DOI: <https://doi.org/10.1167/tvst.9.11.26>

The chapter aims to explain the behaviour of the cornea after ICRS insertion. Some relevant clinical question about ophthalmology community will be also answered.

Chapter Contents

1. Introduction	140
2. Methods	142
<i>In-silico model of intrastromal corneal rings surgery</i>	142
<i>Optical and mechanical analysis</i>	145
<i>Model calibration and validation</i>	145
<i>In-silico scenarios</i>	146
3. Results	148
<i>In-silico model validation</i>	148
<i>Ring design and position</i>	148
<i>Effect of corneal biomechanics</i>	150
4. Discussion	153
5. Conclusions	158

1. Introduction

Intrastromal ring segments (IRS or ICRS) or intrastromal continuous rings (ICR) are small polymeric devices placed in the corneal stroma to regularize the corneal surface and correct high refractive errors. This technique was originally introduced to treat patients suffering from keratoconus (KC),² but it was extended to other conditions such as marginal pellucid degenerations,³ post-LASIK ectasia,⁴ and high myopia where laser refractive correction is not possible.⁵ Three main types of rings are now on the market (see Section 4.2 of Chapter 2): continuous rings (e.g., MyoRing, DiopTex GmbH), almost continuous ring segments covering an arc with a central angle between 320° and 355° (e.g., Keraring, Mediphacos, Belo Horizonte, Brazil), and intrastromal ring segments that cover angles below 210° and can be placed by pairs depending on the classification of the cone and the amount of correction (e.g., Ferrara, Ophthalmic Ltd.; or Intacs, Addition Technology Inc.). Besides their difference in angular coverage, the existing systems differ in the design of their cross-section and diameter. Nomograms based on morphological parameters, such as the central corneal curvature, minimum corneal thickness,⁶ or the KC classification,⁷ are used to plan the intervention and select the appropriate implant.

Surgical outcomes are characterized by a high variability,⁸ thus controlling the post-operative biomechanics is a challenging issue. Several authors⁹ have reported that the shape and size of the cross-section of the implant, its diameter and arc length (in the case of IRS), as well as its implantation position affect the post-surgical shape of the cornea and the respective refractive correction. Also, mechanical factors such as intraocular pressure (IOP) and tissue biomechanics play a role and should be accounted for when designing a nomogram.¹⁰

The implantation depth is one of the surgical parameters that was evaluated clinically. The recommended implantation depth is 75–80% of the stromal thickness. Hashemi *et al.* (2013)¹¹ stressed that, for IRS, there was an optimal range of stromal depth between 60% and 79% for which the refractive correction was maximal, while any other implantation depth had a low impact on the topographical outcomes. Barbara *et al.* (2015)¹² pointed out that the actual insertion depth observed in patients treated with IRS was shallower ($\approx 60\%$) than the intended insertion depth ($\approx 80\%$). This observation could be partly explained by the local variation of corneal thickness while the surgical incision remains at a constant distance from the

² Rabinowitz 1998

³ Akaishi *et al.* 2004

⁴ Yildirim *et al.* 2014

⁵ Rattan 2018

⁶ Jadidi *et al.* 2016, Yousif and Said 2018

⁷ Seleet *et al.* 2015

⁸ Janani *et al.* 2019

⁹ Rattan 2018, Jadidi *et al.* 2016, Kling and Marcos 2013, Daxer 2017

¹⁰ Rattan 2018, Jadidi *et al.* 2016, Seleet *et al.* 2015

¹¹ Hashemi *et al.* 2013c

¹² Barbara *et al.* 2016

anterior surface, but it highlights the difficulty of comparing and interpreting existing clinical data. This 20% mismatch in implantation depth or the uncontrolled post-surgical rotation of the implant within the stroma¹³ could impact the refractive outcomes.

Unlike the placement of ring segments inside an intrastromal tunnel, continuous rings require a complete intrastromal pocket,¹⁴ which has important consequences for the mechanical stability after treatment as the pocket cuts a large surface of the cornea that can include both normal and pathological tissues.¹⁵ Despite providing a higher refractive correction than ring segments, the mechanical impact of the intrastromal pocket remains unclear as it cannot be quantified in clinics. In an attempt to estimate the mechanical impact of this treatment, Daxer (2015)¹⁶ used a simple marker based on the ratio between the Cauchy stress in the corneal tissue before and after ring implantation (see the retrospective study in Section 5.4.1 of Chapter 2). Based on this calculation, Daxer suggested that continuous rings were able to introduce a corneal strengthening that should avoid the progression of KC while ring segments would not, as other clinical studies pointed out.¹⁷ Nevertheless, other authors have stated the need for additional evidence to confirm this claim.¹⁸

Clinical studies have shown that these implants regularised the corneal surface and provided a noticeable correction even for high myopia (> 6D). However, planning the surgery to achieve a specific refractive outcome remains challenging.¹⁹ The mechanical principle underlying this treatment remains poorly understood and it is difficult to extract it from clinical studies alone.²⁰ As clinical studies often present mixed populations with different degrees of myopia, KC severity, or implant typology, it is not possible to isolate the contribution of each parameter to the refractive outcomes. In addition, mechanical properties of the cornea play an important role in the procedure but, unfortunately, it is not possible to characterize corneal biomechanics *in vivo* with current clinical devices. *In-silico* models have been proposed to study the insertion of intrastromal rings²¹ but, to the best of our knowledge, no study has systematically reported the individual contribution of the implant geometry, the surgical and the mechanical parameters to the post-surgical refractive outcomes.

In the present study, we use a calibrated *in-silico* model to understand the mechanical response of the cornea to the treatment and to estimate how different geometrical and biomechanical parameters affect the refractive outcomes. Our hypothesis is that implants do not induce a corneal

¹³ Ibares-Frias et al. 2015

¹⁴ Daxer 2008, Abdellah and Ammar 2019, Rocha et al. 2018

¹⁵ Daxer et al. 2016

¹⁶ Daxer 2015

¹⁷ Alió et al. 2011, 2014, Vega-Estrada and Alio 2016

¹⁸ Bikbova et al. 2018

¹⁹ Daxer 2017

²⁰ Janani et al. 2019

²¹ Kling and Marcos 2013, Lago et al. 2015, Kahn and Shiakolas 2016, Flecha-Lescún et al. 2018, Ebrahimian et al. 2019

strengthening (change in stresses) but a local mechanical effect, which is a combination of the added volume and the position of the implant with respect to the corneal centre. This modifies the corneal kinematics and regularises the corneal surface without producing any great change in the central stromal stresses. More peripheral implants should have a lower impact on refraction as the localised mechanical effect will dissipate before reaching the corneal centre.

2. Methods

2.1. *In-silico* model of intrastromal corneal rings surgery

A normal cornea modelled as a spherical dome with a symmetry of revolution around the optical axis (Y-axis, in Figure 5.1.a.1). This geometric description is sufficient to capture the average curvature at the corneal centre (K_{mean}) and the overall defocus of the optical system (Zernike coefficient, Z_2^0 and Spherical Equivalent, SE). For the sake of simplicity, only corneas with central keratoconus were considered in order to preserve the symmetry of revolution even if they are exceptional cases in clinics. Four different corneal topologies were considered in this study: one cornea with high myopia and three pathological corneas with a central keratoconus of different severity. The mechanical properties of the cornea corresponded to those of a normal tissue except in the region of the cone, described by the radius of extension of the disease (between 0.5 mm and 1.5 mm), where the tissue was modelled with weaker properties to represent the pathologic tissue (Table 5.1).

Generic implants with an elliptical cross-section were used instead of commercial rings to focus on studying the size and diameter of the implants. However, the dimensions and volumes of the generic implants were similar to those of their analogous commercial rings (see in Figure 5.1.e a and supplementary Table IV.1–IV.3 in Appendix IV). Three different typologies were considered: generic intrastromal continuous rings implanted in a

Table 5.1: Pre-surgical morphological description of the *in-silico* models. CCT: central corneal thickness; K_{mean} : average central keratometry; AL: axial length; SPS: scotopic pupil size; SE: spherical equivalent.

Case	Cone Radius [mm]	CCT [μm]	K_{mean} [D]	AL [mm]	SPS [mm]	SE [D]
High myopia	-	550	45	26.5	4	-9.4
KC _{0.5}	0.5	436	50	26.5	4	-11.1
KC ₁	1.0	503	50	26.5	4	-11.9
KC _{1.5}	1.5	528	50	26.5	4	-11.5

pocket (gICRP, analogue to MyoRing), generic intrastromal continuous ring implanted in a tunnel (gICRT, analogue to a 355-degree Keraring), and 2 symmetric 150-degree generic intrastromal ring segments (gIRS, analogue to Intacs/Ferrara inserts). The pocketing procedure was assumed to be performed with a femtosecond laser generating stromal bubbles with a size between 1 and 5 μm .²² The diameter of the intrastromal pocket (ϕ_{Pocket}) was set to 8 mm and its thickness (T_{Pocket}) to 5 μm .²³ The diameter of the intrastromal tunnel (ϕ_{Tunnel}) varies to match the implanted segment. For all configurations, the implantation depth varied between 55% and 75% of the stromal thickness (see in Table 5.2) for more details on the simulated scenarios).

In-silico models were built automatically in Abaqus (Dassault Systèmes, France) using the finite element (FE) method (see Appendix III). This modelling approach allows the calculation of the complex mechanical interaction between the corneal tissue and the implants placed in the stromal bed. Taking advantage of the symmetry for the different ring typologies (Figure 5.1.a.2), the *in-silico* model of the cornea can be reduced to a symmetric model, saving computational resources and time. For intrastromal ring segments, the cornea was reduced to a three-dimensional symmetric quarter model by applying appropriate symmetry boundary conditions. For continuous rings, the symmetry of revolution around the visual axis was exploited to simulate the full corneal response by using a simple two-dimensional section (see in Figure 5.1.a.2). A physiological intraocular pressure (IOP) of 15 mmHg was set as loading condition in the posterior surface of the cornea. Corneal tissue was pre-stretched to its nominal IOP by using an iterative algorithm.²⁴ After pressurization of the cornea, the elements of the pocket (resp. tunnel) were removed, the stroma separated using a simulated surgical tool, and the implants lodged in the corneal stroma either in a pocket or a tunnel (see in Figure 5.1.b,c,d and in Chapter 4, Figure 4.1).

The stroma of the cornea with high myopia was considered as a normal tissue, while KC presented a central area (ϕ_{KC}) with degenerated mechanical properties. Although the cornea is highly anisotropic due to the collagen fibre distribution,²⁵ it is not possible to introduce the distribution of corneal collagen fibres in an axisymmetric model. A Yeoh isotropic hyperelastic strain energy function²⁶ was used to simulate the mechanical behaviour of the corneal stroma. Further information regarding the *in-silico* model (mesh, material model or boundary conditions) can be found in Chapter 4.

²² Lubatschowski et al. 2000

²³ Rattan 2018

²⁴ Ariza-Gracia et al. 2016, Elsheikh et al. 2013

²⁵ Forrester et al. 2015, Winkler et al. 2013

²⁶ Yeoh 1993

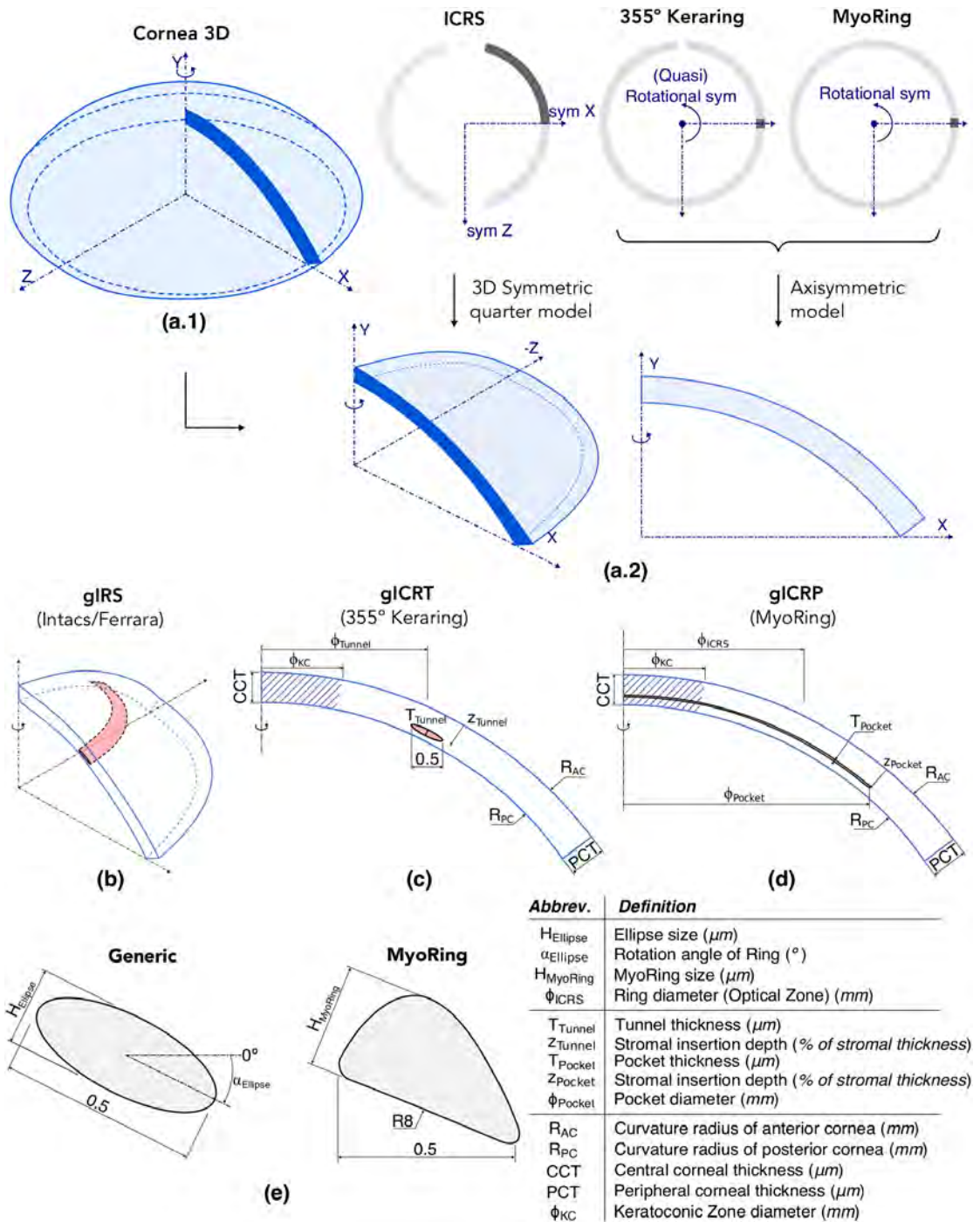


Figure 5.1: Schematic representation of the *in-silico* models used in this study. (a) Symmetry of the model for different ring typologies. Y-axis is the axis of revolution (optical axis); (b, c) *In-silico* models for implants in pocket: segments (gIRS) and continuous (gICRT); (d) *In-silico* model for implants in pocket (MyoRing and gICRP); (e) Implant's cross-section: generic and MyoRing.

2.2. Optical and mechanical analysis

The analysis of the results of the *in-silico* models was done using the following optical parameters: the average curvature of the central cornea (K_{mean}) and the spherical equivalent (SE). K_{mean} ²⁷ was calculated by considering only the refraction of the central part of the anterior cornea (see Equation 4.1 in Chapter 4).

The wavefront error of the optical system was obtained from our in-house ray tracing algorithm²⁸ and fitted using Zernike polynomials²⁹ to calculate the SE³⁰ (see Equation 4.2 in Chapter 4).

The mechanical analysis of the cornea was inspired by the concept of corneal strengthening factor (SFC) introduced by Daxer.³¹ In this study, a generalized three-dimensional of the local strengthening factor (SFC_{3D}) was used rather than a single value describing the global behaviour of the implant, which allows us to quantify the mechanical effects of ring implantation. In short, the SFC_{3D} was defined as the ratio of an equivalent stress at the centroid of each FE element, after ($\sigma_{SFC}^{\text{post}}$) and before ($\sigma_{SFC}^{\text{pre}}$) the insertion of the implants (see Equation 5.1);

$$\sigma_{SFC} = \sqrt{(\sigma_1 - \sigma_2)^2 + (\sigma_1 - \sigma_3)^2 + (\sigma_2 - \sigma_3)^2}$$

$$SFC_{3D} = \frac{\sigma_{SFC}^{\text{post}}}{\sigma_{SFC}^{\text{pre}}} \quad (5.1)$$

where σ_i are the maximum principal stresses in directions ($i=1, 2, 3$). Therefore, $SFC_{3D} > 1$ implies an increment of stress in the stroma while $SFC_{3D} < 1$ corresponds to a relaxation of the corneal stroma.

The probability of corneal stiffening $-p(SFC_{3D} \geq \Theta)$ – was derived from SFC_{3D} as a quantification of the overall increase in corneal stresses. $p(SFC_{3D} \geq \Theta)$ measures the volume of corneal tissue that presents a post-surgical strengthening factor above a given threshold Θ . For example, $p(SFC_{3D} \geq 2)$ reports the volume of corneal tissue with a post-surgical stress two times higher than in the pre-surgical configuration.

2.3. Model calibration and validation

MyoRing simulations were performed to calibrate the numerical model against clinical data, and to provide a numerical benchmark to compare generic implants. The tissue properties of the numerical model were calibrated using clinical data available for two eyes of the same patient

²⁷ Savini et al. 2017

²⁸ Ariza-Gracia et al. 2017a

²⁹ Savini et al. 2017

³⁰ Jaskulski et al. 2017

³¹ Daxer 2015

³² Rattan 2018

treated for high myopia using a MyoRing of 280- μm thickness and 5 mm in diameter, that were implanted inside an 8-mm intrastromal pocket.³² The average changes in the central curvature, δK_{mean} , were 4.9 D and 4.8 D for the right and left eye respectively. Pre-surgical *in-silico* models were built for both eyes and the mechanical properties of the corneal stroma were adjusted using an iterative optimisation procedure until the post-surgical *in-silico* outcomes matched the clinical data.³³ Optimal mechanical properties were determined when, for both eyes, the K_{mean} obtained numerically matched the clinical measurement with a precision below the resolution of clinical topographers (± 0.25 D).

³³ Ariza-Gracia et al. 2017a

³⁴ Daxer 2017

After calibration of the mechanical behaviour in these two eyes, the behaviour of the *in-silico* model was verified using retrospective data obtained from 15 patients treated with MyoRing for high myopia.³⁴ A virtual cohort of patients with high myopia (SE: 10 ± 2 D) was created using the following population data: CCT ($525 \pm 31 \mu\text{m}$), K_{mean} (44.5 ± 1.5 D), axial length (26 ± 1 mm)³⁵ and anterior chamber depth (3.3 ± 0.42 mm).³⁶ Each virtual patient received a 280 μm MyoRing with a diameter of 5 mm, and the change in SE (δSE) was used to compare the predictions of the numerical model with the published clinical data.

³⁵ Sorokin et al. 2019

³⁶ Fernández-Vigo et al. 2016

³⁷ Kling and Marcos 2013

Mechanical properties for the pathological tissue were calibrated using a similar optimisation procedure to the one introduced by Kling *et al.* (2013)³⁷ in which the normal mechanical properties were reduced by a factor F of up to 100. Starting from a normal *in-silico* model (K_{mean} : 45 D), a tissue weakening was introduced in the region ϕ_{KC} of the predefined KC. The mechanical properties of the weakening were iteratively modified until the K_{mean} for the KC reached a typical value of 50 D.³⁸ The material properties for the cone were accepted once the calibration error was below ± 0.25 D.

³⁸ Fernández-Vega et al. 2016,
Kubaloglu et al. 2010a

2.4. *In-silico* scenarios

Seven scenarios were designed to assess the effects of i) the ring design and positioning (Scenarios #1 – #4 in Table 5.2) and ii) the biomechanical environment (Scenarios #5 – #7 in Table 5.2). First, the geometrical parameters of the intrastromal rings and the surgical procedure were studied such as the individual effect of the implantation depth (Scenario #1), the diameter of the ring (Scenario #2), and the size of its cross-section (Scenario #3). Also, the rotation of the ring after surgery was studied for different manufacturing angles of the cross-section (Scenario #4). These evaluations were performed on a cornea having a high myopia. Contin-

#	Z [%]	ϕ_{ICRS} [mm]	H [μm]	α_M [°]	Cornea	Surgery	Ring	Goal
1	55	6	200	25.9	Myopia	Pocket Tunnel	Continuous Segment	Implantation depth
	60							
	75							
2	75	5	200	25.9	Myopia	Pocket Tunnel	Continuous Segment	Ring diameter
		6						
		7						
3	75	6	150	25.9	Myopia	Pocket Tunnel	Continuous Segment	Ring size
			200					
			300					
4	75	6	200	0	Myopia	Pocket	Continuous Segment	Post-surgical rotation of the ring in the stroma
				12.5				
				25.9				
				37.5				
5	75	6	200	25.9	Myopia	Pocket	Continuous	Circadian variation of IOP
6	75	6	300	25.9	Myopia KC	Pocket Tunnel	Continuous	Corneal strengthening (SFC _{3D})
7	75	5, 6	300	25.9	Myopia KC	Pocket Tunnel	Continuous	Normal vs Pathologic corneas)

Table 5.2: Summary of the parameters used for the simulation of each scenario. The geometric parameters are described in Figure 5.1. Additional information can be found in the Appendix IV (Table IV.1–IV.3).

uous rings inserted in a tunnel and in pocket as well as ring segments inserted in a tunnel were studied. The second set of scenarios focused on the effect of the biomechanical environment on the surgical outcomes. Specifically, we studied the effect of the circadian variation of intraocular pressure (Scenario #5), the stress increase after ring implantation (Scenario #6), and the impact of the tissue mechanical properties (Scenario #7) on the optical and mechanical outcomes of the procedure. In particular, the Scenario #7 compared the effect of the treatment between normal mechanical properties found in myopic cases, with pathologic properties found KC corneas. In particular, Scenario #7 compared the effect of the treatment between normal mechanical properties found in myopic cases and pathologic properties found in KC corneas.

Table 5.3: Material parameters for the normal and pathological tissue. KC presents different degrees of tissue weakening depending on the affected area of the cornea (ϕ_{KC}). E_P : tangent modulus at the physiological pre-stretch; C_{10} , C_{20} , C_{30} : parameters of Yeoh material model. Compressibility of the cornea, D_K , was set to 10^{-5} (MPa $^{-1}$) to model a nearly incompressible tissue.

Topology	Tissue	E_P [kPa]	C_{10} [kPa]	C_{20} [kPa]	C_{30} [kPa]
High myopia	Normal	210 (100%)	35.5	3.2	1.9
KC _{0.5}	Severe weakness	14 (7%)	2.1	0.2	0.1
KC ₁	Mild weakness	65 (30%)	10.7	1.0	0.6
KC _{1.5}	Low weakness	118 (55%)	19.5	1.8	1.0

3. Results

3.1. In-silico model validation

The properties describing the mechanical behaviour of normal corneas sustaining MyoRing implantation were identified in two eyes. The iterative approach used to identify the mechanical properties describing the pathology was able to reproduce the morphological alteration observed in KC patients. The K_{mean} obtained at the end of the identification was 50 D, and the identified properties resulted in an important reduction in the stiffness of the tissue³⁹ (see in Table 5.3). The tangent modulus at the corneal pre-stretch (E_P) was used to provide an estimate and compare the biomechanical response of the tissue in the different cases.⁴⁰

The assessment of the predictive power of this model conducted on a cohort of patients with high myopia showed that the numerical model was able to predict the change in SE measured in patients treated with MyoRing,⁴¹ with an overall prediction error below 0.6 D (see in Figure 5.2).

3.2. Ring design and position

Depending on the selected surgical technique, the change in the spherical equivalent (δSE) was driven by different sets of factors. For implants in an intrastromal tunnel (gIRS, gICRT), the size and diameter of the implant were the most important factors affecting the δSE while the intrastromal implantation depth did not have an effect when implanted following clinical recommendations (blue and orange lines in Figure 5.3.a, c). The amount of correction ranged between 1 and 3.5 diopters (see in Figure 5.3.b, c) when individually increasing the size, or decreasing the diameter of the implant. For implants inserted in an intrastromal pocket (gICRP), all the parameters individually contributed to the change in refraction. A 20% variation in depth would have a noticeable impact on visual acuity of up to 5D (see in Figure 5.3.a). The δSE decreased for larger ring diameters with a change of up to -4D when the diameter of the implant increased from 5 to 7 mm (see in Figure 5.3.b). The δSE increased for bigger diameters with

³⁹ Kling and Marcos 2013, Andreassen et al. 1980

⁴⁰ Ariza-Gracia et al. 2017b

⁴¹ Daxer 2017

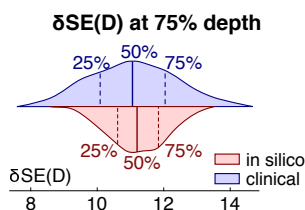


Figure 5.2: Validation of in-silico model. In-silico models (red) predict the change in Spherical Equivalent (δSE) observed clinically by Daxer (2016).

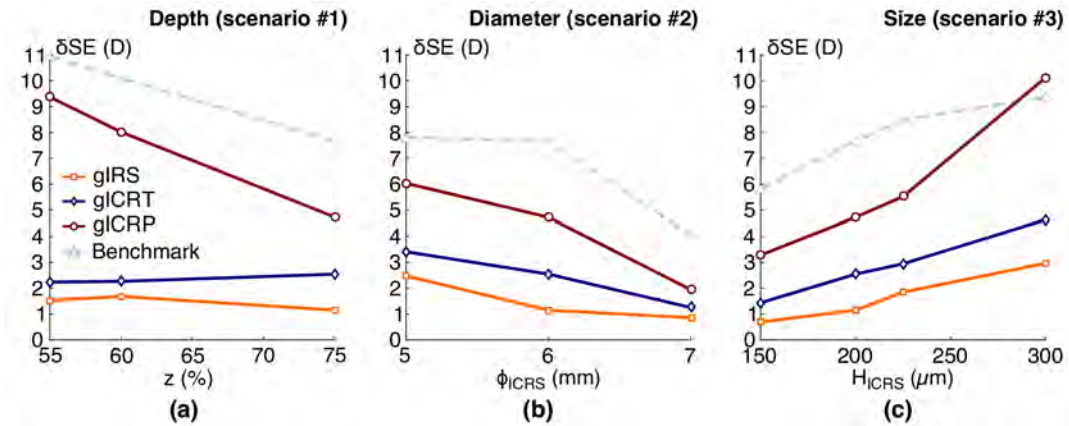


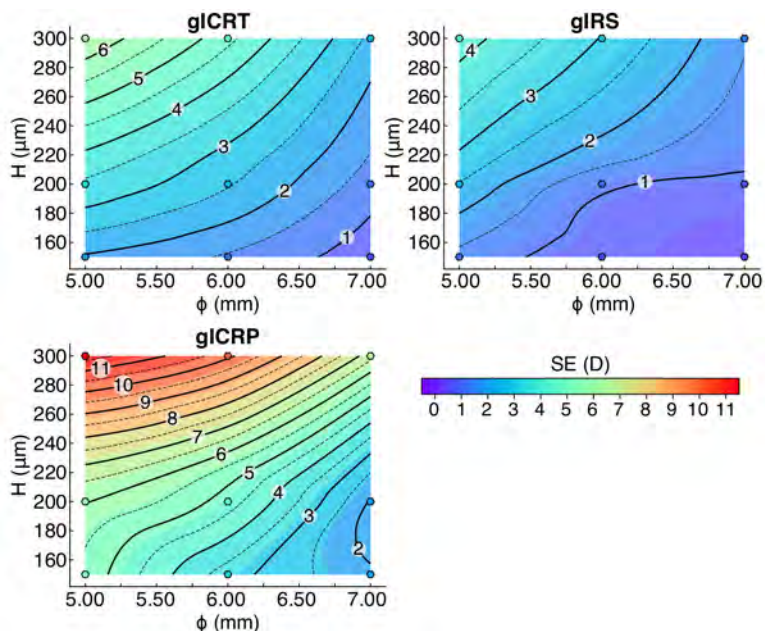
Figure 5.3: Main individual effect of positioning on the change in spherical equivalent (δ SE) between pre- and post-surgical corneas (Scenarios #1–#3). (a) Influence of intrastromal depth of implantation on δ SE; (b) Influence of the diameter of the implant on δ SE; (c) Influence of the size of the implant on δ SE. Results are reported for generic intrastromal ring segments (gIRS in orange) and generic continuous ring in tunnel (gICRT in red) and in a pocket (gICRP in blue). Results for the MyoRing (dashed green) are reported for comparison purposes.

a change up to +6D (see in Figure 5.3.c).

Once any effect of the intrastromal depth is ruled out by selecting the surgical technique, the size and diameter of the implant remain as the most important parameters controlling the refraction. For a given implantation depth of a 75% of the stromal thickness, Figure 5.4 represents a generic nomogram in which the δ SE can be determined based on the surgical procedure and different combinations of implant size and diameter. There are regions in which the δ SE can be kept constant by non-linearly increasing (resp. decreasing) the size of the cross-section while increasing (resp. decreasing) the diameter or, being the same thing, the distance from the local effect of the ring to the corneal centre where the refraction occurs. Care must be taken as this non-linear correlation could include factors such as IOP or mechanical properties of the stroma. Although the trends were similar for all the typologies. Implants in a tunnel were able to achieve less than half of the correction achieved with continuous rings in a pocket. In our case, these higher refractive corrections were all associated with the intrastromal pocket.

The post-surgical rotation of the ring (α_S) was mainly determined by the manufacturing angle (α_M) of the ring's cross-section (see in Figure 5.5). The highest post-surgical rotation was close to 20° when the ring was designed without consideration for the corneal curvature ($\alpha_M = 0^\circ$). Cross-sections with a manufacturing angle that was tangential to the curvature of the posterior corneal surface ($\alpha_M \approx 25^\circ$) presented a post-surgical rotation close to zero. These results indicate that a threshold at around

Figure 5.4: Effect of the interaction between size and diameter of the implant on the change in spherical equivalent (δ SE) between pre- and post-surgical corneas (Scenarios #2–#3). Simulations combined different ring sizes (150, 200, and 300 μm) and diameters (5, 6, and 7 mm) for a given intrastromal depth of 75% of the stromal thickness. gICRT: generic intrastromal continuous tunnel; gICRP: generic intrastromal continuous ring in pocket; gIRS: generic intrastromal ring segment. Dashed contour lines represent increments of +0.5 D.



25° determines whether the ring would rotate towards the corneal centre ($\alpha_M < 25^\circ$) or towards the periphery ($\alpha_M > 25^\circ$). Post-surgical intrastromal rotation of the implant could induce between 1D to 2D of uncontrolled refractive correction.

3.3. Effect of corneal biomechanics

A circadian variation of intraocular pressure (IOP) of $\pm 20\%$ around the baseline of 15 mmHg induced a physiological radial displacement in the surroundings of the implant for the pre-surgical cornea whose vertical component (i.e., vertical displacement) was $\approx 40 \mu\text{m}$. Right after laser pocketing, the cornea was mechanically weaker due to tissue vaporization and experienced a 50% increase in vertical displacement ($\approx 60 \mu\text{m}$). This displacement was 25% lower ($\approx 50 \mu\text{m}$) after continuous ring implantation regardless of whether it was implanted in a pocket or tunnel (gICRP and gICRT). The vertical displacement of continuous ring occurred simultaneously with a radial expansion of the cornea under the variation of IOP. As continuous implants are much stiffer than the cornea and can only move along the in vertical direction, gICRP experienced a tangential sliding of

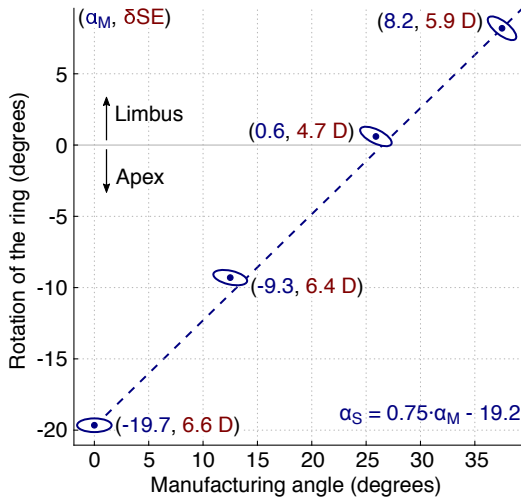


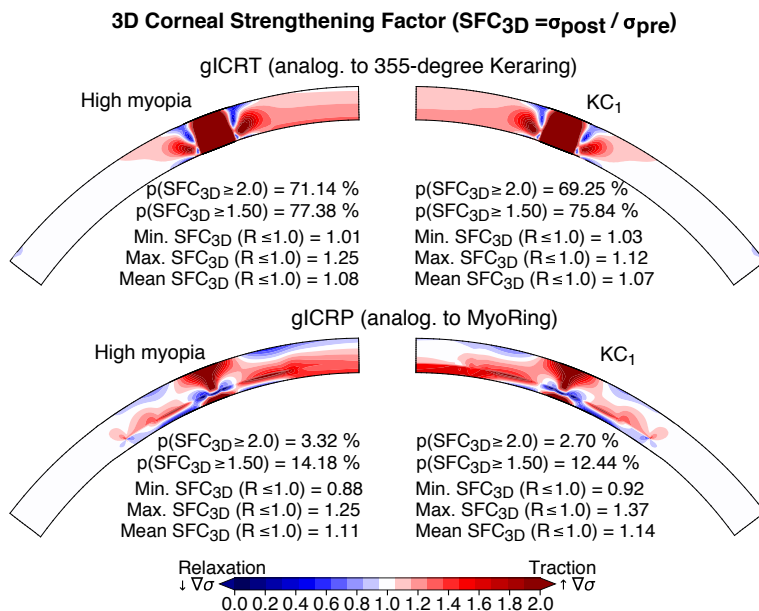
Figure 5.5: Post-surgical rotation (α_S) of gIRS depending on the manufacturing angle (α_M) of the cross-section (Scenario #4). Cross-sections were oriented according to manufacturing angles of 0° , 12.5° , 25.9° and 37.5° . Positive rotations turn gIRS towards the limbus while negative rotations turn gIRS towards the corneal centre.

$30\text{-}\mu\text{m}$ inside the pocket caused by this corneal radial expansion. This sliding behaviour was not present for gICRT implanted in tunnel.

Circadian corneal kinematics further impacted visual perception. In terms of the amount of refractive error induced by a 1-mmHg increment ($\delta SE/\delta IOP$), normal corneas presented refractive stability against IOP variations (0.03 D/mmHg). Due to the corneal weakening derived from the pocketing procedure, this ratio increased up to 0.2 D/mmHg . Immediately following ring implantation, the ratios increased up to 0.67 D/mmHg for gICRT and up to 0.83 D/mmHg for gICRP. Daily variations of IOP induced a qualitatively similar displacement in the region of the implantation, regardless of whether or not an implant was present, but the refractive error was greatly affected in corneas with implants.

Mechanically, the corneas did not present a dramatic increase in stromal stresses at the corneal centre after ring implantation, but just a slight relaxation in a small volume of tissue for gICRP implantations ($SFC \approx 0.9$). The three-dimensional distribution of the corneal strengthening factor (SFC_{3D}) showed that the main stiffening effect occurred in the surroundings of the implant, whereas the centre of the cornea did not present a strengthening greater than 1.5 (Figure 5.6). Moreover, the likelihood of finding corneal strengthening factors greater than 2 at the central cornea was almost non-existent for all typologies (gICRT and gICRP in Figure 5.6; gIRS in Figure IV.1). Accounting for the diminished mechanical properties

Figure 5.6: Spatial distribution of corneal strengthening factor (SFC_{3D}). SFC_{3D} after implantation of generic intrastromal continuous ring in tunnel (gICRT – top) and a generic intrastromal continuous ring in pocket (gICRP – bottom). The overall mechanical strengthening is similar for the high myopic cases (left) and for the pathological cases that have weakened mechanical properties in the central cornea (right).



in KC did not affect the SFC_{3D}, nor the probability of finding strengthening values higher than 2. Corneal strengthening values for the rest of the combinations are provided as Appendix IV (Table IV.4).

The intrastromal pocket produced a discontinuity in the Cauchy stress distribution of the cornea that resulted in higher stresses in the posterior stroma while the anterior stroma slightly relaxed (max. ≈10% relaxation). Such discontinuity was even more noticeable when the pathological weakening of a KC was present (Figure 5.6). When a gICRT was implanted, the SFC_{3D} gradient at the corneal centre was smooth and mostly homogeneous through the corneal cross-section even if a biomechanical discontinuity such as central KC was present. In any case, the SFC_{3D} at the centre never exceeded 1.5, even for the most severe cone (see in Table IV.4), which indicates that the pre- and post-surgical stress distribution was only slightly affected by the ring implantation at the corneal centre.

Trends for the correction of the spherical equivalent (δ SE) were not sensitive to the change in biomechanical properties of the tissue or the extension of the disease and, therefore, the refractive correction for each simulated patient was similar (see in Figure 5.7). Changing the ring design and

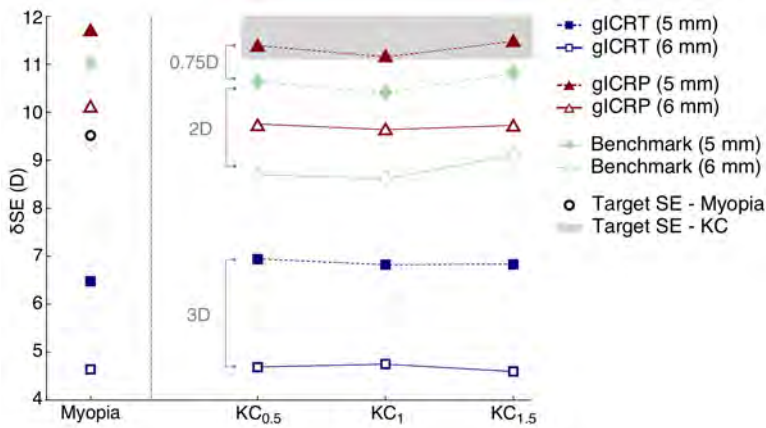


Figure 5.7: Impact of the stromal biomechanical properties on refractive outcomes after continuous ring implantation (diameter of the implant of 5 and 6 mm, 75% depth and 300 μm size). The change in spherical equivalent (δSE) was calculated for different severities of KC ($\text{KC}_{0.5}$, KC_1 , and $\text{KC}_{1.5}$) as well as a reference cornea with high-myopia. Results for the MyoRing (dashed green) are reported for comparison purposes.

position produced similar refractive changes for normal and pathological corneas. As outlined previously (see in Figure 5.3), changing the diameter of the implant from 5 to 6 mm produced a constant shift in δSE (≈ 2 D for glCRP; ≈ 3 D for glCRT). A change in the shape of the cross-section from elliptical to MyoRing produced a constant shift of ≈ 0.75 D.

For both, high myopia and keratoconus, continuous rings introduced a fairly constant δSE between 10 and 11.5 D which corrected the pre-surgical SE with a maximum error of 0.6 D for high myopia ($\text{SE} = -9.4$ D) and of 0.8 D for keratoconus ($\text{SE} = -11.9$ D for $\text{KC}_{1.0}$). However, ring implantation in tunnel fell short of the targeted SE by 50% (5-mm diameter) and 100% (6-mm diameter), presenting a refractive correction that was mostly constant during changes in mechanical properties and extension of the disease.

4. Discussion

An *in-silico* model of the cornea was used to study corneal mechanics after intrastromal ring implantation. This approach enabled us to study the individual impact of the implant design and surgical parameters on the optical and biomechanical outcomes of the procedure, which is not directly possible in clinical practice. The results of the study confirmed our hypothesised that implants do not strengthen the cornea globally but introduce a localised mechanical deformation that regularises the corneal surface by adding volume to the stroma. The correction achieved by the

implantation therefore depends on the amount of added volume and the distance from the corneal centre at which the ring is implanted.

In-silico simulations showed that the stress in the stroma was mostly modified in the surroundings of the implant with little to no impact on the level of mechanical stress in the central region of the cornea. This fact implies that the improvement of the optical outcomes does not result from an overall strengthening of the stromal tissue, but from localised mechanical deformations. The low dependence of the change in spherical equivalent on variations of the mechanical properties of the stroma, even for the large reduction in the mechanical properties used to simulate the different KC cases, supported this finding.

In addition, since an implant only modifies the stress in the vicinity of its implantation, the change in the corneal shape does not result from a general stretching of the tissue but it is rather a consequence of the increased volume associated with it. The size of the intrastromal rings is comparable to half the stromal thickness, which mechanically introduces an important deformation of the cornea and, especially, to the anterior surface located above the ring. Our results showed that the surface regularisation induced by this bulking effect is associated with a change in the optical properties, which is stronger when the ring is placed close to the corneal centre and to the anterior surface as well as for larger ring heights. Our hypothesis is also supported by clinical nomograms⁴² in which the amount of correction is controlled by the appropriate selection of the ring thickness and diameter. In particular, simulations showed refraction changes of ≈ 1.5 D per mm increase in diameter and 0.05 D per μm increase in thickness.

The main difference between surgical techniques is related to the presence of a pocket. Unlike intrastromal tunnels, cutting a pocket across the corneal stroma induces a discontinuity in the stress distribution, which limits the transmission of shear stresses across the cut interface and reduces the apparent corneal stiffness (Figure 5.8). This reduced load-bearing capability makes the cornea more compliant and it therefore presents less resistance to the bulking effect induced by the implant, which allows to achieve higher refractive corrections to be achieved. Although from a mechanical standpoint the corneal centre is barely affected by the treatment, if we assume that KC growth is triggered by an increased level of stress in the tissue and that it develops anteriorly, our results suggest that only intrastromal pocketing could have the potential of limiting KC progression, as stress would relax in the anterior stroma.

⁴² Rattan 2018, Jadidi et al. 2016, Seleet et al. 2015

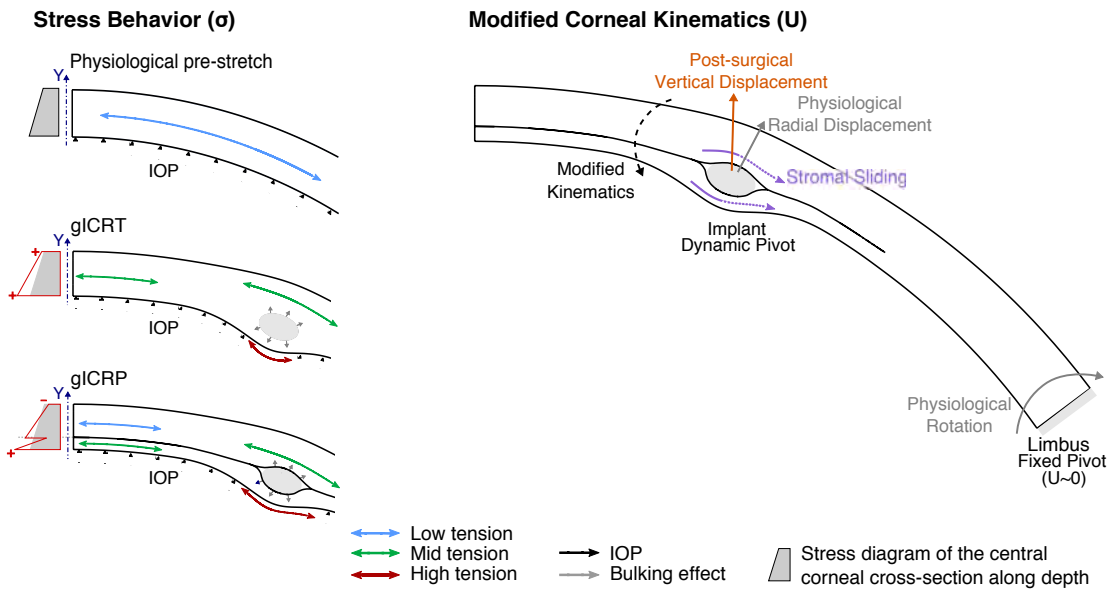


Figure 5.8: Conceptual diagram of corneal kinematics and biomechanics after ring implantation (based on FE simulations). **Stress behaviour (left)** Physiological pre-stretch of the cornea due to IOP induces a membrane stress with a homogeneous distribution of stromal stress. gICRT increased the corneal stress and slightly thinned the cornea. gICRP increased the stress in the posterior stroma but relaxed it in the anterior stroma, and slightly thinned the cornea. Bulking effect (pushing the corneal stroma, in gray) created an uneven stress distribution above and below the implant. Stromal pocket introduced a shear stress discontinuity at the interface. **Corneal Kinematics (right)** Limbus acts as a fixed pivot point (no displacement) around which the cornea can adapt to balance mechanical changes. An intrastromal implant introduces a dynamic pivot (it can move and may rotate) that changes the physiological corneal kinematics by modifying how the stroma can adapt and move in its surroundings. As a result, cornea can flatten. However, this effect is local and loses strength when the implant is located far from the corneal centre.

The presence of the intrastromal implants also modified the physiological kinematical response of the cornea. Our results showed that, while a normal cornea would not present a noticeable change in refraction due to circadian variations in IOP (0.03D/mmHg), corneas with an implant would present modified kinematics that would produce a great change in refraction (0.8D/mmHg). This behaviour is a direct consequence of the rigidity of the implant that restricts the physiological radial and circumferential displacements (see in Figure 5.8). In the surroundings of continuous implants, and since their diameter remains constant, changes in IOP will no longer deform the cornea in the radial direction but will do so in the vertical direction. For implants in intrastromal pockets, a possible stromal sliding might occur depending on the friction between the ring and the stroma. Thus, the overall spherical shape of the cornea cannot be preserved resulting in a straightening of the peripheral region of the tissue and a flattening of its central part. In this context, the implant acts as a dynamic pivot that can move and rotate within the corneal stroma modifying corneal kinematics. However, it is important to note that the ring cannot be considered as an auxiliary limbus since it moves during circadian variation of the pressure, even if this motion is restricted along the visual axis.

At a population level, our calibrated *in-silico* model was able to predict the refractive correction in high-myopic patients with MyoRing. Also, the optical results for generic rings were in good agreement with several clinical studies in which little difference between healthy and keratoconic outcomes at a population level was reported.⁴³ Unfortunately, clinical studies often report mixed ring typologies, corneal geometries and degrees of pathology and, therefore, results for keratoconic corneas would require an *in-silico* population study to fully support that optical results have little difference between healthy and pathological corneas.

The size of the cross-section and the diameter of the implant were key on regulating the amount of refractive correction as reported by many authors. Recommended intrastromal implantation depths are close to the posterior corneal surface ($\approx 70\%$), which creates an uneven distribution of tissue above and below the implant that stabilizes it. For ring segments implanted within an optimal clinical range (60%–79%), refractive correction did not vary with the implantation depth, as reported by Hashemi *et al.* (2013).⁴⁴ For continuous implants in pockets, our results suggest that the refractive correction could increase up to two times if implants were to be placed at shallower depths ($\approx 50\%$ of corneal thickness) instead

⁴³ Jadidi *et al.* 2016, Janani *et al.* 2019, Daxer 2017, Daxer *et al.* 2016, Nobari *et al.* 2014, Mohebbi *et al.* 2016

⁴⁴ Hashemi *et al.* 2013c

of at deeper depths, which could be one of the reasons why MyoRing is advised to be placed at 300 microns with respect to the anterior surface.⁴⁵ Post-surgical rotation of ring segments in the stroma was driven by the manufacturing angle of the cross-section (α_M). Implants that were tangent to the curvature of the posterior corneal surface ($\alpha_M \approx 26^\circ$) presented higher stability. Due to the local stress distribution, the over-stressed corneal stroma results in forces and angular momentum on the implant, which will tend to rotate inside the cornea as reported by Ibares-Frías *et al.* (2015).⁴⁶

⁴⁵ Daxer 2015

Mechanically, our results showed that implants did not cause any remarkable change in stresses at the corneal centre, which is not in agreement with the current literature. Daxer⁴⁷ suggested that continuous rings should act as an auxiliary limbus that constrains and strengthens the cornea by limiting its movement. In particular, he reported that continuous rings would strengthen the cornea up to three times in the corneal centre for continuous rings while there would be no strengthening for ring segments. However, his initial approach used the Laplace equation which disregarded complex physics (e.g., the interaction between the implant and the stroma, or the stress distribution in corneal thickness) and characterized the mechanical behaviour of the whole cornea as a single ratio between the diameter of the cornea and the diameter of the implant. Our results showed that the level of stress at the corneal centre remains close to pre-surgical values with strengthening values of less than 1.5, and that the ring could move along with the corneal stroma even if it modifies the corneal kinematics.

⁴⁶ Ibares-Frías *et al.* 2015

⁴⁷ Daxer 2015

To the best of our knowledge, few *in-silico* studies introduced actual solid implants in the stroma and these only addressed continuous rings using axisymmetric simulations.⁴⁸ All the mechanical models were isotropic hyperelastic, and some of them neglected the corneal pre-stretch due to the intraocular pressure.⁴⁹ Kahn *et al.* (2016),⁵⁰ Ebrahimian *et al.* (2019)⁵¹ and Kling *et al.* (2013)⁵² came to the conclusion that for the smallest diameters, implants could change refraction about 10 D for keratoconus and 12 D for normal corneas while, for the largest optical zones, implants were not effective (0.5 D). All these numerical results are in good agreement with the results provided in the present study.

⁴⁸ Kling and Marcos 2013, Kahn and Shiakolas 2016, Ebrahimian *et al.* 2019

⁴⁹ Kling and Marcos 2013, Kahn and Shiakolas 2016

⁵⁰ Kahn and Shiakolas 2016

⁵¹ Ebrahimian *et al.* 2019

⁵² Kling and Marcos 2013

Although our *in-silico* model was able to reproduce the clinical data described in a small cohort study, it is not exempt from limitations. The main limitation is that the geometry of the model is based on an idealized spherical representation of the cornea that prevents evaluating changes in

astigmatism after ring implantation. The design of the ring used in this study was also based on a simplified cross-section, and not on the geometry of commercial products. This choice allows to draw generic conclusion on the effects of ring implantation and to bulking, but is unable to analyse and compare the performance of specific commercial products.

Other limitations are related to the mechanical material model used for describing the mechanical response of the cornea. First, unless used with care, axisymmetric models could provide a stiffer mechanical response than three-dimensional models. Second, to use axisymmetric models and alleviate the computational costs, we did not use a fibre-reinforced anisotropic model that would take into account the collagen network within the cornea. Although this assumption might modify post-surgical mechanical outcomes in the surroundings of the surgery and might fine-tune optical outcomes (mostly related to astigmatism), we do not expect a change in the global trends as we are comparing pre- and post-surgical situations at the central cornea in which the stress state is not greatly modified. Third, the mechanical model for KC was not validated but simply calibrated to reproduce the typical curvature reported for KC patients. A proper morphological and mechanical characterisation of the cone is needed to assess these particular patients. Nevertheless, the range of variation of mechanical stiffness for the cone ranged from 10% to 50% of the normal corneal stiffness⁵³ which should encompass the most extreme cases and ensure that our general conclusions hold.

⁵³ Kling and Marcos 2013, Andreassen et al. 1980

5. Conclusions

This study showed that implants do not stiffen the cornea but rather create a local bulking effect that regularises the corneal shape, with a stronger effect when the implants are placed close to the central cornea and when their size is thicker. Implants in intrastromal pockets yield the highest refractive correction and this might be the only surgical technique that could limit KC progression providing that it is stress-driven. Implants modify corneal kinematics but without restricting corneal motion: they only affect how the corneal stroma can move and rotate in the surroundings of the implant which, in turn, results in a corneal flattening and a surface regularisation. *In-silico* models are powerful tools to better understand corneal biomechanics and could be used to better plan patient-specific interventions, to create nomograms that explicitly account for the mechanics,

or to help optimise the design of implants without the need for expensive experiments.



Chapter 6

Mechanical nomograms: Application on MyoRing

The chapter aims to be a preliminary study in the use of numerical models for the generation of nomograms. These nomograms are used by doctors to better plan surgeries and, in addition, takes into account optical and biomechanical factors.

Chapter Contents

1. Introduction	162
2. Methods	163
<i>MyoRing surgery</i>	163
<i>Mechanical and material model</i>	163
<i>Virtual cohort of patients</i>	165
3. Results	167
<i>Validation of in-silico models</i>	167
<i>Contribution of mechanics and anatomy to the nomogram</i>	168
<i>Corneal strengthening factor of MyoRing</i>	170
<i>Predictions of refractive outcomes</i>	171
4. Discussion	174

1. Introduction

A nomogram, alignment chart, or abaque, is a graphical calculating device in the form of a two-dimensional diagram designed to approximate a mathematical function. These graphs present several scales arranged so that, using a ruler, the user can trace a line that intersects with the different scales in order to determine a desired output: often, any pair of two variables can be used to find the values of the other interrelated variables.

In the field of Ophthalmology and, more specifically, on the implantation of intrastromal corneal ring segments (ICRS) or intrastromal continuous ring (ICR), current clinical nomograms used to plan which ring to implant are based on empirical data that only take into account anatomical factors such as the anterior curvature of the cornea, the central corneal thickness or the pre-surgical refraction error (spherical equivalent $-SE$). Unfortunately, they do not take into explicit consideration corneal biomechanics, such as the stiffness of the corneal tissue or intraocular pressure (IOP).

To date, table-like nomograms used to select the size of the cross-section and the optical zone of implantation (ring diameter) are mainly based in two biomarkers: pre-surgical average keratometry (K_{mean}) and spherical equivalent (SE).¹ In the present study, which is preliminary and has not been published, we focus on understanding the role of biomarkers used in MyoRing nomograms (Dioptex, GmbH.) on planning the surgery. Besides, we aim at shedding light onto whether explicitly including mechanical factors as input biomarkers for the nomograms is necessary.

In order to do so, *in-silico* models can help to analyze complex biological models as MyoRing surgery and help on exploring whether mechanically-driven ophthalmic nomograms can be designed in order to better plan surgeries by virtually predicting post-surgical optical outcomes.

Therefore, the goal of the study is to explore whether it is possible to create a mechanically-driven nomogram that accounts for anatomical (central corneal thickness, anterior and posterior curvature, axial length) and mechanical (corneal stiffness and intraocular pressure) features. By studying the correlations between pre- and post-surgical variables (anatomical, mechanical and optical), we try to discern which is the set of minimum features needed to create an effective nomogram.

It is important to remark that, as this chapter is an application of the methodology developed in Chapter 4, the aim of the current chapter is to

¹ Daxer 2017, Jadidi et al. 2016

focus on how these models are of use and can be applied on a population study rather than on explaining the technical methodology. As such, readers are referred to Chapter 4 for the technical details on the *in-silico* model.

2. Methods

2.1. MyoRing surgery

The surgery to implant a continuous ring, as the MyoRing, is explained in Section 4.1.2 of Chapter 2 and is summarized in four steps: *i*) a pocket is created within the corneal stroma with a diameter of 8 or 9 mm at a depth estimated by the surgeon (normally 300 μm). The pocket can be done manually with the Pocketmaker microkeratome² or using a femtosecond laser;³ *ii*) a small incision is made on the side of the cornea in the Nasal–Temporal plane whose length is calculated in Daxer 2015;⁴ *iii*) The MyoRing is folded with a forceps before being implanted within corneal stroma; *iv*) The implant is centered within the pocket with a forceps or a hook, and the incision is self–sealing and does not require suturing.

² Daxer 2008

³ Alió et al. 2011

⁴ Daxer 2015

2.2. Mechanical and material model

In-silico surgeries were simulated using the methodology previously described in Chapter 4, Section 2.5 and Chapter 5, Section 2.1. In short, keypoints are:

- Corneas and MyoRing implants are modelled as two–dimensional axisymmetric solids.
- Corneas and MyoRing implants are automatically meshed using Abaqus Python with a variable number of elements which in average are 6,767 and 659, respectively.
- To simulate the surgery, the displacement–based strategy described in Chapter 4 was used.

As described in Chapter 4, although the material behaviour of the corneal tissue is anisotropic due to the presence of two families of collagen fibres that conforms a collagen network, an isotropic Yeoh strain energy function (see Chapter 2, Equation 2.2). The choice of this material law was motivated by two main reasons,

- We chose to use 2D axisymmetric models to alleviate the computational effort of the simulations and, as such, an anisotropic hyperelastic material law with orthogonal arrangement of fibres cannot be used.

- As suggested in Chapter 4, the anisotropy seems not to play a fundamental role in the refractive outcomes of this surgery. Since the stress state at the corneal centre remains mostly invariant between the pre- and post-surgical configurations, it is sensible that the material role will play a minor role in the change of refraction in this particular surgery.

Although the base mechanical properties were the same as the ones described in Table 5.3 (Chapter 5), in the present study we introduced a perturbation of the mechanical properties of the corneal tissue in order to quantify the impact of the corneal stiffness on the refractive outcomes and to simulate different patients. As the Yeoh model is parameterised by three constants (C_{10}, C_{20}, C_{30}), a simultaneous random perturbation on them would be impossible to control. Instead, we directly controlled the perturbation on the tangent modulus E_λ at the corneal pre-stretch ($\lambda = 1.2$). From a continuum mechanics framework, the tangent modulus is defined in Equation 6.1,

$$E_\lambda = \frac{\partial \sigma}{\partial \lambda} \quad (6.1)$$

for the most simple load case (uniaxial extension) and considering that the material is incompressible ($J = 1$), we can find a relation between a given tangent modulus at the corneal stretch and a given set of Yeoh parameters described in Equation 6.2

$$E_{\lambda=1.2} = f(C_{10}, C_{20}, C_{30}, \lambda = 1.2) \quad (6.2)$$

Using this relationship, we set up an iterative process that will look for a set of Yeoh constants that will match a given (random) value of the tangent modulus at the corneal stretch. This approach assumes that the stress-stretch perturbation in the region of interest (corneal centre) will be mostly linear and, therefore, the corneal stiffness will be bound within reasonable limits of $E_{\lambda=1.2}$ except in the surroundings of the surgery. Regardless this assumption, our previous analysis supports that the stress ratio at the corneal centre between the pre- and post-surgical configurations will not vary more than a 50% (see Figure 5.6, in Chapter 5) and, thus, this hypothesis is deemed as reasonable.

2.3. Virtual cohort of patients

To create a mechanically-driven population-based nomogram it is necessary to have an extensive database with variations in anatomical, mechanical, and optical features. Using a stratified latin hypercube sampling,⁵ a cohort of 2,000 virtual patients was designed accounting for the most relevant features that are currently used to assess in the planning of the surgery and might influence on the surgery planning and outcomes. In particular, there are variables that were taken from population studies (see □) while others were derived from the population-based variables or set as design variables (see ■). All the variables are summarized in Figure 6.1.

⁵ Saltelli et al. 2008

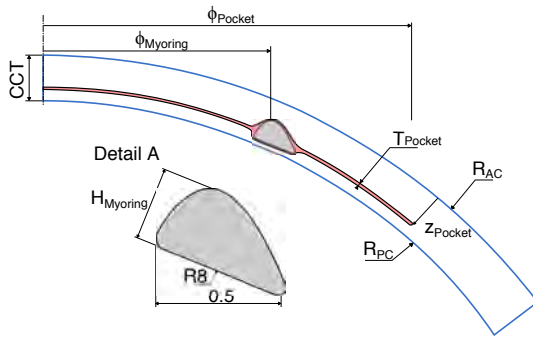


Figure 6.1: Cornea and MyoRing cross-section. Template used to prepare overall simulations. The data table are parametric.

Abbrev.	Definition	Value	Ref.
$H_{MyoRing}$	MyoRing size (μm)	200, 240, 280	Alió et. ⁶
$\phi_{MyoRing}$	MyoRing diameter (Optical Zone) (mm)	5, 6, 7	Alió et. ⁷
ϕ_{Pocket}	Pocket diameter (Optical Zone) (mm)	8, 9	Rattan ⁸
T_{Pocket}	Pocket thickness (μm)	5	Lubatsch. et ⁹
Z_{Pocket}	Stromal insertion depth (% of stromal thickness)	$\mathcal{U}(60, 75)$	Daxer ¹⁰
K_{mean}	Average corneal curvature (Keratometry) of anterior surface (D)	$\mathcal{N}(44.5, 1.5)$	Sorkin et. Wadhwa et. ¹¹
ρ_R	Ratio of anterior and posterior radius of curvature of the cornea (-)	$\mathcal{N}(1.19, 0.02)$	Hasegawa et. ¹²
AL	Axial length high myopia (mm)	$\mathcal{N}(26.66, 1.9)$	Wadhwa et. ¹³
R_{AC}	Curvature radius of anterior cornea (mm)	$R_{AC} = \frac{337.7}{K_{mean}}$	Olsen ¹⁴
R_{PC}	Curvature radius of posterior cornea (mm)	$R_{PC} = \frac{R_{AC}}{\rho_R}$	Hasegawa et. ¹⁵
CCT	Central Corneal Thickness (μm)	$\mathcal{N}(527.7, 35)$	Pedersen et. ¹⁶
IOP	Intraocular Pressure (mmHg)	$\mathcal{N}(15, 3)$	Wadhwa et. ¹⁷
$E_{\lambda=12}$	Young's modulus at physiological stretch (kPa)	$\mathcal{U}(60, 100)$	Ariza et. ¹⁸

2.3.1. MyoRing

- ⁶ Alió et al. 2011 Size of the cross-section ($H_{MyoRing}$) is given by the manufacturer, being the most relevant sizes 200, 240 and 280 μm .⁶
- ⁷ Alió et al. 2011 Diameter of the MyoRing ($\phi_{MyoRing}$) is given by the manufacturer, being the most relevant sizes 5, 6 and 7 mm.⁷
- ⁸ Rattan 2018 Pocket diameter (ϕ_{Pocket}) was set to 8 mm as reported by Rattan (2018).⁸
- ⁹ Lubatschowski et al. 2000 Thickness of the pocket dissection line or laser bubble size (T_{pocket}) was set to 5 μm .⁹
- ¹⁰ Daxer 2017 Stromal insertion depth of the implant (z_{Pocket}) was uniformly varied between 60% and 75% of the stromal thickness where the implant was inserted (i.e., the stromal thickness at an optical zone of 5, 6, or 7 mm).¹⁰

2.3.2. Anatomy

- ¹¹ Sorkin et al. 2019, Wadhawa and Karambelkar 2019 Average keratometry of the cornea (K_{mean}) was assumed to follow a normal distribution with an average 44.5 diopters (D) and a standard deviation of 1.5 D.¹¹
- ¹² Hasegawa et al. 2018 Ratio between the anterior and posterior radius of curvature ($\rho_R = R_{AC}/R_{PC}$) was assumed to follow a normal distribution with an average of 1.19 and a standard deviation of 0.02.¹²
- ¹³ Wadhawa and Karambelkar 2019 Axial length of the eyeball (AL) was assumed to follow a normal distribution with an average of 26.66 mm and a standard deviation of 1.9 mm.¹³ These values were chosen in such a way that the pre-surgical refractive error (Spherical Equivalent – SE –) of the patients ranged between -6 and -20 D, which is considered as high myopia.
- ¹⁴ Olsen 1986 Radius of curvature of the anterior cornea ($R_{AC} = (n - 1)/K_{mean}$) was calculated for a given average keratometry and a refractive index $n=1.337$.¹⁴
- ¹⁵ Hasegawa et al. 2018 Radius of curvature of the posterior cornea ($R_{PC} = R_{AC}/\rho_R$) was calculated for a given R_{AC} and a given ρ_R .¹⁵

- Central corneal thickness (*CCT*) was assumed to follow a normal distribution with an average of 527.7 μm and a standard deviation of 35 μm .¹⁶

¹⁶ Pedersen et al. 2005

2.3.3. Mechanics

- Intraocular pressure (*IOP*) was assumed to follow a normal distribution with an average of 15 mmHg and a standard deviation of 3 mmHg.¹⁷
- Tangent modulus at the corneal pre- ($E_\lambda = 1.2$) was designed as a uniform distribution¹⁸ between 157.5 kPa and 262.5 kPa (which corresponds to a $\pm 25\%$ permutation with respect to the mechanical properties baseline).¹⁹

¹⁷ Wadhawa and Karambelkar 2019

¹⁸ In Monte Carlo analysis, uniform distributions assume that there is not prior knowledge about the distribution of a parameter and, thus, all of them are equally probable

¹⁹ Ariza-Gracia et al. 2017b

Eventually, the cohort of 2,000 patients was evaluated for 3 different ring sizes and 3 different ring diameters resulting in a dataset of 18,000 cases containing pre- and post-surgical *in-silico* information of the MyoRing surgery. The full pipeline made use of GNU Octave²⁰ and Python 3²¹ for file manipulation and post-processing while mechanical simulations were performed in the finite element software Abaqus 6.13–5 (Dassault Systèmes, France).

²⁰ Eaton et al. 2020

²¹ van Rossum and Drake 2009

The opto-mechanical analysis of the population was done as described in Chapter 5 of Biomechanics. First, the optical analysis was performed with an in-house ray tracing software²² in order to determine the change in average keratometry (δK_{mean}) and the change in spherical equivalent (δSE). Second, the three-dimensional corneal strengthening factor (SFC_{3D}) was calculated for each cornea and averaged over the entire dataset in order to determine the degree of corneal stiffening after MyoRing insertion at a population level.

²² Ariza-Gracia et al. 2017a

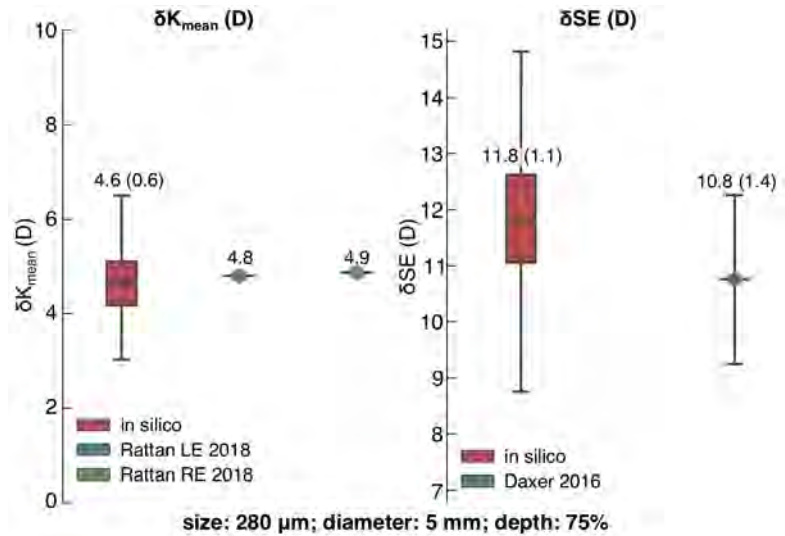
3. Results

3.1. Validation of *in-silico* models

Our *in-silico* model for MyoRing was calibrated previously using the patient reported by Rattan (see Chapter 4 and 5).²³ Maintaining the MyoRing prescribed by Rattan (ring size of 280 microns, diameter of 5 mm and insertion depth of 75%) but accounting for anatomical and mechanical variations resulted in a average prediction of δK_{mean} of 4.6 D (see Figure 6.2.left), being close to the range reported for those MyoRing features (see Figure 6.3).

²³ Rattan 2018

Figure 6.2: Calibration (left) and verification (right) of opto-mechanical simulation of MyoRing. After calibrating the model with data from Rattan et al. (model error within ± 0.25 D), *in-silico* population outcomes were able to predict clinical changes in keratometry (K_{mean}) and Spherical Equivalent (SE) reported by Jadidi et al. and Daxer.



²⁴ Rattan 2018, Daxer 2017

²⁵ Saad and Somali 2019, Yousif and Said 2018, Daxer et al. 2016, Jadidi et al. 2016, Mohebbi et al. 2016, Nobari et al. 2014, Saeed 2014

²⁶ Daxer 2017

Interestingly, although our simulations did not include explicitly keratoconus cases, our optical predictions for δK_{mean} were in line with both high myopic patients²⁴ and patients with keratoconus²⁵ for the same level of refractive error (see Figure 6.3). This preliminary result has tremendous implications as it would suggest that the main refractive correction achieved with these implants is related to its geometry regardless how healthy or how pathological a corneal tissue is (see results in Chapter 5).

Eventually, our *in-silico* predictions were also able to predict the change in spherical equivalent reported by Daxer²⁶ at a population level and without a priori information (see Figure 6.2.right). In sum, our *in-silico* models were able to predict the changes in spherical equivalent (δSE) and average keratometry (δK_{mean}) for a given MyoRing, enabling us to explore the effect of different ring configurations and the impact of different variables on the refractive outcomes.

3.2. Contribution of mechanics and anatomy to the nomogram

Often, clinical results are wrongly analyzed and manipulated as ring sizes and diameters are mixed in the same statistical group. When nomograms are designed, performing a correct statistical analysis is important or the analysis will give more weight to factors that might not contribute as

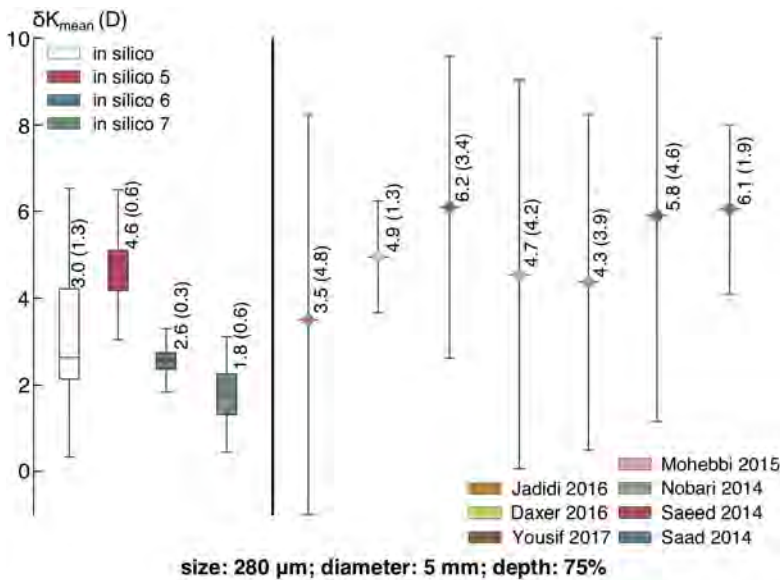


Figure 6.3: Prediction of change in mean keratometry for three different MyoRing diameters (5, 6, and 7 mm). *In-silico* simulations (left) predicted the change in mean keratometry within those changes reported for patients with High Myopia and Keratoconus. Note that clinical cases contain different ring configurations and, as such, it increases the uncertainty.

much or neglect variables that should be accounted for. In fact, if we analyze the Spearman correlation matrix²⁷ between input factors (anatomical and mechanical) and output factors (δK_{mean} and δSE) one might think that only the diameter (inverse correlation) and the pre-surgical optical values such as SE and K_{mean} (direct correlation) are relevant in order to plan the surgery.

When populations are grouped by known variables such as ring diameter, other variables such as ring size, IOP or mechanics seem to have an impact on the change in keratometry and spherical equivalent and cannot be disregarded. In particular, when grouping by diameter size, intraocular pressure (inverse correlation) and mechanics (direct correlation) are of similar importance than the size of the cross-section of the ring (direct correlation). Also, grouping by diameter shows that ring size has a huge impact when implants are located close to the centre (diameter of 5 mm) but its importance decreases quickly towards the periphery. Contrarily, the importance of the pre-surgical refractive error, mechanics and IOP does seem to be constant independently on the diameter of the ring. In any case, central corneal thickness (CCT) does not seem to have a great impact in the post-surgical refractive error and its use as biomarker in a nomogram

²⁷ High Spearman's coefficient means that two variables are monotonically related (even if the correlation is nonlinear). A Spearman correlation of zero indicates that there is no tendency for the independent variable to increase (or decrease) when the dependent variable increases.

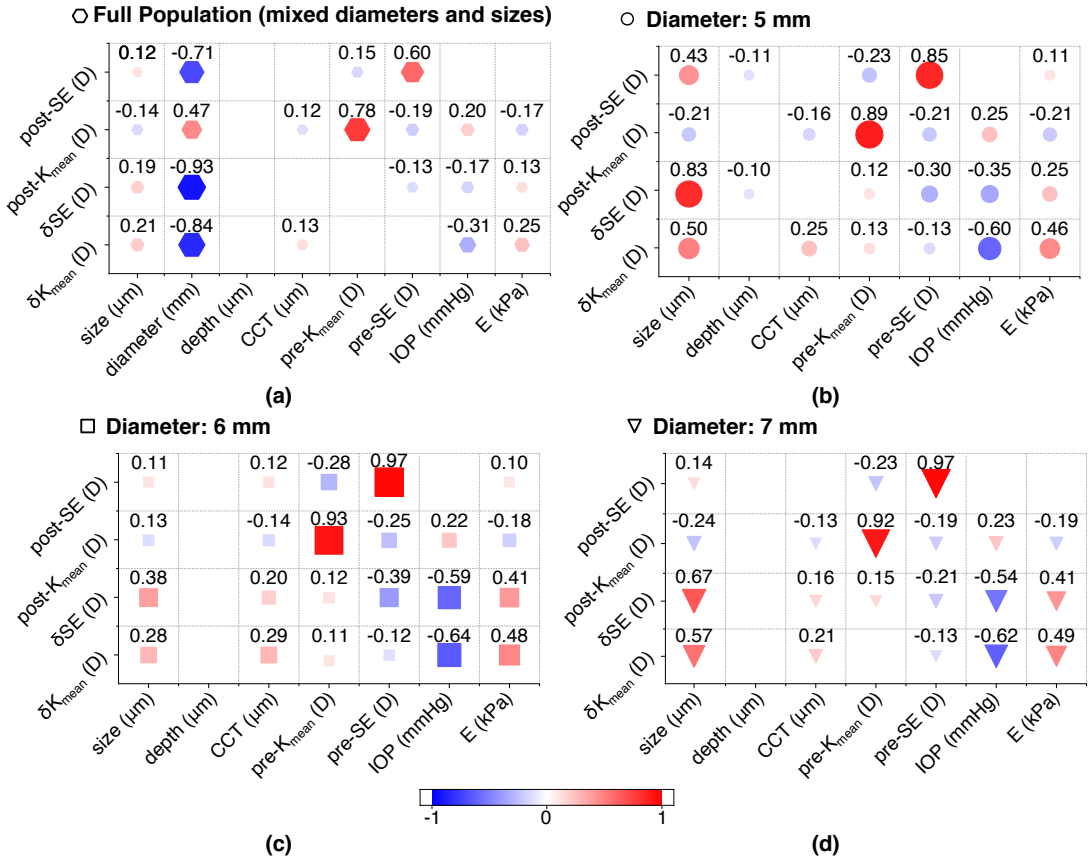


Figure 6.4: Spearman correlation between input parameters and refractive post-surgical outcomes. Only correlations with a significant p-value are shown (p-value < 0.05).

should be reconsidered (not its inclusion as limiting factor for the surgery).

3.3. Corneal strengthening factor of MyoRing

It is an open discussion in the community whether implants stiffen the cornea or not. In particular, it has been estimated that introducing continuous rings in the cornea (i.e., MyoRing) can result in an strengthening factor of two to three.²⁸ At a population level, MyoRing introduces an average strengthening factor at the corneal centre of approximately a 11% (see definition in Equation 5.1, Chapter 5, and in Figure 6.5) which would never reach an increment of 200% even for the worst-case scenario.

²⁸ Daxer 2015

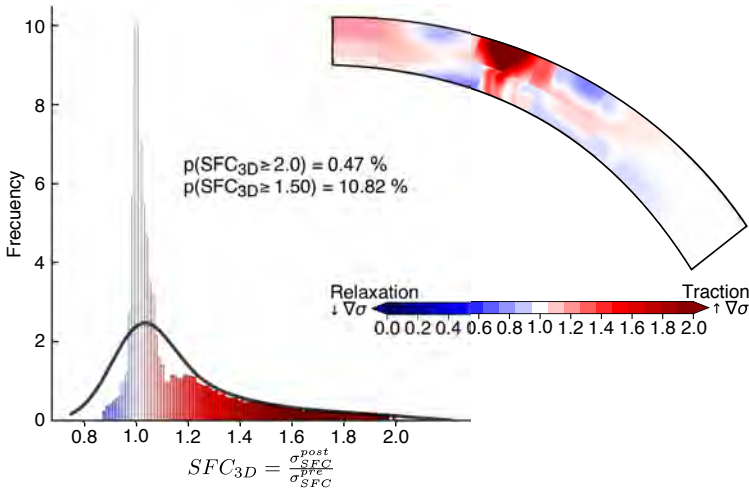


Figure 6.5: Corneal strengthening factor of MyoRing. Ratio between post- and pre-surgical corneal stress in the full cornea. Maximum stiffening occurs close to the ring while the centre of the cornea remains almost unchanged (up to a 20% stiffening on average). The probability of stiffening more than 2 is lower than a 1% and it would occur on the surroundings of the Myoring. Colours in the histogram (left) correspond to colours in the cornea (right).

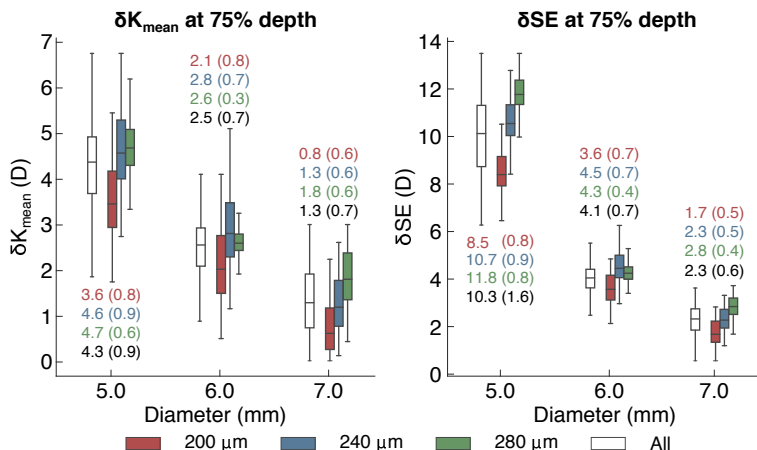
3.4. Predictions of refractive outcomes: towards a mechanically-driven nomogram

Once the model has been validated, it can be used to predict the optical outcomes for different ring combinations. Figure 6.6 outlines that the farther the ring from central cornea, the lower the correction for both δK_{mean} and δSE . In the same vein, the size of the cross-section helps on fine-tuning the average amount of correction achieved by choosing a ring diameter.

Regarding the change in spherical equivalent, the average δSE for a 280- μm MyoRing of 5 mm in diameter at a 75% depth is ≈ 10 D (see white boxplot in Figure 6.6.right) which can be decreased or increased between by ± 1.6 D depending on the implanted ring size (average δSE of ≈ 8.5 D for 200- μm – red boxplot – or average δSE of ≈ 12 D for 280- μm – green boxplot–). It is noteworthy that, as soon as the diameter of the ring increases beyond 5 mm in diameter, the size of the ring plays a minor role and can control a change in diopters of ± 0.4 D.

Regarding the change in average keratometry, the average δK_{mean} for a 280- μm MyoRing of 5 mm in diameter at a 75% depth is ≈ 4.3 D (see white boxplot in Figure 6.6.left) which can be decreased or increased between by ± 0.55 D depending on the implanted ring size (average δK_{mean} of ≈ 3.6 D for 200- μm – red boxplot – or average δK_{mean} of ≈ 4.7 D for 280- μm – green boxplot–). In this case, the increment in diameter of the ring does not

Figure 6.6: Influence of Myoring’s diameter and size on refractive outcomes (average Keratometry and Spherical Equivalent). Change in refraction is mainly dominated by the diameter of the Myoring (greatest change in both Kmean and SE). The size of the Myoring helps in fine-tuning the optical change induced by the diameter. On a population level, the size of the ring would be only decisive for diameters of 5 mm.



seem to dampen the effect of the change in the size of the cross-section.

At this point, Figure 6.7 can be regarded as a first preliminary nomogram in which the clinicians can control the diameter of the ring, the size of the cross-section and the implantation depth in order to achieve a desired refractive correction and, *at the same time*, explicitly including mechanical information such as IOP and mechanics.

In this nomogram the clinicians can observe that, when the implantation depth is a 75% of the stromal thickness, the maximum change in average keratometry will be achieved with highest ring’s cross-section and the lowest diameter (≈ 5 D in average and at a population level), being the same for the maximum change in spherical equivalent (≈ 12 D). Moreover, anatomical and mechanical variations would result in a dispersion in correction below ± 0.5 D (see faded confidence bands around average correction).

Also, by controlling the stromal depth of insertion, the clinician could fine-tune the amount of refractive correction. In particular, changing the implantation depth would always reduce the change in keratometry up to 1.5 D (for MyoRings implanted at a 60%). Regarding the change in spherical equivalent, changing the implantation depth could increase the final refractive correction up to 5 D only for MyoRings of 5 mm in diameter (for MyoRings implanted at a 60%). For MyoRings with higher diameters, changing the implantation depth would decrease up to 2 D the refractive correction in SE (for MyoRings implanted at a 60%).

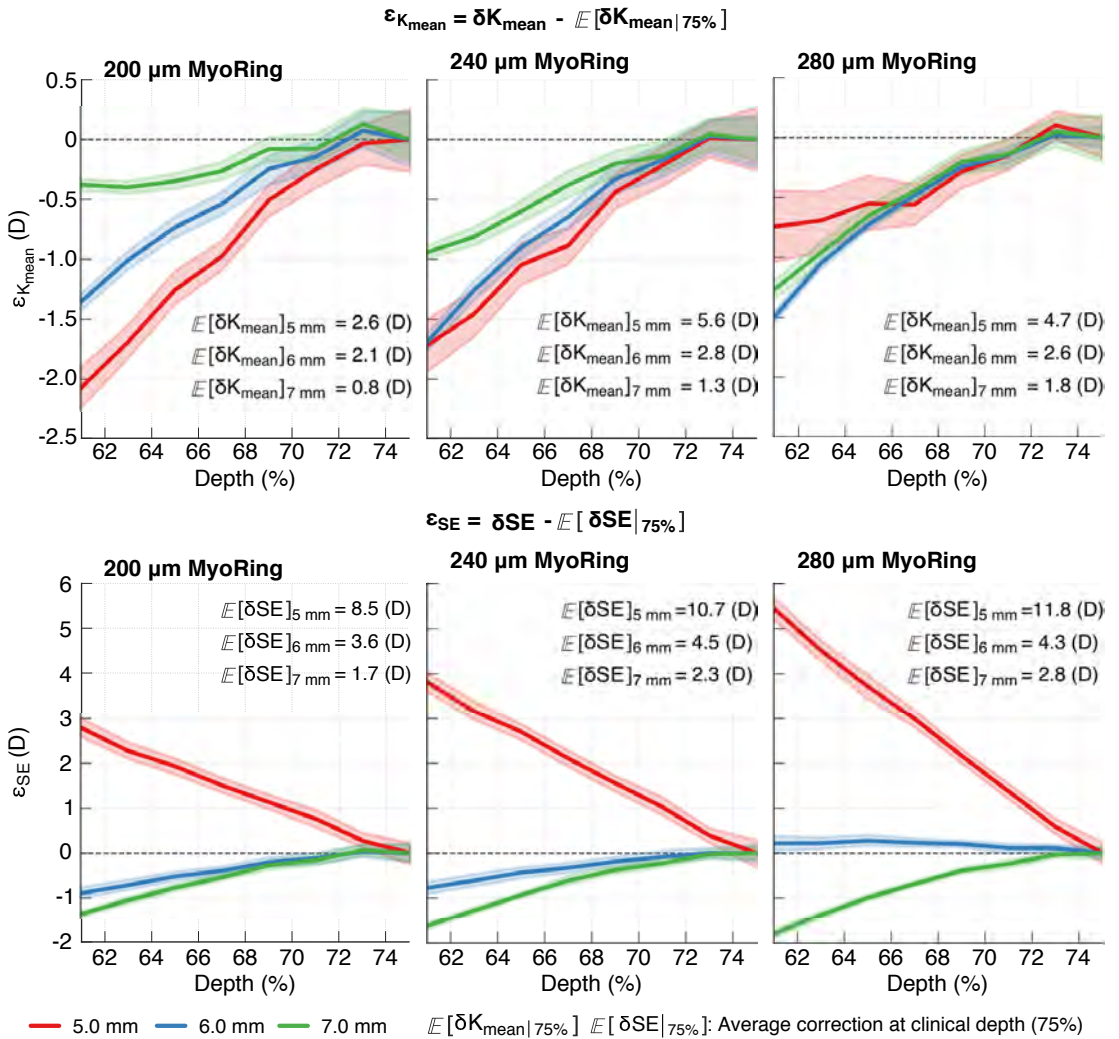


Figure 6.7: Influence of depth on Kmean (left) and SE (right): error introduced on the refractive outcomes of the population due to a change in depth. The depth of reference (ground truth) is 75% of the stromal thickness. The refractive outcomes for the population have been shifted by their average for each diameter (i.e., for a 75% depth, the error has a mean of 0). For example, for a Myoring of 280 microns and 5 mm in diameter, changing the depth by a 15% (from 75% to 60%) would result in a variation of the SE of +6D with respect to its average value (i.e, increasing from 11.5 D in average to 17.5 D).

4. Discussion

Even with the current limitations of our model already described in Chapters 4 and 5, our calibrated *in-silico* simulations were able to predict clinical changes in average keratometry and spherical equivalent at a population level²⁹ and without a priori knowledge of the post-surgical outcomes. This predictive ability enable us to study the effect of different anatomical, mechanical and optical variables in the post-surgical refractive outcomes for MyoRing implantation in high myopia.

Our *in-silico* study in a virtual cohort suggests that mechanical markers should be included as part of the biomarkers used to plan MyoRing insertion. In fact, the study of the correlation matrix outlines two key factors: first, that nomograms must be grouped by surgical features such as ring diameter (otherwise, statistical nomograms can be misleading); second, that apart from the pre-surgical keratometry and spherical equivalent, intraocular pressure and tissue mechanics plays a role in the prediction of the post-surgical outcomes. Nevertheless, our research points towards the direction that it is mainly the amount of added intrastromal volume the one controlling the overall refractive change (see Chapter 5). In particular, MyoRing diameter does seem to be the leading factor in achieving a great refractive correction followed by the size of the cross-section or the intrastromal depth implantation which help to fine-tune the final amount of refractive correction.

From a mechanical standpoint, and contrarily to what it has been suggested in other theoretical studies,³⁰ implants do not seem to introduce a corneal stiffening at the corneal centre and, in fact, the ratio between the post- and pre-surgical stress remains below 1.5 at a population level. Not only that, but it does seem that tissue mechanics or the inclusion of pathological tissue would not be decisive on predicting the average change in refraction at a population level (see Figure 6.3).

Overall, this population study strengthened previous conclusions regarding the effect of the ring diameter (see Chapter 5): the farther the ring is located from the corneal centre, the lower is the achieved correction. These results are strongly related to the quick dissipation of the mechanical bulking effect introduced by the ring, which occurs at a local level. For those cases in which it is necessary to achieve a great refractive correction as it is the case of patients with high myopia, it is advised to place a ring of 5 mm in diameter. Once the ring diameter is bigger than 5 mm, only patients

²⁹ Daxer 2017, Rattan 2018, Saad and Somali 2019, Yousif and Said 2018, Daxer et al. 2016, Jadidi et al. 2016, Mohebbi et al. 2016, Nobari et al. 2014, Saeed 2014

³⁰ Daxer 2015

with a moderate myopia can be treated (≈ 6 D).

Eventually, the present study allowed to propose a first preliminary mechanically-driven graphical nomogram in which the clinician can control the size of the ring, its diameter and its stromal implantation depth at a population level. This nomogram allows to control the expected average correction at a population level while controlling the prediction error (confidence interval) due to anatomical and mechanical uncertainties.



Chapter 7

Mechanical Characterisation of

Intrastromal Corneal Ring Segments¹

¹J. Flecha-Lescún, L. Remón, B. Calvo, and M. Á. Ariza-Gracia. **Mechanical characterization of Intracorneal Ring Segments after mechanization.** J. Mech. Behav. Biomed, (Under Preparation), b

Chapter dedicated to characterise the intrastromal corneal ring segments and to obtain their mechanical properties by combination of *in-silico* simulation with uniaxial experimental tests.

Chapter Contents

1. Introduction	178
2. Material and methods	180
<i>Experimental protocol</i>	181
<i>Numerical protocol</i>	181
3. Results	185
<i>Experimental results</i>	185
<i>Uncertainty analysis results and iFEM optimisation</i>	186
4. Discussion	187

1. Introduction

Polymethylmethacrylate (PMMA) is a synthetic resin produced from the polymerisation of methyl methacrylate. PMMA is often used in contacts lenses, spectacle lenses, laser lenses, eye lenses, micro-structured arrays, etc. All these applications require high quality, accuracy and super finish surface profile. Some features more representative of PMMA are low thermal conductivity, optical characteristics, low cost and biocompatibility.²

² Korkmaz *et al.* 2017

PMMA is one of the more widespread materials used in components and implants in Ophthalmology. One of those implants are the intrastromal corneal ring segments (ICRS) used to correct myopia³ or to stabilise and slow down the progression of keratoconus (KC),⁴ by regularising the corneal shape.⁵ There are different typologies of ICRS depending on the cross-section (triangular or hexagonal) or covered arc (MyoRing).

³ Daxer 2017

⁴ Rabinowitz 1998, Fangjun *et al.* 2016

⁵ Fernández-Vega *et al.* 2016

The complex manufacturing process of PMMA starts with propylene, which together with benzene forms the cumene (isopropylbenzene). The cumene is oxidised and treated with acid to form acetone. The acetone is in turn converted in methyl methacrylate ($CH_2 = C[CH_3CO_2CH_3]$), a flammable liquid. Finally, the methyl methacrylate polymerised (its molecules linked together in large numbers) under the influence of free-radical initiators to form solid PMMA. The mechanical characteristics of PMMA are determined by its elastic modulus or Young's modulus, between 1,800–3,300,⁶ the Poisson coefficient, normally 0.4,⁷ and the stress fracture. These mechanical properties of the raw material can be modified by using high precision modelling processes such as intrastromal corneal ring segments milling technology.

⁶ Kling and Marcos 2013, Flecha-Lescún *et al.* 2018

⁷ Flecha-Lescún *et al.* 2018

Dhakad *et al.* (2017)⁸ studied the most influential parameters which affected the surface of the PMMA samples after cutting them with a CNC lathe machine. The mechanical properties of PMMA were a Young's modulus of 686 GPA, Poisson's ratio of 0.22 and a fracture toughness of $3.8 \text{ MPA}^{1/2}$. The variables which affected the cutting process were the cutting speed, feed rate and depth of cut. They concluded that the surface roughness is mostly influenced by the feed rate, followed by the cutting speed and depth of cut. The depth of cut had a very negligible effect on the surface roughness of PMMA material. Also, to obtain a better surface roughness by facing operation of PMMA material the cutting speed should be maximum, feed rate should be minimum and depth of should be moderate. Korkmaz *et al.* (2017)⁹ presented an experimental investigation on micromachinability

⁸ Dhakad *et al.* 2017

⁹ Korkmaz *et al.* 2017

characteristics of PMMA when using single-crystal diamond microendmills towards enabling rapid, accurate, and reproducible fabrication of PMMA parts for a broad range of applications. They made an experimental analysis including a 3^k full factorial design using a straight single-crystal diamond microendmill with a diameter of 450 microns. The variables included in the design were the spindle rotational speeds, the feed rates, and axial depth of cut. The outcomes were the process forces, surface roughness, burr formation, and shape retention. The study showed that micromilling using single-crystal diamond microendmills reduces surface roughness, burr formation, and force magnitudes, while creating high-quality features as compared to those obtained when using commercially available tungsten carbide microendmills. Favorable cutting conditions and machining strategies for effective creation of micro-scale features on PMMA can be identified using the presented micromachinability study. Finally, Nigrovic *et al.*(2017)¹⁰ focused on the characterisation of the influence of laser cutting on the material made from the PMMA. They made a comparison of mechanical properties between the samples cut by the laser beam and those obtained after the conventional method of cutting by milling. The study concluded that the way of cutting has a strong influence on the PMMA samples mechanical properties. The outcome of the experiment is a direct assessment of roughness of the cut samples. It is shown that the laser cutting produces lower values of the surface roughness. However, for manufacturing the structural elements, the more suitable would be application of the milling technology since it results in better mechanical properties of the cut sample.

¹⁰ Nigrovič *et al.* 2017

Experimentally, the traditional mechanical characterisation tests are uniaxial, shear, and biaxial tests. However, sometimes, due to the size of the samples or the final shape of the implant, such as for intrastromal corneal rings, it is very difficult to use traditional methods to characterise material properties. In those cases, experimental trials become more complex as properties cannot simply be derived from the mechanical test and must be supported by an optimisation procedure in order to determine the mechanical properties of the sample.

To the date, there is only one study about the mechanical characterisation which focused on the analysis of the holes which exist at the ends of the rings.¹¹ They are used to handle the rings by the surgeons and locate them within the corneal stroma. The study established that the minimum material strength requirement for the ICRS product was a maximum load

¹¹ Keravision n/y

of 2.22 N.

It is important to know the properties of ICRS after the milling to plan better the handling of the implants, the logistics processes of manufacturing or packaging, and the computational consequences related directly with the rigidity of the PMMA which is considered: convergences problems.

Our study aims at evaluating, for the first time, the mechanical properties of a final ICRS and whether the milling procedure affects its raw mechanical properties. First, the force–displacement relationship for individual implants is determined using an experimental tension test procedure set up to test different ring configurations (triangular, or hexagonal) and sizes. Second, to determine the material parameters, a numerical optimisation pipeline based on finite element simulations is used to map the numerical and experimental responses. Based on the experimental characterisation we assumed that the implant presented two well differentiated parts. Initially, a linear elastic behaviour could be observe, but then, the samples presented an hyperelastic behaviour with damage. From an optimisation standpoint, two numerical approaches were used in order to determine the mechanical properties: i) a Monte Carlo approach was used to perform an uncertainty analysis on the material parameters (Young's modulus, Poisson coefficient and damage) and determine which one should be included in an optimisation loop; ii) an inverse finite element optimisation (iFEM)¹² was performed for each one of the samples in order to determine the sample-specific material properties.

¹² Ariza-Gracia et al. 2017a

2. Material and methods

The Material and Methods section is divided in two subsections: the experimental and the numerical protocol. On the one hand, the experimental test gathers all information about the samples of ICRS, their preparation, and the tension test experiment. On the other hand, the numerical protocol section gathers the information regarding the simulations used to perform the material characterisation. First, a Monte Carlo analysis was performed in order to determine a population–based distribution of the mechanical parameters and the influence of each material parameter on the force–displacement behaviour of the implant. Afterwards, the knowledge yielded by the Monte Carlo analysis was used to tune the material parameters used in the inverse finite element methodology (iFEM). Figure 7.1 outlines the pipeline of the methodology developed.

2.1. Experimental protocol

2.1.1. Intrastromal Corneal Ring Segments samples

An overall of fifty tension tests ($n=50$) were carried out for different ICRS. In particular, two commercial ICRS were analysed: Intacs (Addition Technology, Sunnyvale, USA), whose cross-section is hexagonal, and Ferrara (AJL Ophthalmic, Vitoria, Spain), whose cross-section is triangular. To study the effect of the cross-section size and shape, two different cross-section thicknesses (250 and 350 μm) were analysed for each cross-section shape ($n=40$ in groups of 10; arc length diameter of 6 mm). Additionally, to study the impact of the change in diameter, a Ferrara of 5-mm in diameter and 250 μm ($n=10$) was evaluated. The covered angle of each sample was always 150° . The geometry of each sample analysed is shown in Figure 7.2 whose dimension are shown in Table 7.1.

2.1.2. Tension test

An INSTRON MicroTester model 5548 was used to characterise the samples. The system is very versatile, since it performs tests with very low forces with very high displacement resolution, and is suitable for loads of at up to 2 kN.

ICRS have a small hole in each extreme, called Sinkey's hole, that aids in manipulating the segments during the surgical procedure. In our case, those holes were used in order to prepare each sample before the tension test. The braided silk suture of 5/0 was threaded into each ring hole and the loose ends were glued with sandpaper to prevent slippage at the grip. The suture was stiff enough so as to guarantee that there will not be a stretch that results in a concomitant force-displacement response (results not shown).

After sample preparation, ICRS were placed between grips by holding the suture thread with the sandpaper (see the Figure 7.1). Only the upper jaw moved upwards until the ICRS was hold vertically and parallel to the test direction. The force-displacement response was recorded until the sample broke. Figure 7.1 shows an example of the sample preparation to be tested in the INSTRON 5548 with a 50 N load cell and a speed of 1.27 mm/min.

2.2. Numerical protocol

The numerical protocol covers both the *in-silico* models used to simulate the tension experimental test and the optimisation strategies used to obtain

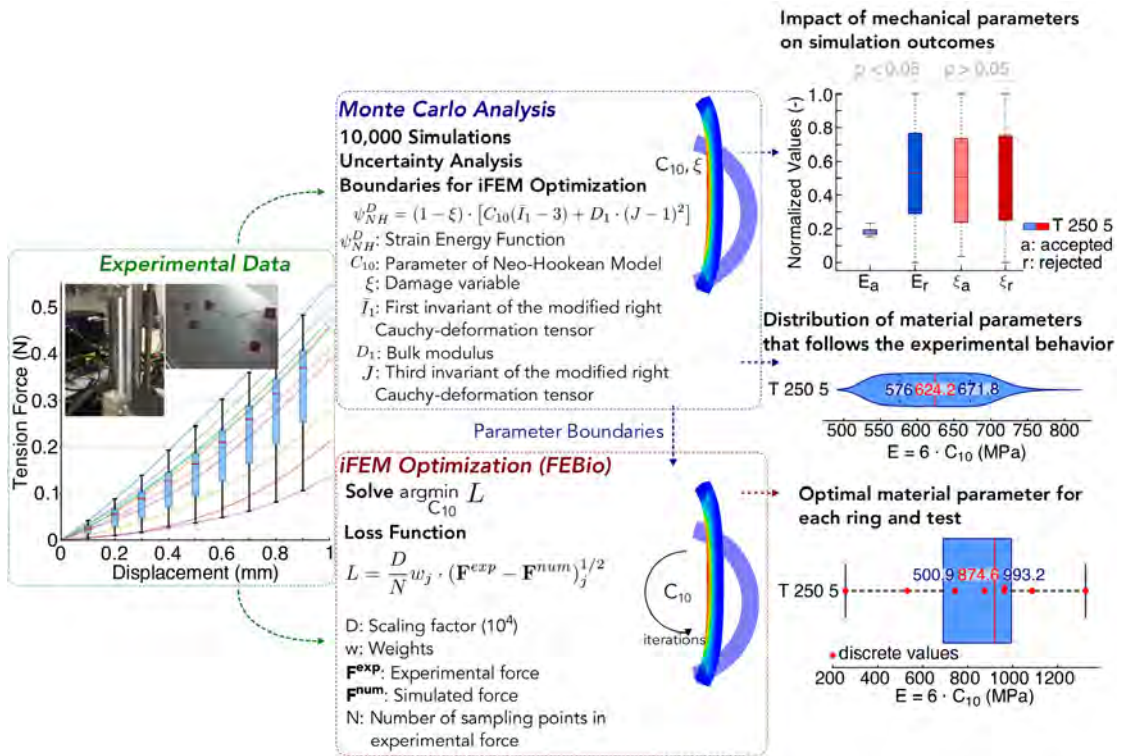


Figure 7.1: Overview of the mechanical characterisation pipeline (experimental and numerical steps). First step, experimental protocol (left): a typical force-displacement behaviour for a given ring typology. Mechanical tests were done in an INSTRON 5548 machine. ICRS were held and pulled from by a suture thread passed through the Sinkey's hole. Second, numerical protocol (center): **1. Monte Carlo Analysis (in blue)** was used to analyse the impact of mechanical parameters on simulation outcomes (**Top**) and to determine a population-based distribution of material parameters for each ring typology (**Bottom**). Results from the Monte Carlo analysis were used a priori to instruct the **2. iFEM optimisation (in red)** which was used to determine the sample-specific material properties.

the mechanical properties for each implant. First, an uncertainty analysis was carried out, based on Monte Carlo simulations, which aims at estimating how the input variables (material parameters) affect the output variable (force) and whether the set of input parameters is sound and necessary for the optimisation. Second, and inverse finite element (iFEM) optimisation was used to determine the sample-specific material properties for each sample individually. Monte Carlo results were used to a priori limit the initial guess and variable bounds of the iFEM optimisation.

All the finite element computations were done using FEBio, an open-source software.¹³ The iFEM optimisation procedure was solved in Matlab (Matrix Laboratory, Mathworks)¹⁴ using a constrained minimisation (fmincon). The Monte Carlo analysis was performed using Python¹⁵ and the HPC cluster UBELIX (University of Bern).

¹³ Maas et al. 2012

¹⁴ MATLAB 2013

¹⁵ van Rossum and Drake 2009

2.2.1. Computational finite element models

Five geometrical models were built, one for each ICRS typology. The dimensions and mesh features are shown in Table 7.1 and Figure 7.2 and geometry features are explained in the Section 2.1.1. All models were composed of linear hexahedral elements (C3D8). A sensitivity analysis was performed in order to determine the mesh size that properly captured the stress distribution at the central cross-section of the ICRS (breaking point), while providing an accurate record of force and the displacement in the extremes of the rings.

Boundary conditions to mimic the tension test were a 1.5 mm vertical displacement was imposed at top of the ring (point B in Figure 7.2) and a restrained displacement at bottom of the ring (point A in Figure 7.2). The remaining solid rigid motions were allowed as in the experiment.

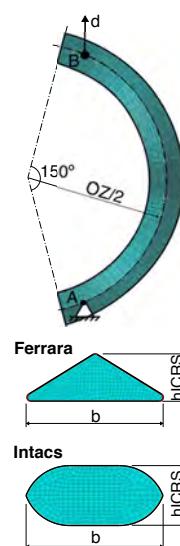


Figure 7.2: ICRS geometry and finite element model.

Ferrara (Triangular cross-section)							
ID	n	hICRS (μm)	b (μm)	OZ (mm)	d.o.f	Elements C3D8	
T 250 5	10	250	600	5	65,367	18,800	
T 250 6	10	250	800	6	88,209	25,600	
T 350 6	10	350	800	6	109,107	32,320	
Intacs (Hexagonal cross-section)							
H 250 6	10	250	800	6	86,994	25,840	
H 350 6	10	350	800	6	93,378	28,158	

Table 7.1: Geometrical and mesh features. The dimensions correspond with the Figure 7.2. ID: Identification name; n: number of samples tested; hICRS: thickness of the ICRS; b: width of the ICRS; OZ: diameter of the ICRS; d.o.f: degrees of freedom.

2.2.2. Material model of the ICRS

Based on the force–displacement behaviour yielded by the experiments (first column of the Figures 7.3 and 7.4) and the large displacements present in the experiment, a 1–parameter hyperelastic material model (Neo–Hookean¹⁶) was chosen to characterise the material parameters. Moreover, due to the brittle fracture observed experimentally, a simple damage penalisation was included (ζ).

¹⁶ Rivlin 1948

$$\psi_{NH}^D = (1 - \zeta) \cdot \underbrace{\left[C_{10} \cdot (\bar{I}_1 - 3) + D_1 \cdot (J - 1)^2 \right]}_{\psi_{NH}} \quad (7.1)$$

where C_{10} is the parameter of Neo–Hookean model, \bar{I}_1 is the first invariant of the modified right Cauchy–deformation tensor, D_1 is the bulk modulus, and J is the third invariant of the modified right Cauchy–deformation tensor. Finally, the evolution of damages over time (ζ) was based on a Weibull cumulative distribution function (Equation 7.2).

$$\zeta(t) = 1 - \exp \left[- \left(\frac{t}{D_{Threshold}} \right)^\alpha \right] \quad (7.2)$$

if $\zeta(t) \geq D_{max}$, then $\zeta(t) = D_{max}$

where t is the simulation time, α took the value of 1, $D_{Threshold}$ is the parameter to adjust with the uncertainty analysis, and D_{max} was 0.95.

As the Neo–Hookean’s FEBio formulation is based on Lamé parameters, the Young’s modulus and Poisson’s ratio were provided and internally converted by FEBio (Equation 7.3).

$$\begin{aligned} C_{10} &= \frac{E}{4 \cdot (1 + \nu)} \\ D_1 &= \frac{2 \cdot E}{3 \cdot (1 - 2\nu)} \end{aligned} \quad (7.3)$$

Force–displacement behaviour was insensitive to changes in the Poisson’s ratio between 0.1 and 0.4 and, thus, a constant value of 0.3 was selected for all the simulations.

2.2.3. Uncertainty Analysis

A global uncertainty analysis aims at providing information about whether or not the input parameters (and, therefore, the experiment) were properly

chosen. Not only that, but it also can be used to estimate the statistical distribution of each material parameter by using appropriate filtering techniques. An overall of 50,000 simulations (10,000 for each ring typology) were simulated using the latin hypercube sampling (LHS).¹⁷ Due to the lack of a priori knowledge, the combinations were generated assuming that each input variable came from a uniform distribution. Two acceptance regions were defined by the standard deviation region (in green) and the interquartile region of the experimental tests (in red; Figures 7.3 and 7.4). A Kolmogorov–Smirnov statistical significance test was performed in order to determine the relevance of all input variables.

¹⁷ Helton and Davis 2002

2.2.4. Inverse finite element method (iFEM) optimisation

The iterative workflow for the constrained optimisation attempted at minimizing the difference between the experimental and numerical responses (loss function, Equation 7.4 and Figure 7.1) so that the optimal set of material parameters are obtained for each ring typology. The initial guesses and boundary constraints were set based on the results of the uncertainty analysis.

$$L = \frac{D}{N} w_j \cdot (\mathbf{F}^{\text{exp}} - \mathbf{F}^{\text{num}})_j^{1/2} \quad (7.4)$$

where, D is a Lagrange penaliser, whose value is 10^5 , w is an array of weights, \mathbf{F}^{exp} is the experimental force, \mathbf{F}^{num} is the numerical force, and N is the number of points where force is evaluated.

3. Results

3.1. Experimental results

Force–displacement experimental results are depicted in the first column in Figures 7.3 and 7.4. All the samples broke beyond a 1 mm displacement with maximum forces below 1 N. The force–displacement behaviour was linear up to a displacement of ≈ 0.4 mm but, from that point on, damage started to propagate resulting in microfractures and sudden drops in force. Beyond the 1 mm displacement, the triangular samples broke before the hexagonal samples, showing clearly that the hexagonal cross-section, withstands more in the tensile test.

Table 7.2: Results of Young's Modulus corresponding with the boxplots of the Figure 7.6.

Representation of the boxplot values in Figure 7.6, where the results provided by the uncertainty analysis (green) and by the iFEM optimisation (blue) are represented. Accepted represents the number of simulations and the percentage located within range between quartiles. Min., q_1 , Mean, q_3 , and Max. values correspond to the minimum, first quartile, mean, third quartile, and maximum values, in MPa, respectively.

ID	Accepted	Min.	q_1	Mean	q_3	Max.
T 250 5	544 (5.44%)	525.1	576	624.2	671.8	790.1
		257.9	500.9	874.6	993.2	1,321.4
T 250 6	937 (9.37%)	390.9	472.8	553.2	634.7	714.3
		187.4	376.9	808.2	1,394	1,766
T 350 6	672 (6.72%)	431.6	493	549.7	607.5	666.5
		140.8	400.2	780.7	1,121.9	1,121.9
H 250 6	200 (2%)	81.1	91.1	101.1	111	121.2
		17.9	75.1	124.3	170.5	200
H 350 6	616 (6.16%)	230.1	262.1	293.2	323.7	435.6
		73	161.9	286	321.2	393.6

3.2. Uncertainty analysis and iFEM optimisation

After filtering the numerical responses falling within the experimental interquartile q_1 – q_3 region (see blue lines falling within the red lines in central column; figures 7.3 and 7.4), only less than 10% of the simulations remained as valid. The statistical distribution for the Young's modulus of the accepted population was evaluated for each ring typology (see data in green in Table 7.2). For the triangular population, Young's modulus varied between 400 and 800 MPa, with an average value of 575 MPa. For the hexagonal population, Young's modulus varied between 80 and 435 MPa, with an average value of 200 MPa.

The Kolmogorov–Smirnov test between the accepted and rejected populations of the material parameters (Young's modulus and damage threshold) outlined that there was a significant difference for the Young's modulus while no difference was present for the damage threshold (Figure 7.5.a). Hence, the damage threshold can be given as a fixed parameter (Table 7.3) for the optimisation, being removed from the optimisation variables as its variation would not affect the mechanical response of the system. When analyzing the correlations between the material parameters (Young's modulus and damage threshold) to the force–displacement experimental data, a strong and direct correlation between Young's modulus and maximum force was observed while no correlation between damage and force was observed.

Results of the sample–specific iFEM optimisation are depicted in the third column in figures 7.3 and 7.4. Contrarily to the population–base approach used in the Monte Carlo simulations, a value of Young's modulus was obtained for each ring typology and experiment. In this specific case, the numerical results seem to better match the experiments because each

ID	$D_{\text{Threshold}}$
T 250 5	5.198
T 250 6	15.984
T 350 6	5.413
H 250 6	60.551
H 350 6	3.520

Table 7.3: Fixed damage value for each population.

individual response was fitted individually. However, no information about the statistical distribution of the mechanical parameters or the uncertainty analysis could be performed. The statistical distribution for the Young's modulus was evaluated for each ring typology (see data in blue in Table 7.2). For the triangular population, Young's modulus varied between 150 and 1400 MPa, with an average value of 820 MPa. For the hexagonal population, Young's modulus varied between 20 and 400 MPa, with an average value of 200 MPa.

Eventually, three main differences can be observed when comparing the statistical distributions obtained with both methods (Figure 7.6). First, average values seemed to slightly differ for both methods (a difference of 200 MPa between Monte Carlo and iFEM optimisations). Second, there was a difference in the average Young's modulus of more than 200 MPa between triangular and hexagonal populations. Third, there was a difference in Young's modulus of more than 150 MPa between sizes for the hexagonal population, while for the triangular population the Young's modulus remained constant regardless size or arc length.

4. Discussion

For the first time the mechanical stiffness of ICRS implants after manufacturing has been assessed. Our results suggest that assuming the same material stiffness as the raw material (1,600–3,600 MPa¹⁸) is wrong. Due to the impossibility of directly testing the final implant with traditional tests, a combined experimental and numerical framework has been developed. The use of *in-silico* models in combination with experimental tests yielded the mechanical stiffness of each individual population (Ferrara–triangular and Intacs–hexagonal). For the Ferrara population, the average Young's modulus was up to 4 times lower than the Young's modulus of the raw material, regardless the numerical method used for its evaluation. Moreover, neither the ring size, nor its diameter affected the mechanical results. For the Intacs population, the average Young's modulus was up to 10 times lower than the Young's modulus of the raw material. Surprisingly, there was a significant difference in mechanical stiffness between the triangular and hexagonal populations and between hexagonal cross-section sizes. Theoretically, as the Young's modulus is independent on the geometry, this should not be the case for hyperelastic materials and, therefore, we cannot find another explanation other than a difference during the manufacturing

¹⁸ Kling and Marcos 2013, Flecha-Lescún et al. 2018, Ebrahimian et al. 2019

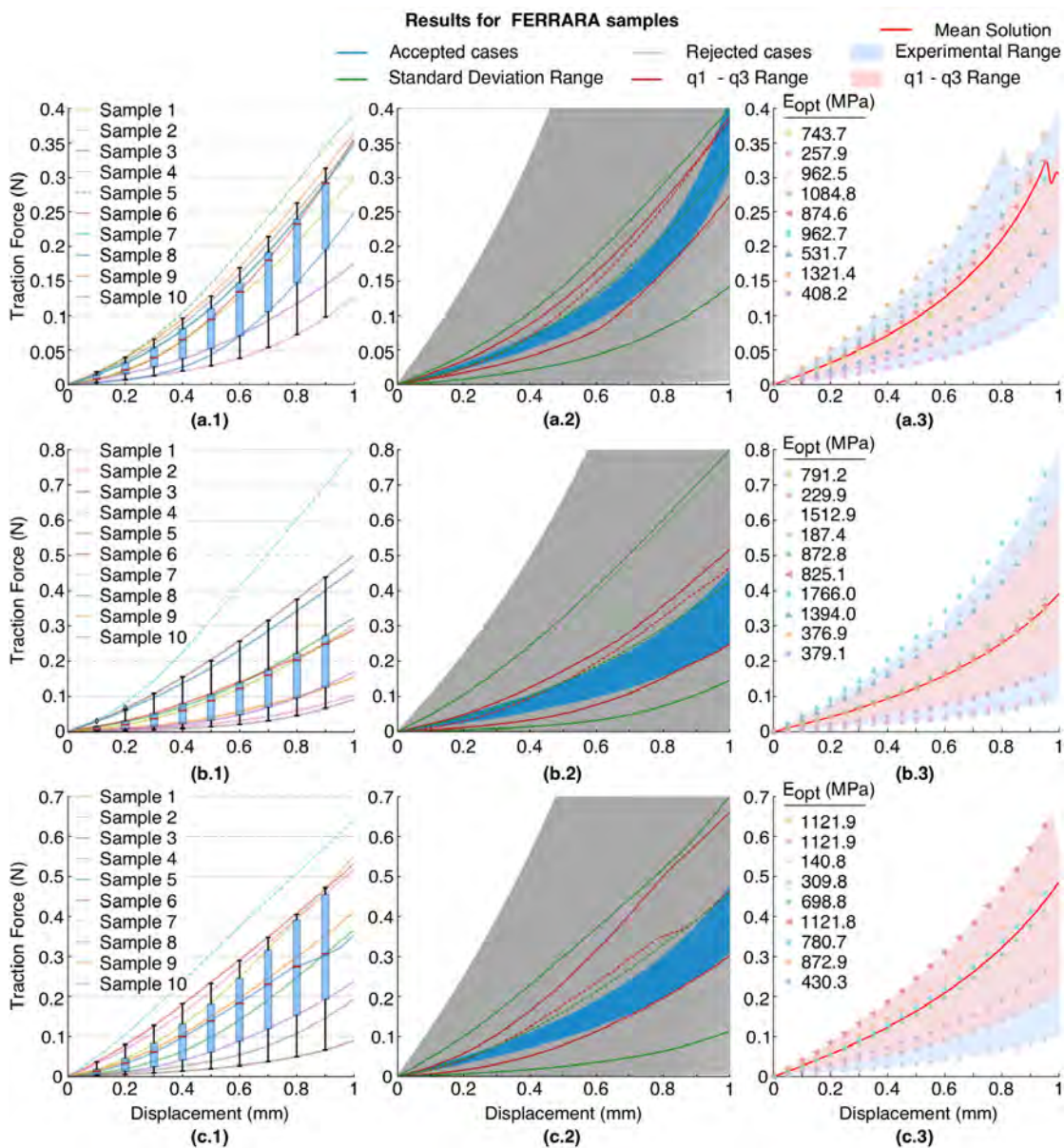


Figure 7.3: Results for ICRS with triangular cross-section. Row (a) shows the results for a diameter of 5-mm and 250 μm thickness; Row (b) shows the results for 6-mm and 250 μm thickness; Row (c) shows the results for 6-mm and 350 μm thickness. Column (1) shows the force–displacement experimental results (the dash lines does not consider to characterise); Column (2) shows the uncertainty analysis (accepted *in-silico* cases in blue; rejected *in-silico* cases in gray); Column (3) shows the results of iFEM optimisation.

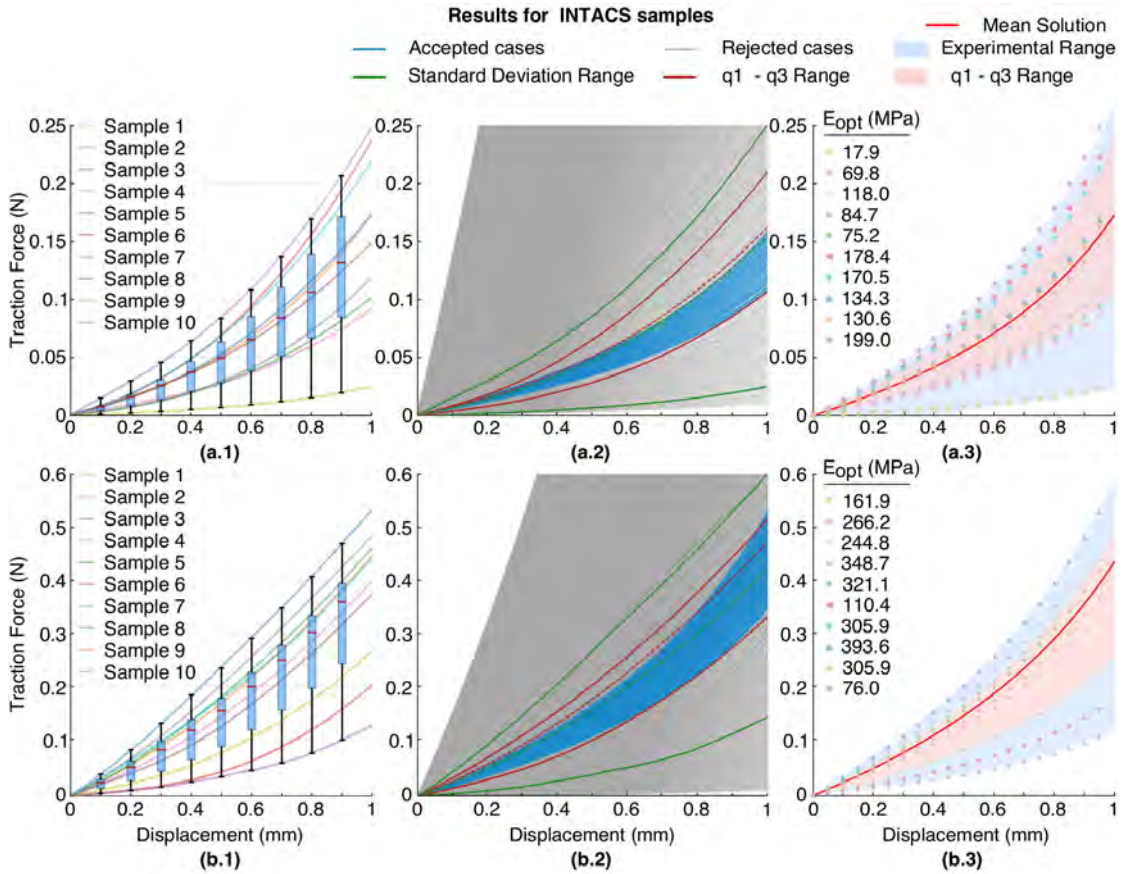
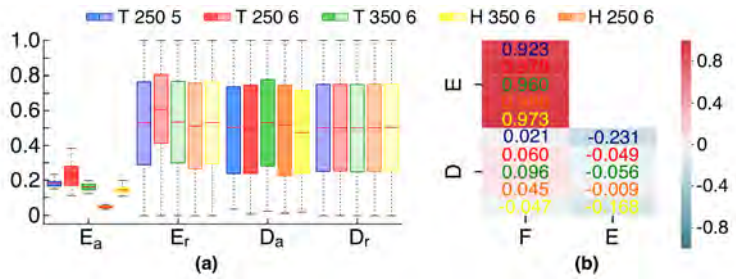


Figure 7.4: Results for ICRS with hexagonal cross-section. Row (a) shows the results for a diameter of 6-mm and 250 μm thickness; Row (b) shows the results for 6-mm and 350 μm thickness; Column (1) shows the force–displacement experimental results (the dash lines does not consider to characterise); Column (2) shows the uncertainty analysis (accepted *in-silico* cases in blue; rejected *in-silico* cases in gray); Column (3) shows the results of iFEM optimisation.

Figure 7.5: Uncertainty analysis: impact of variables. (a) Statistical distributions for the accepted/rejected mechanical parameters. (b) Correlation matrix between the variables traction force (F_{\max}) in N, young's modulus (E) in MPa, and damage ($D_{\text{Threshold}}$).



process such as the presence of regions with stress concentration.

Of course, the present study is not exempt of limitations. From an experimental point of view, a suture thread was included in order to perform the tension test experiments by pulling from it. This would introduce an additional, non-rigid element that should be introduced in the optimisation procedure. However, for the sake of simplicity it was considered as a solid rigid and removed from the simulation. From a modelling point of view, fracture seems to play a role during the experiments as microcracks developed during the experiment causing the force to drop. As fracture was out of the scope of the study, we introduced a simple damage penalisation that could be improved in the future. In any case, when the experimental displacement range is below 1 mm, damage did not seem to affect the output of our simulations.

Moreover, two numerical methods have been presented here in order to determine the mechanical properties of the ICRS. Monte Carlo simulations are regarded as a global optimisation and are useful to perform uncertainty analysis which help us to understand whether the input variables of our experiment were well chosen. Unfortunately, these methods provide a population-based information about the material parameters and are not useful in providing a tailored sample-specific optimisation for each one. On the other hand, iFEM optimisation procedures can provide the optimal set of parameters that fits a specific experimental response, but they are slow (i.e., difficult to implement in HPC clusters) and do not provide insights on the statistical behaviour of a population. In any case, a combination of both can give great results and insights.

In sum, from an operational point of view, there was a direct, linear and strong correlation between the Young's modulus of the sample and the maximum force before breaking, which could be used in the production plant

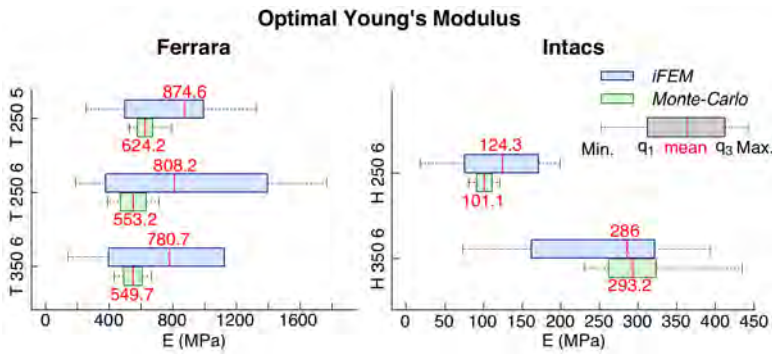


Figure 7.6: Young's Modulus statistical distribution for different populations and methods. Ferrara—triangular (left) and Intacs—hexagonal (right); iFEM (blue boxplots) and Monte Carlo (green boxplots).

in order to assess in the post-milling material stiffness without reproducing the full pipeline presented in this study. In any case, although ICRS are still many order of magnitudes stiffer than the cornea, the surgical procedure is safe and there will not be fracture problems. Nevertheless, care must be taken during in further post-milling manufacturing steps, packaging or explicit numerical simulations in which the stiffness ratio between materials drive the convergence.



Chapter 8

Outcomes and Future Lines

This chapter contains the main findings that have arisen from the current work. It also includes all the scientific publications and conferences where these results and conclusions have been presented.

Chapter Contents

1. Main conclusions and original contributions	194
<i>Clinical contributions</i>	<i>194</i>
<i>Biomechanical and computational contributions</i>	<i>196</i>
2. Scientific publications (Journal Citation Report)	197
3. Conferences	198
4. External fundings	199
5. Other relevant publications	200
6. Future lines	200

1. Main conclusions and original contributions

A novel computational methodology to simulate the additive surgery of the intrastromal corneal ring segments and the intrastromal continuous rings has been developed in the present thesis. Due to the multidisciplinary character of this work and its relation to Ophthalmology, we group the major contributions in clinical and computational and mechanical contributions. Clinical conclusions are focused on helping clinicians and surgeons to understand the post-surgical biomechanical effects of these implants, to help on explaining several phenomena that currently occur in clinics but lack of scientific explanation and, in the future, to better plan the surgery without relying in purely empirical nomograms. Computational and Mechanical contributions are related to the technical details of the simulation.

1.1. Clinical contributions

- Corneal kinematics is modified after ring implantation. This behaviour is a direct consequence of the rigidity of the implant that restricts the physiological radial and circumferential displacement. The implant acts as a dynamic pivot that is able to move and rotate within the corneal stroma, modifying the corneal kinematics. Therefore, both segments and complete rings cannot be considered as an auxiliary limbus, since it moves during circadian variation of the intraocular pressure.
- The main difference between full rings and corneal segments is the amount of optical correction that each can achieve, being higher for continuous implants such as the MyoRing. This higher correction is related to two factors. First, due to the surgical procedure. Complete rings must be inserted into a dissection pocket that crosses the entire cornea from side to side, resulting in a more compliant cornea and, therefore, a higher change in axial length. Second, the amount of volume added by complete rings (i.e., diameter and cross-section size) is higher and, therefore, their impact in the corneal center is higher.
- Implants do not strengthen the cornea globally, but introduce a localised mechanical deformation which regularise the corneal surface by adding a volume within the corneal stroma. The surface regularisation is induced by the bulking effect which is associated with a change of the optical properties: the closer the implant locates of the corneal apex, the more optical change is produced. Therefore, the correction achieved depends on the amount of added volume and the diameter of the implants.

- The corneal strengthening factor (SFC_{3D}) is an indicator of how much stiffer the cornea is once the ring is implanted. It is defined as the ratio between the stress after and before the surgery. A maximum SFC_{3D} of 1.5 is achieved in the center of the cornea with the complete ring (MyoRing). This factor is practically 1 for intrastromal corneal ring segments. This means that if the keratoconus is a stress-driven phenomenon, the only ring which is able to stabilise the disease is the full ring. In addition, it seems that the predictions of the numerical model are similar for corneas with keratoconus and for corneas with high myopia, thus it is likely that the ring is the most important factor, more than corneal tissue.
- Implant extrusion could be related to the gradient of principal stresses in the surroundings of the corneal incision. When the implants are located at 50% depth, the positive stresses in the corneal tissue above the ring tend to tear up the tissue in the surroundings of the scar through where the ring is inserted. At the same time, the positive stresses under the ICRS tend to stretch the tissue and push the ring up. In combination, both behaviours can cause the fibrous tissue of the scar to tear up and the corneal stroma to expel the ring.
- The most relevant implant's parameter affecting patient's vision is the volumen (which comes from the combination of the ring's diameter and cross-section size). Therefore, diameter is the most relevant parameter affecting refractive correction. The closer to the center, the higher the refractive correction. Cross-section size is the second most relevant parameter affecting refractive correction. By combining these two parameters, it is possible to regulate the spherical equivalent in each situation, using the ring size as a fine adjustment if the diameter had been fixed. The smaller the ring diameter, the greater the impact on the spherical power but the smaller the impact on the cylindrical power. Finally, the least relevant parameter affecting patient's visual acuity is the insertion depth providing that implants are located at a clinical depth range between 60% and 75%. 500 μm rings should not be used in diameters lower than 7 mm because they increase high order aberrations.
- The manufacturing angle (α_M) drives the post-surgical rotation of ring segments in the stroma. Implants placed tangentially to the curvature of posterior corneal surface presented higher stability. The over-stressed

corneal stroma resulted in forces and angular momentum of the implant, which resulted in an implant rotation inside the cornea.

- A preliminary mechanically-driven nomogram has been developed for assessing on MyoRing surgical implantation. It can be used to decide the cross-section size, diameter and intrastromal depth at which to insert the MyoRing depending on the amount of correction needed. A further clinical validation is necessary.

1.2. Biomechanical and computational contributions

- Two methodologies to simulate the insertion surgery of intrastromal rings have been developed. The first one is based on generating a hole in the corneal stroma by means of a pressure control. The second one is based on generating a gap by using an auxiliary tool that displaces the stroma. Pressure-based methodologies were disregarded because of the low convergence rate and the lack of versatility. Displacement-controlled methodologies was generic enough to simulate dissection pocket and tunnels, commercial implants such as Keraring, Ferrara (triangular cross-section), Intacs (hexagonal cross-section) or MyoRing, and to use anisotropic mechanical models.
- Calibrated *in-silico* models were able to predict clinical data without further a priori information. Moreover, optical results are in good agreement with different clinical studies including healthy and keratoconic corneas. This low discrepancy, even though pathological tissue was not accounted for in our *in-silico* models, might suggest that, at a population level, mechanical properties or heterogeneity will not drive the post-surgical optical outcomes.
- For implants with an arc length of more than 320° , two-dimensional axisymmetric simulations offer a good trade-off between accuracy in the estimation of refractive correction (spherical equivalent) and saving computational time and resources.
- Anisotropic and isotropic material models resulted in similar optical predictions and, thus, anisotropy could not be necessary for estimating the post-surgical corneal state.
- The friction between tissue and implant is important and cannot be disregarded as, depending on the friction level, up to 3 diopters can be

underestimated.

- The manufacturing process could affect the (apparent) mechanical properties for implants. Post-milling ICRS stiffness was up to 4 orders of magnitude lower than the one of the raw PMMA material (1,600–3,300 MPa). Although this would not affect the surgical procedure itself, it is important to consider the correct stiffness for further mechanical manipulation, packaging or when used in finite element explicit simulations (i.e., slower convergence rate).

2. Scientific publications (Journal Citation Report)

An overall of 2 journals published and 2 more in preparation contain the contribution of the current thesis,

1. **J. Flecha–Lescún**, B. Calvo, J. Zurita, M.Á. Ariza–Gracia. *Template-based methodology for the simulation of intracorneal segment ring implantation in human corneas*. Biomechanics and Modeling in Mechanobiology 2018 Mar; 17(4): 923–938. Doi: 10.1007/s10237-018-1013-z. Impact Factor: 2.527 (2019). Q2 (42/87), Biomedical Engineering. Data base: Web of Knowledge (InCite JCR).
2. M.Á. Ariza–Gracia, **J. Flecha–Lescún**, P. Büchler, B. Calvo. *Corneal biomechanics after intrastromal ring surgery: optomechanical in silico assessment*. Translational Vision Science and Technology 2020 October; 9(11)26: 1–16. Doi: 10.1167/tvst.9.11.26. Impact Factor: 2.112 (2019). Q2 (28/60) Ophthalmology Science. Data base: Web of Knowledge (InCite JCR).¹
3. **J. Flecha–Lescún**, P. Büchler, B. Calvo, M.Á. Ariza–Gracia. *Modelling strategies for the simulation of corneal intrastromal ring surgeries*. Annals of Biomedical Engineering (Under Preparation). Impact Factor: 3.324 (2019). Q2 (30/87) Biomedical Engineering. Data base: Web of Knowledge (InCite JCR).
4. **J. Flecha–Lescún**, L. Remón, B. Calvo, M.Á. Ariza–Gracia. *Mechanical characterisation of intrastromal corneal ring implants*. Journal of the Mechanical Behavior of Biomedical Materials (Under Preparation). Impact Factor: 3.372 (2019). Q2 (27/87) Biomedical Engineering. Data base: Web of Knowledge (InCite JCR).

¹ First and second author contributed equally

3. Conferences

The present work has been presented in an overall of 14 conferences (12 international and 2 national), from which 8 were oral presentation (1 invited presentation) and 6 posters:

1. **J. Flecha–Lescún**, M.Á. Ariza–Gracia, Á. Orillés–Gonzalo, J.F. Rodríguez–Matas, B. Calvo. *Computational simulation of the contact tonometry: can the contact Tonometry predict pathologies of the corneal tissues?* Poster. VII Summer School on Biomechanics and Modeling in Mechanobiology. July 2016, Graz (Austria).
2. **J. Flecha–Lescún**, M.Á. Ariza–Gracia, J. Zurita, B. Calvo. *Simulación 3D de Implantes de anillos intraestromales para la estabilización del queratocono*. Oral Communication. VI Jornada de Jóvenes Investigadores del Instituto de Investigación en Ingeniería de Aragón (I3A). June 2017, Zaragoza (Spain).
3. **J. Flecha–Lescún**, M.Á. Ariza–Gracia, J. Zurita, B. Calvo. *3D Simulation of intrastromal corneal ring implant for keratoconus stabilisation*. Oral Communication. XXIII Congress of European Society of Biomechanics (ESB), July 2017, Seville (Spain).
4. B. Calvo, I. Cabeza, **J. Flecha–Lescún**, L. Remón. *In–Silico biomechanical stability of intraocular lenses*. Poster. XXIII Congress of European Society of Biomechanics (ESB), July 2017, Seville (Spain).
5. **J. Flecha–Lescún**, M.Á. Ariza–Gracia, M.Á. del Buey, J. Zurita, B. Calvo. *3D Simulation of intrastromal corneal ring implant for keratoconus stabilisation*. Electronic Poster. XXXV Congress of European Society of Cataract and Refractive Surgeons (ESCRS), October 2017, Lisbon (Portugal).
6. **J. Flecha–Lescún**, M.Á. Ariza–Gracia, J. Zurita, B. Calvo. *Simulación personalizada de la cirugía de inserción de anillos intraestromales (ICRS). Validación con datos clínicos*. Poster. VII Jornada de Jóvenes Investigadores del Instituto de Investigación en Ingeniería de Aragón (I3A). June 2018, Zaragoza (Spain).
7. **J. Flecha–Lescún**, M.Á. Ariza–Gracia, J. Zurita, B. Calvo. *Intrastromal corneal ring segment surgery simulation for patient–specific (PS)*. Poster. VIII World Congress of Biomechanics. July 2018, Dublin (Ireland).

8. **J. Flecha–Lescún**, M.Á. Ariza–Gracia, J. Zurita, P. Büchler, B. Calvo. *Intrastromal corneal ring segment simulation for keratoconus stabilisation*. Oral Communication. Institute of Surgical Technology and Biomechanics (ISTB) Seminar. October 2018.
9. **J. Flecha–Lescún**, L. Remón, B. Calvo, M.Á. Ariza–Gracia. *Mechanical characterization of intracorneal ring segment after mechanization*. Oral Communication. X Congress on Numerical Methods in Engineering (CMM). July 2019, Guimarães (Portugal).
10. **J. Flecha–Lescún**, M.Á. Ariza–Gracia, P. Büchler, B. Calvo. *On the use of eulerian meshes for large deformation problems: application to corneal surgery*. Oral Communication. XXV Congress of the European Society of Biomechanics (ESB). July 2019, Vienna (Austria).
11. **J. Flecha–Lescún**, M.Á. Ariza–Gracia, P. Büchler, B. Calvo. *Expansion–Tool based methodology for insertion MyoRing in corneas*. Oral Communication. XXV Congress of the European Society of Biomechanics (ESB). July 2019, Vienna (Austria).
12. **J. Flecha–Lescún**, L. Remón, B. Calvo, M.Á. Ariza–Gracia. *Impact of mechanization on the mechanical properties of intracorneal ring segments (ICRS)*. Poster. XXV Congress of the European Society of Biomechanics (ESB). July 2019, Vienna (Austria).
13. M.Á. Ariza–Gracia, **J. Flecha–Lescún**, B. Calvo, P. Büchler. *Biomechanically driven simulations of the MyoRing treatment in subjects with high myopia*. Oral Communication. The anual Congress of the Association for Research in Vision and Ophthalmology (ARVO). May 2020, Baltimore (USA).
14. **J. Flecha–Lescún**, B. Calvo, D. Piñero, P. Büchler, M.Á. Ariza–Gracia. *MyoRing simulations can help to control optical refractive outcomes for high myopia*. Oral Communication. XVI Congress of the European Society of Biomechanics (ESB). July 2020, Milan (Italy).

4. External fundings

1. Competitive Research Contract funded by Ministry of Economy and Competitiveness for PhD education, with the project code DPI2014–54981–R, and reference number BES–2015–073630.

2. Mobility scholarship Fundación Ibercaja–CAI. Three months of funding to continue the research stay at Center for Biomedical Engineering Research (ARTORG) (before Institute for Surgical Technology and Biomechanics, ISTB), in Bern, Switzerland.

5. Other relevant publications

1. **J. Flecha–Lescún**, M.Á. Ariza–Gracia, J. Zurita, B. Calvo. *Simulación 3D de Implantes de anillos intraestromales para la estabilización del queratocono*. Vol. 5: Actas de la VI Jornada de Jóvenes Investigadores del I3A – 2nd june 2017. Doi: 10.26754/jji-i3a.201711949.
2. **J. Flecha–Lescún**, M.Á. Ariza–Gracia, J. Zurita, B. Calvo. *Simulación personalizada de la cirugía de inserción de anillos intraestromales (ICRS). Validación con datos clínicos*. Vol. 6: Actas de la VII Jornada de Jóvenes Investigadores del I3A – 8th june 2018. Doi: 10.26754/jji-i3a.201802823.
3. M.Á. Ariza–Gracia, **J. Flecha–Lescún**, J.F. Rodríguez–Matas, B. Calvo. Book Chapter: *Personalized corneal biomechanics*. Book: *Advances in Biomechanics and Tissue Regeneration*. Editor: Mohamed Hamdy Doweidar. Academic Press 2019. ISBN: 978–0–12–816390–0.

6. Future lines

Among all the future research lines which can be developed from the current thesis, the most immediate are:

1. Patient–specific simulations. To adapt the developed methodology to patient–specific models to predict the optical outcomes once the ICRS is implanted. Apart from the tissue anisotropy or patient-specific geometry, the weakness caused by the keratoconus should be introduced in the affected area. Therefore, it would be necessary to precisely locate the area of influence of the keratoconus.
2. Simulating all other commercial rings on average eyes, such as Keraring (Mediaphacos, BeloHorizonte, Brazil), Ferrara (AJL Ophthalmic Ltd., Spain), and Intacs (Addition Technology Inc., USA). The aim of this line of research is to extend the simulations in average virtual patients to all

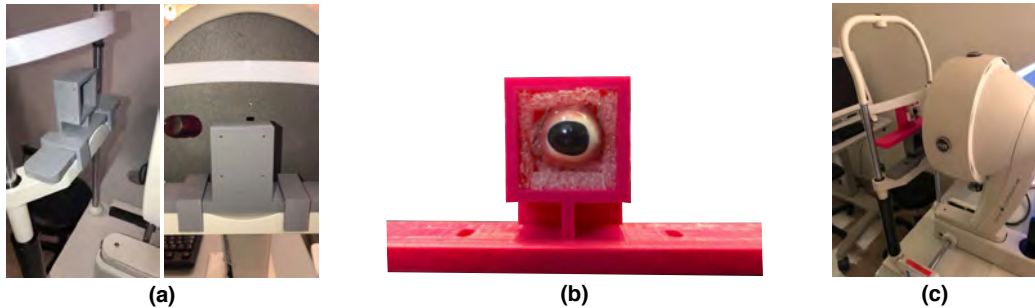


Figure 8.1: Support to hold the eyeball and to be able to make measurements with the topographer. (a) Support made by means of 3D printing placed in the service position on the base that the topographer has to place the patient's chin; **(b)** Eyeball located within the support before making the measurements; **(c)** Topographer making measurements on the eyeball inserted inside the support.

existing commercial intrastromal corneal ring segments to determine the variables that most influence surgery, as well as to propose nomograms that help surgeons to choose the optimal configuration and to better plan the surgery.

3. Create software tools based on artificial intelligent (AI) for helping clinicians in clinics. The application would be developed for the most extended mobile operating systems, iOS and Android. Although it could also be used on a computer. The purpose of this application would be to estimate post-surgical outputs after intrastromal ring insertion and to allow the clinician to choose the optimal configuration.
4. Including tissue remodelling in the surroundings of the ring. Optical coherence tomography (OCT) images showed that there was no gap between the corneal stroma and the implant. This suggests that there was cell and collagen regeneration that should be accounted for in the simulations.
5. Implementation of the combined crosslinking (CXL) and ICRS surgery. Currently, these two methods are combined in order to further stabilize the progression of keratoconus and to improve the patient's vision. Therefore, the aim of this line of research is to propose *in-silico* models which will be able to simulate the combination of these techniques and to validate it with clinical data.
6. To study different techniques of ring insertion through experimental trials in pig eyes. A support has been made by means of 3D printing

(see Figure 8.1) to accommodate the eyeball and to be able to take measurements before and after surgery. These experimental tests will have to be reproduced with *in-silico* models and compare both optical outputs.

Appendix I:

Resumen y Conclusiones en Español

Appendix which contains the summary, the main conclusions and future lines of this PhD Thesis in Spanish, a requirement of the PhD school of the University of Zaragoza.

Chapter Contents

1. Resumen	206
2. Conclusiones principales y contribuciones originales	208
<i>Contribuciones clínicas</i>	<i>208</i>
<i>Contribuciones biomecánicas y computacionales</i>	<i>210</i>
3. Líneas futuras	211

1. Resumen

Esta tesis aborda la simulación mediante elementos finitos de la cirugía de colocación de anillos intrastromales, utilizada en oftalmología para el tratamiento de diferentes patologías corneales, por ejemplo refractivas: miopía y el astigmatismo o la estabilización del queratocono (KC). Esta última patología da lugar a miopías elevadas y a un astigmatismo irregular, provocando la reducción de la agudeza visual en el paciente y, con el tiempo de evolución, incluso la ceguera. En clínica existen varios tratamientos para tratar de estabilizar la progresión del queratocono. En un queratocono leve, basta con utilizar gafas o lentes especiales para intentar corregirlo, pero en casos más avanzados será necesario recurrir a la cirugía para detener la progresión de la enfermedad. Los tratamientos comúnmente utilizados, con el fin de evitar el trasplante de córnea (PK), son el cross-linking y la cirugía aditiva mediante anillos intraestromales.

La planificación actual de la cirugía es fundamentalmente empírica, basadas en nomogramas desarrollados por los fabricantes de anillos apoyada en la experiencia de los cirujanos. Desafortunadamente, no existen herramientas deterministas capaces de estimar los resultados visuales tras la cirugía en función del tipo y dimensiones del anillo. Por tanto, el objetivo de esta tesis es establecer un marco numérico, que sea capaz de simular las cirugías de anillos intraestromales y estimar los resultados mecánicos y ópticos en la córnea tras la inserción de los anillos intrastromales. Esto es posible gracias al avance de la biomecánica computacional, ya que, a día de hoy, es posible crear un gemelo digital de la córnea que nos permita simular el comportamiento de ésta tras simular la cirugía, por ejemplo en función del tipo de anillo implantado.

El cirujano puede seleccionar diferentes tipos de anillos comerciales, dependiendo fundamentalmente del ángulo abarcado y del tipo y dimensiones de la sección transversal. Se pueden establecer dos grandes grupos: los implantes que tienen un ángulo de menos de 360° y los que cubren toda la circunferencia. En el primer grupo se encuentran los anillos de sección triangular como los Keraring (Mediaphacos, Belohorizonte, Brasil) y los Ferrara (AJL Ophthalmic Ltd, España) y los anillos de sección hexagonal como los Intacs (Additional Technology Inc.). En el segundo grupo se enmarca el anillo MyoRing (Dioptex GmbH) cuya sección transversal es una combinación entre parábola y circunferencia y el anillo Intacs SK cuya sección transversal es ovalada.

La simulación de la cirugía es compleja, ya que es necesario establecer un orificio en el estroma corneal, donde posteriormente insertar el anillo y establecer el contacto entre el anillo y el tejido corneal, estando ante un problema no-lineal. Además, para reproducir la cirugía hay que definir múltiples variables, como el tipo de anillos, el modelo del material del tejido corneal, las condiciones de contacto entre ellos, etc. Por todo ello, se han establecido dos escenarios para simular la inserción de los anillos. En el primer escenario, el hueco se generó introduciendo un control en presión, es decir, se define una cavidad y se incrementa la presión en el interior de la misma hasta conseguir el tamaño de la sección transversal del anillo. Su limitación es que sólo se podían simular anillos de sección transversal circular y, en algunas configuraciones, no era posible liberar toda la presión introducida en el hueco. Tras la simulación se pudo observar que la mayor corrección en dioptrías se conseguía colocando los anillos de mayor sección cerca del ápex y, que cuando el anillo se coloca próximo al epitelio corneal, las tensiones generadas en el estroma pueden provocar la extrusión del implante.

En el segundo escenario, se utilizó una herramienta auxiliar, que actuó como un pequeño balón angioplástico (similar al utilizado en la inserción de stents), el cual, mediante un control por desplazamiento, genera el agujero suficiente para insertar los anillos solventándose las limitaciones anteriores. Pudiéndose simular la respuesta de anillos comerciales. Con las simulaciones numéricas se obtiene los siguientes resultados destacables. Primero, el parámetro más influyente es la profundidad de inserción del anillo, seguida del diámetro y espesor de la sección transversal. Gracias al cálculo masivo de simulaciones fue posible desarrollar nomogramas que ayuden a estimar la corrección óptica en función del espesor, diámetro del anillo y profundidad de inserción. Finalmente, el implante no puede ser considerado como un limbo auxiliar ya que el implante actúa como un pivote dinámico que puede moverse a lo largo de la variación de presión intraocular.

También se realizó una caracterización experimental del anillo mediante un ensayo de tracción para posteriormente definir un modelo numérico del material PMMA, ya que las propiedades del material en bruto han podido verse alteradas durante el proceso de tallado de la sección.

Palabras clave: Elementos finitos, córnea, cirugía aditiva, anillo corneal intraestromal (ICRS o ICR), biofísica corneal, planificación de la cirugía de

inserción de ICRS, calidad óptica, equivalente esférico, aberraciones.

2. Conclusiones principales y contribuciones originales

Las conclusiones obtenidas, tras la realización de la tesis, se han organizado en base a dos categorías. Clínicas, que resumen las principales observaciones desde el punto de vista óptico y pueden servir de ayuda a los oftalmólogos de cara a planificar la cirugía de inserción de anillos y seleccionar el tipo de anillo más adecuado en función de la visión del paciente, y biomecánicas y computacionales, relacionadas con la mecánica de la córnea después de la implantación de los anillos, es decir en la modificación del campo de desplazamientos y tensiones.

2.1. Contribuciones clínicas

- El parámetro que da lugar a un mayor cambio en la agudeza visual y en el equivalente esférico del paciente es la profundidad de inserción. Sin embargo, en clínica se ha establecido su colocación a una profundidad $\approx 75\%$ respecto a la superficie anterior,¹ y para dicha posición apenas se produce un cambio significativo en la corrección esférica. Siguiendo cuantificando la influencia, tenemos el diámetro del anillo que coincide con el diámetro de la zona óptica de implantación, y posteriormente el tamaño de la sección transversal de los anillos. Combinando estos dos parámetros es posible regular el equivalente esférico para cada paciente, utilizando el tamaño del anillo para conseguir una mayor corrección si se mantiene fijo el diámetro. Cuanto menor es el diámetro del anillo, mayor fue el impacto en la potencia esférica pero menor el impacto en la potencia cilíndrica. Finalmente el tamaño del anillo no da lugar a correcciones significativas cuando se emplean espesores de 200 o 300 μm . También se ha observado que anillos de 500 μm no deben ser utilizados en diámetros menores de 7 mm porque dan lugar a aberraciones muy elevadas.
- Gracias al cálculo masivo de combinaciones de los diferentes parámetros que definen la cirugía, se ha podido construir un nomograma gráfico para el tipo de anillo MyoRing, que puede ser utilizado por los clínicos para seleccionar el tamaño, la posición y la profundidad en el que insertar el anillo dependiendo de la cantidad de corrección óptica necesaria. Faltaría ser validado clínicamente.

¹ Hashemi et al. 2013c

- En clínica existe la idea de que el anillo refuerza la córnea globalmente, sin embargo numéricamente no se ha observado que se produzca una reducción del estado tensional en el tejido, sino que lo que se produce es una deformación mecánica localizada que regulariza la superficie corneal como consecuencia de introducir un volumen de material en el interior del estroma corneal. La regularización de la superficie es inducida por el efecto de “abultamiento” que repercute en un cambio de las propiedades ópticas: a mayor proximidad del anillo al ápex corneal, mayor cambio óptico se produce. Por lo tanto, la corrección lograda depende de la cantidad de volumen añadido y del diámetro de los implantes.
- La córnea, tras la inserción del anillo presenta una modificación en su cinemática o deformación lo cual da lugar a un cambio en la refracción óptica. Este comportamiento es una consecuencia directa de la rigidez del implante que restringe el movimiento fisiológico del tejido en las direcciones radial y circunferencial. El implante actúa como un pivote dinámico que puede moverse y rotar en el interior del estroma corneal, modificando la cinemática. En consecuencia, tanto los segmentos como los anillos completos no pueden ser considerados como un limbo auxiliar, ya que se mueven ante cambios de presión ocular, como por ejemplo, durante los ciclos circadianos.
- Se ha definido el biomarcador (SFC_{3D}) para analizar el fortalecimiento de la córnea, es decir, cuantificar el nivel de rigidización del tejido tras la implantación de los anillos. Observando que tanto en los segmentos (ICRS) como los anillos completos (ICR) no se alcanza un SFC_{3D} de 3 como refleja la literatura actual.² Para el MyoRing, anillo ICR, se logró un SFC_{3D} de 1.5 en el centro de la córnea, no siendo superior a 1 en los ICRS. Esto implica que si el queratocono es un fenómeno conducido por incrementos de tensión, el único anillo que puede estabilizar la enfermedad es el anillo completo.
- Otro fenómeno asociado al cambio del estado tensional en el tejido corneal es la extrusión del implante, el fuerte gradiente de tensiones producido en la proximidad de la incisión tiende a expulsar el anillo de la cavidad. Cuando los implantes se ubican a una profundidad del 50%, las tensiones de tracción en el tejido corneal por encima del anillo pueden desgarrar el tejido en las zonas próximas a la cicatriz.

² Daxer 2015

Al mismo tiempo, las tensiones de tracción bajo el ICRS tienden a alargar el tejido e impulsar el anillo hacia la superficie anterior de la córnea. La combinación de ambos efectos podría ser la causa de que el tejido fibroso de la cicatriz se desgarre y que el estroma corneal pueda expulsar el anillo.

- Si la sección transversal del anillo no se coloca paralela a la superficie posterior de la córnea (α_M), para alcanzar el equilibrio se produce una rotación de los segmentos intraestromales en el interior del estroma corneal dando lugar a incrementos de tensión en el tejido.
- Los ICR como el MyoRing dan lugar a un mayor cambio óptico que los ICRS. Este efecto puede ser debido, en parte, a la forma en que se realiza la cirugía, ya que los anillos completos deben ser insertados tras la disección de un plano de corte que debilita la córnea.

2.2. Contribuciones biomecánicas y computacionales

- Cuando el hueco o canal, donde posteriormente se ubicará el anillo, se genera mediante un control en presión y el implante se coloca según las recomendaciones clínicas (profundidad 75%), se produce un retroceso del ápex corneal hacia el cristalino disminuyendo la longitud axial del ojo y la curvatura de la córnea. Además, la córnea tiende a flexionarse ligeramente ya que la superficie anterior está solicitada a compresión y la posterior a tracción. Sin embargo, cuando los anillos se insertan cerca del endotelio o superficie posterior, el estroma corneal está sometido a un estado de tensión biaxial o membrana (heterogéneo), similar al estado de tensión en condiciones fisiológicas de la córnea.³
- El segundo escenario o metodología de simulación nos ha permitido simular la cirugía utilizando tanto los anillos genéricos de sección elíptica como los anillos comerciales. En este caso también se ha abordado tanto la implantación de ICRS (segmentos Keraring, Ferrara, Intacs), en los que en la cirugía se genera un túnel, como los ICR (MyoRing) en los que en la cirugía es necesario hacer una disección del tejido y generar un bolsillo.
- Se ha demostrado que los modelos 2D axisimétricos tienen la precisión suficiente para reproducir el comportamiento de anillos con un ángulo superior a 320° , lo que supone un importante ahorro computacional, que es crucial de cara abordar cálculos masivos para realizar los

³ Ariza-Gracia et al. 2016

nomogramas o metodologías de *Machine Learning*. Es decir, se puede sustituir el comportamiento anisótropo del tejido por un comportamiento isótropo equivalente.

- La fricción entre el tejido y el implante es importante y no puede ser ignorada como en otros estudios de simulación clínica.⁴ Dependiendo del coeficiente de rozamiento, una subestimación de 2 o 3 dioptrías podría producirse. Para valores de rozamiento superiores 0.4 no se observan modificaciones en el cambio óptico de la córnea.
- Todos los modelos numéricos desarrollados se ha validados con datos clínicos de la literatura.⁵
- Los resultados experimentales de los implantes reflejan que la fabricación podría dar lugar a una reducción del módulo elástico del material. Su valor real es crucial para abordar simulaciones explícitas. También se ha comprobado que el aguejero de manipulación no se rompe antes las tensiones habituales en clínica.

⁴ Kling and Marcos 2013, Kahn and Shiakolas 2016, Ebrahimian et al. 2019

⁵ Rattan 2018, Daxer 2017, Jaididi et al. 2016, Daxer et al. 2016, Daxer 2017, Nobari et al. 2014, Mohebbi et al. 2016

Todo el trabajo realizado se ha ido publicando en revistas indexadas en ISI web of knowledge (ver Sección 2 del Capítulo 8), conferencias internacionales (ver Sección 3 del Capítulo 8), y en un capítulo de un libro (ver Sección 5 del Capítulo 8).

3. Líneas futuras

Una vez finalizada la Tesis Doctoral han quedado aspectos que podrían ser abordados en trabajos futuros. A continuación se describen los principales actuaciones posibles:

1. Adaptar la metodología desarrollada a modelos de paciente específico para ser capaces de predecir las salidas ópticas una vez que el anillo queda implantado. También tendría que ser incorporada la debilidad en el material producida por el queratocono así como delimitar correctamente el área afectada, por ejemplo a partir del mapa corneal previo a la cirugía del paciente.
2. Simulación masiva del comportamiento para los anillos comerciales más utilizados en clínica (Keraring (Mediaphacos, BeloHorizonte, Brasil), Ferrara (AJL Ophthalmic Ltd., España), e Intacs (Addition Technology Inc., USA)) para crear nomogramas que ayuden a los cirujanos a elegir la

configuración óptima y planificar mejor la cirugía. También se podría crear un gemelo digital que pueda ser implantado en sistemas operativos móviles más extendidos, iOS y Android, de fácil manejo para los cirujanos, para ello sería necesario utilizar modelos simplificados o *Machine Learning* para tener resultados en tiempo real.

3. Incorporar la remodelación celular tras la cicatrización en la zona de inserción. En las imágenes de tomografía de coherencia óptica (OCT) de la inserción del anillo, se observa dicha regeneración celular y no se ven los huecos que quedan en las simulaciones.
4. Abordar la simulación de la cirugía conjunta cross-linking (CXL) e ICRS, ya que en clínica se ha comprobado que la combinación de ambos tratamientos ayudan a mejora la visión del paciente estabilizando la progresión del queratocono.
5. Estudiar diferentes técnicas de inserción de anillos intrastromales numéricamente y validarlas mediante pruebas experimentales con ojos porcinos. Se ha realizado un soporte, por medio de impresión 3D que permite acomodar el globo ocular y ser capaz de tomar las medidas antes y después de la cirugía.

Appendix II: *Publications*

Chapter Contents

1. Biomech. Model. Mechanobiol. 2018	214
2. Transl. Vis. Sci. Technol. 2020	215

1. Template-based methodology for the simulation of intracorneal segment ring implantation in human corneas

Biomechanics and Modeling in Mechanobiology
<https://doi.org/10.1007/s10237-018-1013-z>

REVIEW PAPER



Template-based methodology for the simulation of intracorneal segment ring implantation in human corneas

Julio Flecha-Lescún¹ · Begoña Calvo^{1,2} · Jesús Zurita³ · Miguel Ángel Ariza-Gracia^{1,4}

Received: 22 November 2017 / Accepted: 12 March 2018
 © Springer-Verlag GmbH Germany, part of Springer Nature 2018

Abstract

Keratoconus is an idiopathic, non-inflammatory and degenerative corneal disease characterised by a loss of the organisation in the corneal collagen fibrils. As a result, keratoconic corneas present a localised thinning and conical protrusion with irregular astigmatism and high myopia that worsen visual acuity. Intracorneal ring segments (ICRSs) are used in clinic to regularise the corneal surface and to prevent the disease from progressing. Unfortunately, the post-surgical effect of the ICRS is not explicitly accounted beforehand. Traditional treatments rely on population-based nomograms and the experience of the surgeon. In this vein, in silico models could be a clinical aid tool for clinicians to plan the intervention, or to test the post-surgical impact of different clinical scenarios. A semi-automatic computational methodology is presented in order to simulate the ICRS surgical operation and to predict the post-surgical optical outcomes. For the sake of simplicity, circular cross section rings, average corneas and an isotropic hyperelastic material are used. To determine whether the model behaves physiologically and to carry out a sensitivity analysis, a 3^k full-factorial analysis is carried out. In particular, how the stromal depth insertion, horizontal distance of ring insertion (hDRI) and diameter of the ring's cross section (ϕ_{ICRS}) are impacting in the spherical and cylindrical power of the cornea is analysed. Afterwards, the kinematics, mechanics and optics of keratoconic corneas after the ICRS insertion are analysed. Based on the parametric study, we can conclude that our model follows clinical trends previously reported. In particular and although there is an improvement in defocus, all corneas presented a change in their optical aberrations. The stromal depth insertion is the parameter that affects the corneal optics the most, whereas hDRI and ϕ_{ICRS} are less important. Not only that, but it is almost impossible to achieve an optimal trade-off between spherical and cylindrical correction. Regarding the mechanical behaviour, inserting the rings at 65% depth or above will cause the cornea to slightly bend. This abnormal stress distribution greatly distorts the corneal optics and, more importantly, could be the cause of clinical problems such as corneal extrusion. Not only that, but our model also supports that rings are acting as restraint elements which relax the stresses of the corneal stroma in the cone of the disease. However, depending on the exact spatial location of the keratoconus, the insertion of rings could promote its evolution instead of preventing it. ICRS inserted deeper will prevent keratoconus in the posterior stroma from growing (relaxation of posterior surface), but will promote its growing if they are located in the anterior surface (increment of stress). In conclusion, the methodology proposed is suitable for simulating long-term mechanical and optical effects of ICRS insertion.

Keywords Corneal biomechanics · Template-based automatization · Keratoconus · Intracorneal segment ring · Corneal ectasia · Finite element methodology

Electronic supplementary material The online version of this article (<https://doi.org/10.1007/s10237-018-1013-z>) contains supplementary material, which is available to authorized users.

✉ Julio Flecha-Lescún
jflecha@unizar.es

¹ Applied Mechanics and Bioengineering (AMB); Aragón Institute for Engineering Research(I3A), University of Zaragoza, Zaragoza, Spain

² Bioengineering, Biomaterials and Nanomedicine Online, Biomedical Research Center (CIBBER-BBN), Madrid, Spain

³ Department of Mechanical Engineering, Public University of Navarra, Pamplona, Spain

⁴ Computational Biomechanics (CB), Institute for Surgical Technology and Biomechanics(ISTB), University of Bern, Bern, Switzerland

Published online: 21 March 2018



Figure II.1: Biomech. Model.
 Mechanobiol. 2018

2. Corneal biomechanics after intrastromal ring surgery: optomechanical in-silico assessment

tvst

Article

Corneal Biomechanics After Intrastromal Ring Surgery: Optomechanical In Silico Assessment

Miguel Ángel Ariza-Gracia^{1, #}, Julio Flecha-Lescún^{2, #}, Philippe Büchler¹, and Begoña Calvo^{2, 3}

¹ ARTORG Center for Biomedical Engineering Research, Faculty of Medicine, University of Bern, Bern, Switzerland

² Aragón Institute for Engineering Research (I3A), University of Zaragoza, Zaragoza, Spain

³ CIBER in Bioengineering, Biomaterials & Nanomedicine (CIBER-BBN), Madrid, Spain

Correspondence: Miguel Ángel Ariza-Gracia, ARTORG, Faculty of Medicine, University of Bern, Bern, Switzerland. e-mail: miguel.ariza@artorg.unibe.ch

Received: June 4, 2020

Accepted: September 10, 2020

Published: October 21, 2020

Keywords: intrastromal implants; in silico models; corneal biomechanics; high myopia; keratoconus

Citation: Ariza-Gracia MÁ, Flecha-Lescún J, Büchler P, Calvo B. Corneal biomechanics after intrastromal ring surgery: Optomechanical in silico assessment. *Trans Vis Sci Technol.* 2020;9(11):26. <https://doi.org/10.1167/tvst.9.11.26>

Purpose: To provide a biomechanical framework to better understand the postsurgical optomechanical behavior of the cornea after ring implantation.

Methods: Calibrated in silico models were used to determine the corneal shape and stresses after ring implantation. After mechanical simulations, geometric ray-tracing was used to determine the change in spherical equivalent. The effect of the surgical procedure, circadian variation of intraocular pressure, or the biomechanical weakening introduced by keratoconus (KC) were evaluated for each intrastromal ring.

Results: Models predicted the postsurgical optomechanical response of the cornea at a population level. The localized mechanical effect of the additional intrastromal volume introduced by the implants (size and diameter) drives the postsurgical corneal response. However, central corneal stresses did not increase more than 50%, and thus implants did not strengthen the cornea globally. Because of the biomechanical weakening introduced by laser pocketing, continuous implants in a pocket resulted in higher refractive corrections and in the relaxation of the anterior stroma, which could slow down KC progression. Implants can move within the stroma, acting as a dynamic pivot point that modifies corneal kinematics and flattens the corneal center. Changes in stromal mechanical properties did not impact on refraction for normal or pathological corneas.

Conclusions: Implants do not stiffen the cornea but create a local bulkening effect that regularizes the corneal shape by modifying corneal kinematics without canceling corneal motion.

Translational Relevance: In silico models can help to understand corneal biomechanics, to plan patient-specific interventions, or to create biomechanically driven nomograms.

Introduction

Intrastromal ring segments (IRS or ICRS) or intrastromal continuous rings (ICR) are small polymeric devices that are introduced in the corneal stroma to regularize the corneal surface and correct high refractive errors. This technique was originally introduced to treat patients suffering from keratoconus (KC),¹ but it was extended to other indications, such as marginal pellucid degenerations,² post-LASIK ectasia,³ and high myopia, in which laser refractive correction is not possible.⁴ Three main types of

rings are now on the market: continuous rings (e.g., MyoRing, DiopTex GmbH), almost continuous ring segments covering an arc with a central angle between 320° and 355° (e.g., Keraring, Mediphacos, Belo Horizonte, Brazil), and IRS that cover angles below 210° and can be placed by pairs depending on the classification of the cone and amount of correction (e.g., Ferrara, Ophthalmic Ltd.; or Intacs, Addition Technology Inc.). Beside their difference in angular coverage, the existing systems differ by the design of their cross-section and diameter. Nomograms based on morphological parameters, such as the central corneal curvature, minimum corneal thickness,^{5,6} or the KC

translational vision science & technology

Copyright 2020 The Authors
tvst.arvojournals.org | ISSN: 2164-2591

This work is licensed under a Creative Commons Attribution-NonCommercial-NoDerivatives 4.0 International License.



1



Appendix III:

Automatic model mesh to generate in-silico models

The main target of this appendix is to explain to the reader the programming to develop automatically the axisymmetric cornea models, incorporating both tunnel and pocket surgery, and the different axisymmetric modelled rings: the generic elliptical cross-section and the MyoRing.

Chapter Contents

1. Introduction	218
2. Heading of Abaqus Scripting file	219
3. Geometry of the models	219
<i>Geometry of the cornea</i>	<i>220</i>
<i>Geometry of the rings</i>	<i>239</i>
4. Material and section assignment	247
<i>Material and section assignment for the cornea models</i>	<i>248</i>
<i>Material and section assignment for the ring models</i>	<i>248</i>
5. Mesh of the models	249
<i>Mesh of the cornea</i>	<i>252</i>
<i>Mesh of the ring</i>	<i>266</i>
6. Assembly of the axisymmetric models	269
7. Step modulus	270
8. Boundary conditions	270
9. Job and submission	270
10. Final considerations	271

1. Introduction

The automatic finite element meshing allows to produce an endless number of models by varying the input parameters, such as the dimensions of the model or the material. It also allows to quickly perform mesh sensitivity analysis, since models with coarser or thinner meshes can be built by varying the seed sizes.

Particularly with the models made in this thesis, where different corneas and rings have been automatically generated, it has been possible to study different clinical scenarios, different corneal sizes and rings located at different depths within the corneal stroma and ring implantation diameters. Not only that, thanks to the automatic meshing incorporated to the ring insertion algorithms, more than 5,000 simulations have been solved in the computer cluster of the University of Bern (Ubelix) and uncertainty analysis has been performed to check which variables have the greatest impact on the correction of keratometry mean (K_{mean}) and spherical equivalent (SE), as well as the development of the preliminary nomograms for the MyoRing insertion (see Chapter 6).

All the models performed with this automatic mesher have the same structure able to generate the Abaqus input file (*.inp). The idea is to write the different lines of code in an Abaqus Python Scripting file (*.py) that allow to develop the mesh of the model, either cornea or ring. The structure of the Abaqus Python Scripting input file is the described below:

1. Heading.
2. Geometry.
3. Material and section assignment
4. Mesh.
5. Assembly.
6. Step.
7. Boundary Conditions.
8. Job and submission.

Once the Abaqus Python Scripting file has been generated, it is executed to generate the Abaqus input file (*.inp) from which the nodes, connectivities (elements) and the sets of the model are extracted.

2. Heading of Abaqus Scripting file

All Abaqus Python Scripting files (*.py) begin with the same header, whose purpose is to import the python packages to be going to use throughout the program.

```
from part import *
from material import *
from section import *
from assembly import *
from step import *
from interaction import *
from load import *
from mesh import *
from optimization import *
from job import *
from sketch import *
from visualization import *
from connectorBehavior import *
```

3. Geometry of the models

The modules of Abaqus Python Scripting that correspond to the geometry are the *Sketch* and the *Part*. They define both the cross-section of the cornea with the two different types of surgery (tunnel or pocket) and the rings (the generic with elliptical cross-section and the MyoRing). In addition, the cuttings are incorporated in the cross-section, not only to guarantee a better quality of the mesh but also to be able to discern between healthy and ectatic tissue, in case of the cornea models.

To generate the cross-section of the axisymmetric models, it is initially necessary to generate them in the *Sketch* module. All the instructions used for this purpose must be embraced by the following lines of code:

```
# Generating the Sketch
mdb.models['Model-1'].ConstrainedSketch(name=
    '__profile__', sheetSize=200.0)
mdb.models['Model-1'].sketches['__profile__'].sketchOptions.
    setValues(viewStyle=AXISYM)
:
```

```
# Sketch Closing and Part Creation
mdb.models['Model-1'].Part(dimensionality=AXISYMMETRIC,
    name='NAME_PART', type=DEFORMABLE_BODY)
mdb.models['Model-1'].parts['NAME_PART'].BaseShell(
    sketch=mdb.models['Model-1'].sketches['__profile__'])
del mdb.models['Model-1'].sketches['__profile__']
```

where 'NAME_PART' changes depending on the model.

3.1. Geometry of the cornea

To perform the cornea cross-section, the input parameters are the radius of the anterior (R_a) and posterior (R_p) cornea, the thickness of the central zone (CCT), and radius of the limbus (R_{Limbus}), fixed in 6 mm.

Extrapolating the cross-section of the cornea to a drawing, it is concluded that the cross-section is formed by two arcs of circumference and two straight lines (see Figure III.1). Therefore, to define the cross-section sketch and to implement it in the code, it is necessary to know the following "goal points": the centre (CA_{Centre} and CP_{Centre}) and the initial (CA_{P0} and CP_{P0}) and final points (CA_{PF} and CP_{PF}) of the anterior and posterior cornea. Finally, the cross-section of the cornea is moved vertically, so as to the CP_{PF} point stands on the X-axis.

The "goal points" are defined according to the following process:

Process to define the corneal geometry

Input Parameters (in grey in Figure III.1)

- R_a : radius of anterior cornea, in mm
- R_p : radius of posterior cornea, in mm
- CCT: thickness of central zone, in μm
- R_{Limbus} : radius of limbus, fixed in 6 mm

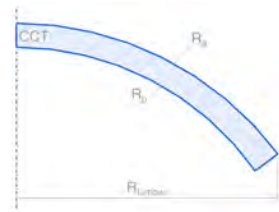


Figure III.1: Input parameters to define the cross section of the cornea. The dimensions are represented in colour grey.

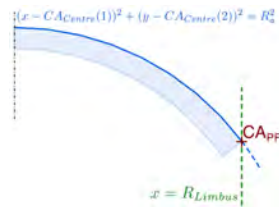


Figure III.2: Calculation of CA_{PF} . Intersection between arc of anterior surface and straight vertical line through R_{Limbus} .

Operations

- i) $CA_{P0} = (0, R_a, 0)$
- ii) $CP_{P0} = (0, R_p, 0)$
- iii) $CA_{Centre} = (0, 0, 0)$
- iv) $CP_{Centre} = (0, CP_{P0} - R_p, 0)$
- v) CA_{PF} : Intersection between anterior surface and the vertical line that goes through R_{Limbus} defined in Equation III.1 and Figure III.2.

$$(x - CA_{centre}(1))^2 + (y - CA_{centre}(2))^2 = R_a^2 \quad (III.1)$$

$$x = R_{Limbus}$$

vi) CP_{PF} : Intersection between posterior surface and the line through CP_{Centre} with CA_{PF} defined in Equation III.2 and Figure III.3.

$$(x - CP_{centre}(1))^2 + (y - CP_{centre}(2))^2 = R_p^2$$

$$y = \underbrace{\frac{CA_{PF}(2) - CP_{Centre}(2)}{CA_{PF}(1) - CP_{Centre}(1)}}_m \cdot x + \underbrace{(CP_{Centre}(2) - m \cdot CP_{Centre}(1))}_n \quad (III.2)$$

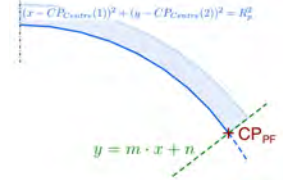


Figure III.3: Calculation of CP_{PF} . Intersection between arc of posterior surface and the line between CA_{PF} and CP_{Centre} .

Outcomes

The four points (in green in Figure III.4) and the two centre of cornea surfaces (in red in Figure III.4) that will be used to define the cross-section of the cornea are moved so as to CP_{PF} stands on the X-axis (see the Equations III.3).

$$\begin{aligned} CA_{P0} &= (CA_{P0}(1), CA_{P0}(2) - CP_{PF}(2), 0) \\ CP_{P0} &= (CP_{P0}(1), CP_{P0}(2) - CP_{PF}(2), 0) \\ CA_{PF} &= (CA_{PF}(1), CA_{PF}(2) - CP_{PF}(2), 0) \\ CP_{PF} &= (CP_{PF}(1), CP_{PF}(2) - CP_{PF}(2), 0) \\ CA_{Centre} &= (CA_{Centre}(1), CA_{Centre}(2) - CP_{PF}(2), 0) \\ CP_{Centre} &= (CP_{Centre}(1), CP_{Centre}(2) - CP_{PF}(2), 0) \end{aligned} \quad (III.3)$$

Finally, once all these points have been obtained, they must be introduced in the corresponding code lines to generate the sketch, described in page 219:

```
# Anterior Surface
mdb.models['Model-1'].sketches['__profile__'].ArcByCenterEnds (
    centre=(CA_Centre(1), CA_Centre(2)), direction=CLOCKWISE,
    point1=(CA_P0(1), CA_P0(2)),
    point2=(CA_PF(1), CA_PF(2)))
# Posterior Surface
mdb.models['Model-1'].sketches['__profile__'].
```

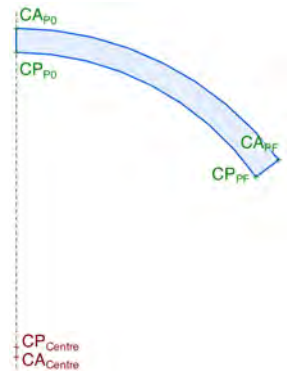


Figure III.4: Points used in code to perform the cornea cross section. The points which define the anterior and posterior surface are represented in colour green and the points which refer to the centres of cornea's surfaces are coloured in red.

```

ArcByCenterEnds (centre=( $CP_{Centre}(1)$ ,  $CP_{Centre}(2)$ ),
direction=CLOCKWISE, point1=( $CP_{P0}(1)$ ,  $CP_{P0}(2)$ ),
point2=( $CP_{PF}(1)$ ,  $CP_{PF}(2)$ ))
# Apex Zone
mdb.models['Model-1'].sketches['__profile__'].Line (
point1=( $CP_{P0}(1)$ ,  $CP_{P0}(2)$ ),
point2=( $CA_{P0}(1)$ ,  $CA_{P0}(2)$ ))
# Interface with the Limbus
mdb.models['Model-1'].sketches['__profile__'].Line (
point1=( $CP_{PF}(1)$ ,  $CP_{PF}(2)$ ),
point2=( $CA_{PF}(1)$ ,  $CA_{PF}(2)$ ))

```

Once the cross-section of cornea has been created, the following step is to generate the surgery. Due to two different types defined along the thesis, i.e. tunnel or pocket, the method used to define the models changes.

The same process as in the surgery procedure is used in order to make the cuttings: first, the part to be cut is selected with a point which belongs to the internal model; then, the sketch module is opened where the different geometries (lines, arcs of circumference, ellipse, splines, etc) are drawn. Finally, the sketch is removed and the geometry drawn generate the different cutting in the model. The cuttings must be embraced in the following code lines, taking the point $O = (0, 0, 0)$ as coordinates origin (see Figure III.5):

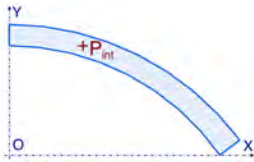


Figure III.5: Interior Point and origin of the system.

```

# Select the part to be cut
mdb.models['Model-1'].ConstrainedSketch(gridSpacing=
0.34, name='__profile__', sheetSize=13.78,
transform=mdb.models['Model-1'].parts['NAME_PART'].
MakeSketchTransform(sketchPlane=mdb.models[
'Model-1'].parts['NAME_PART'].faces.findAt (
( $P_{int}(1)$ ,  $P_{int}(2)$ ,  $P_{int}(3)$ ), (0.0, 0.0, 1.0)),
sketchPlaneSide=SIDE1, sketchOrientation=RIGHT,
origin=( $O(1)$ ,  $O(2)$ ,  $O(3)$ ))
mdb.models['Model-1'].parts['NAME_PART'].
projectReferencesOntoSketch(filter=COPLANAR_EDGES,
sketch=mdb.models['Model-1'].sketches['__profile__'])
:
# Close and remove the sketch
mdb.models['Model-1'].parts['NAME_PART'].
PartitionFaceBySketch(faces=mdb.models['Model-1'].
parts['NAME_PART'].faces.findAt((( $P_{int}(1)$ ,  $P_{int}(2)$ ,
 $P_{int}(3)$ ), )), sketch=mdb.models['Model-1'].

```

```
sketches['__profile__'])
del mdb.models['Model-1'].sketches['__profile__']
```

where, in this case, P_{int} (see Figure III.5) was used to define the inner point of the region to be cut, but it will change depending on the region to be cut.

3.1.1. Tunnel surgery

To insert the intrastromal segments, the surgery is performed by means of the femtosecond laser.¹ An ellipse is chosen to model the surgery, which will be placed within the cross section of the cornea at a distance of ϕ_{ICRS} (Figure III.6) from the optical axis and at a depth expressed as a percentage of the corneal thickness in the implantation area.

To introduce an ellipse in the abaqus python scripting code, it is necessary to know the centre of the ellipse (S_{Centre}) and the points located at the ends of the of the semi-major axis (S_M) and semi-minor (S_m) axis.

Process to define the points of the ellipse

Input Parameters (in grey in Figure III.6).

- ϕ_{ICRS} : optical zone, in mm.
- z_{Tunnel} : stromal depth of insertion, in percentage.
- T_{Tunnel} : thickness of surgery, fixed in $80 \mu m$.
- w : width of the ellipse, fixed in 0.5 mm.

Operations

S_{Centre} : Centre of the surgery which is corresponded to centre of de ellipse. The process to obtain the coordinates of this point is commented below.

- i) S_{p1} : Intersection between the arc of the posterior surface and straight vertical line through ϕ_{ICRS} (see Equation III.4 and Figure III.7).

$$\begin{aligned} (x - CP_{centre}(1))^2 + (y - CP_{centre}(2))^2 &= R_p^2 \\ x &= \frac{\phi_{ICRS}}{2} \end{aligned} \tag{III.4}$$

- ii) S_{p2} : Intersection between the arc of anterior surface and line which joins S_{p1} with CP_{Centre} (see Equation III.5 and represented in Figure III.8).

¹ Seleet et al. 2015

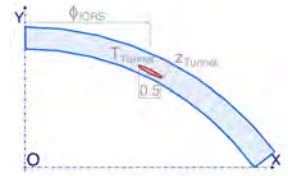


Figure III.6: Input parameters to define the cross-section of the surgery as a tunnel. In blue the cross section of the cornea is represented. In red, the surgery is shown. The input parameters are shown in grey.

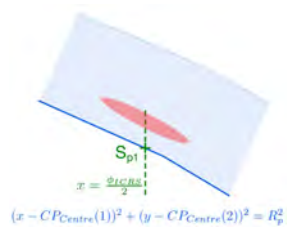


Figure III.7: Calculation of S_{p1} in tunnel surgery. Intersection between the arc of posterior surface and straight vertical line through $\frac{\phi_{ICRS}}{2}$.

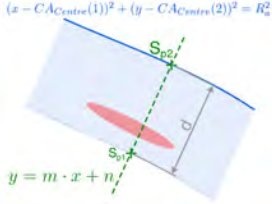


Figure III.8: Calculation of S_{p2} and the distance d in tunnel surgery. S_{p2} is the intersection between the arc of anterior surface and line between S_{p1} and CP_{Centre} . In grey, d is represented as distance between S_{p1} and S_{p2} .

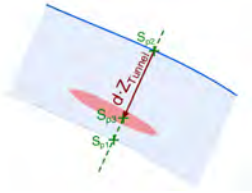


Figure III.9: Calculation of S_{p3} in tunnel surgery. Point located at a distance $d \cdot z_{Tunnel}$ in the direction of vector $S_{p1} \vec{S}_{p2}$.

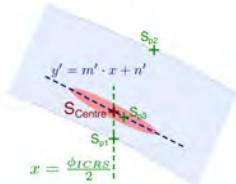


Figure III.10: Calculation of S_{Centre} in tunnel surgery. Intersection between the orthogonal line to the line between S_{p1} and S_{p2} with the vertical straight line through $\phi_{ICRS}/2$.

$$(x - CA_{centre(1)})^2 + (y - CA_{centre(2)})^2 = R_a^2$$

$$y(x) = \underbrace{\frac{S_{p1}(2) - CP_{Centre}(2)}{S_{p1}(1) - CP_{Centre}(1)}}_m \cdot x + \underbrace{(CP_{Centre}(2) - m \cdot CP_{Centre}(1))}_n$$
(III.5)

- iii) d : distance between S_{p1} and S_{p2} , defined in equation III.6 and represented in Figure III.8.

$$d = \|S_{p1} \vec{S}_{p2}\| = \sqrt{(S_{p2}(1) - S_{p1}(1))^2 + S_{p2}(2) - S_{p1}(2)}$$
(III.6)

- iv) S_{p3} : point which is in the direction of vector $S_{p1} \vec{S}_{p2}$ at a distance of $z_{Tunnel} \cdot d$ from anterior cornea (see in Figure III.9).
- v) S_{Centre} : First, the orthogonal line to vector $S_{p1} \vec{S}_{p2}$ and through S_{p3} is determined. Finally, the intersection between this line with the vertical straight line through $\frac{\phi_{ICRS}}{2}$ is S_{Centre} (see Equation III.7, which is corresponded in Figure III.9).

$$m' = -\frac{1}{m}$$

$$y'(x) = -\underbrace{\frac{S_{p2}(1) - S_{p1}(1)}{S_{p2}(2) - S_{p1}(2)}}_{m'} \cdot x + \underbrace{S_{p3}(2) - m' \cdot S_{p3}(1)}_{n'}$$
(III.7)

$$x = \frac{\phi_{ICRS}}{2}$$

S_M : Point located at the end of the semi-major axis of the ellipse, which is shown in Figure III.11. Its coordinates are calculated evaluating the straight line y' , defined by the Equation III.7, in $x = S_{Centre}(1) - w/2$.

S_m : Point located at the end of the semi-minor axis of the ellipse, which is shown in Figure III.11. This point is located at a distance $T_{Tunnel}/2$ from S_{Centre} in the direction of vector $S_{p1} \vec{S}_{p2}$ whose points are shown in Figure III.10.

Outcomes

Surgery Centre: $S_{Centre} = (S_{Centre}(1), S_{Centre}(2), 0)$

Point at end of semi-major axis: $S_M = (S_M(1), S_M(2), 0)$

Point at end of semi-minor axis: $S_m = (S_m(1), S_m(2), 0)$

Finally, the code which draws the ellipse is shown below:

```
# Surgery Ellipse
mdb.models['Model-1'].sketches['__profile__'].
    EllipseByCenterPerimeter(axisPoint1=(S_M(1), S_M(2)),
        axisPoint2=(S_m(1), S_m(2)), centre=(S_Centre(1), S_Centre(2)))
```

Once both the corneal cross-section and the surgery are modelled, the groups of "CORNEA", "SURGERY", "APEX", "APOYO", "CORNEA_ ANTERIOR" and "CORNEA_POSTERIOR" are created as well as the internal surfaces of the surgery (INNER_SURF) and the surface of the posterior cornea (IOP_SURF), where the intraocular pressure (IOP) is applied. In order to define these two typologies (sets and surfaces), it is necessary to obtain the points which belong to the each section what . All these points have already been explained above except for the P_{int} in the Figure III.5.

P_{int} is the point in the corneal stroma that serves both to select the section to be cut and to define the CORNEA group. In order to calculate its coordinates, the following steps are followed:

- i) The angle (α) and formed between S_M and horizontal axis, and the angle (α_{int}) is calculated in Equation III.8 and Figure III.12.
- ii) The interior point is located between S_M and optical axis and it will have an angle (α_{int}) defined in Equation III.8.

$$\alpha = \text{atan} \frac{S_M(2) - CP_{Centre}(2)}{S_M(1) - CP_{Centre}(1)} \quad (III.8)$$

$$\alpha_{int} = \alpha + \frac{\pi/2 - \alpha}{2}$$

- iii) The intersections (Q_{CA} and Q_{CP}) between the line (y_{int}) defined by the angle α_{int} and through CP_{Centre} (equation III.8 and the two corneal surfaces are calculated and shown in Figure III.12.

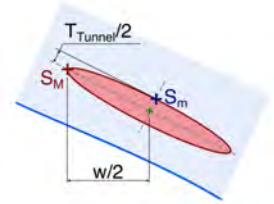


Figure III.11: Calculation of S_M and S_m in tunnel surgery. (Red) S_M and (Blue) S_m .

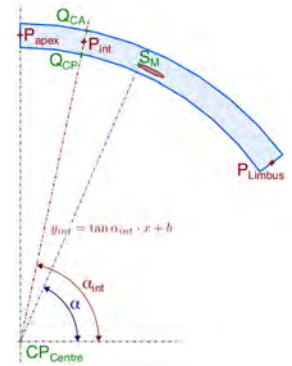


Figure III.12: Calculation of P_{int} , P_{Apex} , and P_{Limbus} . Points in green, CP_{Centre} , S_M , Q_{CA} and Q_{CP} are used to calculate the outcomes points (in red), P_{int} , P_{Apex} , and P_{Limbus} .

$$y_{int}(x) = \tan \alpha_{int} \cdot x + \underbrace{CP_{Centre}(2) - \tan \alpha_{int} \cdot CP_{Centre}(1)}_b \tag{III.9}$$

iv) P_{int} will be in the middle of the distance between Q_{CA} and Q_{CP} , shown in Figure III.12.

P_{Apex} : point used to define the set “APEX” and is calculated as the mid distance between CA_{P0} and CP_{P0} .

P_{Limbus} : point used to define the set “APOYO” and is calculated as the mid distance between CA_{PF} and CP_{PF} .

The Abaqus Python Scripting code for generating groups and surfaces is shown below:

NAME	POINT
CORNEA	P_{int}
SURGERY	S_{Centre}
APEX	P_{apex}
APOYO	P_{Limbus}
CORNEA_ANTERIOR	S_{p2}
CORNEA_POSTERIOR	S_{p1}
IOP_SURF	S_{p1}
INNER_SURF	S_M

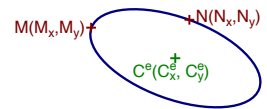
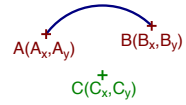
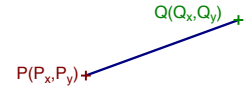
Table III.1: Sets and surfaces definition to tunnel surgery.
The first column represents the name of sets or surfaces and the second column, the point used to define the set or surface.

```
# Generating sets
mdb.models['Model-1'].parts['CORNEA'].Set(faces=
    mdb.models['Model-1'].parts['CORNEA'].faces.findAt(
        ((POINT(1), POINT(2), POINT(3)), ), ), name='NAME')
# Generating surfaces
mdb.models['Model-1'].parts['CORNEA'].Surface(
    name='NAME', side1Edges=mdb.models['Model-1'].
    parts['CORNEA'].edges.findAt( ((POINT(1), POINT(2),
    POINT(3)), ), ), )
```

where “NAME” and “POINT” take the following values depending on the part which refer (Table III.1).

Once the cross-section of the cornea has been defined, with the surgery within the stroma and the groups defined, the next step is to make the different cuttings in the cornea to perform a better and uniform mesh. To do this cuttings, the code for drawing lines, arcs of circumference, and ellipse must be used. In order to select the section to cut (see code in page 222), it is necessary to find an internal point which belongs to the section. To draw the lines, it is necessary to know the initial and final point. To trace arcs of circumference, the centre, initial and final point are required. Finally, the centre, the end points of semi-major and semi-minor axes must be known to draw an ellipse. Although these lines of code have been already commented before, they appear again in their general form, to make it easier for the reader to understand the code and to link it to the instructions to cut the cross-section of the cornea.

```
# Code lines to draw a line
mdb.models['Model-1'].sketches['__profile__'].Line(
    point1=(Px, Py),
    point2=(Qx, Qy)
# Code lines to draw a circumference arc
in clockwise direction
mdb.models['Model-1'].sketches['__profile__'].
    ArcByCenterEnds(centre=(Cx, Cy),
    direction=CLOCKWISE, point1=(Ax, Ay),
    point2=(Bx, By)
# Code lines to draw an ellipse
mdb.models['Model-1'].sketches['__profile__'].
    EllipseByCenterPerimeter(axisPoint1=(Mx, My),
    axisPoint2=(Nx, Ny), centre=(Cxe, Cye))
```



All the following instructions must follow an order to obtain the final cross-section geometry of the Figure III.20. Starting from geometry of Figure III.6, the established order is explained below:

Order of the instructions

- i) The cross-section of the cornea (without surgery) is selected with P_{int} .
 - The medium cover ellipse is drawn calculating the three points: centre (S_{Centre}), point at end of semi-major axis (R_1) and point at end of semi-minor axis. (R_2). These points and scheme of the ellipse are represented in Figure III.13. R_1 is 1.2 times greater than the distance of the semi-major axis of the ellipse that defines the surgery. R_2 is located at a distance that is 2.5 times greater than the distance from the semi-minor axis of the ellipse that defines the surgery. Therefore, $C^e = S_{Centre}$, $M = R_1$, and $N = R_2$ in the code lines described in ellipse code of the page 227.
 - The largest cover ellipse is drawn calculating the three points: centre (S_{Centre}), point at end of semi-major axis (A_2) and point at end of semi-minor axis. (A_5). These points and scheme of the ellipse are represented in Figure III.14. A_2 is 1.5 times greater than the distance of the semi-major axis of the ellipse that defines the surgery. A_5 is located at a distance that is 4.25 times greater than the distance from the semi-minor axis of the ellipse that defines the surgery. Therefore, $C^e = S_{Centre}$, $M = A_2$, and $N = A_5$ in the code lines described in ellipse code of the page 227.

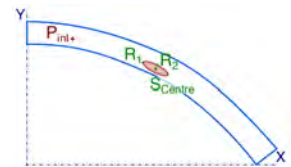


Figure III.13: First cover ellipse. P_{int} is represented in red, whereas the mandatory points of medium cover ellipse are represented in green and coloured in red.

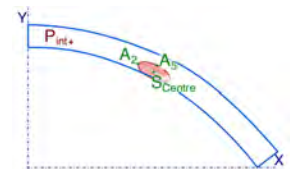


Figure III.14: Second cover ellipse. P_{int} is represented in red, whereas the mandatory points of the largest cover ellipse are represented in green and coloured in red.

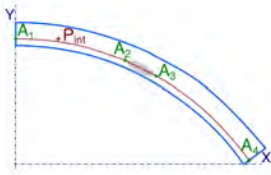


Figure III.15: Internal arcs within stroma corneal. P_{int} in red, Points (A_1 , A_2 , A_3 , and A_4) to define the arcs and straight line in green, and the complete cutting line is drawn in red

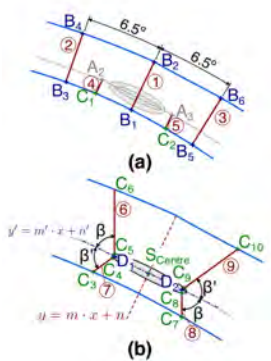


Figure III.16: Lines which cut the stroma around the surgery. (a). Lines which cross the stroma. The line between B_1 and B_2 divides the surgery in two equal parts; $+6.5^\circ$ from this line, the superior line is formed creating the points B_3 and B_4 with the intersection with posterior and anterior cornea respectively; -6.5° from the central line, the inferior line is drawn, forming the points B_5 and B_6 with the intersection with posterior and anterior cornea respectively; the two short lines start from the points located at the ends of the major axis of the largest cover ellipse (A_2 and A_3), and have the same direction as the centre line. The intersection of these two lines with the posterior surface forms C_1 and C_2 . (b) Zoom on surgery. The line numbers are located in red inside of a red circle.

- Two internal arc of circumference are created in order to divide the cornea between anterior and posterior regions (see Figure III.15) and a straight line to divide the ellipse by its major axis.

Arc 1: $C = CP_{Centre}$, $A = A_1$, and $B = A_2$ in the code lines of circumference arc (see the code in page 227).

Straight line: $P = A_2$ and $Q = A_3$ in the code lines to represent a line (see the code in page 227).

Arc 2: $C = CP_{Centre}$, $A = A_3$, and $B = A_4$ in the codes line of circumference arc (see the code in page 227).

- Creation of the cuttings around the surgery, represented in Figure III.16.

Line 1: or central line, straight line between B_1 and B_2 . B_1 is the intersection between the line through S_{Centre} and CP_{Centre} with posterior cornea. B_2 is the intersection between the line through S_{Centre} and CP_{Centre} with anterior cornea. $P = B_1$ and $Q = B_2$ in the programming lines (see the code in page 227).

Line 2: straight line with an angle of $+6.5^\circ$ from central line. B_3 and B_4 are the intersection with posterior and anterior cornea, respectively. $P = B_3$ and $Q = B_4$ in the code lines (see the code in page 227).

Line 3: straight line with an angle of -6.5° from central line. B_5 and B_6 are the intersection with posterior and anterior cornea, respectively. $P = B_5$ and $Q = B_6$ in the programming lines (see the code in page 227).

Line 4: straight line, parallel to central line, which passes by one of the end (A_2) of semi-major axis of the largest cover ellipse. The intersection with posterior surface form the point C_1 . $P = A_2$ and $Q = C_1$ in the code lines (see the code in page 227).

Line 5: straight line, parallel to central line, which passes by the other end (A_3 , symmetric to A_2) of semi-major axis of the largest cover ellipse. The intersection with posterior surface form the point C_2 . $P = A_3$ and $Q = C_2$ in the programming lines (see the code in page 227).

Line 6: vertical straight line defined by $x = S_{Centre}(1) - (w_{ICRS}/2 - 0.025)$. D_1 is the intersection between this vertical line with the line y' defined in equation III.7 and angle β is formed. Finally, C_5

and C_6 arise from the intersection between this vertical straight line with surgery and anterior cornea, respectively (see Figure III.16.b). $P = D_1$ and $Q = C_6$ in the programming lines (see the code in page 227).

Line 7: straight line which forms an angle $\beta' = 2 \cdot \beta - \frac{\pi}{2}$ and passes through D_1 . The points C_3 and C_4 arise from the intersection of this line with the posterior cornea and surgery, respectively. $P = D_1$ and $Q = C_3$ in code lines (see the code in page 227).

Line 8: vertical straight line defined by $x = S_{Centre}(1) + (w_{ICRS}/2 - 0.025)$. D_2 is the intersection between this vertical line with the line y' defined in Equation III.7. C_7 and C_8 arise from the intersection between this vertical straight line with posterior and surgery, respectively (see Figure III.16b). $P = D_2$ and $Q = C_7$ in code lines (see the code in page 227).

Line 9: straight line which also forms an angle β' and passes through D_2 . The points C_9 and C_{10} arise from the intersection of this line with surgery and anterior cornea, respectively. $P = D_2$ and $Q = C_{10}$ in the programming lines (see the code in page 227).

- Creation of keratoconic zone (if exists). First, a vertical straight line through ϕ_{KC} is created and the point KC_2 arises from the intersection with the anterior surface. Then, the coordinates of KC_1 are calculated as the intersection between the line which joins CP_{Centre} and KC_2 and posterior surface (see Figure III.17).

Line 10 starts in $P = KC_1$ and finishes in $Q = KC_2$ (see the code in page 227).

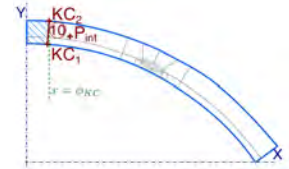


Figure III.17: Keratoconic section in tunnel configuration. The red line shows the straight line which separates the healthy and ectatic region (shaded in blue). The line number is located in red inside of a red circle.

- ii) The cross-section of the surgery is selected with S_{Centre} (see the Figure III.18 and code in page 227). The lines are introduced in the code described in page 227.

Line 11: Line between A_2 and A_3 . $P = A_2$ and $Q = A_3$.

Line 12: Line between B_1 and B_2 . $P = B_1$ and $Q = B_2$.

Line 13: Line between D_1 and C_6 . $P = D_1$ and $Q = C_6$.

Line 14: Line between D_1 and C_3 . $P = D_1$ and $Q = C_3$.

Line 15: Line between D_2 and C_7 . $P = D_2$ and $Q = C_7$.

Line 16: Line between D_2 and C_{10} . $P = D_2$ and $Q = C_{10}$.

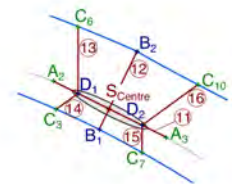


Figure III.18: Lines to cut the surgery. The S_{Centre} (in red) is used to select the region to cut. The different lines are traced between the points calculated previously. The line numbers are located in red inside of a red circle.

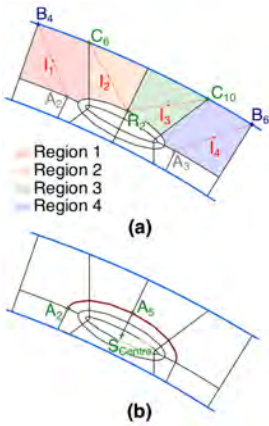


Figure III.19: Points required to draw the largest cover ellipse and the regions where it must be traced. (a) Regions where the largest covered ellipse will be traced. It is defined by the internal points, $I_i, i = 1..4$; (b) Surgery zoom where the largest cover ellipse (in red) is shown.

iii) To complete the surgery zone, the largest covered ellipse is drawn with $C^e = S_{Centre}$, $M = A_2$ and $M = A_5$ (see code in page 222). However, the internal points of each region through which this ellipse passes, must be calculated in advanced (Figure III.19).

Region I is defined by I_1 , internal midpoint between A_2 and B_4 .

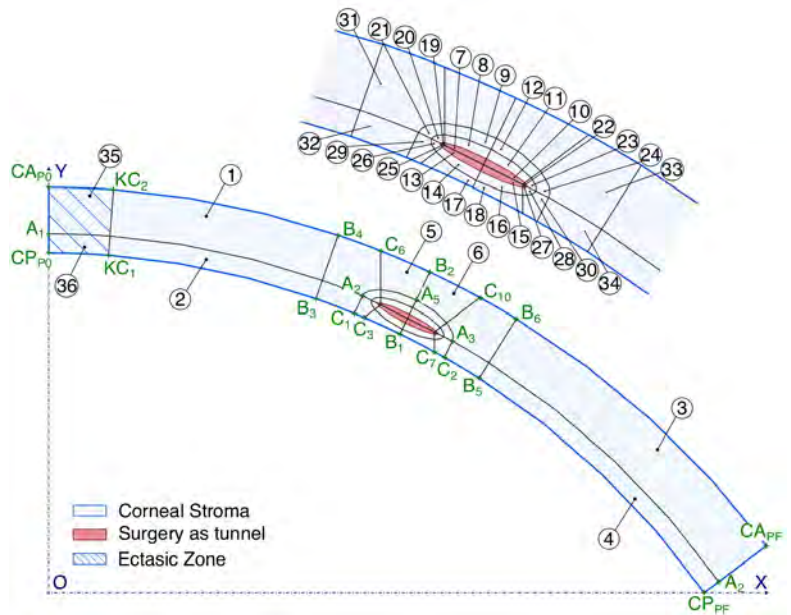
Region II is defined by I_2 , internal midpoint between A_5 and C_6 .

Region III is defined by I_2 , internal midpoint between A_5 and C_{10} .

Region IV is defined by I_2 , internal midpoint between A_3 and B_6 .

After executing all the commands in the proposed order, the cross-section of the cornea will be obtained with the different cuttings which ensure an accurate enough mesh, without distorted elements. The sketch of the cornea with the elliptical surgery which forms the tunnel is shown in Figure III.20. The cornea is divided into 36 regions (ectasic zone included), which correspond to each region that will be created in order to assign the properties of the mesh.

Figure III.20: Sketch of the cornea with the cuttings made to obtain an accuracy mesh. All instructions have the target to built the different cutting in order to define a properly and thin enough mesh to capture the displacement and stress and to assure a good contact between surgery and ring; **(Zoom)** Surgery zone where all regions are defined.



3.1.2. Pocket surgery

To introduce the intrastromal continuous ring, such as the MyoRing, the surgery must be made in the shape of a pocket, whose thickness (T_{Pocket}) is equivalent to the bubbles generated after the application of the femtosecond laser, and fixed in $5 \mu\text{m}$.² Nevertheless this value can be modified by the user. The geometry of the pocket is a combination of circumference arcs and an ellipse.

In order to obtain the geometry described in the Figure III.21, we start from the geometry described in the Figure III.5, where the following points are already calculated in the previous section (see in the Figure III.4): CA_{Centre} , CO_{Centre} , CA_{P0} , CA_{PF} , CP_{P0} , and CP_{PF} . To define the pocket geometry, we need, apart from the thickness of the pocket, its diameter (ϕ_{Pocket}), which is different from the diameter of the optical zone of ring implantation (ϕ_{ICRS}). Firstly, the points which define the ellipse, S_{Centre} , S_M , and S_N , are calculated in order to represent the outermost end of the pocket. Secondly, the arcs of circumference close the pocket in the apex.

² Lubatschowski et al. 2000

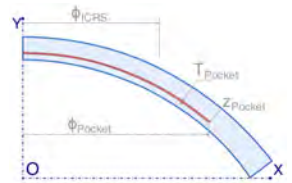


Figure III.21: Input parameters to define the cross-section of the surgery a Pocket. In blue the cross section of the cornea is represented. In red, the surgery is shown. The input parameters are shown in colour grey.

Process to define the points of the ellipse which closes the pocket

Input Parameters (in grey in Figure III.21)

ϕ_{ICRS} : Optical zone, in mm.

ϕ_{Pocket} : Diameter of the pocket, in mm.

Z_{Pocket} : stromal depth of insertion, in percentage.

T_{Pocket} : thickness of the pocket, fixed in $5 \mu\text{m}$.

w : Width of the ellipse, fixed in 0.5 mm.

Operations

S_{Centre} : Centre of the surgery which does not correspond with the centre of the implants, but depends on the diameter of the pocket. The process to obtain the coordinates of this point is commented below.

- i) S_{p1} : Intersection between the arc of the posterior surface and straight vertical line through $\frac{\phi_{Pocket}}{2}$ (see in Equation III.4 but straight vertical line is $x = \frac{\phi_{Pocket}}{2}$ instead of $x = \frac{\phi_{ICRS}}{2}$ and Figure III.22).
- ii) S_{p2} : Intersection between the arc of anterior surface and line which joins S_{p1} with CP_{Centre} (see Equation III.5 and represented in Figure III.23).

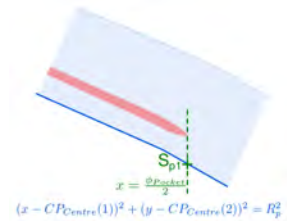


Figure III.22: Calculation of S_{p1} in pocket surgery. Intersection between the arc of posterior surface and straight vertical line through $\phi_{ICRS}/2$.

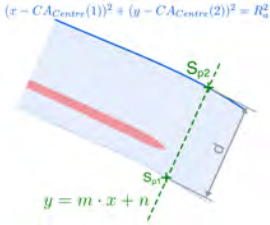


Figure III.23: Calculation of S_{p2} and the distance d in pocket surgery. S_{p2} is the intersection between the arc of anterior surface and the line between S_{p1} and CP_{Centre} . In grey, d is represented as the distance between S_{p1} and S_{p2} .

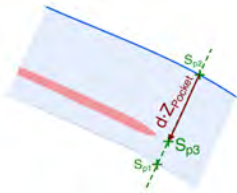


Figure III.24: Calculation of S_{p3} in pocket surgery. Point located at a distance $d \cdot z_{Pocket}$ in the direction of vector $S_{p1}S_{p2}$.

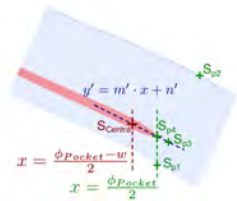


Figure III.25: Calculation of S_{p4} and S_{Centre} in pocket surgery. Intersection between the orthogonal line with the line between S_{p1} and S_{p2} with the vertical straight line through $\phi_{Pocket}/2$. Finally, S_{Centre} is on y' , at a horizontal distance of $w/2$ away from S_{p4} .

- iii) d : distance between S_{p1} and S_{p2} , defined in Equation III.6 and represented in Figure III.23.
- iv) S_{p3} : point which is in the direction of vector $S_{p1}\vec{S}_{p2}$ at a distance of $z_{Pocket} \cdot d$ from anterior cornea (see in Figure III.24).
- v) S_{p4} : First, the orthogonal line (y') to vector $S_{p1}\vec{S}_{p2}$ that passes through S_{p3} is determined. Then, the intersection between that line with the vertical straight line through $\frac{\phi_{Pocket}}{2}$ is the end of the pocket (see Equation III.7, but $x = \frac{\phi_{Pocket}}{2}$ instead of $x = \frac{\phi_{Tunnel}}{2}$). The point is represented in the Figure III.25.
- vi) S_{Centre} : Finally, the centre of the ellipse is calculated as the intersection between the orthogonal line (y') to vector $S_{p1}\vec{S}_{p2}$ that passes through S_{p3} and the straight vertical line through $x = \frac{\phi_{Pocket} - w}{2}$ (see in Figure III.25).

S_M : Point located at the end of the semi-major axis of the ellipse, which is shown in Figure III.26. Its coordinates are calculated evaluating the straight line y' , defined by the Equation III.7 in $x = S_{Centre}(1) + w/2$, which coincides with S_{p4} .

S_{m1} : Point located at the superior end of the semi-minor axis of the ellipse, which is shown in Figure III.26. This point is located at a distance $+T_{Pocket}/2$ from S_{Centre} in the direction of the vector $S_{p1}\vec{S}_{p2}$, whose points are shown in Figure III.25.

S_{m2} : Point located at the inferior end of the semi-minor axis of the ellipse, which is shown in Figure III.26. This point is located at a distance $-T_{Pocket}/2$ from S_{Centre} in the direction of the vector $S_{p1}\vec{S}_{p2}$, whose points are shown in Figure III.25.

Outcomes

Ellipse Centre: $S_{Centre} = (S_{Centre}(1), S_{Centre}(2), 0)$

Point at the end of semi-major axis, the end of the pocket furthest from the apex: $S_M = (S_M(1), S_M(2), 0)$

Point at superior end of semi-minor axis: $S_{m1} = (S_{m1}(1), S_{m1}(2), 0)$

Point at inferior end of semi-minor axis: $S_{m2} = (S_{m2}(1), S_{m2}(2), 0)$

Since the ellipse joins the arcs of the circumference to make the pocket, the whole ellipse cannot be represented. This is caused by the Abaqus code defined by the centre and the points of the semi-axes. Therefore, to

represent the part of the ellipse which corresponds to the end of the pocket, we create it with the Abaqus code to draw splines:

```
# Code lines to draw a spline
mdb.models['Model-1'].sketches['__profile__'].Spline(
    points=((P1x, P1y),
           :
           (Pnx, Pny)))
```

where the points from P_1 to P_n belong to the spline. The more points are used, the more definition the geometry will get. Therefore, it is required to find the points which belong to the ellipse in order to draw the spline. The parametric expression of an ellipse (see in Equation III.10) to calculate the coordinates of the points (see in Figure III.27) is used:

$$\begin{aligned} P_x|_{i=1:N} &= S_{Centre}(x) + a \cdot \cos(\alpha_i) \cdot \cos(\beta) - b \cdot \sin(\alpha) \cdot \sin(\beta) \\ P_y|_{i=1:N} &= S_{Centre}(y) + a \cdot \cos(\alpha_i) \cdot \sin(\beta) + b \cdot \sin(\alpha) \cdot \cos(\beta) \end{aligned} \quad (\text{III.10})$$

where a is the semi-major axis ($\|S_{Centre} \vec{S}_M\|$) and b is the semi-minor axis ($T_{Pocket}/2$), β is the angle which form the major axis of the ellipse with the horizontal, i.e. the inclination of the surgery, and finally, α_i are the angles which are necessary to obtain the points that form the ellipse, being $\alpha = 0^\circ$ the point S_M , $\alpha = 90^\circ$ is S_{m1} , and $\alpha = -90^\circ$ is S_{m2} . In order to draw the ellipse with a spline accurately, we used an overall of $N = 40$ points.

Process to define the arcs of the circumference which close the pocket

Input Parameters

S_{Centre} : Centre of ellipse (see in Figure III.25).

S_{m1} : Point located at the superior end of the semi-minor axis of the ellipse (see in Figure III.26).

S_{m2} : Point located at the inferior end of the semi-minor axis of the ellipse (see in Figure III.26).

CP_{Centre} : Centre of posterior cornea (see in Figure III.12).

Operations

A_{sup} : Intersection between the vertical straight line of apex with the cir-

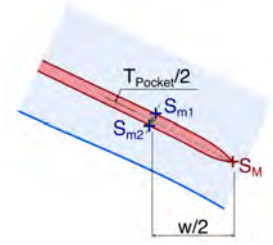


Figure III.26: Calculation of S_M , S_{m1} , and S_{m2} in pocket surgery. S_M is in red and S_{m1} and S_{m2} are in blue.

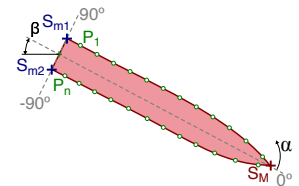


Figure III.27: Representation of the ellipse by spline. In green we represent the points to draw the spline which correspond with the different angles α_i .

cumference arc defined by centre of posterior cornea (CP_{Centre}) and R_{sup} , which is the distance from CP_{Centre} to S_{m1} (see in Figure III.28).

A_{inf} : Intersection between the vertical straight line of apex with the circumference arc defined by centre of posterior cornea (CP_{Centre}) and R_{inf} , which is the distance from CP_{Centre} to S_{m2} (see in Figure III.28).

Outcomes

Superior point of pocket in apex: $A_{sup} = (A_{sup}(1), A_{sup}(2), 0)$

Superior point of pocket in apex: $A_{sup} = (A_{sup}(1), A_{sup}(2), 0)$

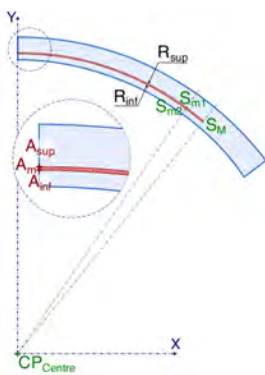


Figure III.28: Arcs of the circumference which close the pocket. Points in green, such as CP_{Centre} , S_M , S_{m1} , and S_{m2} have been already obtained; Points in red, such as A_{sup} , A_m , and A_{inf} represented in zoom, are the three points to define the arcs and to close the pocket.

Finally, once the section to be cut has been selected with P_{int} of Figure III.28 (see code in page 222), the code lines corresponding to the spline creation (see code in page 233), and to the two arcs of circumference, are introduced. The superior arc is defined by the posterior cornea centre (CP_{Centre}), the superior point of the pocket (A_{sup}), and the point located at the superior end of the semi-minor axis (S_{m1}). The inferior arc is defined by CP_{Centre} , the inferior point of the pocket (A_{inf}) and the point placed at the inferior end of the semi-minor axis (S_{m2}). Both arcs are defined in clockwise direction (see code in page 227).

Once the pocket is created within the cornea, the groups “CORNEA”, “SURGERY”, “APEX”, “APOYO”, “CORNEA_ANTERIOR” and “CORNEA_POSTERIOR”, and surfaces, such as “INNER_SURF” and “IOP_SURF” must be generated before making the cuttings to obtain a more accurate mesh. To generate the groups and the surfaces, it is necessary to find points that belong to the regions mentioned before. Some points have been defined previously such as S_{Centre} , which is used to define the group “SURGERY”, or P_{Apex} and P_{Limbus} , which are used to define the groups “APEX” and “APOYO”, respectively. However, the following points must be calculated to define the rest of the groups (“CORNEA”, “CORNEA_ANTERIOR” and “CORNEA_POSTERIOR”) and the two surfaces.

P_{int} : The interior point of the cornea is used not only to select the region to make the slice, but also to define the group “CORNEA”.

Q_{CA} : Point to define the “CORNEA_ANTERIOR” group.

Q_{CP} : Point to define the “CORNEA_POSTERIOR” group and the surface where the intraocular pressure will be applied, “IOP_SURF”.

S_1 : Point to define the superior inner surface.

S_2 : Point to define the inferior inner surface.

These points can be obtained from the following steps.

- i) The angle (α) is formed by S_{m1} and the horizontal axis, and the angle (α_{int}) is calculated in Equation III.8 and Figure III.29.
- ii) The line y_{int} is determined with a slope defined by α_{int} and the centre of posterior cornea (CP_{Centre}) (see Equation III.9).
- iii) Q_{CA} arises from the intersection between the straight line y_{int} and the circumference arc which defines the anterior cornea.
- iv) Q_{CP} arises from the intersection between the straight line y_{int} and the circumference arc which defines the posterior cornea.
- v) S_1 arises from the intersection between the straight line y_{int} and the circumference arc which defines the superior inner surface of the surgery.
- vi) The points S_2 arises from the intersection between the straight line y_{int} and the circumference arc which defines the inferior inner surface of the surgery.
- vii) P_{int} is the middle point between S_1 and Q_{CA} .

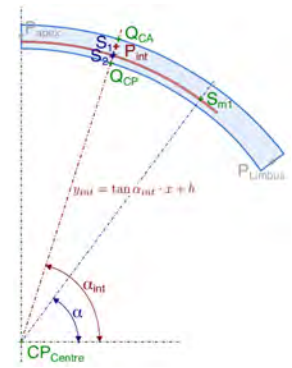


Figure III.29: Calculation of P_{int} , Q_{CA} , and Q_{CP} , S_1 , and S_2 . Points in green, Q_{CA} , Q_{CP} , and S_{m1} are used to calculate the midpoints (in blue), S_1 and S_2 , and in red appears P_{int} . The points which have been calculated before appear in grey: P_{Apex} and P_{Limbus} .

The code to create the groups and the surfaces is explained in page 226, where “NAME” and “POINT” correspond to the values of the Table III.2.

Once the cross–section of the cornea with the pocket has been created, the following step is to make the cuttings in the cornea to obtain a thin and accurate enough mesh. All cuttings have been performed with the code to create lines, ellipses, arcs of circumference (see in page 227) and splines (see in page 233). Each instruction must be included in the code indicated in page 222 for selecting the region of interest with the internal point that belongs to that region.

The following instructions aim to obtain the initial (P) and final points (Q) of each line; the centre (C), initial (A) and final points (B) of the circumference arcs; the centre point (C), which define the semi–major (M) and the semi–minor axis (N); and the different points which form the spline (P_i). In addition, they must follow the order established below to obtain the final cross–section of the cornea (see in Figure III.36), whose starting state is Figure III.21:

NAME	POINT
CORNEA	P_{int}
SURGERY	S_{Centre}
APEX	P_{apex}
APOYO	P_{Limbus}
CORNEA_ANTERIOR	Q_{CA}
CORNEA_POSTERIOR	Q_{CP}
IOP_SURF	Q_{CP}
INNER_SURF	S_{m1}, S_{m2} S_1, S_2

Table III.2: Sets and surfaces definition to pocket surgery. The first column represents the name of sets or surfaces and the second column the points used to define the set or surface.

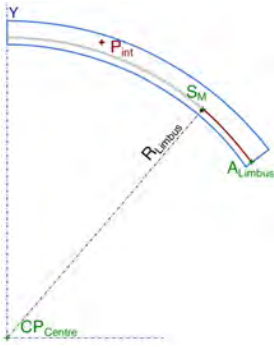


Figure III.30: Internal arc to join the end of the pocket with the limbus. P_{int} is in red. Points CP_{Centre} , S_M , and A_{Limbus} are in green to define the arc, and the complete cutting arc is drawn in red.

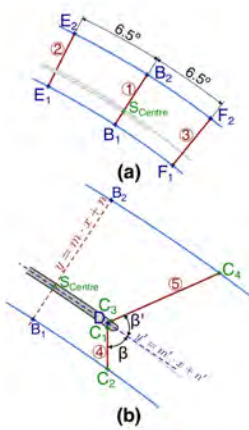


Figure III.31: Lines which cut the end of the pocket. (a). Lines which cross the stroma. The line between B_1 and B_2 divides the surgery in two parts, a semi-ellipse and circumference arcs; $+6.5^\circ$ from this line, the superior line is formed creating the points B_3 and B_4 with the intersection with posterior and anterior cornea respectively; -6.5° from the central line, the inferior line is drawn, resulting in the points B_5 and B_6 with the intersection with posterior and anterior cornea respectively; (b) Zoom of the end of the pocket. The line numbers are in red inside a circle.

Order of the instructions

1. The cross-section of the cornea (without surgery) is selected with P_{int} .
 - Arc of circumference which joins the end of the pocket with the limbus, to divide the cross-section of the cornea into two parts is created (see in Figure III.30). Therefore, the points to be introduced in the code of the arc of circumference are the centre of the posterior cornea ($C = CP_{Centre}$), the point of the end of the semi-major axis ($A = S_M$), and the point of the limbus ($B = A_{Limbus}$) which is calculated as follows:
 - i) The radius (R_{Limbus}) of the circumference arc is calculated:

$$R_{Limbus} = \|CP_{Centre}S_M\|.$$
 - ii) The centre of the posterior cornea and the radius (R_{Limbus}) form the circumference which intersects with the straight line of the limbus, formed by the points CP_{Final} and CA_{Final} .
 - iii) The intersection between these geometries is the point A_{Limbus} .
 - Creation of the cuttings around the end of the pocket (see in Figure III.31).

Line 1: (or central line) Straight line between B_1 and B_2 . B_1 is the intersection between the line that passes through S_{Centre} and CP_{Centre} with the posterior cornea. B_2 is the intersection between the line that passes through S_{Centre} and CP_{Centre} with the anterior cornea. $P = B_1$ and $Q = B_2$ in the programming lines.

Line 2: Straight line with angle of $+6.5^\circ$ from central line. E_1 and E_2 are the intersection of this line with the posterior and anterior cornea, respectively. $P = E_1$ and $Q = E_2$ in the programming lines.

Line 3: Straight line with angle of -6.5° from central line. F_1 and F_2 are the intersection of this line with the posterior and anterior cornea, respectively. $P = F_1$ and $Q = F_2$ in the programming lines. The point f arises from the intersection between the Line 3 and the arc of circumference which joins the end of the pocket with the limbus.

Line 4: Vertical straight line defined by $x = S_{Centre}(1) + (w_{ICRS}/2 - 0.025)$. D is the intersection between this vertical line with the line y' defined in Equation III.7. As a result, angle β is formed. C_1 and C_2 arise from the intersection between this vertical straight

line with the surgery and posterior cornea, respectively (see in Figure III.31.b). $P = D$ and $Q = C_2$ in the code to draw the lines.

Line 5: Straight line which forms an angle $\beta' = 2 \cdot \beta - \frac{\pi}{2}$ with y' , and passes through D . The points C_3 and C_4 arise from the intersection between the Line 5 with the surgery and anterior cornea, respectively. $P = D$ and $Q = C_4$ in the code to draw the lines.

- The cuttings are generated around the optical zone of implantation ($\phi_{ICRS}/2$) (see in Figure III.32).

- The corneal area, where the optical zone is placed between the apex and the Line 2 defined by points E_1 and E_2 , is determined. The angle (α_{OZ}) of the region is determined in the Equation III.11.

$$\alpha_{sup} = \text{atan} \frac{E_1(y) - CP_{Centre}(y)}{E_1(x) - CP_{Centre}(x)} \quad (\text{III.11})$$

$$\alpha_{OZ} = \frac{\pi}{2} - \alpha_{sup}$$

- The first of the two straight lines for the cuttings will be defined with a slope which forms an angle with respect to the horizontal line of $\alpha_1 = \alpha_{sup} + \frac{\alpha_{OZ}}{2}$. Equation III.12 represents this line (g_1). Finally, the points H_1 and H_2 arise from the intersection between this line with the posterior and anterior cornea, respectively. Once these points have been calculated, **Line 6** is created with the corresponding code, where $P = H_1$ and $Q = H_2$.

$$g_1(x) = \underbrace{\tan \alpha_1}_{a_1} \cdot x + \underbrace{CP_{Centre}(y) - \tan \alpha_1 \cdot CP_{Centre}(x)}_{b_1} \quad (\text{III.12})$$

- The second of the straight lines will be defined with a slope which forms an angle with respect to the horizontal line of $\alpha_2 = \alpha_{sup} + \frac{\alpha_{OZ}}{4}$ (see the Equation III.13). Finally, the points J_1 and J_2 arise from the intersection between this line with the posterior and anterior cornea, respectively. Once these points have been calculated, **Line 7** is created with the corresponding code, where $P = J_1$ and $Q = J_2$.

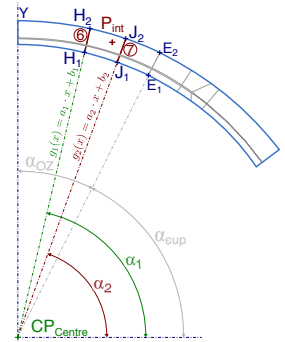


Figure III.32: Lines around the optical zone. The intersection of the lines g_1 and g_2 with the posterior and anterior cornea create the points B_7 , B_8 , B_9 , and B_{10} . The line numbers are located inside of a red circle.

$$g_2(x) = \underbrace{\tan \alpha_2}_{a_2} \cdot x + \underbrace{CP_{Centre}(y) - \tan \alpha_2 \cdot CP_{Centre}(x)}_{b_2} \tag{III.13}$$

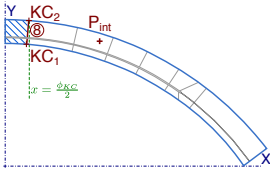


Figure III.33: Keratoconic section in pocket configuration. The red line shows the straight line which separates the healthy and ectasic region (shaded in blue). The line number is located inside a red circle.

- Creation of keratoconic zone (if exists). First, the point KC_2 arises from the intersection between the anterior surface of the cornea and the vertical straight line that passes through $\phi_{KC}/2$. Then, the coordinates of KC_1 are calculated as the intersection between the line which joins CP_{Centre} and KC_2 and posterior surface (see Figure III.33). **Line 8** starts in $P = KC_1$ and finishes in $Q = KC_2$.

2. The cross-section of the surgery is selected with S_{Centre} (see in Figure III.34), and the following orders must be accomplished to create the cuttings.

Line 9: Line between S_{Centre} and S_M . $P = S_{Centre}$ and $Q = S_M$ in the programming lines.

Line 10: Arc of circumference which divides the pocket into two equal parts, with CP_{Centre} as the centre and radius defined by the euclidean distance, $R_{med} = \|CP_{Centre} \vec{S}_{Centre}\|$. The point A_{med} arise from the intersection of this circumference with the apex (see in Figure III.28). Therefore, $C = CP_{Centre}$, $A = A_{med}$, and $B = S_{Centre}$.

Line 11: Line between B_1 and B_2 . $P = B_1$ and $Q = B_2$ in the programming lines.

Line 12: Line between D and C_2 . $P = D$ and $Q = C_2$ in the programming lines.

Line 13: Line between D and C_4 . $P = D$ and $Q = C_4$ in the programming lines.

Line 14: Line between E_1 and E_2 . $P = E_1$ and $Q = E_2$ in the programming lines. The points e_1, e_2 , and e_3 (from posterior to anterior cornea) arise from the intersections of the Line 14 with the arcs of circumference which define the pocket.

Line 15: Line between H_1 and H_2 . $P = H_1$ and $Q = H_2$ in the programming lines. The points h_1, h_2 , and h_3 (from posterior to anterior cornea) arise from the intersections of the Line 15 with the arcs of circumference which define the pocket,

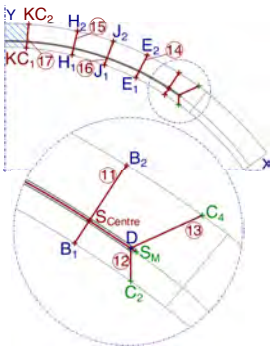


Figure III.34: Lines to cut the pocket. The S_{Centre} (in red) is used to select the region to cut. The different lines are traced between the points calculated previously. The line numbers are located inside a red circle.

Line 16: Line between J_1 and J_2 . $P = J_1$ and $Q = J_2$ in the programming lines. The points j_1, j_2 , and j_3 (from posterior to anterior cornea) arise from the intersections of the Line 16 with the arcs of circumference which define the pocket.

Line 17: Line between KC_1 and KC_2 . $P = KC_1$ and $Q = KC_2$ in the programming lines. The points kc_1, kc_2 , and kc_3 (from posterior to anterior cornea) arise from the intersections of the Line 17 with the arcs of circumference which define the pocket.

3. To complete the cross-section cuttings of the cornea, a semi-ellipse is drawn on the elliptical edge of the pocket. The centre of the ellipse is S_{Centre} , R_M is the point located in the semi-major axis, which is 1.2 times greater than the distance to the semi-major axis of the ellipse that defines the end of the pocket. R_m is the point located in semi-minor axis, which is placed at a distance of 2.5 times greater than the distance from the semi-minor axis of the ellipse that defines the end of the pocket. Consequently, the points which define the code to draw an ellipse are: $C^e = S_{Centre}$, $M = R_M$, and $N = R_m$ (see code in page 227), but previously the internal points of each region, through which this ellipse passes, must be calculated (see Figure III.35):

Region I is defined by I_1 , the internal midpoint between S_{m1} and C_4 .

Region II is defined by I_2 , the internal midpoint between S_M and F_2 .

Region III is defined by I_3 , the internal midpoint between S_M and F_1 .

Region IV is defined by I_4 , the internal midpoint between S_{m2} and C_2 .

After executing all these commands in the proposed order, the cross-section of the cornea will be obtained with the different cuttings that ensure an accurate enough mesh, without distorted elements. The sketch of the cornea including the pocket as surgery, is shown in Figure III.36. The cornea is divided into 34 regions (ectasic zone included), which correspond to each region that will be created in order to assign the properties of the mesh.

3.2. Geometry of the rings

The option to perform two types of rings has been prepared automatically. The first one is a generic ring whose cross-section is an ellipse, while the second option, more complex, tries to represent the cross-section of the MyoRing, which is a commercial ring proposed by Daxer.³

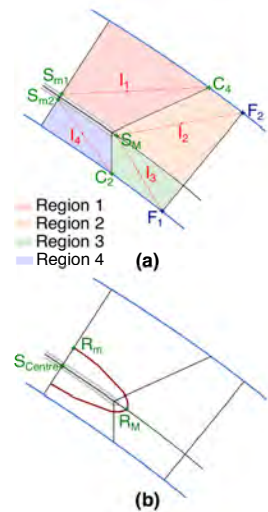
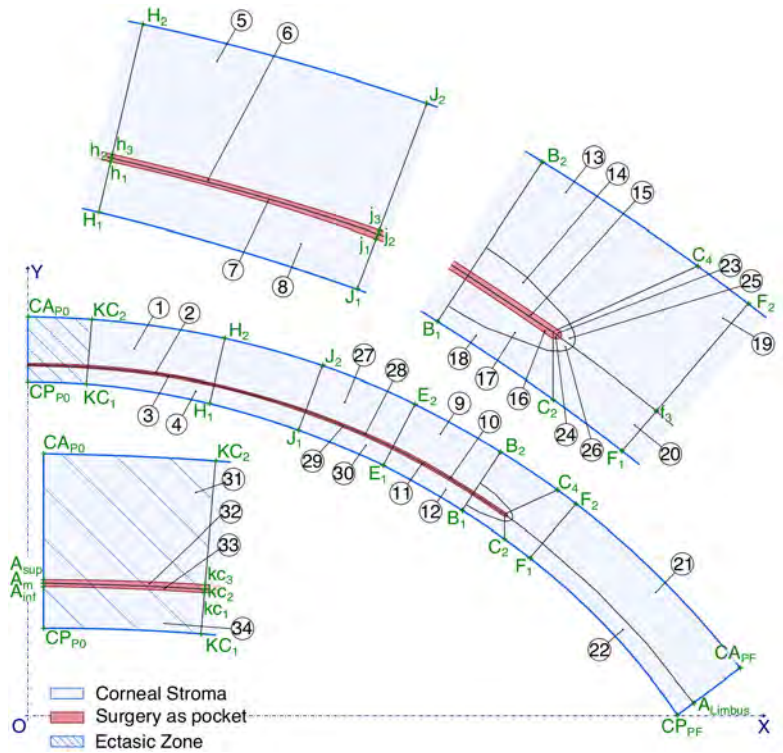


Figure III.35: Points required to draw the cover ellipse at the elliptical zone of the pocket. (a) Regions where the cover ellipse will be traced. It is defined by the internal points, $I_i, i = 1..4$; (b) Extreme pocket zoom where the cover ellipse (in red) is shown.

³ Daxer 2008

Figure III.36: Sketch of the cornea with pocket including the cuttings made to obtain an accurate mesh. All the instructions aim to built the different cuttings in order to define a proper and thin enough mesh. As a result, the displacement and stress field is captured. In addition, the better and precise contact between the tissue and the implants is assured; **(Zooms)** Ectasic Zone, optical zone of implantation and the end of the pocket where all regions are defined.



3.2.1. Generic cross-section ring

The cross-section of generic rings is elliptical. The input parameters to introduce in the geometry are: the width of the ring (w_{ICRS}), fixed in 0.5 mm, and the thickness of the ring, which is a parametric value, described by h_{ICRS} . Then, the centre of the ellipse (C_e) is defined by the diameter of the optical zone implantation (ϕ_{ICRS}), and the height (h_{ICRS}) from the horizontal axis (see Figure III.37). Finally, the last parameter, which depends on the cornea cross-section, is the angle of inclination of the ring (α_M) respect to the horizontal. The ring was placed parallel to the posterior surface cornea. Therefore, the major axis of the ring forms an angle that is perpendicular to the line that joins the centre of the posterior cornea (CP_{Centre}) with S_{Centre} , if the surgery is a tunnel (see dashed line y' in Figure III.10). On the other hand, if the surgery is a pocket, the angle will

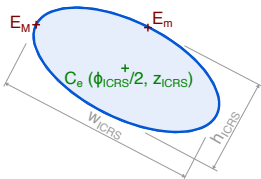


Figure III.37: Cross-section of the generic ring. The cross-section of the generic ring is elliptical. The dimension of major and minor axis appear in grey. The point E_M in red is located on the end of semi-major axis and the point E_m in red appears on the end of semi-minor axis.

be perpendicular to the line that joins the centre of the posterior cornea with the point S_{OZ} formed by the intersection between the middle circumference arc (intermediate arc between superior and inferior arcs), which divides the pocket, and the straight vertical line through $\phi_{ICRS}/2$ (see Equation III.14 and Figure III.38):

$$(x - CP_{Centre}(1))^2 + (y - CP_{Centre}(2))^2 = R_{med}^2 \quad (III.14)$$

$$x = \phi_{ICRS}$$

In order to represent the elliptical cross-section in Abaqus, it is necessary to know three points which will introduce in the code (see in page 227): the centre of the ellipse (C_e) and the points located on the ends of the ellipse's axis (E_M and E_m).

Process to define the cross-section of the generic rings

Input Parameters

C_e : Centre of ellipse (see in Figure III.37): $C_e = (\phi_{ICRS}/2, z_{ICRS})$.

w_{ICRS} : Width of the ellipse fixed to 0.5 mm (see in Figure III.37).

h_{ICRS} : Thickness or height of the ellipse (see in Figure III.37).

α_M : Inclination of the ellipse with respect to horizontal (see in Figure III.38).

Operations

E_M : Point located at the end of the semi-major axis (see in Figure III.37). This point is calculated with the parametric expression of the ellipse (see Equation III.10), where $S_{Centre} = C_e, a = w_{ICRS}/2, b = h_{ICRS}/2, \alpha = 180^\circ, \beta = \alpha_M$.

E_m : Point located at the end of the semi-minor axis (see in Figure III.37). This point is calculated with the parametric expression of the ellipse (see Equation III.10), where $S_{Centre} = C_e, a = w_{ICRS}/2, b = h_{ICRS}/2, \alpha = 90^\circ, \beta = \alpha_M$.

Outcomes

Point on semi-major axis. $E_M = (E_M(1), E_M(1), 0)$.

Point on semi-minor axis. $E_m = (E_m(1), E_m(1), 0)$.

Once the geometry of the ring is drawn, the following step is to create the sets and surfaces. The Table III.3 shows the names with their corresponding points which must be introduced in the Abaqus code to create sets and

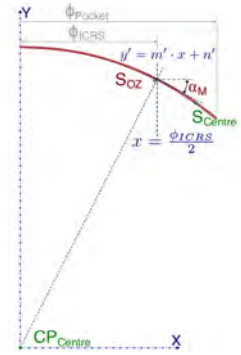


Figure III.38: Inclination of the generic ring when the surgery is a pocket. In grey, the dimension of the pocket and the optical zone implantation are shown. S_{Centre} is represented in green. Finally, the point S_{OZ} , which arises from the intersection between vertical straight line that passes through $\phi_{ICRS}/2$ and the middle circumference arc, and the inclination angle α_M are shown in red.

NAME	POINT
ANILLO_G	C_e
PERIMETRO ANILLO_G_EXT	E_M
ANILLO_G_SURF	E_m

Table III.3: Sets and surfaces definition to generic ring. The first column represents the name of sets or surfaces and the second column, the points used to define the set or surface.

surfaces (see in page 226).

Finally, the cuttings along the cross-section must be performed in order to obtain a thin enough mesh with uniform elements. Firstly, it is necessary to select the cross-section (see the code in page 222) with the point of the centre of ellipse (C_e). Then, the points at the other ends of the axis of the ellipse are obtained:

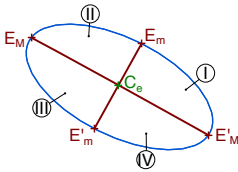


Figure III.39: Cuttings of the cross-section of the generic ring. The points which are required to define the lines in Abaqus code are presented in red.

E'_M : Point located at the other end of the semi-major axis (see in Figure III.39). This point is calculated with the parametric expression of the ellipse (see Equation III.10), where $S_{Centre} = C_e$, $a = w_{ICRS}/2$, $b = h_{ICRS}/2$, $\alpha = 0^\circ$, $\beta = \alpha_M$.

E'_m : Point located at the other end of the semi-minor axis (see in Figure III.39). This point is calculated with the parametric expression of the ellipse (see Equation III.10), where $S_{Centre} = C_e$, $a = w_{ICRS}/2$, $b = h_{ICRS}/2$, $\alpha = -90^\circ$, $\beta = \alpha_M$.

In the last step, two lines that cut the cross-section (see in Figure III.39) are introduced with the Abaqus code for lines (see the code in page 227), where the initial (P) and the final point (Q) are required.

Line 1: Straight line which forms the major axis of the ellipse through the points E_M and E'_M . $P = E_M$ and $Q = E'_M$.

Line 2: Straight line which forms the minor axis of the ellipse through the points E_m and E'_m . $P = E_m$ and $Q = E'_m$.

⁴ Daxer 2008

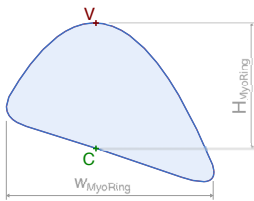


Figure III.40: Cross-section of the MyoRing. The cross-section of the MyoRing is determined by the intersection of a circumference and a parabola. The main dimensions are in grey. The point V in red is located at a distance of $H_{MyoRing}$ from the base (C).

3.2.2. MyoRing

The cross-section of the MyoRing according to Daxer 2008⁴ is determined by the intersection of two geometries. The base is a circumference of radius 8 mm, while its upper part is determined by a parabola, whose sides are opened downwards and whose vertex is at a distance which coincides with the thickness of the ring ($H_{MyoRing}$) from the base. Finally, the distance between the points of the intersection of the parabola with the circumference is $w_{MyoRing} = 0.5$ mm (see in Figure III.40).

The process to obtain the parabolic part of the MyoRing is described below (see in Figure III.41):

- i) The base of the MyoRing is part of a circumference of radius 8 mm (R) and centred in the origin $O = (0, 0)$ (see Equation III.15).

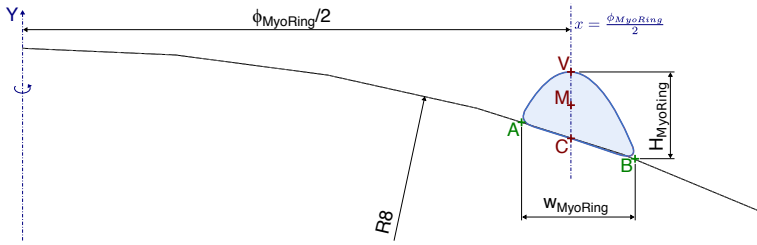


Figure III.41: Procedure to obtain the MyoRing cross-section. The vertex of the parabola is found at a vertical of $H_{MyoRing}$ from the base (C) and at a horizontal distance of $\phi_{MyoRing}/2$ from the optical axis. The point located at the base (C) is the intersection between the circumference of radius 8 mm with the vertical straight line through $x = \phi_{MyoRing}/2$. The points A and B are the intersections of the parabola with the circumference. Finally, the point M is calculated to select the MyoRing cross-section.

- ii) The point C is the intersection between the circumference and the straight vertical line through $\frac{\phi_{MyoRing}}{2}$.
- iii) The vertex of the parabola (V) is found at a vertical distance of $H_{MyoRing}$ from the point C.
- iv) A minimisation process is generated to guarantee that the distance between the points of the parabola which intersect with circumference is $w_{MyoRing} = 0.5$ mm. From this process, the points A and B are obtained, as well as the coefficients which define the parabola (a_p , b_p , and c_p in Equation III.15:

$$\text{Circumference: } (x - O(1))^2 + (y - O(2))^2 = R^2 \quad (\text{III.15})$$

$$\text{Parabola: } y = a_p \cdot x^2 + b_p \cdot x + c_p$$

- v) Finally, to select the MyoRing, the middle point (M) is at a distance $H_{MyoRing}/2$ from the vertex V, i.e: $M = \left(V(1), V(2) - \frac{H_{MyoRing}}{2} \right)$ (see in Figure III.41).

In order to trace the MyoRing cross-section in Abaqus, only the spline code is necessary. As the previous section has been explained in (see Section 3.1.2 and code in page 233), to trace a spline it is necessary to find the points that belong to the contour of the parabola. The more points in the contour, the better definition of the section will be obtained. Two parts can be differentiated at the MyoRing contour: the parabola and the circumference.

Process to define the cross-section of the MyoRing

Input Parameters

a_p , b_p , and c_p : Coefficients of the parabola equation.

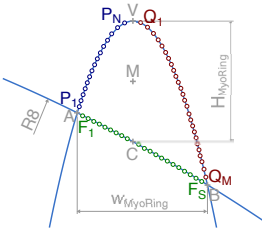


Figure III.42: References to obtain the points to trace the splines. Part 1 is shown in blue, Part 2 is shown in red, and the spline points of the circumference appear in green. The previous points and measurements are represented in grey.

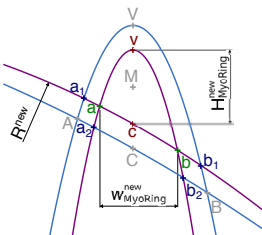


Figure III.43: Points to define the interior cuttings and the fillet parts. The points, v and c , vertically aligned to V and C , are shown in red; the points which define the width of the new geometry are drawn in green; the points which are going to be used for the round corner appear in blue; finally, previous points are represented in grey. The exterior MyoRing (the previous one) appears in blue and the new geometry is drawn in purple.

V : Vertex of the parabola (see in Figure III.40).

A and B : Points which result from the intersection between the parabola and the circumference (see in Figure III.41).

$w_{MyoRing}$: Width of the MyoRing, which is the distance between A and B .

O and R : The circumference centre and radius, respectively.

Operations

The parabola is divided into 2 parts, from A to V , and from V to B . In order to represent it, the points that belong to each part must be calculated.

Part 1: Part of the parabola from A to V (blue in Figure III.42), formed by $N = 30$ points. The coordinates of the points, P_1 to P_N , are defined with the parabola expression (see Equation III.15), where x is an array of points which starts in $P_1 = A$ and finishes in $P_N = V$, with a step of $\frac{V(1)-A(1)}{N-1}$.

Part 2: Part of the parabola from V to B (red in Figure III.42), formed by $M = 50$ points. The coordinates of the points, Q_1 to Q_M , are defined with the parabola expression (see Equation III.15), where x is an array of points which starts in $Q_1 = V$ and finishes in $Q_M = B$, with a step of $\frac{B(1)-V(1)}{M-1}$.

The points which form the circumference, formed by $S = 100$ points (green in Figure III.42). The coordinates of these points, F_1 to F_S , are defined with the circumference expression (see Equation III.15), where x is an array of points which starts in $F_1 = A$ and finishes in $F_S = B$, with a step of $\frac{B(1)-A(1)}{S-1}$.

Outcomes

P_1 to P_N : array of points to define the first parabolic part.

Q_1 to Q_M : array of points to define the second parabolic part.

F_1 to F_S : array of points to define the circumferential part.

The next step is to determine the points to build the splines that form the rounded corners of the MyoRing. During the process (see in Figure III.43), the points which will serve to make the interior cuts are obtained. These will help to achieve a thin enough mesh without distorted elements. The strategy is to find a geometry similar to the exterior MyoRing but $t = 60\%$ smaller. Therefore, a new parabola and circumference must be calculated:

- i) The vertex, v , is located at a distance $\frac{H_{MyoRing}^{new}}{2}$ from the middle point (M), where:

$$v = \left(V(1), M(2) + \frac{H_{MyoRing}^{new}}{2} \right) \quad (III.16)$$

- ii) The point on the base, c , of the new section is also located at $\frac{H_{MyoRing}^{new}}{2}$ from the middle point (M), but downwards:

$$c = \left(V(1), M(2) - \frac{H_{MyoRing}^{new}}{2} \right) \quad (III.17)$$

- iii) The centre of the new circumference, O^{new} , is located at a distance from the centre of the initial circumference, O equal to $(1 - t)\%$ of the distance between O and M .
- iv) The radius of the new circumference, R^{new} , is the distance between O^{new} and c .
- v) The intersection points, a and b , between the new sections are calculated using the same minimization process assuring that the distance ($w_{MyoRing}^{new}$) between them is $w_{MyoRing} \cdot t/100$.

Finally, to perform the rounded corners, the points a_1 and b_1 arise from the intersection between the new circumference (in purple in Figure III.43) and the previous parabola (in blue); the points a_2 and b_2 are the intersection between the new parabola (in purple) and the previous circumference (in blue). The first fillet is formed between a_1 and a_2 , and the second rounded corner is drawn between b_1 and b_2 .

The geometry in order to round the the two corners is a parabola (see in Figure III.44), whose general expression is Equation III.15:

Corner 1: The vertex of this parabola (V_1) is located at the line that joins the points A and a . The distance d_1 and the coordinates of V_1 are calculated in Equation III.18. The coefficients of the parabola are adjusted so that the parabola passes through V_1 , a_1 and a_2 .

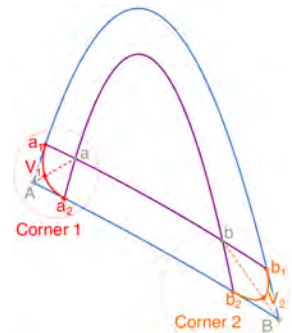


Figure III.44: Corner rounding of the MyoRing. The Corner 1, in red, is formed by a parabola through a_1 , V_1 , and a_2 ; The Corner 2, in orange, is formed by a parabola through b_2 , V_2 , and b_1 .

$$d_1 = \|\vec{A}a\|$$

$$V_1 = A + 0.275 \cdot d_1 \cdot \frac{(a - A)}{\|(a - A)\|} \tag{III.18}$$

Corner 2: The vertex of this parabola (V_2) is located at the line that joins the points B and b . The distance d_2 and the coordinates of V_2 are calculated in Equation III.19. The coefficients of the parabola are adjusted so that the parabola passes through V_2 , b_1 and b_2 .

$$d_2 = \|\vec{B}b\|$$

$$V_2 = B - 0.275 \cdot d_2 \cdot \frac{(B - b)}{\|(B - b)\|} \tag{III.19}$$

The new internal geometry and the fillet, which are used to perform the internal cuttings, are defined by splines. Thus, the points which form them must be obtained.

The points which form the internal cuttings are defined in the corresponding expressions of the circumference and parabola (see Equation III.15):

$$O = O^{new} \text{ and } R = R^{new} \text{ and } x \text{ is an array of } S = 100 \text{ points which starts in } f_1 = a_1 \text{ and finishes in } f_S = b_1, \text{ with a step of } \frac{b_1(1)-a_1(1)}{S-1}.$$

The parabola, divided in 2 parts of $N = 30$ and $M = 50$ points, where the array of points of the first part starts in $p_1 = a_2$ and finishes in $p_N = v$ with a step of $\frac{v(1)-a_2(1)}{N-1}$; and the array of points of the second part begins in $q_1 = v$ and ends in $q_M = b_2$, with a step of $\frac{b_2(1)-v(1)}{M-1}$.

Each corner is divided in $W = 10$ points.

The coordinates of the points which form the Corners 1 and 2, h_1 to h_W and j_1 to j_W , respectively, are defined with the expression of the parabola (Equation III.15), where x is an array of points which starts in $h_1 = a_1$ and $j_1 = b_2$ and finishes in $h_W = a_2$ and $j_W = b_1$, with the steps of $\frac{a_2(1)-a_1(1)}{W-1}$ and $\frac{b_1(1)-b_2(1)}{W-1}$, respectively (see Figure III.45).

Once all points are calculated, the next step is to write the code in Abaqus Python scripting in the following order to obtain the MyoRing cross-section geometry.

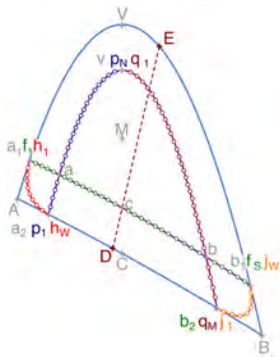


Figure III.45: Points to draw the splines corresponding on internal cuttings and round corners. The first part of the parabola is in blue, and the second one is in red, and the circumferential part is in green. The points D and E which are used to divide the MyoRing appear in red. The previous points appear in grey.

1. The main part of the cross-section of the MyoRing is built with the spline code (see page 233) that embeds the points corresponding to the parabola (P_1 to P_N and Q_1 to Q_M), the circumference (F_1 to F_S), and the rounded corners (h_1 to h_W and j_1 to j_W). These code lines must be included in the code to open the sketch (see page 219).
2. Once the cross-section of the MyoRing has been created, the following step is to create the sets and surfaces. The Table III.4 shows the names with their corresponding points which must be introduced in the Abaqus code (see page 226) to create the sets and surfaces.
3. The cuttings along the cross-section must be performed in order to obtain a thin enough mesh with uniform elements.
 - i) Firstly, the cross-section is selected with the point M (see the code in page 222).
 - ii) The points from p_1 to p_n and from q_1 to q_M which define the interior parabola are introduced in the spline code described in page 233.
 - iii) The points from f_1 to f_S which define the interior circumference are introduced in the spline code described in page 233.
 - iv) Finally, the straight line which divides the MyoRing in two parts is created with the line code (see page 227), where $P = D$ is the intersection between the line which connects O^{new} with c and the circumference centred in O with radius R ; and $Q = E$, is the intersection between the line which connects O^{new} with c with the exterior parabola (see Figure III.45).

NAME	POINT
ANILLO_G	M
PERIMETRO ANILLO_G_EXT	V
ANILLO_G_SURF	V

Table III.4: Sets and surfaces definition to MyoRing. The first column represents the name of sets or surfaces, and the second column, the point used to define the set or surface.

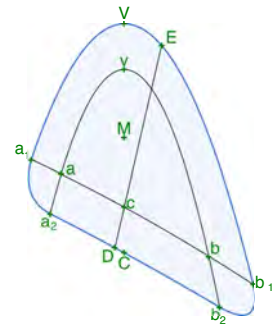


Figure III.46: Sketch of the MyoRing including the cuttings to obtain an accurate mesh.

After executing all these commands in the established order, the cross-section of the MyoRing is obtained with the different cuttings to ensure an accurate mesh without distorted elements. The sketch of the MyoRing is shown in Figure III.46.

4. Material and section assignment

Two different material models could be assigned depending on whether it is a cornea or a ring. When the model is a cornea, Neo-Hookean strain-energy function is used, with the material constants $C_{10} = 0.01 \text{ MPa}$ and $D_1 = 0.1 \text{ MPa}^{-1}$. On the other hand, when the concerned model is a ring, then an elastic model defined by the Young's modulus (E_{PMMMA}) of

⁵ Flecha-Lescún et al. 2018

3,300 MPa and a Poisson's ratio (ν_{PMMA}) of 0.4 is used.⁵ In addition, the density of both materials is also added: $\rho_{Cornea} = 1 \text{ g/cm}^3$ and $\rho_{PMMA} = 1.18 \text{ g/cm}^3$.

Afterwards, the sections of each model are generated and the corresponding materials are assigned.

The codes to generate both the material and its assignment to each model are presented below:

4.1. Material and section assignment for the cornea models

The material, called *CORNEAL_TISSUE*, is assigned to both element sets of the cornea, denominated as *CORNEA* and *CIRUGIA*. Particularly, in the second case, the set refers to elements of the surgery that can be either tunnel or pocket.

```
# Material Definition
mdb.models['Model-1'].Material(name='CORNEAL_TISSUE')
mdb.models['Model-1'].materials['CORNEAL_TISSUE'].
    Density(table=( $\rho_{Cornea}$ , ), )
mdb.models['Model-1'].materials['CORNEAL_TISSUE'].
    Hyperelastic(materialType=ISOTROPIC, table=( $C_{10}$ ,
     $D_1$ ), ), testData=OFF, type=NEO_HOOKE,
    volumetricResponse=VOLUMETRIC_DATA)
# Section Creation
mdb.models['Model-1'].HomogeneousSolidSection(material=
    'CORNEAL_TISSUE', name='CORNEA', thickness=None)
mdb.models['Model-1'].HomogeneousSolidSection(material=
    'CORNEAL_TISSUE', name='CIRUGIA', thickness=None)
# Section Assignment
mdb.models['Model-1'].parts['CORNEA'].SectionAssignment
    (offset=0.0, offsetField="", offsetType=MIDDLE_SURFACE,
    region=mdb.models['Model-1'].parts['CORNEA'].sets[
    'CORNEA'], sectionName='CORNEA', thicknessAssignment=
    FROM_SECTION)
mdb.models['Model-1'].parts['CORNEA'].SectionAssignment
    (offset=0.0, offsetField="", offsetType=MIDDLE_SURFACE,
    region=mdb.models['Model-1'].parts['CORNEA'].sets[
    'CIRUGIA'], sectionName='CIRUGIA', thicknessAssignment=
    FROM_SECTION)
```

4.2. Material and section assignment for the ring models

The material, called *PMMA*, is assigned to all elements of the ring, defined in the group *ANILLO_G*.

```

# Material Definition
mdb.models['Model-1'].Material(name='PMMA')
mdb.models['Model-1'].materials['PMMA'].Density(table=(
    ( $\rho_{PMMA}$ , ), ))
mdb.models['Model-1'].materials['PMMA'].Elastic(table=(
    ( $E_{PMMA}$ ,  $\nu_{PMMA}$ ), ))
# Section Creation
mdb.models['Model-1'].HomogeneousSolidSection(material=
    'PMMA', name='ANILLO_G', thickness=None)
# Section Assignment
mdb.models['Model-1'].parts['MY_200_6'].Section-
Assignment(offset=0.0, offsetField="", offsetType=
MIDDLE_SURFACE, region= mdb.models['Model-1'].parts[
'MY_200_6'].sets['ANILLO_G'], sectionName='ANILLO_G',
thicknessAssignment=FROM_SECTION)

```

5. Mesh of the models

The meshing part of the program aims to select the different properties of the mesh. To choose the element types and the seed of the elements, and create the mesh. Depending on the number of seeds by side, we can obtain a thinner or coarser mesh. Therefore, the followed steps to create the different meshes, i.e. cornea with tunnel, cornea with pocket, and implants, elliptical and MyoRing, are described below. First of all, the general programming lines will be explained. Secondly, the different models will be introduced relating the programming lines with each particular case.

1. Selecting the element type: there are several types of element depending on the model, features of the system, etc. In all our models, quadrilateral elements are chosen. In order to select the different regions, it is necessary to know all the internal points of each region.

```

mdb.models['Model-1'].parts['NAME_PART'].setMeshControls(
    elemShape=QUAD, regions=mdb.models['Model-1'].
    parts['NAME_PART'].faces.findAt(
    (( $P_x^1$ ,  $P_y^1$ ,  $P_z^1$ ), ),
    :
    (( $P_x^n$ ,  $P_y^n$ ,  $P_z^n$ ), ), ))

```

where `NAME_PART` is the name of the part which wants to mesh, and “QUAD” implies cuadrilateral elements, in the “n” regions selected with from P^1 to P^n .

2. The different algorithms and techniques to mesh are imposed. As we have done before, the regions will be chosen with their internal points. By default, the algorithm to mesh selected is called “Advancing Front”, but if it is necessary to change to “Medial axis”, as it happens in some regions of our models, the following code must be introduced:

```
mdb.models['Model-1'].parts['NAME_PART'].setMeshControls(
    algorithm='MEDIAL_AXIS', regions=mdb.models['Model-1'].
    parts['NAME_PART'].faces.findAt(
        ((Q1x, Q1y, Q1z)), ),
    :
    ((Qnx, Qny, Qnz)), ), )
```

where from Q^1 to Q^n are the different internal points which belong to the regions that are meshed by Medial Axis algorithm.

In addition, the meshing technique selected by default is called “Free”. However, other options such as “Sweep” or “Structured” can be selected using the following code:

```
mdb.models['Model-1'].parts['NAME_PART'].setMeshControls(
    regions=mdb.models['Model-1'].parts['NAME_PART'].faces.
    findAt(((R1x, R1y, R1z)), ),
    :
    ((Rnx, Rny, Rnz)), ), ), technique=NAME_TECHNIQUE)
```

where `NAME_TECHNIQUE` would be replaced by `SWEEP` or `STRUCTURED`, and the internal points (from R^1 to R^n) are used to select the regions.

3. Next, the size of the seed will be imposed on the edges of the regions. Therefore, the points of each edges must be found.

- Seed Parts. With the following instruction, all edges of the model will have the same size of seed. Thanks to this order, we ensure that all edges of the model have a seed.

```
mdb.models['Model-1'].parts['NAME_PART'].seedPart(
    deviationFactor=0.1, minSizeFactor=0.1,
    size=Global_Size)
```

where `Global_Size` is the size of the element. The models of the cornea have a value of 0.04.

- Seed Edges. The seed of the edges of the model is specified by the number of elements or by the size of element (Uniform). The seed on each edge can be uniform or gather more elements in one side (Byas).

```
# Uniform seed by size
mdb.models['Model-1'].parts['NAME_PART'].seedEdgeBySize(
    constraint=FINER, # or FIXED
    deviationFactor=0.1, edges=
    mdb.models['Model-1'].parts['NAME_PART'].edges.findAt(
        ((Sx1, Sy1, Sz1)), ),
    :
    ((Sxn, Syn, Szn)), ), ), size=SizeEdge)
```

where `SizeEdge` will be the size of the elements of the “n” edges selected from S^1 to S^n .

```
# Uniform seed by number
mdb.models['Model-1'].parts['NAME_PART'].seedEdgeByNumber(
    constraint=FINER, # or FIXED, edges=
    mdb.models['Model-1'].parts['NAME_PART'].edges.findAt(
        ((Tx1, Ty1, Tz1)), ),
    :
    ((Txn, Tyn, Tzn)), ), ), number=NumEl)
```

where `NumEl` will be the number of the elements of the “n” edges selected from T^1 to T^n .

```
# Byas seed by size
mdb.models['Model-1'].parts['NAME_PART'].seedEdgeByBias(
    biasMethod=SINGLE,
    constraint=FINER, # or FIXED,
    end1Edges=mdb.models['Model-1'].parts['NAME_PART'].
    edges.findAt(((Vx1, Vy1, Vz1)), ),
    :
    ((Vxn, Vyn, Vzn)), ), ) maxSize=maxSize, minSize=minSize)
```

where `maxSize` and `minSize` determine the size range of the elements. In addition, the instruction `end1Edges` gathers the elements in the counter-clockwise direction of the edge. If you wish to concentrate the elements on the clockwise direction of the edge, you will use `end2Edges`. The points from V^1 to V^n will select the “n” edges that will be meshed.

4. Finally, it is required to introduce the order to create the mesh. Therefore,

the mesh module will finish with the following code line:

```
mdb.models['Model-1'].parts['NAME_PART'].generateMesh()
```

Once the lines of code used to mesh the different models are explained, the next step is to find the different internal points to select those regions that do not use the default algorithm or techniques. Also, we have to calculate the points on the edges to select the corresponding seed size.

5.1. Mesh of the cornea

In order to create the different sections described in Figure III.20 if the surgery is a tunnel, or in Figure III.36 is a pocket, the internal points must be calculated in advance. At the same time those internal points are obtained, the points on edges arise.

5.1.1. Tunnel Surgery

First, the internal points of the sections around the surgery are calculated (Sections 1, 2, 3, 4, 5, 6, 31 and 32 and keratoconic section, 35 and 36, if there is keratoconus). Figure III.47 shows the sections and the points that arise from the edges. Next, the internal points of the sections of the surgery are determined (Figure III.47.Zoom Central, Zoom Surgery 1 and 2), as well as the points located on the edges. The different internal points needed to select each region are described below:

Regions 1 and 2 (Figure III.47.Central image)

- i. Intermediate angle (α_{int}) defined by the line formed by KC_1 and KC_2 and line formed by B_3 and B_4 .
- ii. Line (r_1) with slope $\tan \alpha_{int}$ and through CP_{Centre} .
- iii. S_1^1 : Intersection between r_1 and mid arc defined by the centre CP_{Centre} and radius $\|(\overline{CP_{Centre}A_1})\|$.
- iv. S_1^2 : Intersection between r_1 and anterior cornea.
- v. P_1 : Midpoint between S_1^1 and S_1^2 .
- vi. S_2^1 : Intersection between r_1 and posterior cornea.
- vii. S_2^2 : Same point as S_1^1 .
- viii. P_2 : Midpoint between S_2^1 and S_2^2 .

Regions 3 and 4 (Figure III.47.Central image)

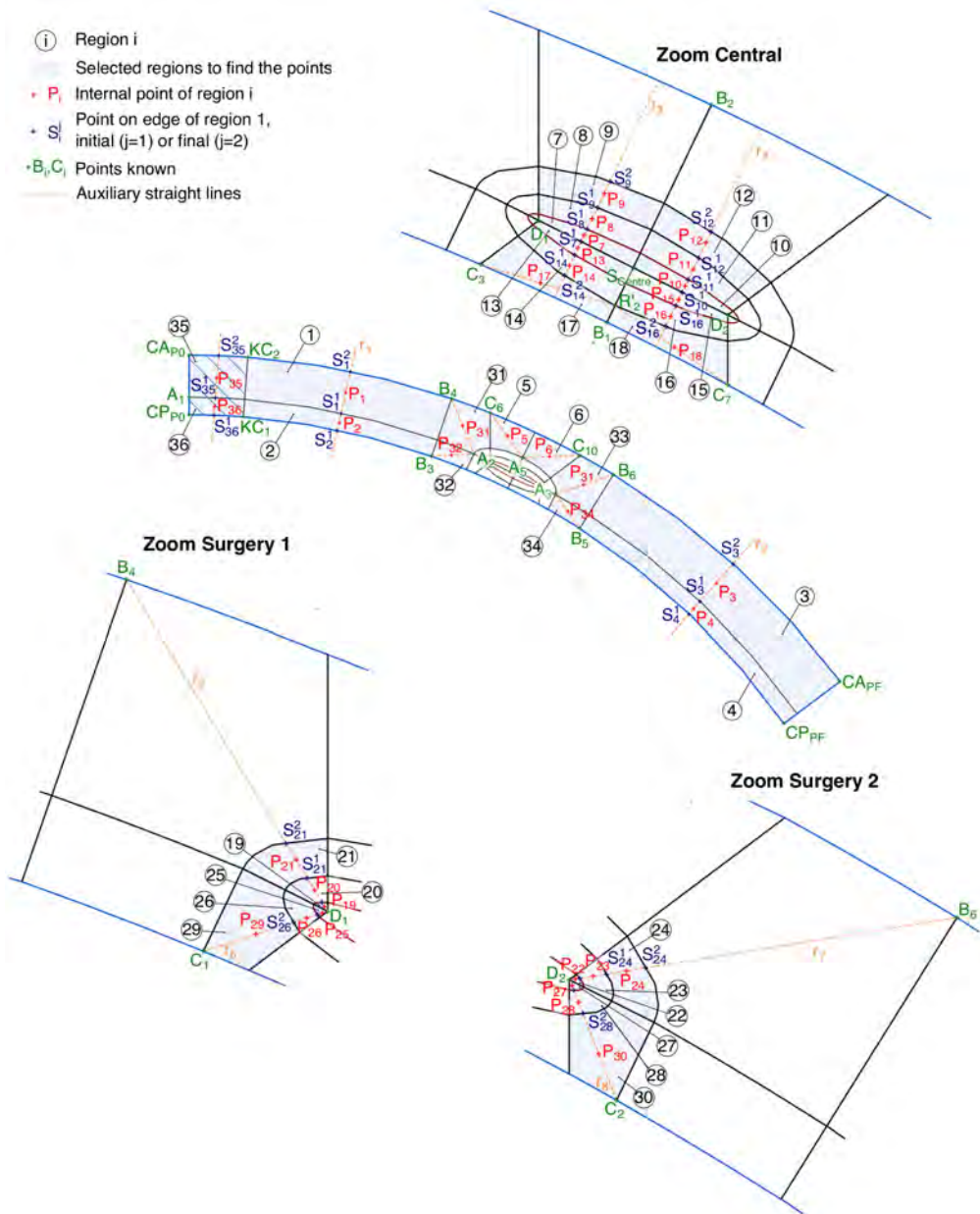


Figure III.47: Points in order to select the regions of cornea cross-section with tunnel. (Main) the regions around the surgery are shown. (Regions 1–6, 31, 32, 35 and 36); **(Zoom Central)** The regions of the surgery are shown (Regions 7–18); **(Zoom Surgery 1)** The regions of the left surgery are shown (Regions 19–21, 25, 26, 29); **(Zoom Surgery 2)** The regions of the right surgery are shown (Regions 22–24, 27, 28, 30). Points in red are the internal points that are required to select and create the section (P_i), where i is the region; points in blue are the points located on the edges and they are necessary to select the edges and introduce the seed (S_j^i), where i is the region, and j has the value 1 (initial) or 2 (final). The straight lines with dash points in orange represent the auxiliary lines, which are not drawn with the program. Finally, the points in green are points which are already known.

- i. Midangle (β_{int}) between the angles defined between the vertical line and line between B_5 and B_6 and line between CP_{PF} and CA_{PF} .
- ii. Line r_2 with slope $\tan \beta_{int}$ and through CP_{Centre} .
- iii. S_3^1 : Intersection between r_2 and mid arc defined by the centre CP_{Centre} and radius $\|(\overline{CP_{Centre}A_1})\|$.
- iv. S_3^2 : Intersection between r_2 and anterior cornea.
- v. P_3 : Midpoint between S_3^1 and S_3^2 .
- vi. S_4^1 : Intersection between r_2 and posterior cornea.
- vii. S_4^2 : Same point as S_3^1 .
- viii. P_4 : Midpoint between S_4^1 and S_4^2 .

Regions 5, 6, 31, 32, 33 and 34 (Figure III.47.Central image)

- i. P_5 : Midpoint between A_5 and C_6 .
- ii. P_6 : Midpoint between A_5 and C_{10} .
- iii. P_{31} : Midpoint between A_2 and B_4 .
- iv. P_{32} : Midpoint between A_3 and B_6 .
- v. P_{33} : Midpoint between A_3 and B_5 .

Regions 7, 8, 9, 13 and 14 (Figure III.47.Zoom Central)

- i. S_7^1 (same point as S_{13}^1): Midpoint between S_{Centre} and D_1 .
- ii. Line r_3 with the same slope as y in Figure III.16.b through S_7^1 .
- iii. S_8^1 (same point as S_7^2): Intersection between the ellipse corresponding with surgery and r_3 .
- iv. P_7 : Midpoint between S_7^1 and S_7^2 .
- v. S_9^1 (same point as S_8^2): Intersection between the ellipse corresponding with medium cover ellipse (Figure III.13) and r_3 .
- vi. P_8 : Midpoint between S_8^1 and S_8^2 .
- vii. S_9^2 : Intersection between the ellipse corresponding with largest cover ellipse (Figure III.14) and r_3 .
- viii. P_9 : Midpoint between S_9^1 and S_9^2 .
- ix. S_{14}^1 (same point as S_{13}^2): Intersection between the ellipse corresponding with surgery and r_3 .

- x. P_{13} : Midpoint between S_{13}^1 and S_{13}^2 .
- xi. S_{14}^2 : Intersection between the ellipse corresponding with medium cover ellipse (Figure III.13) and r_3 .
- xii. P_{14} : Midpoint between S_{14}^1 and S_{14}^2 .

Regions 10, 11, 12, 15 and 16 (Figure III.47.Zoom Central)

- i. S_{10}^1 (same point as S_{15}^1): Midpoint between S_{Centre} and D_2 .
- ii. Line r_4 with the same slope as y in Figure III.16.b through S_{10}^1 .
- iii. S_{11}^1 (same point as S_{10}^2): Intersection between the ellipse corresponding with surgery and r_4 .
- iv. P_{10} : Midpoint between S_{10}^1 and S_{10}^2 .
- v. S_{12}^1 (same point as S_{11}^2): Intersection between the ellipse corresponding with medium cover ellipse (Figure III.13) and r_4 .
- vi. P_{11} : Midpoint between S_{11}^1 and S_{11}^2 .
- vii. S_{12}^2 : Intersection between the ellipse corresponding with largest cover ellipse (Figure III.14) and r_4 .
- viii. P_9 : Midpoint between S_{12}^1 and S_{12}^2 .
- ix. S_{16}^1 (same point as S_{15}^2): Intersection between the ellipse corresponding with surgery and r_4 .
- x. P_{15} : Midpoint between S_{15}^1 and S_{15}^2 .
- xi. S_{16}^2 : Intersection between the ellipse corresponding with medium cover ellipse (Figure III.13) and r_4 .
- xii. P_{16} : Midpoint between S_{16}^1 and S_{16}^2 .

Regions 19, 20, 21, 25, 26 and 29 (Figure III.47.Zoom Surgery 1)

- i. The straight line r_5 is defined between the points D_1 and B_4 .
- ii. S_{20}^1 (same point as S_{19}^2): Intersection between the ellipse corresponding with surgery and r_5 .
- iii. P_{19} : Midpoint between D_1 and S_{19}^2 .
- iv. S_{21}^1 (same point as S_{20}^2): Intersection between the ellipse corresponding with medium cover ellipse (Figure III.13) and r_5 .
- v. P_{20} : Midpoint between S_{20}^1 and S_{20}^2 .

- vi. S_{21}^2 : Intersection between the ellipse corresponding with largest cover ellipse (Figure III.14) and r_5 .
- vii. P_{21} : Midpoint between S_{21}^1 and S_{21}^2 .
- viii. The straight line r_6 is defined between the points D_1 and C_1 .
- ix. S_{26}^1 (same point as S_{25}^2): Intersection between the ellipse corresponding with surgery and r_6 .
- x. P_{25} : Midpoint between D_1 and S_{25}^2 .
- xi. S_{26}^2 : Intersection between the ellipse corresponding with medium cover ellipse (Figure III.13) and r_6 .
- xii. P_{26} : Midpoint between S_{26}^1 and S_{26}^2 .
- xiii. P_{29} : Midpoint between S_{26}^2 and C_1 .

Regions 22, 23, 24, 27, 28 and 30 (Figure III.47.Zoom Surgery 2)

- i. The straight line r_7 is defined between the points D_2 and B_6 .
- ii. S_{23}^1 (same point as S_{22}^2): Intersection between the ellipse corresponding with surgery and r_7 .
- iii. P_{22} : Midpoint between D_2 and S_{22}^2 .
- iv. S_{24}^1 (same point as S_{23}^2): Intersection between the ellipse corresponding with medium cover ellipse (Figure III.13) and r_7 .
- v. P_{23} : Midpoint between S_{23}^1 and S_{23}^2 .
- vi. S_{24}^2 : Intersection between the ellipse corresponding with largest cover ellipse (Figure III.14) and r_5 .
- vii. P_{21} : Midpoint between S_{24}^1 and S_{24}^2 .
- viii. The straight line r_8 is defined between the points D_2 and C_2 .
- ix. S_{28}^1 (same point as S_{27}^2): Intersection between the ellipse corresponding with surgery and r_8 .
- x. P_{27} : Midpoint between D_2 and S_{27}^2 .
- xi. S_{28}^2 : Intersection between the ellipse corresponding with medium cover ellipse (Figure III.13) and r_8 .
- xii. P_{28} : Midpoint between S_{28}^1 and S_{28}^2 .
- xiii. P_{30} : Midpoint between S_{28}^2 and C_2 .

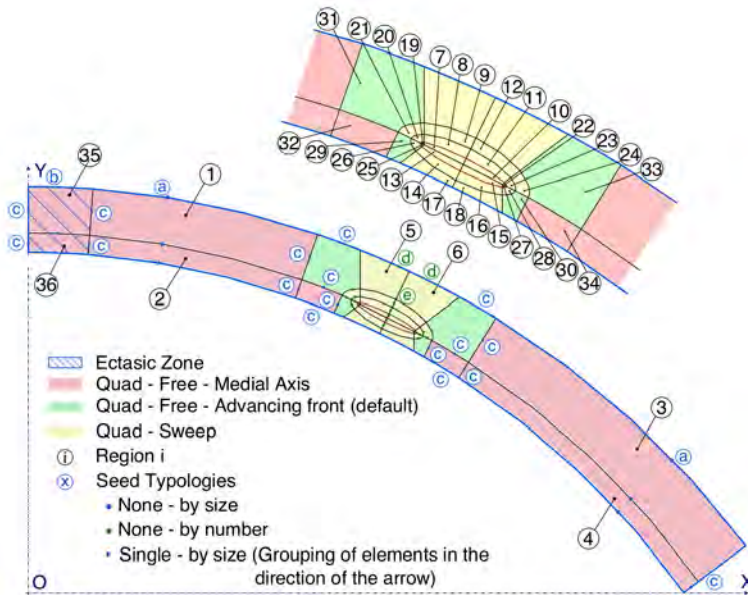


Figure III.48: Meshing techniques and seeds in the cornea with tunnel as surgery. Different colours show different meshing techniques and seeds. Therefore, regions which are meshed with quad elements, free technique and medial axis algorithm are in red; regions whose meshing techniques and algorithm are by default those introduced by the Abaqus mesher: quad elements, free technique and advancing front algorithm are in green; finally, regions with quad elements and sweep technique are in yellow. The filled blue circles represent the edges whose seed is constant (called none in Abaqus), defined by size of elements; the filled green circles represent edges whose seed is constant too, but defined by number of elements; the filled blue triangle shows the gathering direction of the elements.

Regions 35 and 36 (Figure III.47.Central image). Keratoconic zone if it exists.

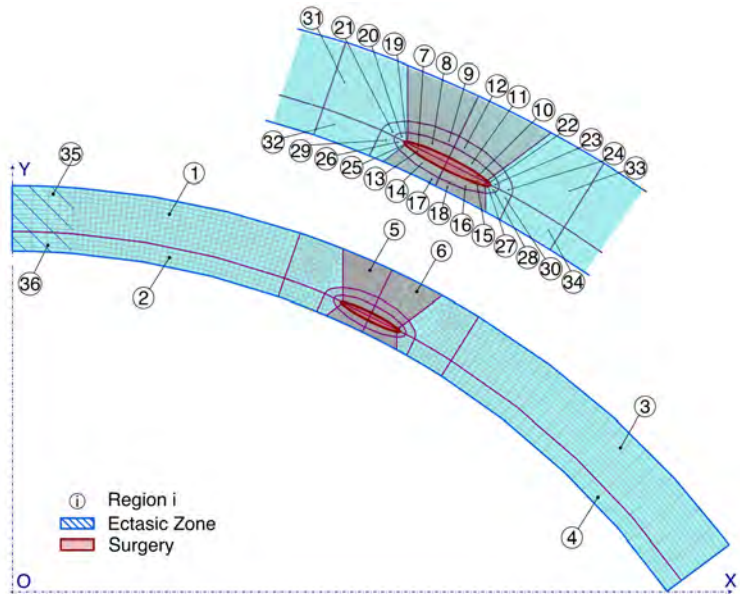
- i. Midangle (γ_{KC}) between the angles defined by KC_1 and KC_2 and $\frac{\pi}{2}$
- ii. Line (r_{KC}) with slope $\tan \gamma_{KC}$ and through CP_{Centre} .
- iii. S_{35}^1 : Intersection between r_{KC} and mid arc defined by the centre CP_{Centre} and radius $\|(\overline{CP_{Centre}A_1})\|$.
- iv. S_{35}^2 : Intersection between r_{KC} and anterior cornea.
- v. P_{35} : Midpoint between S_{35}^1 and S_{35}^2 .
- vi. S_{36}^1 : Intersection between r_{KC} and posterior cornea.
- vii. S_{36}^2 : Same point as S_{35}^1 .
- viii. P_{36} : Midpoint between S_{36}^1 and S_{36}^2 .

All sections of the cornea have been meshed with quadrilateral elements. Therefore, all internal points are used to select the element type in the

Edge	Seed
a	Max : 0.2 (s) Min : 0.05 (s)
b	0.05 (s)
c	0.04 (s)
d	125 (e)
e	4 (e)

Table III.5: Seeds of edges showed in Figure III.48. The first column represents the edges which correspond with Figure III.48, and the second column represents the size or number of elements to mesh. (s) is the seed expressed in size of each element, and (e) indicates the number of elements.

Figure III.49: Mesh of the cornea cross-section with tunnel as surgery.



code described in page 249. The different meshing techniques which have been used to mesh each region are indicated in Figure III.48. They have been introduced in the code of the page 250. The edges named as *a*, follow a seed growing in the arrow direction whose maximum and minimum seed appear in Table III.5. They have been introduced in the code of page 251. The edges named as *b* and *c* have a uniform seed whose corresponding size is shown in Table III.5. They have been introduced in the code of page 251. The last edges, *d* and *e*, are introduced by a uniform mesh with number, instead of size (see in Table III.5). They have been introduced in the code of page 251. Finally, the mesh of the cornea cross-section with tunnel is generated with the code described in page 252 (see in Figure III.49).

5.1.2. Pocket surgery

First, the internal points of the each section must be obtained. From Figure III.50 shows the sections and the points which arise from the edges. The different internal points required to select each region are described below:

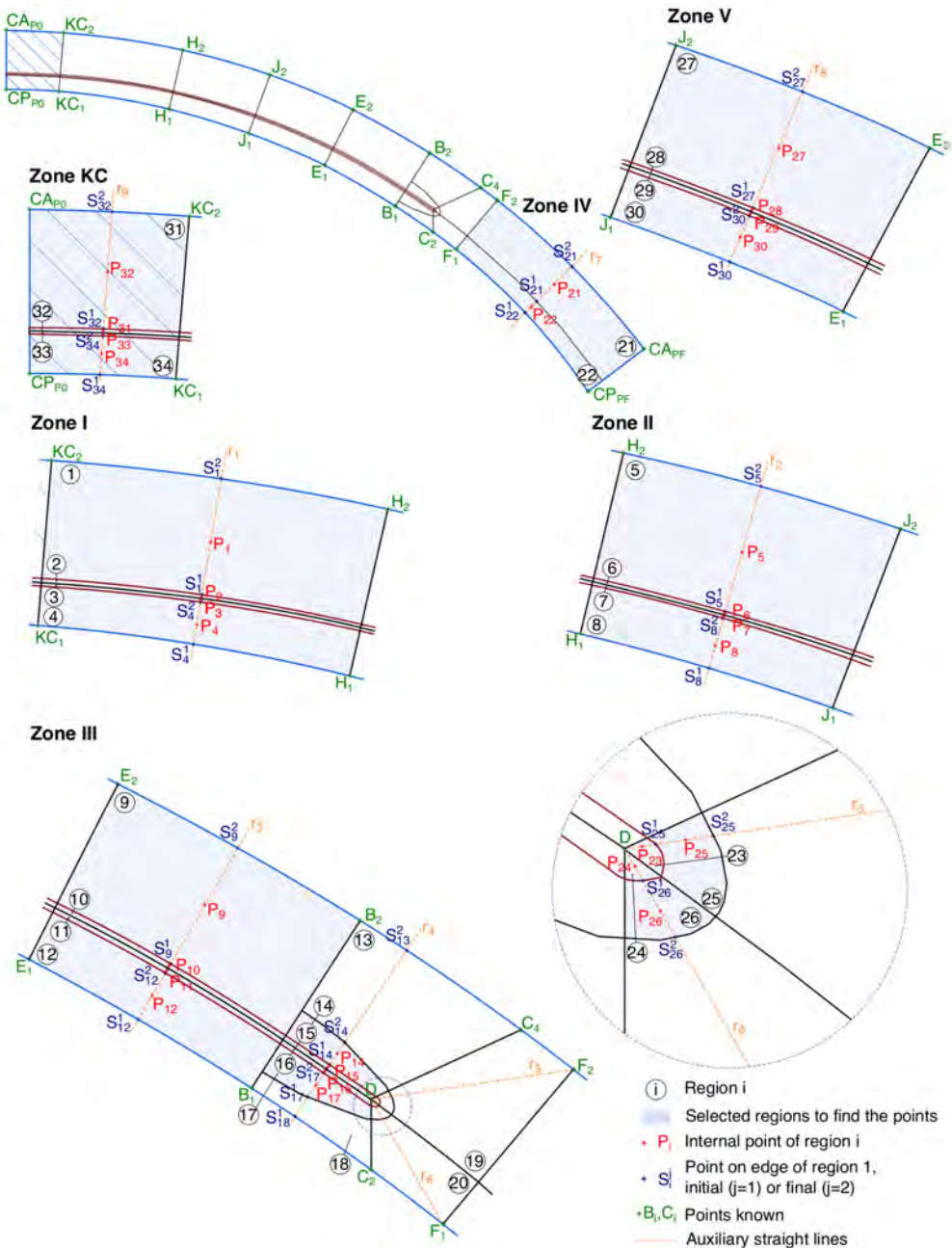


Figure III.50: Points to select the regions of cornea cross-section with pocket. (Zone KC) Region where emerges the central keratoconus, if exists (Regions 31–34); (Zone I) Region near the apex, it would be bigger if KC did not exist (Regions 1–4); (Zone II) Regions around the optical zone implantation I (Regions 5–8); (Zone III) Extreme of the pocket region (Regions 9–20 and 23–26); (Zone IV) Region which connects the end of the pocket with the limbus (Regions 21 and 22); (Zone V) Regions around the optical zone implantation II (Regions 27–30). The points in red are the internal points that are required to select and create the section (P_i), where i is the region; the points in blue are the points located on the edges and they are necessary to select the edges and to introduce the seed (S_j^i), where i is the region, and j has the value 1 (initial) or 2 (final). The straight lines with dash points in orange represent the auxiliary lines, which are not drawn in the program. Finally, the points in green are points which were already calculated.

Zone I (Regions 1, 2, 3, and 4) (Figure III.50.Zone I)

- i. Middle angle (α_{med}^1) between the line defined by KC_1 and KC_2 and the line defined by H_1 and H_2 .
- ii. Line (r_1) with slope $\tan \alpha_{med}^1$ and through CP_{Centre} .
- iii. S_1^1 : Intersection between r_1 and superior arc of the pocket defined by the centre CP_{Centre} and radius $\|(\overline{CP_{Centre}S_{m1}})\|$.
- iv. S_1^2 : Intersection between r_1 and anterior cornea.
- v. P_1 : Midpoint between S_1^1 and S_1^2 .
- vi. S_2^1 : Intersection between r_1 and middle arc of the pocket defined by the centre CP_{Centre} and radius $\|(\overline{CP_{Centre}S_{Centre}})\|$.
- vii. S_2^2 : Same point as S_1^1 .
- viii. P_2 : Midpoint between S_2^1 and S_2^2 .
- ix. S_3^1 : Intersection between r_1 and inferior arc of the pocket defined by the centre CP_{Centre} and radius $\|(\overline{CP_{Centre}S_{m2}})\|$.
- x. S_3^2 : Same point as S_2^1 .
- xi. P_3 : Midpoint between S_3^1 and S_3^2 .
- xii. S_4^1 : Intersection between r_1 and posterior cornea.
- xiii. S_4^2 : Same point as S_3^1 .
- xiv. P_4 : Midpoint between S_4^1 and S_4^2 .

Zone II (Regions 5, 6, 7, and 8) (Figure III.50.Zone II)

- i. Middle angle (α_{med}^2) between the line defined by H_1 and H_2 and the line defined by J_1 and J_2 .
- ii. Line (r_2) with slope $\tan \alpha_{med}^2$ and through CP_{Centre} .
- iii. S_5^1 : Intersection between r_2 and superior arc of the pocket defined by the centre CP_{Centre} and radius $\|(\overline{CP_{Centre}S_{m1}})\|$.
- iv. S_5^2 : Intersection between r_2 and anterior cornea.
- v. P_5 : Midpoint between S_5^1 and S_5^2 .
- vi. S_6^1 : Intersection between r_2 and middle arc of the pocket defined by the centre CP_{Centre} and radius $\|(\overline{CP_{Centre}S_{Centre}})\|$.
- vii. S_6^2 : Same point as S_5^1 .
- viii. P_6 : Midpoint between S_6^1 and S_6^2 .

- ix. S_7^1 : Intersection between r_2 and inferior arc of the pocket defined by the centre CP_{Centre} and radius $\|(\overline{CP_{Centre}S_{m2}})\|$.
- x. S_7^2 : Same point as S_6^1 .
- xi. P_7 : Midpoint between S_7^1 and S_7^2 .
- xii. S_8^1 : Intersection between r_2 and posterior cornea.
- xiii. S_8^2 : Same point as S_7^1 .
- xiv. P_8 : Midpoint between S_8^1 and S_8^2 .

Zone III.1 (Regions 9, 10, 11, 12) (Figure III.50.Zone III)

- i. Middle angle (α_{med}^3) between the line defined by E_1 and E_2 and the line defined by B_1 and B_2 .
- ii. Line (r_3) with slope $\tan \alpha_{med}^3$ and through CP_{Centre} .
- iii. S_9^1 : Intersection between r_3 and superior arc of the pocket defined by the centre CP_{Centre} and radius $\|(\overline{CP_{Centre}S_{m1}})\|$.
- iv. S_9^2 : Intersection between r_3 and anterior cornea.
- v. P_9 : Midpoint between S_9^1 and S_9^2 .
- vi. S_{10}^1 : Intersection between r_3 and middle arc of the pocket defined by the centre CP_{Centre} and radius $\|(\overline{CP_{Centre}S_{Centre}})\|$.
- vii. S_{10}^2 : Same point as S_9^1 .
- viii. P_{10} : Midpoint between S_{10}^1 and S_{10}^2 .
- ix. S_{11}^1 : Intersection between r_3 and inferior arc of the pocket defined by the centre CP_{Centre} and radius $\|(\overline{CP_{Centre}S_{m2}})\|$.
- x. S_{11}^2 : Same point as S_{10}^1 .
- xi. P_{11} : Midpoint between S_{11}^1 and S_{11}^2 .
- xii. S_{12}^1 : Intersection between r_3 and posterior cornea.
- xiii. S_{12}^2 : Same point as S_{11}^1 .
- xiv. P_{12} : Midpoint between S_{12}^1 and S_{12}^2 .

Zone III.2 (Regions 14, 15, 16, 17) (Figure III.50.Zone III)

- i. S_{15}^1 or S_{16}^2 : Midpoint between S_{Centre} and D .
- ii. The angle β is formed by the line between B_1 and B_2 with the horizontal.

- iii. Line (r_4) with slope $\tan \beta$ and through S_{15}^1 .
- iv. S_{14}^1 : Intersection between line r_4 and ellipse which forms the end of the pocket.
- v. S_{14}^2 : Intersection between line r_4 and the bigger ellipse which covers the end of the pocket.
- vi. P_{14} : Midpoint between S_{14}^1 and S_{14}^2 .
- vii. S_{15}^2 : Same point as S_{14}^1 .
- viii. P_{15} : Midpoint between S_{15}^1 and S_{15}^2 .
- ix. S_{16}^1 : Intersection between line r_4 and ellipse which forms the end of the pocket.
- x. P_{16} : Midpoint between S_{16}^1 and S_{16}^2 .
- xi. S_{17}^1 : Intersection between line r_4 and the bigger ellipse which covers the end of the pocket.
- xii. S_{17}^2 : Same point as S_{16}^1 .
- xiii. P_{17} : Midpoint between S_{17}^1 and S_{17}^2 .
- xiv. The regions 13, 18, 19 and 20 have been already calculated in Figure III.35.a.

Zone III.Zoom (Regions 23, 24, 25, 26) (Figure III.50.Zone III.Zoom)

- i. Line (r_5) which starts in D and finishes in F_2 .
- ii. S_{23}^2 : Intersection between line r_5 and the ellipse that closes the pocket.
- iii. P_{23} : Midpoint between D and S_{23}^2 .
- iv. S_{25}^1 : same point as S_{23}^2 .
- v. S_{25}^2 : Intersection between line r_5 and the ellipse which covers the end of the pocket.
- vi. P_{25} : Midpoint between S_{25}^1 and S_{25}^2 .
- vii. Line (r_6) which starts in D and finishes in F_1 .
- viii. S_{24}^2 : Intersection between line r_6 and the ellipse that closes the pocket.
- ix. P_{24} : Midpoint between D and S_{24}^2 .
- x. S_{26}^1 : same point as S_{24}^2 .

- xi. S_{26}^2 : Intersection between line r_6 and the ellipse which covers the end of the pocket.
- xii. P_{26} : Midpoint between S_{26}^1 and S_{26}^2 .

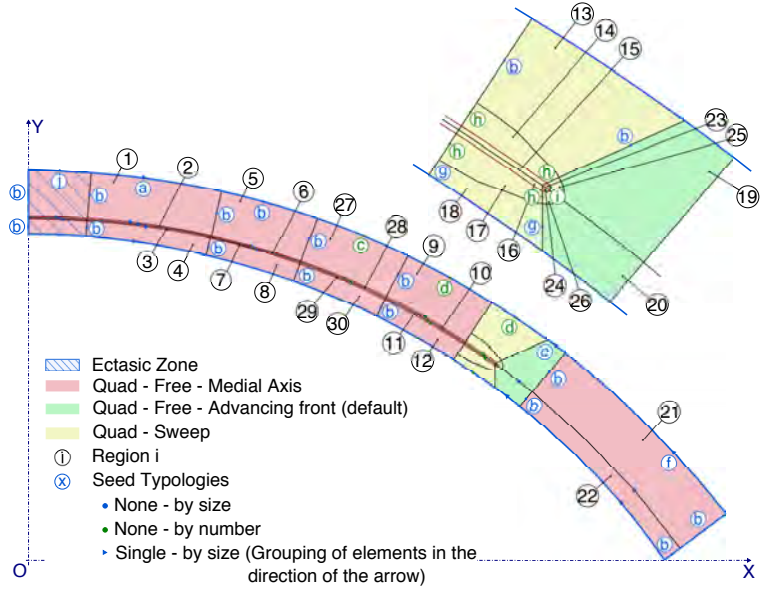
Zone IV (Regions 21, and 22) (Figure III.50.Zone IV)

- i. Middle angle (α_{med}^4) between the line defined by F_1 and F_2 and the line defined by CP_{PF} and CA_{PF} .
- ii. Line (r_7) with slope $\tan \alpha_{med}^4$ and through CP_{Centre} .
- iii. S_{21}^1 : Intersection between r_7 and arc of circumference which joins the end of the pocket with the limbus.
- iv. S_{21}^2 : Intersection between r_7 and anterior cornea.
- v. P_{21} : Midpoint between S_{21}^1 and S_{21}^2 .
- vi. S_{22}^1 : Intersection between r_7 and posterior cornea.
- vii. S_{22}^2 : Same point as S_{21}^1 .
- viii. P_{22} : Midpoint between S_{22}^1 and S_{22}^2 .

Zone V (Regions 27, 28, 29, and 30) (Figure III.50.Zone V)

- i. Middle angle (α_{med}^5) between the line defined by J_1 and J_2 and the line defined by E_1 and E_2 .
- ii. Line (r_8) with slope $\tan \alpha_{med}^5$ and through CP_{Centre} .
- iii. S_{27}^1 : Intersection between r_8 and superior arc of the pocket defined by the centre CP_{Centre} and radius $\|(\overline{CP_{Centre}S_{m1}})\|$.
- iv. S_{27}^2 : Intersection between r_8 and anterior cornea.
- v. P_{27} : Midpoint between S_{27}^1 and S_{27}^2 .
- vi. S_{28}^1 : Intersection between r_8 and middle arc of the pocket defined by the centre CP_{Centre} and radius $\|(\overline{CP_{Centre}S_{Centre}})\|$.
- vii. S_{28}^2 : Same point as S_{27}^1 .
- viii. P_{28} : Midpoint between S_{28}^1 and S_{28}^2 .
- ix. S_{29}^1 : Intersection between r_8 and inferior arc of the pocket defined by the centre CP_{Centre} and radius $\|(\overline{CP_{Centre}S_{m2}})\|$.
- x. S_{29}^2 : Same point as S_{28}^1 .
- xi. P_{29} : Midpoint between S_{29}^1 and S_{29}^2 .

Figure III.51: Meshing techniques and seeds in the cornea with pocket as surgery. Different colours show different meshing techniques and seeds. Therefore, regions which are meshed with quad elements, free technique and medial axis algorithm are in red; regions whose meshing techniques and algorithm are by default those introduced by the Abaqus mesher: quad elements, free technique and advancing front algorithm are in green; finally, regions with quad elements and sweep technique are in yellow. The filled blue circles represent the edges whose seed is constant (called none in Abaqus), defined by size of elements; the filled green circles represent edges whose seed is constant too, but defined by number of elements; the filled blue triangle shows the gathering direction the elements.



- xii. S_{30}^1 : Intersection between r_2 and posterior cornea.
- xiii. S_{30}^2 : Same point as S_{29}^1 .
- xiv. P_{30} : Midpoint between S_{30}^1 and S_{30}^2 .

Zone KC (Regions 31, 32, 33, and 34) (Figure III.50.Zone KC)

- i. Middle angle (α_{med}^{KC}) between the line defined by CA_{P0} and CP_{P0} and the line defined by KC_1 and KC_2 .
- ii. Line (r_9) with slope $\tan \alpha_{med}^{KC}$ and through CP_{Centre} .
- iii. S_{31}^1 : Intersection between r_9 and superior arc of the pocket defined by the centre CP_{Centre} and radius $\|(CP_{Centre}S_{m1})\|$.
- iv. S_{31}^2 : Intersection between r_9 and anterior cornea.
- v. P_{31} : Midpoint between S_{31}^1 and S_{31}^2 .
- vi. S_{32}^1 : Intersection between r_9 and middle arc of the pocket defined by the centre CP_{Centre} and radius $\|(CP_{Centre}S_{Centre})\|$.
- vii. S_{32}^2 : Same point as S_{31}^1 .
- viii. P_{32} : Midpoint between S_{32}^1 and S_{32}^2 .
- ix. S_{33}^1 : Intersection between r_9 and inferior arc of the pocket defined by the centre CP_{Centre} and radius $\|(CP_{Centre}S_{m2})\|$.

Edge	Seed
a	Max : 0.1 (s) Min : 0.05 (s)
b	0.05 (s)
c	140 (e)
d	20 (e)
e	Max : 0.05 (s) Min : 0.02 (s)
f	Max : 0.2 (s) Min : 0.05 (s)
g	0.025 (s)
h	4 (e)
i	3 (e)
j	0.1 (s)

Table III.6: Seeds of edges showed in Figure III.51. The first column represents the edges that correspond to Figure III.51 and the second column represents the size or number of elements to mesh. (s) is the seed expressed in size of each element, and (e) indicates the number of elements.

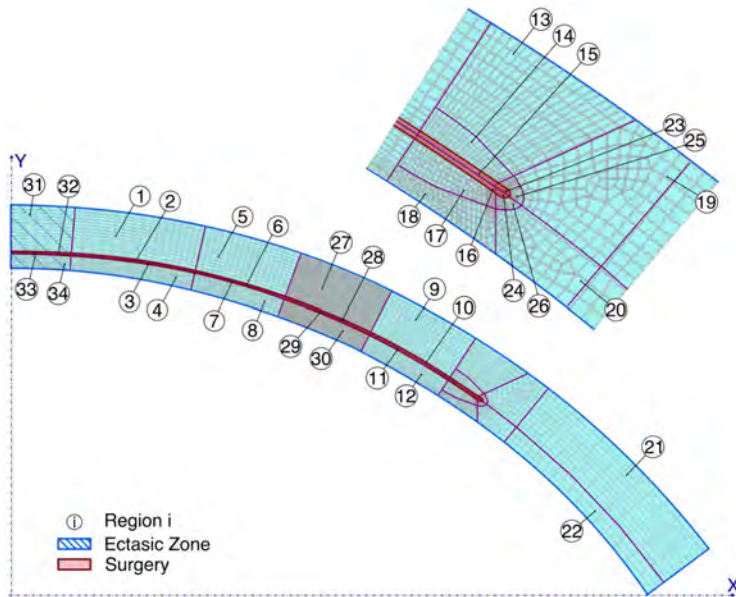


Figure III.52: Mesh of the cornea cross-section with pocket as surgery.

- x. S_{33}^2 : Same point as S_{32}^1 .
- xi. P_{33} : Midpoint between S_{33}^1 and S_{33}^2 .
- xii. S_{34}^1 : Intersection between r_9 and posterior cornea.
- xiii. S_{34}^2 : Same point as S_{33}^1 .
- xiv. P_{34} : Midpoint between S_{34}^1 and S_{34}^2 .

All sections of the cornea have been meshed with quadrilateral elements. Therefore, all internal points are used to select the element type in the code described in page 249. The different meshing techniques which have been used to mesh each region, which are indicated in Figure III.51, are introduced in the code of page 250. The edges named as a , e , and f follow a growing seed in the direction of the arrow. Maximum and minimum seed appear in the Table III.6, and are introduced in the code of page 251. The edges named as b , g , and j have uniform seed, whose corresponding size is shown in Table III.6. They have been introduced in the code of page 251. The last edges, c , d , h , and i are introduced by a uniform mesh with number, instead of size (see in Table III.5). They have been introduced in the code of page 251. Finally, the mesh of the cornea cross-section with pocket is generated with the code described in page 252 (see in Figure III.52).

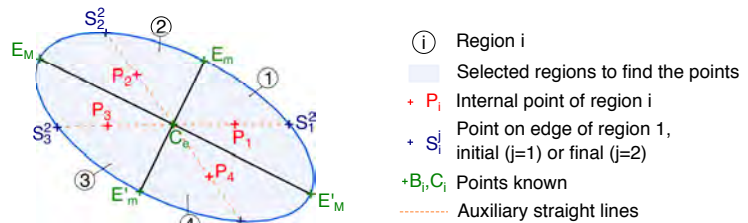
5.2. Mesh of the ring

In order to create the different sections described in Figure III.39 if it is a generic ring, or the Figure III.46 if it is MyoRing, the internal points must be calculated before. The points on the edges arise at the same time as the internal points are obtained.

5.2.1. Generic Ring

First, the internal points of the each section must be obtained. From Figure III.53 shows the sections and the points which arise from the edges. The different internal points to select each region are described below:

Figure III.53: Points to select the regions of generic cross-section. The points in red are the internal points that are required to select and create the section (P_i), where i is the region; the points in blue are the points located on the edges and are necessary to select the edges and introduce the seed (S_i^j), where i is the region, and j has the value 1 (initial) or 2 (final). The straight lines with dash points in orange represent the auxiliary lines, which are not drawn in the program. Finally, the points in green are points which were already calculated.



Regions 1, 2, 3, and 4 (Figure III.53)

The points on the edges are calculated with the parametric general equation of the ellipse (Equation III.10), where $S_{Centre} = C_e$, $a = w_{ICRS}/2$, $b = h_{ICRS}/2$, $\beta = \alpha_M$, and α is the angle to obtain the following points:

- i. S_1^2 : $\alpha = 45^\circ$.
- ii. P_1 : Midpoint between C_e and S_1^2 .
- iii. S_2^2 : $\alpha = 135^\circ$.
- iv. P_2 : Midpoint between C_e and S_2^2 .
- v. S_3^2 : $\alpha = 225^\circ$.
- vi. P_3 : Midpoint between C_e and S_3^2 .
- vii. S_4^2 : $\alpha = 315^\circ$.
- viii. P_4 : Midpoint between C_e and S_4^2 .

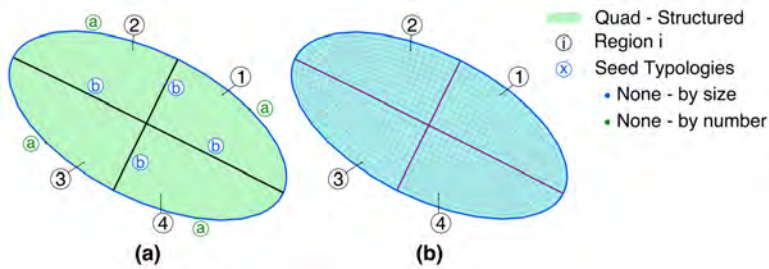


Figure III.54: Meshing techniques, seeds and mesh of generic ring. (a) Meshing techniques and seeds of the generic cross-section ring. All regions are meshed by structured techniques; (b) Mesh of generic cross-section ring.

All sections of the ring have been meshed with quadrilateral elements. Therefore, all the internal points are used to select the element type in the code described in page 249. The structured technique is used to perform the mesh of the generic ring (see in Figure III.54.a and code in page 250). The perimeter of the ellipse (denominated a in Figure III.54.a) is meshed with 25 elements by size and the size of the elements of ellipse axis denominated b in Figure III.54.a, code in page 251) is of 0.01. Finally, the mesh of the generic ring is generated with the code described in page 252 (see in Figure III.54.b).

5.2.2. MyoRing

The first step is to generate the internal points of each section of the MyoRing to select the type of elements and the different meshing techniques. At the same time, the points on the edges which will be used to select the corresponding mesh sizes arise. The different internal and edge points are described below:

Regions 1 and 4 (see in Figure III.55)

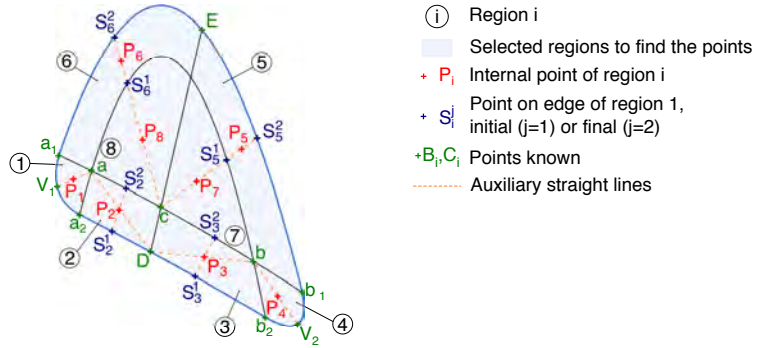
- i. P_1 : Midpoint between V_1 and a .
- ii. P_4 : Midpoint between b and V_2 .

Regions 2 and 3 (see in Figure III.55)

- i. P_2 : Midpoint between a and D .
- ii. S_2^1 : Intersection between the straight line through O and P_2 and the circumference centred in O and radius R .
- iii. S_2^2 : Intersection between the straight line through O and P_2 and the circumference centred in O^{new} and radius R^{new} .

Figure III.55: Internal and edge points of the MyoRing.

The points in red are the internal point that are required to select and create the section (P_i), where i is the region; the points in blue are the points located on the edges which are necessary to select the edges and introduce the seed (S_i^j), where i is the region, and j has the value 1 (initial) or 2 (final). The straight lines with dash points in orange represent the auxiliary lines, which is not drawn. Finally, the points in green are points which were already calculated.



- iv. P_3 : Midpoint between D and b .
- v. S_3^1 : Intersection between the straight line through O and P_3 and the circumference centred in O and radius R .
- vi. S_3^2 : Intersection between the straight line through O and P_3 and the circumference centred in O^{new} and radius R^{new} .

Regions 5 and 6 (see in Figure III.55)

- i. S_5^1 : Point which belongs to the internal parabola, located between the points E and b .
- ii. S_5^2 : Intersection between the straight line through c and S_5^1 and the external parabola.
- iii. P_5 : Midpoint between S_5^1 and S_5^2 .
- iv. S_6^1 : Point which belongs to the internal parabola, located between the points a and E .
- v. S_6^2 : Intersection between the straight line through c and S_6^1 and the external parabola.
- vi. P_6 : Midpoint between S_6^1 and S_6^2 .

Regions 5 and 6 (see in Figure III.55)

- i. P_7 : Midpoint between c and S_5^1 .
- ii. P_8 : Midpoint between c and S_6^1 .

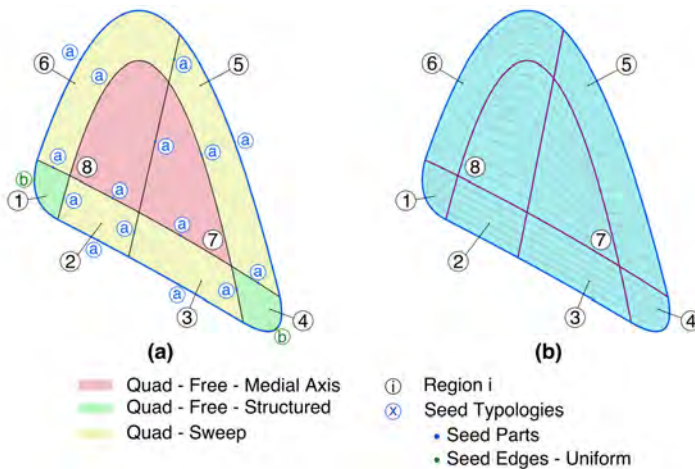


Figure III.56: Mesh techniques, seeds and mesh of MyoRing. (a) Mesh techniques and seeds of the MyoRing cross-section; (b) Mesh of the MyoRing cross-section.

All sections of the MyoRing have been meshed with quadrilateral elements. Therefore, all the internal points (from P_1 to P_8) are used to select the element type in the code described in page 249. The different meshing techniques are represented in the Figure III.56.a, and introduced in the code described in page 250. A global size of 0.015 is used in the all edges of the MyoRing (a in Figure III.56.a, see code in page 250), except the edges corresponding to the fillet, whose size of elements is of 0.01 (b in Figure III.56.a, code in page 251).

Finally, the mesh of the MyoRing is generated with the code described in page 252 (see in Figure III.56.b).

6. Assembly of the axisymmetric models

The assembly in each implemented model consists of only one part. In addition, and as they are axisymmetric models, the Y axis is defined as the rotation axis. For this purpose, the origin coordinate is defined as $O = (0, 0, 0)$, and the two points that define the cylindrical coordinate system are $P_1 = (1, 0, 0)$ and $P_2 = (0, 0, -1)$.

```

mdb.models['Model-1'].rootAssembly.DatumCsysByThree-
    Points(coordSysType=CYLINDRICAL, name='CysSist',
    origin=(0.0, 0.0, 0.0), point1=(1.0, 0.0, 0.0),
    point2=(0.0, 0.0, -1.0))
mdb.models['Model-1'].rootAssembly.Instance(dependent=

```

```
ON, name='NAME-PART-1', part=mdb.models['Model-1'].  
parts['NAME-PART'])
```

7. Step modulus

In order to create each model (cornea or ring), only one step, apart from the initial step, is generated.

```
mdb.models['Model-1'].StaticStep(name='ObtainMesh',  
nlgeom=ON, previous='Initial')
```

8. Boundary conditions

The boundary conditions for all the models are always the same to generate the input files of Abaqus (*.inp), which restricts the movement of all the nodes that conform the model.

```
mdb.models['Model-1'].DisplacementBC(amplitude=UNSET,  
createStepName='Initial', distributionType=UNIFORM,  
fieldName="", localCsys=None, name='BC-NAME',  
region=mdb.models['Model-1'].rootAssembly.  
instances['NAME-PART-1'].sets['ALL-NODES'],  
u1=SET,  
u2=SET,  
u3=SET)
```

where `ALL-NODES` is the group formed by all the nodes of the model.

9. Job and submission

The code that generates both the job and the submission are always the same for all Abaqus scripting files, regardless of if it is a cornea or a ring model.

```
mdb.Job(atTime=None, contactPrint=OFF, description="",  
echoPrint=OFF, explicitPrecision=SINGLE,  
getMemoryFromAnalysis=True, historyPrint=OFF,  
memory=90, memoryUnits=PERCENTAGE, model='Model-1',  
modelPrint=OFF, multiprocessingMode=DEFAULT, name=  
'ObtainMesh', nodalOutputPrecision=SINGLE, numCpus=1,  
numGPUs=0, queue=None, scratch="", type=ANALYSIS,  
userSubroutine="", waitHours=0, waitMinutes=0)
```

```
mdb.jobs['ObtainMesh'].submit(consistencyChecking=OFF)
```

10. Final considerations

Once each model is built in Abaqus scripting file (*.py), the following steps must be followed:

1. The Abaqus scripting file (*.py) is run to obtain the Abaqus input file (*.inp) with the following instruction:

```
abaqus cae noGUI=NAME_FILE.py
```

where `NAME_FILE` is CORNEA or ANILLO_G.

2. Once the Abaqus input file (*.inp) has been obtained, a Matlab script aim to extract in separate files the nodes, the elements and the sets of the model to continue with the process.

Finally, the expansion tool used to perform the methodology based on the displacement (Chapter 4) is also built automatically following the same process as the generic ring (see the Sections 3.2.1 and 5.2.1 of this Appendix). The geometry of the expansion tool is also elliptical, but with an elliptical hole in its interior. As the program is completely parametric, only the dimension of the ellipse must be introduced.



Appendix IV: Additional Tables and Results

Appendix aim to introduce additional *in-silico* results used in the clinical contributions.

Chapter Contents

1. Additional tables	274
2. Additional results	275

1. Additional tables

The Tables IV.1, IV.2, IV.3, and IV.4 show the different geometric details of clinical scenarios addressed in Chapter 5.

Table IV.1: Geometrical details for continuous ring in pocket.

z_{Pocket} : intrastromal depth of insertion (%); ϕ_{IRS} : manufacturing diameter of intrastromal ring; H_{MyoRing} (μm): size of intrastromal ring; V (mm^3): volume of generic intrastromal ring; Real V (mm^3): volume of analogous MyoRing.

Continuous ring in intrastromal pocket (in Figure 5.1.d)
[analogous to MyoRing]

Scenarios	z_{Pocket} (%)	ϕ_{IRS} (mm)	H_{MyoRing} (μm)	V (mm^3)	Real V (mm^3)
3	75	6	150	1.11	1.01
1 to 5 and 7	75	6	200	1.48	1.30
3	75	6	225	1.66	1.45
3 and 6	75	6	300	2.22	1.89
2 and 7	75	5	200	1.23	1.08
2	75	7	200	1.73	1.52
1	60	6	200	1.48	1.52
1	55	6	200	1.48	1.30

Table IV.2: Geometrical details for continuous ring in tunnel.

z_{Tunnel} : intrastromal depth of insertion (%); ϕ_{IRS} : manufacturing diameter of intrastromal ring; H_{Ellipse} (μm): size of intrastromal ring; V (mm^3): volume of generic intrastromal ring; Real V (mm^3): volume of analogous 355° Keraring.

Continuous ring in intrastromal tunnel (in Figure 5.1.c)
[analogous to 355° Keraring]

Scenarios	z_{Tunnel} (%)	ϕ_{IRS} (mm)	H_{Ellipse} (μm)	V (mm^3)	Real V (mm^3)
3	75	6	150	1.09	1.12
1 to 5 and 7	75	6	200	1.46	1.49
3	75	6	225	1.64	1.67
3 and 6	75	6	300	2.19	2.23
2 and 7	75	5	200	1.22	1.24
2	75	7	200	1.70	1.73
1	60	6	200	1.46	1.49
1	55	6	200	1.46	1.49

Table IV.3: Geometrical details for ring segments in tunnel.

z_{Tunnel} : intrastromal depth of insertion (%); ϕ_{IRS} : manufacturing diameter of intrastromal ring; H_{Ellipse} (μm): size of intrastromal ring; V (mm^3): volume of generic intrastromal ring; Real V (mm^3): volume of analogous 150° Ferrara.

Ring segments in intrastromal tunnel (in Figure 5.1.b)
[analogous to Intacs/Ferrara]

Scenarios	z_{Tunnel} (%)	ϕ_{IRS} (mm)	H_{Ellipse} (μm)	V (mm^3)	Real V (mm^3)
3	75	6	150	0.92	0.94
1 to 5 and 7	75	6	200	1.23	1.26
3	75	6	225	1.39	1.41
3 and 6	75	6	300	1.85	1.88
2 and 7	75	5	200	1.03	1.05
2	75	7	200	1.44	1.47
1	60	6	200	1.23	1.26
1	55	6	200	1.23	1.26

Case		$p(SFC_{Daxer} \geq 2)$ (R=6mm)	$p(SFC_{3D} \geq 2)$ (R=6mm)	Min. SFC (R<1mm)	Mean SFC (R<1mm)	Max. SFC (R<1mm)
gICRP	HM	2.10%	3.32%	0.89	1.11	1.25
	KC _{0.5}	1.99%	2.93%	0.85	1.13	1.44
	KC ₁	1.91%	2.70%	0.93	1.13	1.37
	KC _{1.5}	1.88%	2.75%	0.95	1.13	1.33
gICRT	HM	0.03%	71.14%	1.01	1.08	1.15
	KC _{0.5}	0.01%	68.73%	1.02	1.07	1.14
	KC ₁	0.01%	69.25%	1.03	1.07	1.12
	KC _{1.5}	0.00%	69.95%	1.03	1.07	1.12

Table IV.4: Corneal strengthening analysis. Probability of corneal stiffening for Daxer ($SFC = \sigma_{Before} / \sigma_{After}$) and new probability of SFC_{3D} for the full cornea (R = 6 mm); minimum, average and maximum corneal strengthening factor at the corneal center (R < 1 mm) for generic intrastromal continuous rings in tunnel/pocket (gICRT/gICRP). High myopia (HM) and three keratoconus are analysed (KC).

2. Additional results

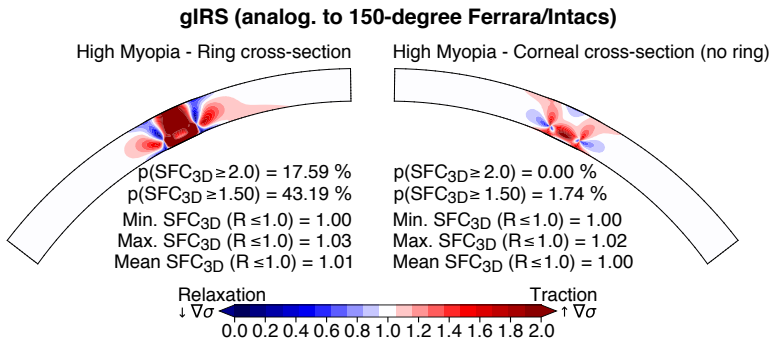


Figure IV.1: Spatial distribution of corneal strengthening factor (SFC_{3D}). SFC_{3D} after implantation of generic intrastromal ring segment (gIRS). The mechanical strengthening in the highest curvature cross-section (left) is similar to the one of the generic intrastromal continuous ring segment (gICRT). The mechanical strengthening in the lowest curvature cross-section (right) with no ring does not present a change in stresses but in the very surroundings of the tunnel.



Appendix V: Abbreviations

Appendix which show the overall abbreviations which have been used in the current Thesis. All abbreviations is in alphabetic order.

ACK: Average Central Keratometry.

AL: Axial Length.

AS–OCT: Anterior Segment Optical Coherence Tomography.

ATR: Against the rule.

BCVA: Best–Corrected Visual Acuity.

CA: Anterior Cornea.

CAS: Central Phenotype Symmetrical Astigmatism.

CCT: Central Corneal Thickness.

CHP: Central Hyperprolate.

CP: Posterior Cornea.

CRF: Corneal Resistance Factor.

CVS: Computer Vision Syndrome.

CXL: Cross–Linking Treatment.

Cyl: Cylindrical Power, in diopters (D).

DES: Digital Eye Strains.

DNA: Deoxyribonucleic Acid.

d.o.f: Degrees of Freedom.

FDA: Food and Drug Administration.

FE: Finite Element.

FEM: Finite Element Method.

G.A.G: Glycosaminoglycans.

gICRP: Generic Intrastromal Continuous Ring implant in a Pocket.

gICRT: Generic Intrastromal Continuous Ring implant in a Tunnel.

gIRS: Generic Intrastromal Ring Segment.

hDRI: Horizontal Distance of Ring Insertion.

HOA: High Order Aberrations.

ICR: Intrastromal Continuous Ring.

ICRS: Intrastromal Corneal Ring Segment.

IF: Impact Factor.

iFEM: Inverse Finite Element Method.

IOP: Intraocular Pressure.

IVCM: *In-Vivo* Confocal Microscopy.

JCR: Journal Citation Report.

KC: Keratoconus.

K_{mean}: Mean Keratometry.

LASIK: Laser in-situ Keratomileusis.

LCA: Leber's Congenital Amaurosis.

LHS: Latin Hypercube Sampling.

LOA: Low Order Aberrations.

MHC: Myeloid-derived major Histocompatibility Complex.

MRSE: Mean Refraction Spherical Equivalent.

OCT: Optical Coherence Tomography.

ORA: Ocular Response Analyzer.

OZ: Optical Zone.

PCC: Paracentral phenotype with Coinciding topographic and Comatose axes.

PCnC: Paracentral phenotype with non-Coinciding topographic and Comatose axes.

PCP: Paracentral phenotype with Perpendicular topographic and Comatose axes.

PCT: Peripheral Corneal Thickness.

PK: Penetrating Keratoplasty.

PMMA: Polymethylmethacrylate.

PS: Patient-Specific.

PRK: Photorefractive Keratectomy

Q: Mean Cornea Asphericity.

RE: Right Eye.

RGP: Rigid Gas Permeable.

sDI: Stromal Depth insertion.

SE: Spherical Equivalent.

SEF: Strain Energy Function.

SFC: Corneal Strengthening Factor.

SIM-K: Steepest corneal meridian.

SK: Severe Keratoconus.

SO: Left Eye.

Sph: Spherical Power, in diopters (D).

SPS: Scotopic Pupil Size.

UCVA: Uncorrected Visual Acuity.

UVA: UltraViolet Ray.

WHO: World Healthy Organization.

WTR: With The Rule.

ϕ_{ICRS} : Diameter of Cross-Section.

Bibliography

- M. S. Abd-Elaziz, A. R. E. S. Sarhan, A. M. Ibrahim, and H. A. E. Haggag. **Anterior segment changes after femtosecond laser-assisted implantation of a 355-degree intrastromal corneal ring segment in advanced keratoconus.** *Cornea*, 37(11):1438–1443, Nov 2018. ISSN 1536–4798. DOI: <http://dx.doi.org/10.1097/ICO.0000000000001702>.
- M. M. Abdellah and H. G. Ammar. **Femtosecond laser implantation of a 355-degree intrastromal corneal ring segment in keratoconus: a three year follow up.** *J. Ophthalmol.*, 2019(6783181):1–7, Oct 2019. ISSN 2090–0058. DOI: <https://doi.org/10.1155/2019/6783181>.
- Y. Abdelmassih, S. el Khoury, E. Chelala, E. Slim, C. G. Cherfan, and E. Jarade. **Toric ICL implantation after sequential intracorneal ring segments implantation and corneal cross-linking in keratoconus: 2-year follow-up.** *J. Refract. Surg.*, 33(9):610–616, Sep 2017. ISSN 1938–2391. DOI: <https://doi.org/10.3928/1081597X-20170621-02>.
- L. Akaishi, P. F. Tzelikis, and I. M. Raber. **Ferrara intracorneal ring implantation and cataract surgery for the correction of pellucid marginal corneal degeneration.** *J. Cataract. Refract. Surg.*, 30(11):2427–2430, Nov 2004. ISSN 0886–3350. DOI: <http://dx.doi.org/10.1016/j.jcrs.2004.04.047>.
- E. K. Akcay, M. Ackay, B. S. Uysal, P. Kosekahya, A. N. Aslan, M. Caglayan, C. Koseoglu, F. Yulek, and N. Cagil. **Impaired corneal biomechanical properties and the prevalence of keratoconus in mitral valve prolapse.** *J. Ophthalmol.*, 2014(402193):1–7, Apr 2014. ISSN 2090–0058. DOI: <http://dx.doi.org/10.1155/2014/402193>.
- A. Al-Muammar. **Comparison of visual, refractive and topographic keratometry outcomes of Intacs and Intacs SK in mild to moderate keratoconus eyes.** *Middle East Afr. J. Ophthalmol.*, 22(1):74–79, Jan 2015. ISSN 0974–9233. DOI: <https://doi.org/10.4103/0974-9233.148353>.
- W. S. Al-Tuwairqui, U. L. Osuagwu, H. Razzouk, A. AlHarbi, and K. C. Ogbuehi. **Clinical evaluation of two types of intracorneal ring segments (ICRS) for keratoconus.** *Int. Ophthalmol.*, 37(5):1185–1198, Nov 2016. ISSN 1573–2630. DOI: <http://dx.doi.org/10.1007/s10792-016-0385-2>.
- J. F. Alfonso, C. Lisa, J. Merayo-Llodes, L. Fernández-Vega, and R. Montés-Micó. **Intrastromal corneal ring segment implantation in paracentral keratoconus with coincident topographic**

- and coma axis. *J. Cataract Refract. Surg.*, 38(9):1576–1582, Sep 2012. ISSN 1873–4502. DOI: <http://dx.doi.org/10.1016/j.jcrs.2012.05.031>.
- J. F. Alfonso, L. Fernández-Vega-Cueto, C. Lisa, T. Monteiro, and D. Madrid-Costa. **Long-term follow-up of intrastromal corneal ring segment implantation in pediatric keratoconus.** *Cornea*, 38(7):840–846, Apr 2019. ISSN 1536–4798. DOI: <https://doi.org/10.1097/ICO.0000000000001945>.
- J. L. Alió and M. H. Shabayek. **Corneal higher order aberrations: a method to grade keratoconus.** *J. Refract. Surg.*, 22(6):539–545, Jul 2006. ISSN 1938–2391. DOI: <https://doi.org/10.3928/1081-597X-20060601-05>.
- J. L. Alió, A. Artola, A. Jassanein, H. Haroun, and A. Galal. **One or 2 Intacs segments for the correction of keratoconus.** *J. Cataract. Refract. Surg.*, 31:943–953, May 2005. ISSN 0886–3350. DOI: <https://doi.org/10.1016/j.jcrs.2004.09.050>.
- J. L. Alió, M. H. Shabayek, and A. Artola. **Intracorneal ring segments for keratoconus correction: Long-term follow-up.** *J. Cataract. Refract. Surg.*, 32:978–985, Jun 2006. ISSN 0886–3350. DOI: <https://doi.org/10.1016/j.jcrs.2006.02.044>.
- J. L. Alió, D. Piñero, and A. Daxer. **Clinical outcomes after complete ring implantation in corneal ectasia using the femtosecond technology.** *Ophthalmology*, 118(7):1282–1290, Jul 2011. ISSN 0161–6420. DOI: <http://dx.doi.org/10.4103/2008-322X.180713>.
- J. L. Alió, A. Vega-Estrada, S. Esperanza, R. I. Barraquer, M. A. Teus, and J. Murta. **Intrastromal corneal ring segments: How succesful is the surgical treatment of keratoconus?** *Middle East Afr. J. Ophthalmol.*, 21(1):3–9, Jan–Mar 2014. ISSN 0974–9233. DOI: <https://doi.org/10.4103/0974-9233.124076>.
- K. Amanzadeh, R. Elham, and E. Jafarzadepur. **Effects of single-segment Intacs implantation on visual acuity and corneal topographic indices of keratoconus.** *J. Curr. Ophthol.*, 29(3):289–193, Oct 2017. ISSN 2452–2325. DOI: <http://dx.doi.org/10.1016/j.joco.2016.10.004>.
- R. J. Ambrosio, S. Klyce, and S. Wilson. **Corneal topographic and pachymetric screening of keratorefractive patients.** *J. Refract. Surg.*, 19(1):24–29, Feb 2003. ISSN 1938–2391. DOI: <https://doi.org/10.3928/1081-597X-20030101-05>.
- M. A. A. Ameerh, G. I. Hamad, O. H. Ababneh, A. M. Gharaibeh, R. M. A. Refai, and M. D. Albdour. **Ferrara ring segments implantation for treating keratoconus.** *Int. J. Ophthalmol.*, 5(5):586–590, Oct 2012. ISSN 2222–3959. DOI: <http://dx.doi.org/10.3980/j.issn.2222-3959.2012.05.08>.
- M. Amsler. **The “forme fruste” of keratoconus.** *Wien. Klin. Wochenschr.*, 73:842–843, Dec 1961. ISSN 1613–7671.
- E. Ancèle, F. Malecaze, J.-L. Arné, and P. Fournié. **Facteurs prédictifs de succès des anneaux intracornéens de Ferrara dans le kératocône.** *J. Fr. Ophthalmol.*, 34(8):513–520, Feb 2011. ISSN 0181–5512. DOI: <http://dx.doi.org/10.1016/j.jfo.2011.02.006>.

- T. T. Andreassen, A. H. Simonsen, and H. Oxlund. **Biomechanical properties of keratoconus and normal corneas.** *Exp. Eye Res.*, 31:435–441, Feb 1980. ISSN 0014–4835. DOI: [https://doi.org/10.1016/s0014-4835\(80\)80027-3](https://doi.org/10.1016/s0014-4835(80)80027-3).
- M. Á. Ariza-Gracia, J. Zurita, D. P. Piñero, J. F. Rodríguez-Matas, and B. Calvo. **Coupled biomechanical response of the cornea assessed by non–contact tonometry. A simulation study.** *PLoS One*, 10(3): 1–10, Mar 2015. ISSN 1932–6203. DOI: <https://doi.org/10.1371/journal.pone.0121486>.
- M. Á. Ariza-Gracia, J. Zurita, D. P. Piñero, B. Calvo, and J. F. Rodríguez-Matas. **Automatized patient–specific methodology for numerical determination of biomechanical corneal response.** *Ann. Biomed. Eng.*, 44(5):1753–1772, Aug 2016. ISSN 1573–9686. DOI: <https://doi.org/10.1007/s10439-015-1426-0>.
- M. Á. Ariza-Gracia, A. Ortilles, J. Cristóbal, J. F. Rodríguez-Matas, and B. Calvo. **A numerical–experimental protocol to characterize corneal tissue with an application to predict astigmatic keratotomy surgery.** *J. Mech. Behav. Biomed. Mater.*, 74(2017):304–314, Oct 2017a. ISSN 1751–6161. DOI: <https://doi.org/10.1016/j.jmbbm.2017.06.017>.
- M. Á. Ariza-Gracia, S. Redondo, D. P. Llorens, B. Calvo, and J. F. Rodríguez-Matas. **A predictive tool for determining patient-specific mechanical properties of human corneal tissue.** *Comput. Methods. Appl. Mech. Eng.*, 317(Supplement C):226–247, Apr 2017b. ISSN 0045–7825. DOI: <https://doi.org/10.1016/j.cma.2016.12.013>.
- M. Á. Ariza-Gracia, W. Wi, B. Calvo, M. Malvé, P. Büchler, and J. F. Rodríguez-Matas. **Fluid–structure simulation of a general non-contact tonometry. A required complexity?** *Comput. Methods. Appl. Mech. Eng.*, 340(1):202–215, Jun 2018. ISSN 0045–7825. DOI: <https://doi.org/10.1016/j.cma.2018.05.031>.
- A. A. Assiri, B. I. Yousuf, A. J. Quantock, and P. J. Murphy. **Incidence and severity of keratoconus in Asir province, Saudi Arabia.** *Br. J. Ophthalmol.*, 89(11):1403–1406, Nov 2005. ISSN 1468–2079. DOI: <http://dx.doi.org/10.1136/bjo.2005.074955>.
- G. U. Auffarth, L. Wang, and H. E. Völcker. **Keratoconus evaluation using the Orbscan topography system.** *J. Cataract. Refract. Surg.*, 26(2):222–228, 2000. ISSN 0886–3350. DOI: [https://doi.org/10.1016/S0886-3350\(99\)00355-7](https://doi.org/10.1016/S0886-3350(99)00355-7).
- M. A. Bamashmus, M. F. Saleh, and M. A. Awadalla. **Reasons for not performing keratorefractive surgery in patients seeking refractive surgery in a hospital–based cohort in “Yemen”.** *Middle East Afr. J. Ophthalmol.*, 17(4):349–353, Dec 2010. ISSN 0974–9233. DOI: <http://dx.doi.org/10.4103/0974-9233.71605>.
- R. Barbara, A. Barbara, and M. Naftali. **Depth evaluation of intended vs Intacs intrastromal ring segments using optical coherence tomography.** *Eye*, 30(1):102–110, Oct 2016. ISSN 1476–5454. DOI: <http://dx.doi.org/10.1038/eye.2015.202>.
- S. Barros and S. Offenbacher. **Epigenetics: Connecting environment and genotype to phenotype and disease.** *J. Dent. Res.*, 88(5):400–408, Jan 2009. ISSN 1544–0591. DOI: <http://dx.doi.org/10.1177/0022034509335868>.

- A. M. Bawazeer, W. G. Hodge, and B. Lorimer. **Atopy and keratoconus: a multivariate analysis.** *Br. J. Ophthalmol.*, 84(8):834–836, Aug 2000. ISSN 1468–2079. DOI: <https://doi.org/10.1136/bjo.84.8.834>.
- A. M. Bayoumy, A. A. R. Farag, M. M. Shawky, and M. N. A. Hamid. **Intrastromal corneal Kerating segments for keratoconus.** *ZUMJ*, 20(3):399–403, May 2014. ISSN 2357–0717. DOI: <https://doi.org/10.21608/zumj.2014.4393>.
- U. Beckh, U. Schönherr, and G. O. Naumann. **Autosomal dominanter Keratokonus als okuläres Leitsymptom bei Osteogenesis imperfecta tarda Lobstein.** *Klin. Monbl. Augenheilkd.*, 206(4):268–272, Feb 1995. ISSN 1439–3999. DOI: <https://doi.org/10.1055/s-2008-1035438>.
- A. Benoit, G. Latour, M.-C. Schanne-Klein, and J.-M. Allain. **Simultaneous microstructural and mechanical characterization of human corneas at increasing pressure.** *J. Mech. Behav. Biomed. Mater.*, 60(2016): 93–105, Jul 2016. ISSN 1751–6161. DOI: <https://doi.org/10.1016/j.jmbbm.2015.12.031>.
- G. Bikbova, G. Kazakbaeva, M. Bikbov, and E. Usumov. **Complete corneal ring (MyoRing) implantation versus MyoRing implantation combined with corneal collagen crosslinking for keratoconus: 3-year follow-up.** *Int. Ophthalmol.*, 38(3):1285–1293, Jun 2018. ISSN 1573–2630. DOI: <https://doi.org/10.1007/s10792-017-0593-4>.
- R. R. Bourne, S. R. Flaxman, T. Braithwaite, M. V. Cicinelli, A. Das, J. B. Konas, J. Keeffe, J. H. Kempen, J. Leasher, H. Limburg, K. Naidoo, K. Pesudovs, S. Resnikoff, A. Silvester, G. A. Stevens, N. Thahhan, T. Y. Wong, and H. R. Taylor. **Magnitude, temporal trends, and projections of the global prevalence of blindness and distance and near vision impairment: a systematic review and meta-analysis.** *Lancet. Glob. Health.*, 5(9):e888–e897, Aug 2017. ISSN 2214–109X. DOI: [http://dx.doi.org/10.1016/S2214-109X\(17\)30293-0](http://dx.doi.org/10.1016/S2214-109X(17)30293-0).
- P. Breitenfeld, T. Ripken, and H. Lubatschowski. **Finite element method-simulation of the human lens during accommodation.** In H. van den Bergh and A. Vogel, editors, *Therapeutic Laser Applications and Laser-Tissue Interactions II*, volume 5863, pages 1–9. International Society for Optics and Photonics, SPIE, Aug 2005. DOI: <https://doi.org/10.1117/12.633086>.
- K. P. Burdon, D. J. Coster, J. C. Charlesworth, R. A. Mills, K. J. Laurie, C. Giunta, A. W. Hewitt, P. Latimer, and J. E. Craig. **Apparent autosomal dominant keratoconus in a large Australian pedigree accounted for by digenic inheritance of two novel loci.** *Hum. Genet.*, 124(4):379–386, Nov 2008. ISSN 1432–1203. DOI: <http://dx.doi.org/10.1007/s00439-008-0555-z>.
- P. Caroline, M. Andre, B. Kinoshita, and J. Choo. **Etiology, diagnosis and management of keratoconus: new thoughts and new Understandings.** *Pacific. Univ. Coll. Optom.*, 2008.
- M. Castori. **Ehlers–Danlos Syndrome, Hypermobility Type: An Underdiagnosed Hereditary Connective Tissue Disorder with Mucocutaneous, Articular, and Systemic Manifestations.** *ISRN Dermatol.*, 2012(751768):1–23, Oct 2012. ISSN 2090–4606. DOI: <http://dx.doi.org/10.5402/2012/751768>.
- J. Colin and A. Kiliç. **Surgical techniques for ICRS implantation.** *CRSEurope*, pages 23–24, Jul–Aug 2012.

- J. Colin and F. J. Malet. **Intacs for the correction of keratoconus: two-year follow-up.** *J. Cataract Refract. Surg.*, 33(1):69–74, Jan 2007. ISSN 1873–4502. DOI: <http://dx.doi.org/10.1016/j.jcrs.2006.08.057>.
- J. Colin, B. Cochener, G. Savary, F. Malet, and D. Holmes-Higgin. **INTACS inserts for treating keratoconus.** *Ophthalmology*, 108(8):1409–1414, Aug 2001. ISSN 0161–6420. DOI: [http://dx.doi.org/10.1016/s0161-6420\(01\)00646-7](http://dx.doi.org/10.1016/s0161-6420(01)00646-7).
- E. Coskunseven, G. D. Kymionis, N. S. Tsiklis, S. Atun, E. Arslan, M. R. Jankov, and I. G. Pallikaris. **One-Year results of intrastromal corneal ring segment implantation (Keraring) using femtosecond laser in patients with keratoconus.** *Am. J. Ophthalmol.*, 145(5):775–779.e1, May 2008. ISSN 0002–9394. DOI: <https://doi.org/10.1016/j.ajo.2007.12.022>.
- B. Coudrillier, J. Pijanka, J. Jefferys, T. Sorensen, H. A. Quigley, C. Boote, and T. D. Nguyen. **Effects of age and diabetes on scleral stiffness.** *J. Biomech. Eng.*, 137(7):1–10, Jun 2015. ISSN 1528–8951. DOI: <https://doi.org/10.1115/1.4029986>.
- I. Cozma, C. Atherley, and N. James. **Influence of ethnic origin on the incidence of keratoconus and associated atopic disease in Asian and white patients.** *Eye*, 19:924–925, Sep 2004. ISSN 1476–5454. DOI: <https://doi.org/10.1038/sj.eye.6701677>.
- A. J. Cunningham and P. Barry. **Intraocular pressure–physiology and implications for anaesthetic management.** *Can. Anaesth. Soc. J.*, 33(2):195–208, Mar 1986. ISSN 1496–8975. DOI: <https://doi.org/10.1007/BF03010831>.
- A. da Candelaria, F. E. Hirai, and M. Campos. **Refractive and visual outcomes after Ferrara corneal ring segment implantation at a 60% depth in keratoconic eyes: case series.** *Arq. Bras. Oftalmol.*, 82(6):488–494, Jan 2019. ISSN 1678–2925. DOI: <http://dx.doi.org/10.5935/0004-2749.20190091>.
- G.-M. G. Dai. **Wavefront optics for vision correction.** SPI press, Bellingham, Washington USA, Washington, 2008. ISBN 978–0–819–47841–2. DOI: <https://doi.org/10.1117/3.769212>.
- R. Dan Z., A. Timothy J, G. Marine, U. Raksha, and S. Ronald H. **Keratoconus: recent advances in diagnosis and treatments**, chapter 12, pages 141–150. Springer Nature, 2017. ISBN 978-3-319-43879-5. DOI: <https://doi.org/10.1007/978-3-319-43881-8>.
- P. D. Davies, D. Lobascher, J. A. Menon, A. H. S. Rahi, and M. Ruben. **Immunological studies in keratoconus.** *Trans. Ophthalmol. Soc. U. K.*, 96(1):173–178, Apr 1976. ISSN 0950–222X.
- A. Daxer. **Corneal intrastromal implantation surgery for treatment of moderate and high myopia.** *J. Cataract. Refract. Surg.*, 34(2):94–198, Feb 2008. ISSN 0886–3350. DOI: <https://doi.org/10.1016/j.jcrs.2007.10.011>.
- A. Daxer. **Biomechanics of Corneal Ring Implants.** *Cornea*, 34(11):1493–1498, Sep 2015. ISSN 1536–4798. DOI: <http://dx.doi.org/10.1097/ICO.0000000000000591>.

- A. Daxer. **MyoRing treatment of myopia**. *J. Optom.*, 10(3):194–198, Jul–Sep 2017. ISSN 1888–4296. DOI: <https://doi.org/10.1016/j.optom.2016.06.003>.
- A. Daxer, A. Ettl, and R. Hörantner. **Long-term results of MyoRing treatment of keratoconus**. *J. Optom.*, 10(2):123–129, Feb 2016. ISSN 1888–4296. DOI: <http://dx.doi.org/10.1016/j.optom.2016.01.002>.
- M. Dhakad, K. Mahajan, and A. Mitra. **Experimental analysis and optimization of cutting parameters for the surface roughness in the facing operation of PMMA material**. *IOSR-JMCE*, 136277391, Mar 2017. ISSN 2278–1684. DOI: <http://dx.doi.org/10.9790/1684-17010015260>.
- J. W. Eaton, D. Bateman, S. Hauberg, and R. Wehbring. **GNU Octave version 5.2.0 manual: a high-level interactive language for numerical computations**, 2020. URL <https://www.gnu.org/software/octave/doc/v5.2.0/>.
- A. Ebrahimian, P. Mosaddegh, N. M. Bagheri, and S. Pirhadi. **A simple numerical approach to mimic MyoRing surgery in keratoconus corneas based on optical coherence tomography**. *EC Ophthalmol.*, 10(5):345–356, Apr 2019.
- M. Edwards, C. N. McGhee, and S. Dean. **The genetics of keratoconus**. *Clin. Exp. Ophthalmol.*, 29(6):345–351, Dec 2001. ISSN 1442–6404. DOI: <http://dx.doi.org/10.1046/j.1442-9071.2001.d01-16.x>.
- M. Elder. **Leber congenital amaurosis and its association with keratoconus and keratoglobus**. *J. Pediatr. Ophthalmol. Strabismus*, 31(1):38–40, Jan–Feb 1994. ISSN 1938–2405.
- A. Elsheikh, C. Whitford, R. Hamarashid, W. Kassem, A. Joda, and P. Büchler. **Stress free configuration of the human eye**. *Med. Eng. Phys.*, 35(2):211–216, Sep 2013. ISSN 1873–4030. DOI: <https://doi.org/10.1016/j.medengphy.2012.09.006>.
- E. Elsheikh, D. Alhasso, and P. Rama. **Assessment of the epithelium’s contribution to corneal biomechanics**. *Exp. Eye Res.*, 86(2):445–451, Feb 2008. ISSN 0014–4835. DOI: <http://dx.doi.org/10.1016/j.exer.2007.12.002>.
- A. Ertan and O. Muftuoglu. **Keratoconus Clinical Findings According to Different Age and Gender Groups**. *Cornea*, 27(10):1109–1113, Dec 2008. ISSN 1536–4798. DOI: <https://doi.org/10.1097/ICO.0b013e31817f815a>.
- A. Ertan, G. Kamburoglu, and Ü. Akgün. **Comparison of outcomes of 2 channel sizes for intrastromal ring segment implantation with a femtosecond laser in eyes with keratoconus**. *J. Cataract Refract. Surg.*, 33(4):648–653, Apr 2007. ISSN 1873–4502. DOI: <http://dx.doi.org/10.1016/j.jcrs.2007.01.014>.
- B. Fangjun, G. Brendan, W. QinMei, and E. Ahmed. **Consideration of corneal biomechanics in the diagnosis and management of keratoconus: is it important?** *Eye Vis.*, 2016(4):3–18, Jul 2016. ISSN 2326–0254. DOI: <http://dx.doi.org/10.1186/s40662-016-0048-4>.

- T. Fatima, M. C. Acharya, U. Mathur, and P. Barua. **Demographic profile and visual rehabilitation of patients with keratoconus attending contact lens clinic at a tertiary eye care centre.** *Cont. Lens Anterior Eye.*, 33(1):19–22, Feb 2010. ISSN 1367–0484. DOI: <https://doi.org/10.1016/j.clae.2009.09.004>.
- L. Fernández-Vega, C. Lisa, A. Poo-López, D. Madrid-Costa, J. Merayo-Llodes, and J. F. Alfonso. **Intrastromal corneal ring segment implantation in 409 paracentral keratoconic eyes.** *Cornea*, 35(11):1421–1426, Nov 2016. ISSN 1536–4798. DOI: <https://doi.org/10.1097/ICO.0000000000000978>.
- L. Fernández-Vega, C. Lisa, A. Poo-López, J. F. Alfonso, and D. Madrid-Costa. **Three-year follow-up of intrastromal corneal ring segment implantation in central keratoconus with regular astigmatism: “Bow-tie” shape.** *Eur. J. Ophthalmol.*, 30(4):643–649, Feb 2019. ISSN 1120–6721. DOI: <http://dx.doi.org/10.1177/1120672119835397>.
- J. I. Fernández-Vigo, J. Á. Fernández-Vigo, A. Macarro-Merino, C. Fernández-Pérez, J. M. M. de-la Casa, and J. García-Feijó. **Determinants of anterior chamber depth in a large Caucasian population and agreement between intra-ocular lens master and Pentacam measurements of this variable.** *Acta Ophthalmol.*, 94(2):e150–e155, Mar 2016. ISSN 1755–3768. DOI: <https://doi.org/10.1111/aos.12824>.
- F. Fimiani, A. Iovine, R. Carelli, M. Pansini, G. Sebastio, and A. Magli. **Incidence of ocular pathologies in Italian children with Down syndrome.** *Eur. J. Ophthalmol.*, 17(5):817 – 822, Apr 2007. ISSN 1120–6721. DOI: <https://doi.org/10.1177/112067210701700521>.
- B. A. Fink, H. Wagner, K. Steger-May, C. Rosenstiel, T. Roediger, T. T. McMahon, M. O. Gordon, and K. Zadnik. **Differences in Keratoconus as a Function of Gender.** *Am. J. Ophthalmol.*, 140(3):459.e1–459.e12, Sep 2005. ISSN 0002–9394. DOI: <http://dx.doi.org/10.1016/j.ajo.2005.03.078>.
- S. R. Flaxman, R. R. A. Bourne, S. Resniko, P. Ackland, T. Braithwaite, M. V. Cicinelli, A. Das, J. B. Jonas, J. Keeffe, J. H. Kempen, J. Leasher, H. Limburg, K. Naidoo, K. Pesudovs, A. Silvester, G. A. Stevens, N. Tahhan, T. Y. Wong, and H. R. Taylor. **Global causes of blindness and distance vision impairment 1990–2020: a systematic review and meta-analysis.** *Lancet. Glob. Health.*, 5(12):e1221–e1234, Dec 2017. ISSN 2214–109X. DOI: [http://dx.doi.org/10.1016/S2214-109X\(17\)30393-5](http://dx.doi.org/10.1016/S2214-109X(17)30393-5).
- J. Flecha-Lescún, P. Büchler, B. Calvo, and M. Á. Ariza-Gracia. **Modelling strategies for the simulation of corneal intrastromal ring surgeries.** *Ann. Biomed. Eng.*, (Under Preparation), a.
- J. Flecha-Lescún, L. Remón, B. Calvo, and M. Á. Ariza-Gracia. **Mechanical characterization of Intracorneal Ring Segments after mechanization.** *J. Mech. Behav. Biomed.*, (Under Preparation), b.
- J. Flecha-Lescún, B. Calvo, J. Zurita, and M. Á. Ariza-Gracia. **Template-based methodology for the simulation of intracorneal segment ring implantation in human corneas.** *Biomech. Model. Mechanobiol.*, 17(4):923–938, Aug 2018. ISSN 1617–7940. DOI: <https://doi.org/10.1007/s10237-018-1013-z>.
- J. Flecha-Lescún[#], M. Á. Ariza-Gracia[#], P. Büchler, and B. Calvo. **Corneal biomechanics after intrastromal ring surgery: opto-mechanical *in-silico* assessment.** *Transl. Vis. Sci. Technol.*, 9(11):26: 1–16, Oct 2020. ISSN 2164–2591. DOI: <https://doi.org/10.1167/tvst.9.11.26>.

- J. V. Forrester, A. D. Dick, P. G. McMenamin, F. Roberts, and E. Pearlman. **The Eye: Basic Science in practice.** Elsevier Health Sciences, 4 edition, 2015. ISBN 978-0-7020-5554-6. DOI: <https://doi.org/10.1111/j.1444-0938.2008.00321.x>.
- M. Fraldi, A. Cutolo, L. Esposito, and F. Guarracino. **The role of the viscoelasticity and stress gradient on the outcome of conductive keratoplasty.** *Biomech. Model. Mechanobiol.*, 10:397–412, Jul 2010. ISSN 1617–7940. DOI: <http://dx.doi.org/10.1007/s10237-010-0242-6>.
- T. R. Fricke, N. Tahhan, S. Resnikoff, E. Papas, A. Burnett, S. M. Ho, T. Naduvilath, and K. S. Naidoo. **Global Prevalence of Presbyopia and Vision Impairment from Uncorrected Presbyopia.** *Ophthalmology*, 125(10):1492–1499, Oct 2018. ISSN 0161-6420. DOI: <http://dx.doi.org/10.1016/j.ophtha.2018.04.013>.
- M. A. Galin and R. Berger. **Atopy and Keratoconus.** *Am. J. Ophthalmol.*, 45(6):904–906, Jun 1958. ISSN 0002–9394. DOI: [https://doi.org/10.1016/0002-9394\(58\)90403-3](https://doi.org/10.1016/0002-9394(58)90403-3).
- V. Galvis, T. Sherwin, A. Tello, J. Merayo, R. Barrera, and A. Acera. **Keratoconus: an inflammatory disorder?** *Eye*, 29(7):843–859, Apr 2015. ISSN 1476–5454. DOI: <https://doi.org/10.1038/eye.2015.63>.
- G. P. García-García and J. Belmonte-Martínez. **Outcomes of Penetrating Keratoplasty in Mentally Retarded Patients With Keratoconus.** *Cornea*, 27(9):980–987, Oct 2008. ISSN 1536–4798. DOI: <https://doi.org/10.1097/ICO.0b013e31817618d7>.
- N. Garcia-Porta, P. Fernandes, A. Queiros, J. Salgado-Borges, M. Parafita-Mato, and J. M. González-Méijome. **Corneal Biomechanical Properties in Different Ocular Conditions and New Measurement Techniques.** *ISRN Ophthalmol.*, 2014:1–20, Mar 2014. ISSN 2090–5696. DOI: <http://dx.doi.org/10.1155/2014/724546>.
- N. Garzón and F. P. Galán. **ORBSCAN: Topographical maps.** *Gaceta Optica*, 420:24–28, Nov 2013.
- T. Gasser, R. Ogden, and G. Holzapfel. **Hyperelastic modelling of arterial layers with distributed collagen fibre orientations.** *J. R. Soc. Interface*, 3(6):15–35, Feb 2006. ISSN 1742–5662. DOI: <https://doi.org/10.1098/rsif.2005.0073>.
- A. Gasset, W. Hinson, and J. Frias. **Keratoconus and atopic diseases.** *Ann Ophthalmol.*, 10(8):991–994, Aug 1978. ISSN 0003–4886.
- Z. Gatzioufas, A. Khine, M. Elalfy, I. Guber, C. McLintock, F. Sabatino, S. Hamada, and D. Lake. **Clinical outcomes after Keraring implantation for keratoconus management in patients older than 4 years: a retrospective, interventional, cohort study.** *Ophthalmol. Ther.*, 7(1):95–100, Mar 2018. ISSN 2193–6528. DOI: <http://dx.doi.org/10.1007/s40123-017-0117-3>.
- A. S. Gauthier, M. Friot, R. Montard, M. Saleh, and B. Delbosc. **Anneaux intra-cornéens Ferrara implantés au laser femtoseconde dans le traitement du kératocône : résultats fonctionnels à 1 an.** *J. Fr. Ophthalmol.*, 39(5):428–436, May 2016. ISSN 0181–5512. DOI: <http://dx.doi.org/10.1016/j.jfo.2016.01.006>.

- T. Georgiou, C. Funnell, A. Cassels-Brown, and R. O'Connor. **Influence of ethnic origin on the incidence of keratoconus and associated atopic disease in Asians and white patients.** *Eye*, 18:379–383, May 2004. ISSN 1476–5454. DOI: <http://dx.doi.org/10.1038/sj.eye.6700652>.
- A. M. Gharaibeh, S. M. Muhsen, I. B. AbuKhader, O. H. Ababneh, M. A. Abu-Ameerh, and M. D. Albdour. **Keraring intrastromal corneal ring segments for correction of keratoconus.** *Cornea*, 31(2):115–120, Feb 2012. ISSN 1536–4798. DOI: <https://doi.org/10.1097/ICO.0b013e3182215a15>.
- C. Gökgöl, N. Diehm, and P. Büchler. **Numerical Modeling of Nitinol Stent Oversizing in Arteries with Clinically Relevant Levels of Peripheral Arterial Disease: The Influence of Plaque Type on the Outcomes of Endovascular Therapy.** *Ann. Biomed. Eng.*, 45(6):1420–1433, Jun 2017. ISSN 1573–9686. DOI: <https://doi.org/10.1007/s10439-017-1803-y>.
- J. A. Gomes, D. Tan, C. J. Rapuano, M. W. Belin, J. Renato Ambrósio, J. L. Guell, F. Malecaze, K. Nishida, and V. S. Sangwan. **Global Consensus on Keratoconus and Ectatic Disease.** *Cornea*, 34(4):359–369, Apr 2015. ISSN 1536–4798. DOI: <http://dx.doi.org/10.1097/ICO.0000000000000408>.
- A. Gordon-Shaag, M. Millodot, and E. Shneor. **The Epidemiology and Etiology of Keratoconus.** *Int. J. Keratoconus Ectatic Dis.*, 1(1):7–15, Jan–Apr 2012. ISSN 2277–3800. DOI: <https://doi.org/10.5005/jp-journals-10025-1002>.
- A. Gordon-Shaag, M. Millodot, M. Essa, J. Garth, M. Ghara, and E. Shneor. **Is consanguinity a risk factor for keratoconus?** *Optom. Vis. Sci.*, 90(5):448–454, May 2013. ISSN 1538–9235. DOI: <http://dx.doi.org/10.104610.1097/OPX.0b013e31828da95c>.
- A. Gordon-Shaag, M. Millodot, and E. S. amd Yutao Liu. **The Genetic and Environmental Factors for Keratoconus.** *Biomed Res. Int.*, 2015(795738):1–20, Jan 2015. ISSN 2314–6141. DOI: <http://dx.doi.org/10.1155/2015/795738>.
- G. Greenfield, A. Romano, R. Stein, and R. M. Goodman. **Blue sclerae and keratoconus: Key features of a distinct heritable disorder of connective tissue.** *Clin. Genet*, 4:8–16, Oct 1973. ISSN 1399–0004. DOI: <https://doi.org/10.1111/j.1399-0004.1973.tb01115.x>.
- F. A. Guarnieri, P. Ferrara, and L. Torquetti. **Biomechanics of Additive Surgery: Intracorneal Rings**, chapter 5, pages 73–107. Fabio A. Guarnieri, 2015. ISBN 978–1–4939–1766–2. DOI: <http://dx.doi.org/10.1007/978-1-4939-1767-9>.
- I. Guber, Z. Gatzioufas, D. Goldblum, M. Elalfy, S. Hamada, and D. Lake. **Klinische Ergebnisse nach Keraring-Implantation zur Behandlung von Keratokonuspatienten mit sehr dünnen Hornhäuten.** *Klin. Monbl. Augenheilkd.*, 236(12):1435–1438, Jul 2018. ISSN 1439–3999. DOI: <https://doi.org/10.1055/a-0659-2549>.
- W. Hammerstein. **Konkordanter Keratokonus bei eineiigen Zwillingen.** *Ophthalmologica*, 165:449–452, Dec 1972. ISSN 1423-0267. DOI: <https://doi.org/10.1159/000308537>.

- A. Hasegawa, T. Kojima, M. Yamamoto, Y. Kato, A. Tamoki, and K. Ichikawa. **Impact of the anterior-posterior corneal radius ratio on intraocular lens power calculation errors.** *Clin. Ophthalmol.*, 12:1549–1558, 2018. ISSN 1177–5483. DOI: <https://doi.org/10.2147/OPHTH.S161464>.
- H. Hashemi, A. Beiranvand, M. Khabazkhoob, S. Asgari, M. H. Emamian, M. Shariati, and A. Fotouhi. **Prevalance of keratoconus in population-based study in Sharoud.** *Cornea*, 32(11):1441–1445, Nov 2013a. ISSN 1536–4798. DOI: <http://dx.doi.org/10.1097/ICO.0b013e3182a0d014>.
- H. Hashemi, M. Khabazkhoob, and A. Fotouhi. **Topographic keratoconus is not rare in an Iranian population: the Tehran eye study.** *Ophthalmic Epidemiol.*, 20(6):385–391, Oct 2013b. ISSN 1744–5086. DOI: <http://dx.doi.org/10.3109/09286586.2013.848458>.
- H. Hashemi, A. Yazdani-Abyaneh, A. Beheshtnejad, M. Jabbarvand, A. Kheirkhah, and S. R. Ghaffary. **Efficacy of Intacs intrastromal corneal ring segment relative to depth of insertion evaluated with the anterior segment optical coherence Tomography.** *Middle East Afr. J. Ophthalmol.*, 20(3):234–238, Sep 2013c. ISSN 0974–9233. DOI: <https://doi.org/10.4103/0974-9233.114800>.
- H. Hashemi, M. Khabazkhoob, N. Yazdani, H. Ostadimoghaddam, R. Norouzirad, K. Amanzadeh, M. Mirafteb, A. Derakhshan, and A. Yekta. **The prevalence of keratoconus in a young population in Mashhad, Iran.** *Ophthalmic. Physiol Opt.*, 34(5):519–527, Sep 2014. ISSN 1475–1313. DOI: <http://dx.doi.org/10.1111/opo.12147>.
- M. N. Hashemian, M. A. Zare, M. Mohammadpour, F. Rahimi, M. R. Fallah, and F. K. Panah. **Outcomes of single segment implantation of conventional Intacs versus Intacs SK for keratoconus.** *J. Ophthalmic. Vis. Res.*, 9(3):305–309, Feb 2014. ISSN 2008–322X. DOI: <https://doi.org/10.4103/2008?322X.143359>.
- S. J. Hashemian, N. Farshchian, A. Foroutam-Jazi, M. E. Jafari, M. S. Hashemian, and S. M. Hashemian. **Visual and refractive outcomes and ytomographic changes after femtosecond laser? Assisted intrastromal corneal ring segment implantation in patients with keratoconus.** *J. Ophthalmic. Vis. Res.*, 13(4): 376–382, Dec 2018. ISSN 2008–322X. DOI: <https://doi.org/10.4103/jovr.jovr-42-17>.
- S. Hayes, C. S. Kamma-Lorger, C. Boote, R. D. Young, A. J. Quantock, A. Rost, Y. Khatib, J. Harris, N. Yagi, N. Terrill, and K. M. Meek. **The effect of riboflavin/UVA collagen cross-linking therapy on the structure and hydrodynamic behaviour of the ungulate and rabbit corneal stroma.** *PLoS One*, 8(1):1–12, Jan 2013. ISSN 1932–6203. DOI: <http://dx.doi.org/10.1371/journal.pone.0052860>.
- M. A. Heikal, M. Abdelshafy, T. T. Soliman, and A. M. Hamed. **Refractive and visual outcomes after Keraring intrastromal corneal ring segment implantation for keratoconus assisted by femtosecond laser at 6 months follow-up.** *Clin. Ophthalmol.*, 11:81–86, Dec 2017. ISSN 1177–5483. DOI: <https://doi.org/10.2147/OPHTH.S120267>.
- T. Hellstedt, J. Mäkelä, R. Uusitalo, S. Emre, and R. Uusitalo. **Treating keratoconus with Intacs corneal ring segments.** *J. Refract. Surg.*, 21(3):236–246, May–Jun 2005. ISSN 1938–2391.
- J. C. Helton and F. J. Davis. **Latin hypercube sampling and the propagation of the uncertainty in analysis of complex systems.** Sandia National Laboratories, Nov 2002.

- G. Hernández-Gómez, D. Malacara-Doblado, Z. Malacara-Hernández, and D. Malacara-Hernández. **Modal processing of Hartmann and Shack–Hartmann patterns by means of a least squares fitting of the transverse aberrations.** *App. Opt.*, 53(31):7422–7434, 2014. ISSN 1539–4522. DOI: <http://dx.doi.org/10.1364/AO.53.007422>.
- R. Hetherington. **The Snellen Chart as a test of visual acuity.** *Psychol. Forsch.*, 24(4):349–357, Nov 1954. ISSN 1430–2772. DOI: <http://dx.doi.org/10.1007/BF00422033>.
- J. Hong, J. Xu, A. Wei, S. X. Deng, X. Cui, X. Yu, and X. Sun. **A new tonometer? the CorVis ST tonometer: clinical comparison with non–contact and Goldmann applanation tonometers.** *Invest. Ophthalmol. Vis. Sci.*, 54(1):659–665, Jan 2013. ISSN 1552–5783. DOI: <http://dx.doi.org/10.1167/iov.12-10984>.
- M. Hosny, E. El-Mayah, M. K. Sidky, and M. Anis. **Femtosecond laser–assisted implantation of complete versus incomplete rings for keratoconus treatment.** *Clin. Ophthalmol.*, 9:121–127, Jan 2015. ISSN 1177–5483. DOI: <https://doi.org/10.2147/OPHTH.S73855>.
- L. Ibares-Frías, P. Gallego, R. Cantalapiedra-Rodríguez, M. C. Valseo, S. Mar, J. Merayo-Llodes, and M. C. Martínez-García. **Tissue reaction after intrastromal corneal ring implantation in an experimental animal model.** *Graefes Arch. Clin. Exp. Ophthalmol.*, 253(7):1071–1083, Mar 2015. ISSN 1435–702X. DOI: <https://doi.org/10.1007/s00417-015-2959-5>.
- A. Ihalainen. **Clinical and epidemiological features of keratoconus genetic and external factors in the pathogenesis of the disease.** *Acta Ophthalmol. Suppl.*, 178:1–64, 1986. ISSN 1395–3907.
- K. Jadidi, S. A. Mosavi, F. Nejat, M. Naderi, L. Janani, and S. Serahati. **Intrastromal corneal ring regment implantation (Keraring 355°) in patients with central keratoconus: 6–month follow–up.** *J. Ophthalmol*, 2015(916385):1–8, Jan 2015. ISSN 2090–0058. DOI: <http://dx.doi.org/10.1155/2015/916385>.
- K. Jadidi, F. Nejat, S. A. Mosavi, M. Naderi, A. katirae, L. Janani, and H. Aghamollaei. **Full–ring intrastromal corneal implantation for correcting high myopia in patients with severe keratoconus.** *Med. Hypothesis Discov. Innov. Ophthalmol.*, 5(3):89–95, Oct 2016. ISSN 2322–3219.
- L. Janani, K. Jadidi, S. A. Mosavi, F. Nejat, M. Naderi, and K. Nourijelyani. **MyoRing implantation in keratoconic patients: 3 years follow–up data.** *J. Ophthalmic. Vis. Res.*, 11(1):26–31, Aug 2016. ISSN 2008–322X. DOI: <http://dx.doi.org/10.1016/j.optha.2010.12.012>.
- L. Janani, K. Tanha, F. Najafi, K. Jadidi, F. Nejat, S. J. Hashemian, M. Dehghani, and M. Sadeghi. **Efficacy of complete rings (MyoRing) in treatment of keratoconus: a systematic review and meta–analysis.** *Int. Ophthalmol.*, 39(12):2929–2946, Dec 2019. ISSN 1573–2630. DOI: <https://doi.org/10.1007/s10792-019-01121-9>.
- M. Jaskulski, A. Martínez-Finkeshtein, and NorbertoLópez-Gil. **New objective refraction metric based on sphere fitting to the wavefront.** *J. Ophthalmol*, 2017(1909348):1–9, Sep 2017. ISSN 2090–0058. DOI: <https://doi.org/10.1155/2017/1909348>.

- J. B. Jonas, V. Nangia, A. Matin, M. Kulkarni, and K. Bhojwani. **Prevalence and associations of keratoconus in rural Maharashtra in Central India: the Central India eye and medical study.** *Am. J. Ophthalmol.*, 148(5):760–765, Nov 2009. ISSN 0002–9394. DOI: <https://doi.org/10.1016/j.ajo.2009.06.024>.
- S. N. Kahn and P. S. Shiakolas. **To study the effects of intrastromal corneal ring geometry and surgical conditions on the postsurgical outcomes through finite element analysis.** *J. Mech. Med. Biol.*, 16(7): 1–16, Nov 2016. ISSN 1793–6810. DOI: <http://dx.doi.org/10.1142/S0219519416501013>.
- A. J. Kanellopoulos, L. H. Pe, H. D. Perry, and E. D. Donnenfeld. **Modified intracorneal ring segment implantations (Intacs) for the management of moderate to advanced keratoconus: efficacy and complications.** *Cornea*, 25(1):29–33, Jan 2006. ISSN 1536–4798. DOI: <http://dx.doi.org/10.1097/01.ico.0000167883.63266.60>.
- M.-J. Kang, Y.-S. Byon, Y.-S. Yoo, W.-J. Whang, and C.-K. Joo. **Long-term outcome of intrastromal corneal ring segments in keratoconus: five-year follow-up.** *Sci. Rep.*, 9(315):1–7, Jan 2019. ISSN 2045–2322. DOI: <http://dx.doi.org/10.1038/s41598-018-36668-7>.
- R. H. Kennedy, W. M. Bourne, and J. A. Dyer. **A 48-Year clinical and epidemiologic study of keratoconus.** *Am. J. Ophthalmol.*, 101(3):267 – 273, Mar 1986. ISSN 0002–9394. DOI: [https://doi.org/10.1016/0002-9394\(86\)90817-2](https://doi.org/10.1016/0002-9394(86)90817-2).
- M. C. Kenney and D. J. Brown. **The cascade hypothesis of keratoconus.** *Cont. Lens Anterior Eye.*, 26(3): 139–146, Sep 2003. ISSN 1367–0484. DOI: [http://dx.doi.org/10.1016/S1367-0484\(03\)00022-5](http://dx.doi.org/10.1016/S1367-0484(03)00022-5).
- M. C. Kenney, D. J. Brown, and B. Rajeev. **Everett Kinsey lecture. The elusive causes of keratoconus: a working hypothesis.** *CLAO J.*, 26(1):10–13, Jan 2000. ISSN 0733-8902.
- Keravision. **Attachment 6: Stress and Wear studies of Corneal implants. IntactsR.** *n/j, n/y.*
- B. Khosravi, M. Khorrami-Nejad, S. Rajabi, M. Amiri, H. Hashemian, and mehdi Khodaparast. **Characteristics of astigmatism after MyoRing implantation.** *Med. Hypothesis Discov. Innov. Ophthalmol.*, 6(4):130–135, Feb 2017. ISSN 2322–3219.
- S. Kling and S. Marcos. **Finite-element modeling of intrastromal ring segment implantation into a hyperelastic cornea.** *Invest. Ophthalmol. Vis. Sci.*, 54(1):881–889, Jan 2013. ISSN 1552–5783. DOI: <http://dx.doi.org/10.1167/iovs.12-10852>.
- S. Kling, N. Bekesi, C. Dorrnsoro, D. Pascual, and S. Marcos. **Corneal viscoelastic properties from finite-element analysis of in vivo air-puff deformation.** *PLoS One*, 9(8):e104904, Aug 2014. ISSN 1932–6203. DOI: <http://dx.doi.org/10.1371/journal.pone.0104904>.
- H. Kobashi and S. S. Rong. **Corneal collagen cross-linking for keratoconus: systematic review.** *Biomed Res. Int.*, 2016(8145651):1–7, Jun 2017. ISSN 2314–6141. DOI: <http://dx.doi.org/10.1155/2017/8145651>.

- C. Koppen, I. Leysen, and M.-J. Tassignon. **Riboflavin/UVA cross-linking for keratoconus in Down Syndrome.** *J. Refract. Surg.*, 26(9):623–624, Sep 2010. ISSN 1938–2391. DOI: <https://doi.org/10.3928/1081597X-20100824-01>.
- E. Korkmaz, R. Onler, and O. B. Ozdoganlar. **Micromilling of poly(methyl methacrylate, PMMA) using single crystal diamond tools.** *Procedia Manuf.*, 10(2017):683–693, 2017. ISSN 2351–9789. DOI: <https://doi.org/10.1016/j.promfg.2017.07.017>.
- J. H. Krachmer, R. S. Feder, and M. W. Belin. **Keratoconus and related noninflammatory corneal thinning disorders.** *Surv. Ophthalmol.*, 28(4):293–322, Jan–Feb 1984. ISSN 0039–6257. DOI: [https://doi.org/10.1016/0039-6257\(84\)90094-8](https://doi.org/10.1016/0039-6257(84)90094-8).
- A. Kubaloglu, Y. Cinar, E. S. Sari, A. Koytak, B. Ozdemir, and Y. Ozertürk. **Comparison of 2 intrastromal corneal ring segment models in the management of keratoconus.** *J. Cataract. Refract. Surg.*, 36(6): 978–985, Jun 2010a. ISSN 0886–3350. DOI: <https://doi.org/10.1016/j.jcrs.2009.12.031>.
- A. Kubaloglu, E. S. Sari, Y. Cinar, K. Cingu, A. Koytak, E. Coxskun, and Y. Özertürk. **Comparison of mechanical and femtosecond laser tunnel creation for intrastromal corneal ring segment implantation in keratoconus.** *J. Cataract. Refract. Surg.*, 36(9):1556–1561, Sep 2010b. ISSN 0886–3350. DOI: <http://dx.doi.org/10.1016/j.jcrs.2010.04.028>.
- M. Kubrak-Kisza, K. J. Kisza, and M. Misiuk-Hojło. **Corneal cross-linking: an example of photoinduced polymerization as a treatment modality in keratoconus.** *Polim. Med.*, 46(1):89–94, Jan–Jun 2016. ISSN 2451–2699. DOI: <http://dx.doi.org/10.17219/pim/65010>.
- S. Kwitko and N. S. Severo. **Ferrara intracorneal ring segments for keratoconus.** *J. Cataract Refract. Surg.*, 30(4):812–820, 2004. ISSN 1873–4502. DOI: <http://dx.doi.org/10.1016/j.jcrs.2003.12.005>.
- M. Lago, M. Rupérez, C. Monserrat, F. Martínez-Martínez, S. Martínez-Sanchís, E. Larra, M. Díez-Ajenjo, and C. Peris-Martínez. **Patient-specific simulation of the intrastromal ring segment implantation in corneas with keratoconus.** *J. Mech. Behav. Biomed. Mater.*, 51:260–268, Nov 2015. ISSN 1751–6161. DOI: <https://doi.org/10.1016/j.jmbbm.2015.07.023>.
- V. Lakshminarayanan and A. Fleck. **Zernike polynomials: a guide.** *J. Mod. Opt.*, 58(7):545–561, Apr 2011. ISSN 0950–0340. DOI: <http://dx.doi.org/10.1080/09500340.2011.554896>.
- H. Laqua. **Hereditary diseases in keratoconus.** *Klin. Monbl. Augenheilkd.*, 159(5):609–618, Nov 1971. ISSN 1439–3999.
- X.-L. Liu, P.-H. Li, P. Fournie, and F. Malecaze. **Investigation of the efficiency of intrastromal ring segments with cross-linking using different sequence and timing for keratoconus.** *Int. J. Ophthalmol.*, 8(4): 703–708, Aug 2015. ISSN 2222–3959. DOI: <http://dx.doi.org/10.3980/j.issn.2222-3959.2015.04.11>.
- H. Lubatschowski, G. Maatz, A. Heisterkamp, U. Hetzel, W. Drommer, H. Welling, and W. Ermer. **Application of ultrashort laser pulses for intrastromal refractive surgery.** *Graefes Arch. Clin. Exp. Ophthalmol.*, 238(1):33–39, Jun 2000. ISSN 1435–702X. DOI: <https://doi.org/10.1007/s004170050006>.

- J. M. Lyra, D. Lyra, G. Ribeiro, L. Torquetti, P. Ferrara, and A. Machado. **Tomographic findings after implantation of Ferrara intrastromal corneal ring segments in keratoconus.** *J. Refract. Surg.*, 33(2):110–115, Oct 2017. ISSN 1938–2391. DOI: <http://dx.doi.org/10.3928/1081597X-20161027-02>.
- S. A. Maas, B. J. Ellis, G. A. Ateshian, and J. A. Weiss. **FEBio: Finite elements for biomechanics.** *J. Biomech. Eng.*, 134(1):011005–1–011005–10, 2012. ISSN 1528–8951. DOI: <https://doi.org/10.1115/1.4005694>.
- P. Maier, T. Reinhard, and M. Kohlhass. **Corneal collagen cross-linking in the stabilization of keratoconus.** *Dtsch. Arztebl. Int.*, 116(11):184–190, Mar 2019. ISSN 1866–0452. DOI: <http://dx.doi.org/10.3238/arztebl.2019.0184>.
- D. Malacara and Z. Malacara. **Handbook of Optical Design.** Marcel Dekker, 2nd edition, 2003. ISBN 0–8247–4613–9.
- F. Malecaze, N. Chassaing, and P. Calvas. **Textbook on keratoconus: new insights**, chapter 2, pages 12–17. Jaypee Brothers Medical Publishers, 1st edition, 2012. ISBN 978–93–5025–404–2.
- S. A. Marchitti, Y. Chen, D. C. Thompson, and V. Vasiliou. **Ultraviolet radiation: cellular antioxidant response and the role of ocular aldehyde dehydrogenase enzymes.** *Eye Contact Lens*, 37(4):206–213, Apr 2011. ISSN 1542–233X. DOI: <http://dx.doi.org/10.1097/icl.0b013e3182212642>.
- MATLAB. *version 7.13.0 (R2013a)*. The MathWorks Inc., Natick, Massachusetts, 2013.
- I. H. Maumenee. **The eye in the Marfan syndrome.** *Trans. Am. Ophthalmol. Soc.*, 79:684–733, 1981. ISSN 1545–6110.
- C. W. McMonnies. **Keratoconus fittings: apical clearance or apical support?** *Eye Contact Lens*, 30(3): 147–155, Jul 2004. ISSN 1542–233X. DOI: <http://dx.doi.org/10.1097/01.icl.0000138717.57592.36>.
- C. W. McMonnies. **Mechanisms of Rubbing-Related Corneal Trauma in Keratoconus.** *Cornea*, 28(6): 607–615, Jul 2009. ISSN 1536–4798. DOI: <http://dx.doi.org/10.1097/ICO.0b013e318198384f>.
- C. W. McMonnies. **Screening for keratoconus suspects among candidates for refractive surgery.** *Clin. Exp. Optom.*, 97:492–498, Apr 2014. ISSN 1444–0938. DOI: <http://dx.doi.org/10.1111/cxo.12169>.
- M. Millodot, E. Shneor, S. Albou, E. Atlani, and A. Gordon-Shaag. **Prevalence and associated factors of keratoconus in Jerusalem: a cross-sectional study.** *Ophthalmic Epidemiol.*, 18(2):91–97, Mar 2011. ISSN 1744–5086. DOI: <https://doi.org/10.3109/09286586.2011.560747>.
- M. Mohebbi, H. Hashemi, S. Asgari, S. Bigdeli, and K. A. Zamani. **Visual outcomes after femtosecond-assisted intracorneal MyoRing implantation: 18 months of follow-up.** *Graefes Arch. Clin. Exp. Ophthalmol.*, 254(5):917–922, May 2016. ISSN 1435–702X. DOI: <https://doi.org/10.1007/s00417-015-3231-8>.
- D. C. Montgomery. **Design and Analysis of Experiments.** John Wiley and Sons, 10th edition, Jun 2019. ISBN 978–1–119–49244–3.

- R. Navarro, L. González, and J. L. Hernández. **Optics of the average normal cornea from general and canonical representations of its surface topography.** *J. Opt. Soc. Am.*, 23(2):219–32, Feb 2006. ISSN 1084–7529. DOI: <https://doi.org/10.1364/JOSAA.23.000219>.
- K. Nielsen, J. Hjortdal, E. A. Nohr, and N. Ehlers. **Incidence and prevalence of keratoconus in Denmark.** *Acta Ophthalmol. Scand.*, 85(8):890–892, Dec 2007. ISSN 1395–3907. DOI: <http://dx.doi.org/10.1111/j.1600-0420.2007.00981.x>.
- R. R. Nigrovič, J. Meško, R. R. Nikolić, V. Lazić, D. Arsić, and B. Hadzima. **Comparison of the PMMA mechanical properties after cutting by the laser beam and milling.** *FME Trans.*, 46(1):57–61, Nov 2017. ISSN 1451–2092. DOI: <http://dx.doi.org/10.5937/fmet1801057N>.
- S. M. Nobari, C. Villena, and K. Jadidi. **Predictability, stability and safety of MyoRing implantation in keratoconic eyes during one year follow-up.** *Iran. J. Ophthalmol.*, 26(3):136–143, Dec 2014. ISSN 2452–2325.
- D. M. Nowak and M. Gajecka. **The genetics of keratoconus.** *Middle East Afr. J. Ophthalmol.*, 18(1):2–6, Mar 2011. ISSN 0974–9233. DOI: <http://dx.doi.org/10.4103/0974-9233.75876>.
- D. O’Brat. **Keratoconus: recent advances in diagnosis and treatments**, chapter 19, pages 219–238. Springer Nature, 2017. ISBN 978-3-319-43879-5. DOI: <https://doi.org/10.1007/978-3-319-43881-8>.
- T. Olsen. **On the calculation of power from curvature of the cornea.** *Br. J. Ophthalmol.*, 70(2):152–154, Jun 1986. ISSN 1468–2079. DOI: <https://doi.org/10.1136/bjo.70.2.152>.
- H. Owens and G. Gamble. **A profile of keratoconus in New Zealand.** *Cornea*, 22(2):122–125, Jan 2003. ISSN 1536–4798. DOI: <http://dx.doi.org/10.1097/00003226-200303000-00008>.
- A. Pandolfi and G. A. Holzapfel. **Three-dimensional modeling and computational analysis of the human cornea considering distributed collagen fibril orientation.** *J. Biomech. Eng.*, 130(6):1–11, Dec 2008. ISSN 1528–8951. DOI: <https://doi.org/10.1115/1.2982251>.
- A. Pandolfi and M. Vasta. **Fiber distributed hyperelastic modeling of biological tissues.** *Mech. Mater.*, 44 (Supplement C):151–162, Jan 2012. ISSN 0167–6636. DOI: <https://doi.org/10.1016/j.mechmat.2011.06.004>. Microstructures and anisotropies.
- A. Pearson, B. Soneji, N. Sarvananthan, and J. Sandford-Smith. **Does ethnic origin influence the incidence or severity of keratoconus?** *Eye*, 14(Pt 4):625–628, Feb 2000. ISSN 1476–5454. DOI: <http://dx.doi.org/10.1038/eye.2000.154>.
- L. Pedersen, J. Hjortdal, and N. Ehlers. **Central corneal thickness in high myopia.** *Acta Ophthalmol. Scand.*, 83(5):539–542, Jul 2005. ISSN 1395–3907. DOI: <https://doi.org/10.1111/j.1600-0420.2005.00498.x>.

- P. Peña-García, J. L. Alió, A. Vega-Estrada, and R. I. Barraquer. **Internal, corneal, and refractive astigmatism as prognostic factors for intrastromal corneal ring segment implantation in mild to moderate keratoconus.** *J. Cataract. Refract. Surg.*, 40(10):1633–1644, Oct 2014. ISSN 0886–3350. DOI: <http://dx.doi.org/10.1016/j.jcrs.2014.01.047>.
- C. Perez-Straziota, R. N. Gaster, and Y. S. Rabinowitz. **Corneal cross-linking for pediatric keratoconus (Review).** *Cornea*, 37(6):802–809, Jun 2018. ISSN 1536–4798. DOI: <http://dx.doi.org/10.1097/ICO.0000000000001579>.
- C. Peris-Martínez and Á. L. Cisneros Lanuza. **Biomechanics and architecture corneal**, chapter 3, pages 25–34. 2014. ISBN 978–84–9022–649–0.
- D. P. Piñero, J. L. Alio, B. E. Kady, E. Coskunseven, H. Morbelli, A. Uceda-Montanes, M. J. Maldonado, D. Cuevas, and I. Pascual. **Refractive and aberrometric outcomes of intracorneal segments for Keratoconus: mechanical versus femtosecond–assisted procedures.** *Ophthalmology*, 116(9):1675–1687, Jul 2009. ISSN 0161–6420. DOI: <http://dx.doi.org/10.1016/j.ophtha.2009.05.016>.
- D. P. Piñero, J. L. Alió, R. I. Barraquer, R. Michael, and R. Jiménez. **Corneal biomechanics, refraction, and corneal aberrometry in keratoconus: an integrated study.** *Invest. Ophthalmol. Vis. Sci.*, 51(4): 1948–1955, Apr 2010. ISSN 1552–5783. DOI: <http://dx.doi.org/10.1167/iovs.09-4177>.
- D. P. Piñero, J. L. Alió, M. A. Teus, R. I. Barraquer, and A. Uceda-Montañes. **Modeling the intracorneal ring segment effect in keratoconus using refractive, keratometric, and corneal aberrometric data.** *Invest. Ophthalmol. Vis. Sci.*, 51(11):5583–5591, Nov 2010. ISSN 1552–5783. DOI: <http://dx.doi.org/10.1167/iovs.09-5017>.
- S. Pirhadi, N. Mohammadi, S. A. Mosavi, H. Daryabari, H. Aghamollaei, and K. Jadidi. **Comparison of the MyoRing implantation depth by mechanical dissection using PocketMaker microkeratome versus Melles hook via AS-OCT.** *BMC Ophthalmol.*, 18(1):1–8, Jun 2018. ISSN 1471–2415. DOI: <http://dx.doi.org/10.1186/s12886-018-0806-2>.
- Y. Pouliquen, M. Forman, and J. Giraud. **Evaluation of the rapidity of progression of keratoconus by a study of the relationship between age when first detected and age at operation.** *J. Fr. Ophthalmol.*, 4(3):219–221, 1981. ISSN 0181–5512.
- Y. S. Rabinowitz. **Keratoconus.** *Surv. Ophthalmol.*, 42(4):297–319, Jan–Feb 1998. ISSN 0039–6257. DOI: [http://dx.doi.org/10.1016/S0039-6257\(97\)00119-7](http://dx.doi.org/10.1016/S0039-6257(97)00119-7).
- Y. S. Rabinowitz. **The genetics of keratoconus.** *Ophthalmol. Clin. North. Am.*, 16(4):607–620, Dec 2003. ISSN 0896–1549. DOI: [http://dx.doi.org/10.1016/s0896-1549\(03\)00099-3](http://dx.doi.org/10.1016/s0896-1549(03)00099-3).
- Y. S. Rabinowitz. **Intacs for keratoconus.** *Int. Ophthalmol. Clinics*, 46(3):91–103, Mar 2006. ISSN 0020–8167.
- J. Rada, S. Shelton, and T. Norton. **The sclera and myopia.** *Exp. Eye. Res.*, 82(2):185–200, Feb 2006. ISSN 0014–4835. DOI: <http://dx.doi.org/10.1016/j.exer.2005.08.009>.

- A. H. S. Rahi, P. Davies, M. Ruben, D. Lobascher, and J. Menon. **Keratoconus and coexisting atopic disease.** *Br. J. Ophthalmol.*, 61(12):761–764, Dec 1977. ISSN 1468–2079. DOI: <https://doi.org/10.1136/bjo.61.12.761>.
- B. Ramez, T. Andrew MJ, H. Parwez, A. David F, and B. Adel. **Keratoconus: recent advances in diagnosis and treatments**, chapter 3, pages 13–23. Springer Nature, 2017. ISBN 978-3-319-43879-5. DOI: <https://doi.org/10.1007/978-3-319-43881-8>.
- S. A. Rattan. **Continuous intracorneal ring implantation for treatment of myopic astigmatism.** *International Medical Case Reports Journal*, 2018(11):217–220, Sep 2018. ISSN 1179–142X. DOI: <https://doi.org/10.2147/IMCRJ.S173167>.
- L. Remón, D. Siedlecki, I. Cabeza-Gil, and B. Calvo. **Influence of material and haptic design on the mechanical stability of intraocular lenses by means of finite-element modeling.** *J. Biomed. Opt.*, 23(3):1–10, Mar 2018. ISSN 1560–2281. DOI: <https://doi.org/10.1117/1.JBO.23.3.035003>.
- F. Ridley. **Contact lenses in treatment of keratoconus.** *Br. J. Ophthalmol.*, 40(295):295–304, 1956. ISSN 1468–2079. DOI: <http://dx.doi.org/10.1136/bjo.40.5.295>.
- R. S. Rivlin. **Large elastic deformations of isotropic materials IV. Further developments of the general theory.** *Philos. Trans. R. Soc. Lond.*, 241(835):379–397, Oct 1948. ISSN 1471–2962. DOI: <https://doi.org/10.1098/rsta.1948.0024>.
- N. Roba, E. Duncan, G. Hill, N. Spencer, and S. Tosatti. **Friction measurements on contact lenses in their operating environment.** *Tribol. Lett.*, 44:387–397, Sep 2011. ISSN 1573–2711. DOI: <https://doi.org/10.1007/s11249-011-9856-9>.
- G. A. d. N. Rocha, P. F. de Almeida Cunha, L. T. Costa, and L. B. de Sousa. **Outcomes of a 320-degree intrastromal corneal ring segment implantation for keratoconus: results of a 6-month follow-up.** *Eur. J. Ophthalmol.*, 30(1):139–146, Nov 2018. ISSN 1120–6721. DOI: <https://doi.org/10.1177/1120672118818018>.
- S. Romagnani. **The increased prevalence of allergy and the hygiene hypothesis: missing immune deviation, reduced immune suppression, or both?** *Immunology*, 112(3):352–363, Apr 2004. ISSN 1365–2567. DOI: <http://dx.doi.org/10.1111/j.1365-2567.2004.01925.x>.
- H. L. Roth and R. R. Kierland. **The natural history of atopic dermatitis: a 20-year follow-up study.** *Arch. Dermatol. Res.*, 89(2):209–214, Feb 1964. ISSN 0003–987X. DOI: <https://doi.org/10.1001/archderm.1964.01590260047008>.
- Y. Saad and A. I. A. Somali. **Outcomes of MyoRing implantation in eyes with keratoconus in the eastern province of Saudi Arabia: “a single-arm cohort study”.** *J. Ophthalmol.*, 2019(2630704):1–4, Aug 2019. ISSN 2090–0058. DOI: <https://doi.org/10.1155/2019/2630704>.
- A. M. Saeed. **Corneal intrastromal MyoRing implantation in keratoconus treatment.** *J. Egypt. Ophthalmol. Soc.*, 107(2):108–112, Mar 2014. ISSN 2314–6648. DOI: <https://doi.org/10.4103/2090-0686.140647>.

- D. Sakellaris, M. Balidis, O. Gorou, N. Szentmary, A. Alexoudis, M. C. Grieshaber, D. Sagri, H. Scholl, and Z. Gatzioufas. **Intracorneal ring segment implantation in the management of keratoconus: an evidence-based approach.** *Ophthalmol. Ther.*, 8(S1):S5–S14, Aug 2019. ISSN 2193–6528. DOI: <https://doi.org/10.1007/s40123-019-00211-2>.
- A. Saltelli, M. Ratto, T. Andrés, F. Campolongo, J. Cariboni, D. Gatelli, M. Saisana, and S. Tarantola. **Global Sensitivity Analysis. The Primer.** John Wiley and Sons, 2008. ISBN 978–0–4700–5997–5. DOI: <https://doi.org/10.1002/9780470725184>.
- E. L. Sancho. **Modelado Biomecánico de los componentes refractivos del ojo humano y tratamientos refractivos asociados.** Phd Thesis. PhD thesis, University of Zaragoza, 2010.
- J. Sandes, L. R. S. Stival, M. P. de Ávila, P. Ferrara, G. Ferrara, L. Magacho, L. P. N. Araújo, and L. Torquetti. **Clinical outcomes after implantation of a new intrastromal corneal ring with 140-degree of arc in patients with corneal ectasia.** *Int. J. Ophthalmol.*, 11(5):808–806, May 2018. ISSN 2222–3959. DOI: <http://dx.doi.org/10.18240/ijo.2018.05.14>.
- G. Savini, K. J. Hoffer, D. S. Lomoriello, and P. Ducoli. **Simulated keratometry versus total corneal power by ray tracing: a comparison in prediction accuracy of intraocular lens power.** *Cornea*, 36(11): 1368–1372, Nov 2017. ISSN 1536–4798. DOI: <https://doi.org/10.1097/ICO.0000000000001343>.
- T. Seiler, M. Matallana, S. Sendler, and T. Bende. **Does Bowman’s layer determine the biomechanical properties of the cornea?** *Refract Corneal Surg.*, 8(2):139–142, Mar–Apr 1992. ISSN 1042–962X.
- M. M. Seleet, A. H. Soliman, and O. M. Alaaeldin. **Femtosecond laser intracorneal ring segment implantation based on a nomogram modification in type 1 and type 2 ectasia.** *J. Egypt. Ophthalmol. Soc.*, 108(1):1–5, Jan 2015. ISSN 2314–6648. DOI: <https://doi.org/10.4103/2090-0686.160328>.
- M. H. Shabayek and J. L. Alio. **Intrastromal corneal ring segment implantation by femtosecond laser for keratoconus correction.** *Ophthalmology*, 114(9):1643–1652, Sep 2007. ISSN 0161–6420. DOI: <http://dx.doi.org/10.1016/j.ophtha.2006.11.033>.
- S. Shahhoseini, H. Hashemi, and S. Asgari. **Intracorneal ring segment depth in keratoconus patients: a long-term follow-up study.** *Int. Ophthalmol.*, 38(4):1379–1383, Jun 2018. ISSN 1573–2630. DOI: <http://dx.doi.org/10.1007/s10792-017-0595-2>.
- A. L. Sheppard and J. S. Wolffsohn. **Digital eye strain: prevalence, measurement and amelioration.** *BMJ Open Ophthalmol.*, 3(1):1–10, Mar 2018. ISSN 2397–3269. DOI: <http://dx.doi.org/10.1136/bmjophth-2018-000146>.
- T. Sherwin, S. Ismail, I.-P. Loh, and J. J. McGhee. **Keratoconus: recent advances in diagnosis and treatments**, chapter 4, pages 25–41. Springer Nature, 2017. ISBN 978-3-319-43879-5. DOI: <https://doi.org/10.1007/978-3-319-43881-8>.

- R. Shetty, M. Kurian, D. Anand, P. Mhaske, K. M. Narayana, and B. K. Shetty. **Intacs in advanced keratoconus.** *Cornea*, 27(9):1022–1029, Oct 2008. ISSN 1536–4798. DOI: <http://dx.doi.org/10.1097/ICO.0b013e318172fc54>.
- E. Shneor, M. Millodot, A. Gordon-Shaag, M. Essa, M. Anton, R. Barbara, and A. Barbara. **Prevalence of keratoconus among young Arab students in Israel.** *IJKECD*, 3(1):9–14, Jan–Apr 2014. ISSN 2277–4203. DOI: <https://doi.org/10.5005/jp-journals-10025-1070>.
- I. Simonini, M. Angelillo, and A. Pandolfi. **Theoretical and numerical analysis of the corneal air puff test.** *J. Mech. Phys. Solids*, 93:118–134, Aug 2016. ISSN 0022–5096. DOI: <http://dx.doi.org/10.1016/j.jmps.2016.04.012>.
- N. Sorkin, A. Rosenblatt, D. Samadja, E. Cohen, M. R. Santhiago, D. Varsano, and Y. Yatziv. **Early refractive and clinical outcomes of high-myopic photorefractive keratectomy as an alternative to LASIK surgery in eyes with high preoperative percentage of tissue altered.** *J. Ophthalmol.*, 2019(6513143):1–6, Jan 2019. ISSN 2090–0058. DOI: <https://doi.org/10.1155/2019/6513143>.
- W. H. Spencer and J. J. Fischer. **The association of keratoconus with atopic dermatitis.** *Am. J. Ophthalmol.*, 47(3):332–334, Mar 1959. ISSN 0002–9394. DOI: [https://doi.org/10.1016/S0002-9394\(14\)76533-X](https://doi.org/10.1016/S0002-9394(14)76533-X).
- E. Spörl, M. Huhle, M. Kasper, and T. Seiler. **Erhöhung der Festigkeit der Hornhaut durch Vernetzung.** *Ophthalmologe*, 94:902–906, 1997. ISSN 1433–0423. DOI: <https://doi.org/10.1007/s003470050219>.
- E. Spörl, M. Huhle, and T. Seiler. **Induction of cross-linking in corneal tissue.** *Exp. Eye. Res.*, 66(1):97–103, Jan 1998. ISSN 0014–4835. DOI: <https://doi.org/10.1006/exer.1997.0410>.
- E. Spörl, J. Schreiber, K. Hellmund, T. Seiler, and P. Knuschke. **Untersuchungen zur Verfestigung der Hornhaut am Kaninchen.** *Ophthalmologe*, 97:203–206, Mar 2000. ISSN 1433–0423. DOI: <https://doi.org/10.1007/s003470050515>.
- E. Spörl, M. Mrochen, D. Sliney, S. Trokel, and T. Seiler. **Safety of UVA–Riboflavin cross-linking of the cornea.** *Cornea*, 26(4):385–389, Apr 2007. ISSN 1536–4798. DOI: <https://doi.org/10.1097/ICO.0b013e3180334f78>.
- D. A. Street, E. T. Vinokur, G. O. Waring, S. J. Pollak, S. D. Clements, and J. V. Perkins. **Lack of Association between Keratoconus, Mitral Valve Prolapse, and Joint Hypermobility.** *Ophthalmology*, 98(2):170–176, Feb 1991. ISSN 0161–6420. DOI: [https://doi.org/10.1016/S0161-6420\(91\)32320-0](https://doi.org/10.1016/S0161-6420(91)32320-0).
- J. Sugar and M. S. Macsai. **What causes keratoconus?** *Cornea*, 31(6):716–719, Jun 2012. ISSN 1536–4798. DOI: <http://dx.doi.org/10.1097/ICO.0b013e31823f8c72>.
- L. N. Thibos, X. Hong, A. Bradley, and R. A. Applegate. **Accuracy and precision of objective refraction from wavefront aberrations.** *J. Vis.*, 4(9):329–351, Apr 2004. ISSN 1534–7362. DOI: <http://dx.doi.org/10.1167/4.4.9>.

- L. Torquetti, G. Ferrara, F. Almeida, L. Cunha, P. Ferrara, and J. Merayo-Llodes. **Clinical outcomes after intrastromal corneal ring segments reoperation in keratoconus patients.** *Int. J. Ophthalmol.*, 6(6): 796–800, Dec 2013. ISSN 2222–3959. DOI: <http://dx.doi.org/10.3980/j.issn.2222-3959.2013.06.10>.
- L. Torquetti, C. Arce, J. Merayo-Llodes, G. Ferrara, P. Ferrara, B. Signorelli, and A. Signorelli. **Evaluation of anterior and posterior surfaces of cornea using a dual Scheimpflug analyzer in keratoconus patients implanted with intrastromal corneal ring segments.** *Int. J. Ophthalmol.*, 9(9):1283–1288, Sep 2016. ISSN 2222–3959. DOI: <http://dx.doi.org/10.18240/ijo.2016.09.08>.
- G. van Rossum and F. L. Drake. **Python 3 Reference Manual.** CreateSpace, Scotts Valley, CA, 2009. ISBN 978-1-4414-1269-0. DOI: <https://doi.org/10.5555/1593511>.
- J. van Splunder, J. S. Stilma, R. M. D. Bernsen, and H. M. Evenhuis. **Prevalence of ocular diagnoses found on Screening 1539 adults with intellectual disabilities.** *Ophthalmology*, 111:1457–1463, Jan 2004. ISSN 0161-6420. DOI: <https://doi.org/10.1016/j.ophtha.2003.12.051>.
- A. Vega-Estrada and J. Alio. **The use of intracorneal ring segments in keratoconus.** *Eye Vis.*, 3(8):1–7, Mar 2016. ISSN 2326–0254. DOI: <https://doi.org/10.1186/s40662-016-0040-z>.
- B. Wadhawa and V. Karambelkar. **Ocular biometrics: study of myopia, using A-Scan and keratometer.** *Int. J. Contemp. Med. Res.*, 6(3):C5–C8, Mar 2019. ISSN 2393–915X. DOI: <http://dx.doi.org/10.21276/ijcmr.2019.6.3.16>.
- N. Waked, A. Fayad, A. Fadlallah, and H. E. Rami. **Dépistage du kératocône dans une population universitaire au Liban.** *J. Fr. Ophthalmol.*, 35(1):23–29, Jun 2012. ISSN 0181–5512. DOI: <https://doi.org/10.1016/j.jfo.2011.03.016>.
- K. Weed, C. MacEwen, T. Giles, J. Low, and C. McGhee. **The Dundee UNiversity Scottish Keratoconus study: demographics, corneal signs, assoated diseases, and eye rubbing.** *Eye*, 22(2008):534–541, Jan 2007. ISSN 1476–5454. DOI: <http://dx.doi.org/10.1038/sj.eye.6702692>.
- M. Winkler, G. Shoa, Y. Xie, S. J. Petsche, P. M. Pinsky, T. Juhasz, D. J. Brown, and J. V. Jester. **Three-Dimensional distribution of transverse collagen fibers in the anterior human corneal stroma.** *Invest. Ophthalmol. Vis. Sci.*, 54(12):7293–7301, Oct 2013. ISSN 1552–5783. DOI: <https://doi.org/10.1167/iovs.13-13150>.
- G. Wollensak and E. Iomdina. **Long-term biomechanical properties of rabbit cornea after photodynamic collagen cross-linking.** *Acta Ophthalmol.*, 87(1):48–51, Feb 2009. ISSN 1755–3768. DOI: <https://doi.org/10.1111/j.1755-3768.2008.01190.x>.
- G. Wollensak, E. Spörl, F. Reber, L. Pillunat, and R. Funk. **Corneal endothelial cytotoxicity of riboflavin/YVA treatment *in vitro*.** *Ophthalmic Res.*, 35(6):324–328, Jun 2003a. ISSN 1423–0259. DOI: <https://doi.org/10.1159/000074071>.

- G. Wollensak, E. Spörl, and T. Seiler. **Riboflavin/ultraviolet-a-induced collagen cross-linking for the treatment of keratoconus.** *Am. J. Ophthalmol.*, 135(5):620–627, Jun 2003b. ISSN 0002–9394. DOI: [http://dx.doi.org/10.1016/S0002-9394\(02\)02220-1](http://dx.doi.org/10.1016/S0002-9394(02)02220-1).
- G. Wollensak, E. Spörl, and T. Seiler. **Stress–strain measurements of human and porcine corneas after riboflavin–ultraviolet–a–induced cross–linking.** *J. Cataract. Refract. Surg.*, 29(9):1780–1785, Mar 2003c. ISSN 0886–3350. DOI: [https://doi.org/10.1016/s0886-3350\(03\)00407-3](https://doi.org/10.1016/s0886-3350(03)00407-3).
- G. Wollensak, E. Spörl, M. Wilsch, and T. Seiler. **Endothelial cell damage after riboflavin-ultraviolet-A treatment in the rabbit.** *J. Cataract. Refract. Surg.*, 29(9):1786–1790, Sep 2003d. ISSN 0886–3350. DOI: [https://doi.org/10.1016/s0886-3350\(03\)00343-2](https://doi.org/10.1016/s0886-3350(03)00343-2).
- G. Wollensak, E. Spörl, F. Reber, and T. Seiler. **Keratocyte cytotoxicity of riboflavin/UVA-treatment *in vitro*.** *Eye*, 18(7):718–722, Jul 2004. ISSN 1476–5454. DOI: <https://doi.org/10.1111/10.1038/sj.eye.6700751>.
- O. Yeoh. **Some forms of the strain energy function for rubber.** *Rubber Chem. Technol.*, 66(5):754–771, Nov 1993. ISSN 1943–4804. DOI: <https://doi.org/10.5254/1.3538343>.
- A. Yildirim, H. Cakir, N. Kara, and H. Uslu. **Long-term outcomes of intrastromal corneal ring segment implantation for post–LASIK ectasia.** *Cont. Lens Anterior Eye.*, 37(6):469–472, Dec 2014. ISSN 1367–0484. DOI: <https://doi.org/10.1097/ICO.0b013e3180334f78>.
- M. O. Yousif and A. M. A. Said. **Comparative study of 3 intracorneal implant types to manage central keratoconus.** *J. Cataract. Refract. Surg.*, 44(3):295–305, Mar 2018. ISSN 0886–3350. DOI: <http://dx.doi.org/10.1016/j.jcrs.2017.12.020>.
- M. A. Zare, H. Hashemi, and M. R. Salari. **Intracorneal ring segment implantation for the management of keratoconus: safety and efficacy.** *J. Cataract. Refract. Surg.*, 33(11):1886–1891, Nov 2007. ISSN 0886–3350. DOI: <http://dx.doi.org/10.1016/j.jcrs.2007.06.055>.

